

Fiscal Year 2020: Third Quarter

Progress Reports:  
**Advanced Battery Materials Research  
(BMR) Program  
&  
Battery500 Consortium**

**Released September 2020  
for the period of April – June 2020**

*Approved by*

Tien Q. Duong, Program Manager  
Advanced Battery Materials Research Program & Battery500 Consortium  
Vehicle Technologies and Electrification Program  
Energy Efficiency and Renewable Energy

## TABLE OF CONTENTS

### A Message from the Manager:

**Advanced Battery Materials Research Program and Battery500 Consortium ..... xxv**

### Advanced Battery Materials Research Program

<b>Task 1 – Liquid/Polymer Solid-State Electrolytes.....</b>	<b>1</b>
Task 1.1 – Advanced Lithium-Ion Battery Technology: High-Voltage Electrolyte (Joe Sunstrom, Ron Hendershot, and Alec Falzone, Daikin) .....	4
Task 1.2 – Multi-Functional, Self-Healing Polyelectrolyte Gels for Long-Cycle-Life, High-Capacity Sulfur Cathodes in Lithium-Sulfur Batteries (Alex Jen and Jihui Yang, University of Washington) .....	7
Task 1.3 – Dual Function Solid-State Battery with Self-Forming, Self-Healing Electrolyte and Separator (Esther Takeuchi, Stony Brook University) .....	12
Task 1.4 – Characterization and Modeling of Li-Metal Batteries: Characterization of Li <sup>+</sup> Transport in Polyelectrolytes (Bryan D. McCloskey, University of California at Berkeley) .....	16
Task 1.5 – Advanced Polymer Materials for Batteries (Zhenan Bao and Yi Cui, Stanford University) .....	19
Task 1.6 – Improving the Stability of Lithium-Metal Anodes and Inorganic-Organic Solid Electrolytes (Nitash Balsara, Lawrence Berkeley National Laboratory) .....	23
Task 1.7 – Development of Thin, Robust, Lithium-Impenetrable, High-Conductivity, Electrochemically Stable, Scalable, and Low-Cost Glassy Solid Electrolytes for Solid-State Lithium Batteries (Steve Martin, Iowa State University of Science and Technology) .....	27
Task 1.8 – Composite Solid Ion Conductor with Engineered Lithium Interface (Kyler Carroll and Cam Peebles, Wildcat Discovery Technologies) .....	35
Task 1.9 – Physical and Mechano-Electrochemical Phenomena of Thin-Film Lithium-Ceramic Electrolyte Constructs (Jeff Sakamoto, University of Michigan).....	39
Task 1.10 – Lithium Dendrite-Free Li <sub>7</sub> N <sub>2</sub> I-LiOH Solid Electrolytes for High-Energy Lithium Batteries (Chunsheng Wang, University of Maryland).....	41
Task 1.11 – Hot Pressing of Reinforced Li-NMC All-Solid-State Batteries with Sulfide Glass Electrolyte (Thomas Yersak, General Motors) .....	46
Task 1.12 – Low Impedance Cathode/Electrolyte Interfaces for High-Energy-Density Solid-State Batteries (Eric Wachsman and Yifei Mo, University of Maryland).....	50

Task 1.13 – Developing an <i>In Situ</i> Formed Dynamic Protection Layer to Mitigate Lithium Interface Shifting: Preventing Dendrite Formation on Metallic Lithium Surface to Facilitate Long Cycle Life of Lithium Solid-State Batteries (Deyang Qu, University of Wisconsin Milwaukee) .....	52
Task 1.14 – Molecular Ionic Composites: A New Class of Polymer Electrolytes to Enable All-Solid-State and High-Voltage Lithium Batteries (Louis Madsen, Virginia Polytechnic Institute and State University) .....	55
Task 1.15 – All-Solid-State Batteries Enabled by Multifunctional Electrolyte Materials (Pu Zhang, Solid Power, Inc) .....	60
Task 1.16 – Developing Materials for High-Energy-Density Solid-State Lithium-Sulfur Batteries (Donghai Wang, Pennsylvania State University) .....	63
<b>Task 2 – Diagnostics .....</b>	<b>66</b>
Task 2.1 – Characterization and Modeling of Li-Metal Batteries: Model-System Synthesis and Advanced Characterization (Guoying Chen, Lawrence Berkeley National Laboratory) .....	67
Task 2.2 – Interfacial Processes – Diagnostics (Robert Kostecki, Lawrence Berkeley National Laboratory) .....	70
Task 2.3 – Advanced <i>In Situ</i> Diagnostic Techniques for Battery Materials (Xiao-Qing Yang and Seong-Min Bak, Brookhaven National Laboratory) .....	73
Task 2.4 – Probing Interfacial Processes Controlled Electrode Stability in Rechargeable Batteries (Chongmin Wang, Pacific Northwest National Laboratory) .....	76
Task 2.5 – Integrated Atomic-, Meso-, and Micro-Scale Diagnostics of Solid-State Batteries (Yi Cui, William Chueh, and Michael Toney; Stanford University/SLAC National Accelerator Laboratory) .....	79
Task 2.6 – Investigating the Stability of Solid/Solid Interface (Zonghai Chen, Argonne National Laboratory) .....	81
Task 2.7 – Fundamental Understanding of Interfacial Phenomena in Solid-State Batteries (Xingcheng Xiao, General Motors) .....	83
Task 2.8 – Multidimensional Diagnostics of the Interface Evolutions in Solid-State Lithium Batteries (Yan Yao, University of Houston) .....	87

<b>Task 3 – Modeling</b> .....	<b>90</b>
Task 3.1 – Characterization and Modeling of Li-Metal Batteries: First-Principles Modeling and Machine Learning (Kristin Persson, Lawrence Berkeley National Laboratory) .....	91
Task 3.2 – Understanding and Strategies for Controlled Interfacial Phenomena in Lithium-Ion Batteries and Beyond (Perla Balbuena and Jorge Seminario, Texas A&M University; Partha Mukherjee, Purdue University).....	94
Task 3.3 – Electrode Materials Design and Failure Prediction (Venkat Srinivasan, Argonne National Laboratory).....	97
Task 3.4 – Dendrite Growth Morphology Modeling in Liquid and Solid Electrolytes (Yue Qi, Michigan State University).....	100
Task 3.5 – Modeling of Amorphous Solid-State Conductors (Gerbrand Ceder, University of California Berkeley).....	103
Task 3.6 – Characterization and Modeling of Li-Metal Batteries: Force Field Theory and Lithium-Sulfur Battery Simulations (Lin-Wang Wang, Lawrence Berkeley National Laboratory) .....	106
Task 3.7 – <i>In Situ</i> and <i>Operando</i> Thermal Diagnostics of Buried Interfaces in Beyond Lithium-Ion Cells (Ravi Prasher, Lawrence Berkeley National Laboratory).....	108
Task 3.8 – Multi-Scale Modeling of Solid-State Electrolytes for Next-Generation Lithium Batteries (Anh Ngo, Larry A. Curtiss, and Venkat Srinivasan, Argonne National Laboratory).....	112
Task 3.9 – Integrated Multi-Scale Modeling for Design of Robust 3D Solid-State Lithium Batteries (Brandon Wood, Lawrence Livermore National Laboratory) .....	115
Task 3.10 – First-Principles Modeling of Cluster-Based Solid Electrolytes (Puru Jena, Virginia Commonwealth University) .....	119
Task 3.11 – Predictive Engineering of Interfaces and Cathodes for High-Performance All-Solid-State Lithium-Sulfur Batteries (Badri Narayanan, University of Louisville) .....	122
Task 3.12 – First-Principles Modeling and Design of Solid-State Interfaces for the Protection and Use of Lithium-Metal Anodes (Gerbrand Ceder, University of California Berkeley) .....	126
Task 3.13 – Predicting the Nucleation and Evolution of Interphases in All-Solid-State Lithium Batteries (Sabrina (Liwen) Wan, Lawrence Livermore National Laboratory) .....	128
Task 3.14 – Design of Strain Free Cathode – Solid-State Electrolyte Interfaces Using Chemistry-Informed Deep Learning (Hakim Iddir, Argonne National Laboratory).....	131
Task 3.15 – Tackling Solid-State Electrochemical Interfaces from Structure to Function Utilizing High-Performance Computing and Machine Learning Tools (Shinjae Yoo, Feng Wang, and Deyu Lu, Brookhaven National Laboratory; Nongnuch Artrith and Alexander Urban, Columbia University) .....	137

<b>Task 4 – Metallic Lithium .....</b>	<b>141</b>
Task 4.1 – Lithium Dendrite Prevention for Lithium Batteries (Wu Xu and Ji-Guang Zhang, Pacific Northwest National Laboratory) .....	143
Task 4.2 – Composite Electrolytes to Stabilize Metallic Lithium Anodes (Nancy Dudney and X. Chelsea Chen, Oak Ridge National Laboratory).....	146
Task 4.3 – Enabling Solid-State Batteries through Characterization and Modeling (Nenad M. Markovic and Larry A. Curtiss, Argonne National Laboratory) .....	151
Task 4.4 – 3D Printing of All-Solid-State Lithium Batteries (Jianchao Ye, Lawrence Livermore National Laboratory) .....	155
Task 4.5 – Interfacial Studies on Lithium Thiophosphate Based Solid Electrolytes and Cathodes (Jagjit Nanda, Oak Ridge National Laboratory) .....	157
Task 4.6 – Prelithiation of Silicon Anode for High-Energy Lithium-Ion Batteries (Yi Cui, Stanford University) .....	160
<b>Task 5 – Sulfur Electrodes .....</b>	<b>163</b>
Task 5.1 – Novel Chemistry: Lithium Selenium and Selenium Sulfur Couple (Khalil Amine, Argonne National Laboratory) .....	165
Task 5.2 – Development of High-Energy Lithium-Sulfur Batteries (Dongping Lu and Jun Liu, Pacific Northwest National Laboratory) .....	167
Task 5.3 – Nanostructured Design of Sulfur Cathodes for High-Energy Lithium-Sulfur Batteries (Yi Cui, Stanford University).....	170
Task 5.4 – Investigation of Sulfur Reaction Mechanisms (Enyuan Hu, Brookhaven National Laboratory; Deyang Qu, University of Wisconsin at Milwaukee).....	173
Task 5.5 – New Electrolytes for Lithium-Sulfur Battery (Gao Liu, Lawrence Berkeley National Laboratory) .....	176
<b>Task 6 – Air Electrodes/Electrolytes.....</b>	<b>179</b>
Task 6.1 – Rechargeable Lithium-Air Batteries (Ji-Guang Zhang and Wu Xu, Pacific Northwest National Laboratory).....	181
Task 6.2 – Lithium-Air Batteries (Khalil Amine, Larry A. Curtiss, and Jun Lu, Argonne National Laboratory) .....	184
Task 6.3 – Lithium Oxygen Battery Design and Predictions (Larry A. Curtiss/Anh Ngo, Argonne National Laboratory; Amin Salehi-Khojin, University of Illinois at Chicago).....	187
<b>Task 7 – Sodium-Ion Batteries .....</b>	<b>190</b>
Task 7.1 – Exploratory Studies of Novel Sodium-Ion Battery Systems (Xiao-Qing Yang and Enyuan Hu, Brookhaven National Laboratory).....	191
Task 7.2 – Development of a High-Energy Sodium-Ion Battery with Long Life (Chris Johnson and Khalil Amine, Argonne National Laboratory).....	194

Task 7.3 – High-Capacity, Low-Voltage Titanate Anodes for Sodium-Ion Batteries  
(Marca Doeff, Lawrence Berkeley National Laboratory) ..... 197

Task 7.4 – Electrolytes and Interfaces for Stable High-Energy Sodium-Ion Batteries  
(Ji-Guang Zhang, Pacific Northwest National Laboratory) ..... 200

**Battery500 Consortium Program**

**Innovation Center for Battery500**

(Jun Liu, Pacific Northwest National Laboratory; Yi Cui, Stanford University) ..... 203

## TABLE OF FIGURES

Figure 1. (left) Schematic of contact-less components. (center) Incident angle of laser off glass slide resting on a 200-mAh pouch cell. (right) Depiction of the time-resolved camera setup tracking the laser position throughout the duration of the experiment. ....	5
Figure 2. (left) Normalized discharge capacity as a function of cycle number. (right) Cell thickness change (%) as a function of state of charge (right). ....	5
Figure 3. Cycle capacity tests of improved and control cells in group A at 0.1C rate, including Al <sub>2</sub> (4.67 mgS/cm <sup>2</sup> ), Al <sub>4</sub> (5.1 mgS/cm <sup>2</sup> ), Al <sub>5</sub> (5.2 mgS/cm <sup>2</sup> ), AC <sub>2</sub> (6.0 mgS/cm <sup>2</sup> ), AC <sub>3</sub> (6.0 mgS/cm <sup>2</sup> ), and AC <sub>5</sub> (6.4 mgS/cm <sup>2</sup> ). (a) Specific discharge capacity and (b) Coulombic efficiency of improved and control cells.....	10
Figure 4. Conditioning and cycle capacity tests of improved and control cells in group B at 0.1C rate, including Bl <sub>7</sub> (5.1 mgS/cm <sup>2</sup> ), Bl <sub>11</sub> (5.1 mgS/cm <sup>2</sup> ), Bl <sub>12</sub> (5.2 mgS/cm <sup>2</sup> ), BC <sub>7</sub> (6.2 mgS/cm <sup>2</sup> ), BC <sub>8</sub> (6.1 mgS/cm <sup>2</sup> ), and BC <sub>11</sub> (6.2 mgS/cm <sup>2</sup> ). (a) Specific discharge capacity and (b) Coulombic efficiency of improved and control cells.....	10
Figure 5. Scanning electron microscopy / energy dispersive X-ray spectroscopy (EDS) of the cross-section of pristine solid electrolyte (SE) – carbon nanotube (CNT). (a-b) Backscattered electrons (BSE) images and corresponding EDS map; blue for iodine, green for carbon, and red for oxygen. (c-d) BSE images of CNT area, with the bright area for Lil and dark area for CNT. (e-f) BSE images of Lil-Lil(HPN) <sub>2</sub> area, with bright area for Lil and grey area for Lil(HPN) <sub>2</sub> .....	13
Figure 6. Scanning electron microscopy / energy dispersive X-ray spectroscopy (SEM-EDS) of the cross-section of cycled Li-SE. (a-b) SEM and backscattered electrons (BSE) images. (c-d) BSE from the yellow rectangle area in (b), with the bright area for Lil, grey area for Lil(HPN) <sub>2</sub> , and dark area for Li. (e-f) BSE image and EDS map, with blue for iodine, purple for nitrogen, and red for oxygen.....	13
Figure 7. Scanning electron microscopy (SEM) images for the cross-section of cycled solid electrolyte (SE) carbon nanotube (CNT) in charged state. (a) SEM images. (b) Backscattered electrons (BSE) images of cathode side with CNT, the bright area for Lil and grey area for CNT. (C) High-resolution BSE images where the grey area is for CNT and the dark area for lithium. (d-e) BSE images of SE anode side; bright area for Lil and grey area for Lil(HPN) <sub>2</sub> . ....	14
Figure 8. Scanning electron microscopy (SEM) images for the cross-section view of cycled lithium – solid electrolyte – carbon nanotube (Li-SE-CNT) in charged state. (a-b) Backscattered electrons (BSE) images of cycled at cathode side, where the dark area is for CNT and the bright area for lithium. (c-d) High-resolution SEM images of CNT area with lithium dendrite. (e-f) BSE images of SE anode side, with bright area for Lil, grey area for Lil(HPN) <sub>2</sub> , and dark area for lithium. ....	14

- Figure 9. Applied voltage breakdown for 1 M LiPF<sub>6</sub> in EC:EMC (3:7 by wt.) as calculated in a lithium symmetric cell using COMSOL Multiphysics. Note the most significant contribution is from the SEI resistance (using a typical experimentally measured value), with the Nernst potential, the desired measured quantity, representing less than 2% of the applied voltage. .... 17
- Figure 10. Concentration gradient ( $\Delta c$ ) and electrolyte potential ( $\Delta\phi$ ) relaxation across a 250- $\mu\text{m}$  lithium symmetric cell after 1 hour of polarization at 10 mV for a range of LiPF<sub>6</sub> in EC:EMC (3:7) concentrations as modeled in COMSOL Multiphysics..... 18
- Figure 11. Cation transference number as a function of polyanion chain length at four concentrations, computed using coarse-grained molecular dynamics simulations ..... 18
- Figure 12. Polymer coating on Li-metal electrode. (a) Schematic showing the structure of ionic polymer coated on the Li-metal electrode. The ionic polymer comprises of x: perfluoropolyether-dimethacrylate (PFPE-DMA) backbone, y: pentaerythritol tetrakis(3-mercaptopropionate) or PETMP crosslinker, and z: (4 styrenesulfonyl) (trifluoromethanesulfonyl) imide (STFSI-Li) monomeric salts. The PFPE polymer acts as blocking agents for the liquid electrolyte, while the STFSI anions provide Li-ion transport pathways. (b) Comparison of peak heights obtained from <sup>1</sup>H NMR measurements showing the relative content of the methyl groups in the polymer backbone and the tethered anions (spectra referenced to residual protons in CD<sub>3</sub>OD). The NMR trend follows the trend of varying salt moieties in the polymer backbone. .... 21
- Figure 13. Stability with carbonate-based electrolytes: (a) Nyquist diagrams of symmetric lithium cells obtained using impedance spectroscopy measurement with and without the ionic polymer coating on the lithium. The different results were obtained after varying rest times of the batteries. (b) Cycling stability of lithium versus copper cells, where the copper electrodes were either bare or coated with ionic polymers containing 1.5 moles/kg of grafted salts. The bare electrode fails in 50 cycles, while that with coating showed enhanced stability. (c) Li | NMC full-cell cycling using 25  $\mu\text{m}$  lithium and 1.7 mAh/cm<sup>2</sup> NMC-532, such that the anode (N) to cathode capacity (P) ratio is 3:1. The lithium metal utilized either bare or coated with the ionic polymer (1.5 moles/kg of salts). The inset shows the comparison of the overall efficiency obtained using the formula:  $(1-N/(n \times P))100\%$ . The electrolyte in all the subparts was 1 M LiPF<sub>6</sub> in EC/EMC with 10% FEC. .... 22
- Figure 14. Ionic conductivity of PEO-POSS, POSS-PEO-POSS/LiTFSI mixtures. (a) POSS-PEO-POSS(5-35-5) ionic conductivity is plotted as a function of temperature alongside PEO(35)<sup>[1]</sup> and SEOS(5-35-5)<sup>[1]</sup> of comparable molecular weights at a salt concentration of  $r = [\text{Li}]/[\text{EO}] = 0.04$  to 0.05. (b) PEO-POSS(5-2), PEO-POSS(10-4), and POSS-PEO-POSS(5-35-5) ionic conductivity are plotted as a function of salt concentration and compared to PEO(10) at 90°C. .... 24

Figure 15. Electrochemical characterization of PEO-POSS, PEO <sup>[2]</sup> , and SEO <sup>[2]</sup> . (a) Diffusion coefficient ( $D$ ). (b) Current fraction ( $\rho_{+SS}$ ) as a function of salt concentration, $r$ at 90°C.....	25
Figure 16. (a) Thermodynamic factor ( $T_f$ ) and (b) cation transference number ( $t_{+,Ne}$ ) in PEO-POSS(5-2) and lamellar SEO <sup>[3]</sup> of varying molecular weights as a function of salt concentration, $r$ , at 90°C.....	25
Figure 17. Thermal stability of ISU glasses as shown via differential scanning calorimetry (DSC) thermograms for selected ISU glassy solid electrolytes (GSEs). All of these GSEs are thermally stable from -20°C to 100°C. ....	28
Figure 18. Arrhenius plot comparing the temperature-dependent ionic conductivity for two ISU glassy solid electrolytes, SLIP-3 and ISU-3. These data show that SLIP-3 exceeds the milestone 1.1b value of 1 mS/cm. ....	29
Figure 19. Complex plane plots of lithium metal   glassy solid electrolyte (GSE)   lithium metal symmetric cells as a function of time up to 10 hours for a reactive pure sulfide glass (left) whose impedance grows strongly with time and for a mixed-oxy-sulfide-nitride (MOSN) glass (right) whose impedance remains small for the same period of time, indicating that this MOSN GSE, ISU-4, is stable in contact with lithium metals. ....	30
Figure 20. Cyclic voltammetry plots of stable ISU-4 mixed-oxy-sulfide-nitride (MOSN) glassy solid electrolyte (GSE) with a maximum oxidative current of 20.6 nA/cm <sup>2</sup> (active area: 0.3563 cm <sup>2</sup> , average thickness: 1.076 mm) and right ISU-4 MOS GSE with a maximum oxidative current of 29.0 n/cm <sup>2</sup> (active area: 0.7126 cm <sup>2</sup> ).....	30
Figure 21. Change in peak anodic current with respect to peak anodic current of the 1 <sup>st</sup> cycle ( $i_1 - i_c$ ).....	31
Figure 22. Thermogravimetric analysis (TGA) results for a typically sulfide glass, compared to the mixed-oxy-sulfide-nitride (MOSN) glassy solid electrolyte (GSE) ISU-4.....	31
Figure 23. (a-c) External view of draw tower assembly and scaffolding. (d) Preform grip assembly.....	32
Figure 24. Consistent 20- $\mu$ m film being drawn.....	33
Figure 25. Picture of a consistent 8-cm wide by 40- $\mu$ m thick film being drawn.....	33
Figure 26. Mn-doped borosilicate glass preform prior to drawing. The MnO <sub>2</sub> doping gives the glass a strong color that allows it to be easily visualized, even at 20- $\mu$ m thick. This glass is used as glass typical of the thermal properties of GSEs, but it is more easily handled to enable faster optimization of the draw conditions. ....	33
Figure 27. Flexible 20- $\mu$ m film folded over in fingers, which demonstrates that these GSEs can be handled and will be able to be rolled up into long length spools.....	33

Figure 28. (a) Additive screening using the Wildcat high-throughput tri-layer cell geometry. More than 5200 electrochemical impedance spectroscopy measurements ran during the past three quarters. (b/c) Best hit families that show lowest interfacial impedance in tri-layer cell geometry. The baseline system is shown in the left-most panels of (b/c).....	36
Figure 29. Results of the PEO/ceramic composite with and without the additive C. These results show that having the additive in the composite improves ionic conductivity. ....	37
Figure 30. (a) Baseline system (no Li-metal protection) performance in Li/Li symmetric cell showing the point of cell failure (marked with arrow). The cumulative capacity plated is calculated from cycle life (h) and plating current (mA). (b) Li-metal protection screening using the Wildcat high-throughput Li/Li cell platform showing 160+ protection layers. The baseline system is visualized with a dotted line. ....	37
Figure 31. (a) Li/Li symmetric cells showing the point of cell failure (marked with arrows) for the baseline system and selected Li-metal protection artificial SEIs (ASEIs) found via screening. (b) Cumulative capacity plated (mAh/cm <sup>2</sup> ) for 17 different ASEIs screened having similar cations and anions to see relative differences in Li/Li cell performance.....	38
Figure 32. X-ray photoelectron surface analysis of as-densified thin-film construct LLZTO.....	40
Figure 33. Scheme and digital picture of molten metal lithium on Li <sub>7</sub> N <sub>2</sub> I-LiOH pellet surface with and without surface treatment.....	42
Figure 34. Digital picture for the process of assembling Li Li <sub>7</sub> N <sub>2</sub> I-LiOH Li cell.....	42
Figure 35. (a) Schematic of the all-solid-state Li Li <sub>7</sub> N <sub>2</sub> I-LiOH Li cell. (b) Equivalent circuit for fitting the electrochemical impedance spectroscopy (EIS) data of the Li Li <sub>7</sub> N <sub>2</sub> I-LiOH Li cell. (c) EIS data Li Li <sub>7</sub> N <sub>2</sub> I-LiOH Li cell at room temperature. ....	43
Figure 36. (a) Lithium plating/stripping of Li Li <sub>7</sub> N <sub>2</sub> I-LiOH Li cell at room temperature with step increased current density from 0.01 to 0.2 mA/cm <sup>2</sup> at an incremental step of 0.02 mA/cm <sup>2</sup> . (b) Lithium plating/stripping of Li Li <sub>7</sub> N <sub>2</sub> I-LiOH Li cell at 80°C with increased current, but fixed capacity of 0.025 mAh/cm <sup>2</sup> . ....	43
Figure 37. Lithium plating/stripping of Li Li <sub>7</sub> N <sub>2</sub> I-LiOH Li cell at 80°C with current density of 0.1 mA/cm <sup>2</sup> and capacity of 0.05 mAh/cm <sup>2</sup> .....	44
Figure 38. Geometry of the cell and its corresponding parameters. ....	44

- Figure 39. The preparation of a baseline dataset utilizes composite electrodes that are a 7:3 (w/w) mixture of NCM-851505 and  $\beta$ -Li<sub>3</sub>PS<sub>4</sub>. (a) 1<sup>st</sup> and 10<sup>th</sup> cycle voltage profiles of test cells confirming that a LiNbO<sub>3</sub> coating on NCM improves performance. (b) 10<sup>th</sup> cycle voltage profiles of test cells showing that preparation of composite electrodes by ball milling (BM) instead of hand mixing (HM) improves performance. The improvement is only noticeable at higher loading (15.4 mg/cm<sup>2</sup>). (c) 10<sup>th</sup> cycle voltage profiles of test cells with electrode loadings of 7.7 (black), 15.4 (red), 30.8 (blue), and 46.2 (green) mg/cm<sup>2</sup>. The cell with 46.2 mg/cm<sup>2</sup> electrode loading delivers an areal capacity of > 3 mAh/cm<sup>2</sup>. ..... 47
- Figure 40. Preliminary data on the evaluation of a candidate catholyte for hot pressing. (a) Differential scanning calorimetry (DSC) scans for 7:3 (w/w) composites of NCM@LiNbO<sub>3</sub> with either  $\beta$ -Li<sub>3</sub>PS<sub>4</sub>, Li<sub>6</sub>PS<sub>5</sub>Cl, or a candidate catholyte. The onset temperature of an exothermic feature is highest for the candidate catholyte suggesting that it has superior thermal stability. (b) First cycle voltage profiles for hot pressed test cells with 7:3 (w/w) composite cathodes of NCM@LiNbO<sub>3</sub> and either  $\beta$ -Li<sub>3</sub>PS<sub>4</sub> (black) or the candidate catholyte (Blue). ..... 48
- Figure 41. X-ray diffraction patterns of LLZTO and 50/50 w/w mixtures with various cathode materials before and after co-sintering at 700°C. Cathode material for each figure is (a) LCO, (b) LMO, (c) LNMO, and (d) NMC-111. .... 51
- Figure 42. Molecular structure of trisaminocyclopropenium (TAC). ..... 53
- Figure 43. Electrochemical performance of lithium plating/stripping in trisaminocyclopropenium (TAC) electrolyte. (a) Voltage profiles of Li | Li symmetric cells cycling at 1 mA cm<sup>-2</sup> 1 mAh cm<sup>-2</sup>. (b) Coulombic efficiencies of Li | Cu asymmetric cells cycling at 0.5 mA cm<sup>-2</sup> 1 mAh cm<sup>-2</sup>. (c) Voltage profiles of Li | Cu cell at 1<sup>st</sup> and 120<sup>th</sup> cycles. (d) *In situ* optical microscopic images during lithium plating process at 4 mA cm<sup>-2</sup>, scale bar 200  $\mu$ m. (e) Schematic illustration of a cation-shield mechanism. Note: The TAC is not drawn to scale. The manuscript is under review. .... 54
- Figure 44. Cyclic voltammetry (CV) of the molecular ionic composite (MIC) electrolyte membrane and a liquid electrolyte (LE) composed of LiTFSI and Pyr<sub>14</sub>TFSI in a 1:8 mass ratio. These CV measurements were recorded at room temperature using stainless steel as working electrode and lithium metal as counter and reference electrode with a scan rate of 0.1 mV s<sup>-1</sup>. The main peak near 0 V corresponds to lithium plating and stripping. The reductive peaks at 0.7 V and 1.5 V and oxidative peaks at 1.0 V and 2.0 V appear both in the MIC membrane and in the LE, suggesting they are caused by the ionic liquid. An oxidative peak at 3.9 V is evident only in the MIC membrane, indicating it is caused by either the polymer or an impurity. .... 56
- Figure 45. Voltage profiles of lithium / molecular ionic composites (MIC) / lithium symmetric cells cycled at 23°C using current density of 0.1 mA/cm<sup>2</sup> and 100°C using current density of 0.6 mA/cm<sup>2</sup>. The cells lasted for 800 and 700 hours, respectively, under these two conditions before cell failure, indicating durable compatibility between the MIC material and lithium metal over a wide temperature range. .... 57

Figure 46. (a) Li-ion transference number measurement of the molecular ionic composite (MIC) electrolyte through the dc polarization technique. Inset is the impedance spectrum before and after polarization. (b) Temperature dependence of the shear storage and loss moduli ( $G'$ and $G''$ ) at heating rate = $5^{\circ}\text{C min}^{-1}$ . (c) Frequency dependence of imaginary modulus ( $M''$ ) at varying temperature. The main peak is the $\alpha$ relaxation, and the minor peak at higher frequency is the $\beta$ relaxation. (d) Temperature dependence of the $\alpha$ relaxation frequency ( $\omega_{\text{max}}$ ) of the MIC electrolyte. ....	58
Figure 47. (a) Charge/discharge profiles of a cell containing NMC as the cathode, 1 M $\text{LiPF}_6$ in EC/EMC with 2 v.% VC as the electrolyte, and lithium metal as the anode, the cell was cycled at C/10 within 2.5–4.5 V in the 1 <sup>st</sup> cycle and then stopped at the charge 4.2 V. This charged cathode then serves as a testing platform to evaluate the stability of the MIC electrolyte. (b) The nickel L3-edge soft X-ray absorption spectra in the total electron yield mode of the NMC-811 electrode (charged to 4.2 V) after storing under various conditions. These spectra show that the MIC electrolyte is stable against layered cathodes. ....	58
Figure 48. (a) Separator film coated by a slot-die coater. (b) Flexibility of the separator. ....	61
Figure 49. Cycle life of an NMC/Li-metal solid-state pouch cell with the multifunctional solid-state electrolyte.....	62
Figure 50. (a) X-ray diffraction spectra. (b) Ionic conductivity at $25^{\circ}\text{C}$ and activation energy of various $65\text{Li}_2\text{S}-65\text{Li}_2\text{S}-26\text{P}_2\text{S}_5-10\text{Li}_3\text{N}-x\text{Al}_2\text{S}_3$ (LPSNAI-x) glass-type solid electrolyte ( $x = 0 - 20$ ).....	64
Figure 51. Rate performance of sulfur cathode with $\text{TiS}_2$ additive. ....	64
Figure 52. (a) Rate performance and (b) corresponding voltage profile at 1 <sup>st</sup> cycle of sulfur cathode using Ketjen Black EC-600J (KB) as carbon additive.....	65
Figure 53. Crystal structure of (a) $\text{InCl}_3$ and (b) $\text{Li}_3\text{InCl}_6$ . (c) Atomic arrangement of indium and chlorine in $\text{Li}_3\text{InCl}_6$ .....	68
Figure 54. Scanning electron microscopy images of secondary-particle $\text{Li}_3\text{InCl}_6$ sample (a/b) and single-grain $\text{Li}_3\text{InCl}_6$ sample (c/d) synthesized by mechanical ball milling. ....	68
Figure 55. Scanning electron microscopy images of secondary-particle $\text{Li}_3\text{InCl}_6$ sample before (a) and after (b) annealing. (c) Comparison of electrochemical impedance spectroscopy Nyquist plots of the samples.....	68

Figure 56. (a) Optical image of the top of the solid-state full cell device. The blue inset highlights the spatial region to be studied, which has both exposed solid-state electrolyte (SSE) (PEO+ LiTFSI mixtures at EO/Li ratios of 10:1) on the left and graphene-capped SSE on the right. (b) Topography data collected within the blue inset in panel (a). (c) White light infrared imaging (second harmonic of the optical amplitude) collected simultaneously with the data in panel (b). The brighter region on the right-hand side is graphene-capped SSE. (d) Spatially dependent nano-FTIR spectra whose color coordinates to the similarly colored diamonds in varied spatial locations displayed in panel (c).....	71
Figure 57. (a) Nickel and manganese K-edge hard X-ray absorption spectroscopy (hXAS) spectra. (b) Total electron yield (TEY) and partial fluorescence yield (PFY) of nickel and manganese L-edge soft X-ray absorption spectroscopy (sXAS). (c) Linear combination fitting (LCF) results for TEY and PFY of nickel L-edge spectra. (d) LCF results for TEY of manganese L-edge spectra. ....	74
Figure 58. Schematic diagram of preserving and stabilizing SEI formed on copper current collector by cryo – transmission electron microscopy (TEM). (a) Commercial copper foil as current collector. (b) Copper foil with 3-mm diameter prepared from copper foil. (c) TEM copper foil prepared by precision ion polishing system. (d) Assembling TEM foil into coin cell. (e) Retrieved TEM copper foil from the coin cell in an argon-filled glovebox. (f) The TEM copper foil with SEI formed on is sealed in argon environment, plunged into liquid nitrogen, and then transferred to the cryo-TEM holder. ....	77
Figure 59. High-resolution transmission electron microscopy (HR-TEM) micrographs of SEI formed on TEM copper foil in the electrolytes without/with 5% vinylene carbonate (VC) additive. (a-c) High-magnification images of the SEI formed on TEM copper foil at different cut-off voltages of 1.0 V, 0.5 V, and 0 V in the electrolyte without VC additive. (d-f) High-magnification images of the SEI formed on TEM copper foil at different cut-off voltages of 1.0 V, 0.5 V, and 0 V in the electrolyte with VC additive. Insets: Fast Fourier transform patterns from SEI (red) and copper foil (blue). ....	77
Figure 60. (a) Digital image of a Ta-LLZO pallet fabricated by hot pressing. (b) Scanning electron microscopy image of the hot pressed Ta-LLZO pallet showing a clear contrast between the core part and the outer layers. (c) Space resolved high-energy X-ray diffraction (HEXRD) patterns showing the phase evolution along the thickness direction. (d) Zoomed view of HEXRD patterns. (e) Evolution of concentration profiles for different species in the thickness direction of Ta-LLZO pallet.....	82
Figure 61. (a) Curvature and voltage versus time measured by multi-beam optical stress sensor (MOSS) using LLZO solid electrolyte. (b) Membrane force F and measured voltage versus time. ....	84

Figure 62. (a) Cross-sectional image of a fractured surface (near copper side) after short circuiting. (b) Lithium metal penetration through the LLZO solid electrolyte along the grain boundary. ....	84
Figure 63. (a) Charge density difference, $\Delta\rho = \rho_{\text{Li/coating}} - \rho_{\text{Li}} - \rho_{\text{coating}}$ , (upper panel) and planar-averaged charge density difference (lower panel) of Li(001)/Li <sub>2</sub> O(110)(left), Li(001)/LiF(001)(middle), and Li(001)/Li <sub>2</sub> PO <sub>2</sub> N(010)(right) interfaces. (b) Cross-view (bottom) and side view (side) of charge density difference of Li(001)/Li <sub>2</sub> O(110)(left), Li(001)/LiF(001)(middle), and Li(001)/Li <sub>2</sub> PO <sub>2</sub> N(010)(right) interfaces. Note: The yellow region corresponds to charge accumulation, and the blue region corresponds to charge depletion. Oxygen in red, lithium in green, fluorine in grey, nickel in blue, and sulfur in yellow. The atoms with a cross indicate the atoms of Li <sub>2</sub> O, LiF, and Li <sub>2</sub> PO <sub>2</sub> N.....	85
Figure 64. Solid-state electrolyte thin films tape-cast with slurries based on (a) less-optimized and (b) improved formulations. ....	88
Figure 65. Design and applications of an air-free transfer vessel with an <i>in situ</i> cell test platform built-in. (a) Cell test platform equipped with micro-cell mount, heater, pressure applicator, and sensor. (b) Installation of the vessel in instruments where characterizations are performed inside a chamber [for example, focused ion beam/scanning electron microscopy (SEM)]. (c) Vessel remains closed when used with (d) instruments without a chamber (for example, laser-based spectrometers); analytical beams come in through a window in the vessel. (e) The cover of the vessel opens up, revealing the test platform and lifting up toward the electron gun. (f) SEM image of the cross-section of a thin-format cell obtained using the vessel. (g) Raman spectrum of the LPSCI electrolyte obtained using the vessel. (h) Optical image of the cross-section of a thin-format cell obtained with a Raman spectrometer using the vessel.....	88
Figure 66. Voltage profile and pressure change of an NMC/LPSCI/Li-In micro-cell tested in the transfer vessel. ....	89
Figure 67. Averaged number of O <sup>2-</sup> neighbors during Li <sup>+</sup> diffusion (a/c) and averaged number of Al <sup>3+</sup> and Zn <sup>2+</sup> neighbors during O <sup>2-</sup> diffusion (b/d) for amorphous Al <sub>2</sub> O <sub>3</sub> and ZnO at 2000 K for 40 ps.....	92
Figure 68. (a) Representative illustration of a dendritic morphology formed for single metal electrodeposition. Co-electrodeposition morphologies exhibiting (b) film-type, (c) mossy, and (d) dendritic features depending on the surface diffusion barrier of the deposited atom and the electrochemical reaction rate. An increase in the porosity and number of branches is observed with an increase in the surface diffusion barrier (that is, decrease in surface diffusion rate) and an increase in the reaction rate.....	95

Figure 69. (a) NMC/LLZO cathode electrolyte microstructure with a 5-nm thick LBCO interphase layer in between. (b) NMC/LBCO/LLZO cathode/interphase-layer/electrolyte microstructure with thickness of interphase layer being 25 nm. (c) Evolution of fractional delamination with increasing thickness of the LBCO interphase layer. Addition of interphase layer helps to minimize the delamination. ....	98
Figure 70. (a) Voltage versus capacity performance curves with interphase layer thickness 0 nm (black dashed line), 5 nm (blue line), and 25 nm (red line). (b) Discharge capacity with increasing thickness of the interphase layer. Addition of interphase layer helps to minimize delamination and enhances discharge capacity. Increasing thickness of interphase layer also increases the ohmic resistance.....	99
Figure 71. Amorphous grain boundaries (GBs) have even lower band gap than ordered GBs, and can trap electrons.....	101
Figure 72. Phase-field simulations on (a-d) lithium and magnesium plating morphologies using implicit SEI model. (e-h) Lithium dendrite suppression by Li <sup>+</sup> -affinity porous media at anode. (i-l) Lithium metal/coating interfacial adhesion impact on electrodeposition. ....	101
Figure 73. Li <sup>+</sup> -ion migration pathways and corresponding energy barriers in the intermediates. ....	104
Figure 74. The charge status of PF6 at different positions and under different potential. ....	107
Figure 75. The dissolution behavior of lithium from the Li(111) surface under different potential. ....	107
Figure 76. (a) 3 $\omega$ sensor used for anode of the lithium symmetric cell. (b) LLZO pellet with a 3 $\omega$ sensor. ....	109
Figure 77. Assembled lithium symmetric cell with a 3 $\omega$ sensor. ....	110
Figure 78. Sensitivity of the temperature rise at different harmonics of the applied charging frequency (1 $\omega$ , 2 $\omega$ , and 4 $\omega$ ) due to different electrochemical processes at the interfaces and the electrolyte. The 2 $\omega$ temperature rise (both in-phase and out-of-phase) at low frequencies is the most sensitive to the ionic transport resistance in the electrolyte. The 4 $\omega$ temperature rise (both in-phase and out-of-phase) at high frequencies is the most sensitive to the kinetics at the interface (exchange current density). ....	110
Figure 79. The magnitude of NMC/LBCO exchange current density as a function of the NMC Li-ion concentration. $\Delta G$ and $v$ can be extracted directly from the <i>ab initio</i> molecular dynamics calculations. ....	114
Figure 80. Mean square displacement (MSD) of Li-ion in various LLZO structure models from <i>ab initio</i> molecular dynamics. "C" and "A" refer to crystalline and amorphous LLZO structures.....	116

- Figure 81. Snapshot of the LLZO(001)/LCO(100) interface from *ab initio* molecular dynamics. Lithium, lanthanum, zirconium, oxygen, and cobalt atoms are green, yellow, cyan, red, and blue, respectively. The diffusion trajectory is highlighted by the orange spheres in the zoomed-in representation at right. .... 117
- Figure 82. Parametric study of an electrochemical impedance spectroscopy (EIS) model for a polycrystalline sample. A sinusoidally varying voltage with a varying frequency (zero to  $10^8$  Hz) is applied, simulating an EIS experiment. Grain and grain boundary (GB) conductivity play a strong effect, while the GB permittivity plays a weak effect for the considered example system. .... 118
- Figure 83. Calculated diffusivities of five typical cluster-based solid electrolytes (SEs) fitted by the Arrhenius relation. The diffusivity of stoichiometric  $\text{Li}_6\text{PS}_5\text{Cl}$  (Ref. Calc.) is used as a benchmark for comparison, with a poor room-temperature (RT) ionic conductivity in the order of  $10^{-7}$ - $10^{-6}$  S/cm and a high activation energy between 5.0-6.0 eV. Clearly, these new SE materials exhibit much (3 to 5 orders of magnitude) higher RT diffusivity than that of the stoichiometric  $\text{Li}_6\text{PS}_5\text{Cl}$ . The corresponding ionic conductivities at RT are over  $10^{-4}$ - $10^{-2}$  S/cm, with activation energies between 1.5-3.5 eV. In particular, the calculated RT conductivity of “SE-1” is 0.08-0.09 S/cm with a low activation energy just over 1.5 eV. .... 120
- Figure 84. *Ab initio* molecular dynamics simulations of evolution of anode / solid-state electrolyte (SSE) interface at 300 K. The equilibrated atomic-scale structure of the interface between Li (001) and SSE (001) is shown for three different electrolyte compositions, namely (a)  $\text{Li}_6\text{PS}_5\text{F}$ , (b)  $\text{Li}_6\text{PS}_5\text{F}_{0.5}\text{Cl}_{0.5}$ , and (c)  $\text{Li}_6\text{PS}_5\text{Cl}$ . In each panel, the spatial distribution of lithium (purple), phosphorus (blue), sulfur (green), fluorine (red), and chlorine (grey) atoms (in terms of number density) is shown in the direction normal to the interface. .... 123
- Figure 85. Partial distribution function (PDF) of (a) Li-P, (b) Li-S, (c) Li-X, and (d) P-S pairs in equilibrated structure of the anode / solid-state electrolyte interfaces obtained from *ab initio* molecular dynamics (AIMD) simulations. The PDFs for the three electrolyte compositions  $\text{Li}_6\text{PS}_5\text{F}$ ,  $\text{Li}_6\text{PS}_5\text{Cl}$ , and  $\text{Li}_6\text{PS}_5\text{F}_{0.5}\text{Cl}_{0.5}$  are shown as red, blue, and green lines, respectively. The PDFs are averaged over the last 3 ps. .... 124
- Figure 86. Thermogravimetric analysis of mesoporous carbon architectures made up of pristine carbon nanocages (CNCs, black), and those containing CNCs infiltrated with sulfur and solid-state electrolyte. The team has also investigated the effect of order of infiltration (red: S first; blue: S last). .... 124
- Figure 87. Charge-discharge characteristics of coin-cells made up of (a) CNC-S-SSE (60% sulfur based on thermogravimetric analysis) cathode, and (b) S-C65 cathode with  $\text{Li}_6\text{PS}_5\text{Cl}$  electrolyte. The team used a current of C/20 for the tests. .... 125
- Figure 88. Schematic illustration of different stages of metal deposition in the void. .... 127
- Figure 89. Pressure developed in the metal under three applied current densities ..... 127

Figure 90. Initial structure models of (a) LLZO(001) LCO(100), (b) LLZO(001) LFP(010), and (c) LiPON(100) LCO(100) interfaces. The lithium, lanthanum, zirconium, oxygen, cobalt, iron, phosphorus, and nitrogen atoms are represented as green, yellow, purple, red, dark blue, light blue, orange, and magenta spheres, respectively. ....	129
Figure 91. (a) Initial density functional theory relaxed interfacial structure of LLZO(001) LCO(100). (b-d) Snapshots from <i>ab initio</i> molecular dynamics trajectory showing lithium, lanthanum, and cobalt migration toward the interfacial region. ....	130
Figure 92. Representative structures of the LLZO(001) LCO(100) interface during minimization of potential energy surface using basin hopping. The lithium, lanthanum, zirconium, oxygen, and cobalt ions are shown in green, yellow, purple, red, and blue, respectively. ....	130
Figure 93. The unit cell volume obtained from crystallographic data versus the state of lithiation of positive electrode materials. <sup>[1]</sup> .....	133
Figure 94. Polyhedral representation of LiNiO <sub>2</sub> super cell at different lithium content (x) with oxygen stacking in the H-2 (ABC) and H-3 (AC) phases. Grey octahedrons represent nickel sites, green octahedrons represent lithium sites, and small red spheres represent oxygen atoms.....	133
Figure 95. Energy of the dissociated limit as a function of the interlayer spacing for PBE, SCAN, and SCAN+rVV10 for NiO <sub>2</sub> (a) in O1 stacking and (b) in O3 stacking. ....	134
Figure 96. Polyhedral representation of LiNi <sub>0.8</sub> Mn <sub>0.1</sub> Co <sub>0.1</sub> O <sub>2</sub> ; (a) transition metal (TM) layer top view, and (b) whole super-cell side view. The grey polyhedral represents nickel site, blue polyhedral represents cobalt site, purple polyhedral represents manganese site, and green sphere represents lithium ion. (c) Procedure to find minimal energy TM configuration.....	134
Figure 97. (a) Neural network (NN) predicted versus density functional theory (DFT) predicted energies. Additionally, 1-sigma uncertainty intervals are plotted for the NN predictions. (b) Procedure to find minimal energy transition metal (TM) configuration. (c) DFT-calculated energies for 50 configurations (round 1) where TMs are positioned randomly in the TM layers and energies after Bayesian optimization (round 2). (d) TM layer top view polyhedral representation of LiNi <sub>0.8</sub> Mn <sub>0.1</sub> Co <sub>0.1</sub> O <sub>2</sub> . The grey polyhedral represents nickel site, blue polyhedral represents cobalt site, purple polyhedral represents manganese site, and green sphere represents lithium ion. ....	135
Figure 98. (a) Calculated formation energies of NMC-811 with varying lithium content. The thermodynamically stable compositions lie on the lower convex hull (black points). Metastable and unstable compositions are shown as green crosses. (b) Comparison of the predicted voltage with experimentally measured voltage profiles.....	138

Figure 99. Iterative refinement of the artificial neural network (ANN) potential using interface structures from Monte Carlo / molecular dynamics simulations with aenet. <sup>[2]</sup> The newly developed approach facilitates training potentials on fewer density functional theory reference calculations. <sup>[3]</sup> .....	139
Figure 100. (a) LLZO structure energies predicted by artificial neural network (ANN) potential compared to the density functional theory reference (green crosses). The dashed line indicates ideal agreement. (b) Arrhenius plot with lithium conductivities in Al-LLZO from molecular dynamics simulations at different temperatures.....	139
Figure 101. Room-temperature cycling performance of Li   NMC-811 and Li-Mg   NMC-811 coin cells comprising flooded electrolyte of LiFSI-1.2DME-3TTE at 1C charge and discharge rate after two formation cycles at C/10 rate in the voltage range of 2.8-4.4 V. Cathode areal capacity loading is $\sim 1.5 \text{ mAh cm}^{-2}$ . .....	144
Figure 102. Cryo – transmission electron microscopy (TEM) images of SEI formed on TEM copper foil in the electrolytes without and with 5% VC additive. (a-c) At different cut-off voltages of 1.0 V, 0.5 V, and 0 V in the electrolyte without VC additive. (d-f) At different cut-off voltages of 1.0 V, 0.5 V, and 0 V in the electrolyte with VC additive. Insets: Fast Fourier transform patterns from SEI (red) and copper foil (blue). .....	144
Figure 103. (a) Li <sup>+</sup> conductivity of gel polymer and composite electrolytes. (b) Charge and discharge curves of full cell NMC-532   CEM-50   Li at cycle number 1, 2, 5, and 10, and (c) cycling performance of the cell. ....	147
Figure 104. (a ) The current as a function of relaxation time with 10-mV bias for the polymer electrolyte, XPEO, and the composites containing 30-70 wt% LICGC <sup>TM</sup> . (b) Expanded plot of the same results, plotted as the ratio of the current to the initial current. ....	148
Figure 105. Simulated relaxation behavior of different electrolyte arrangements under 10-mV DC bias. ....	148
Figure 106. Simulated development of lithium cation concentration profiles in (a) PEO:LiTFSI; (b) PE/Ohara/PE; and (c) PE/CPE/PE. (d) Comparison of steady state concentration profiles among the three configurations.....	149
Figure 107. Atomic force microscopy measurements on bare LLTO films for the (001) and (100) orientations are shown in the insets. X-ray reflectivity for crystalline LiCoO <sub>2</sub> / LLTO (hkl) is shown at the top, and amorphous LiCoO <sub>2</sub> / LLTO (hkl) is shown at the bottom. ....	152

Figure 108. Neutron reflectometry measurement on bilayer thin films of LiCoO <sub>2</sub> (104) / LLTO (hkl), where (hkl) is (001) for films grown of SrTiO <sub>3</sub> (001) and is (100) for films grown on NdGaO <sub>3</sub> (110). .....	153
Figure 109. (a) X-ray reflectivity and (b) neutron reflectivity, along with the fitted density profile for the amorphous LiCoO <sub>2</sub> / LLTO superlattice (c). (d) The two-time correlation function, as measured using a coherent X-ray beam at the APS. The results at different temperatures allow measurement of the activation energy for Li-ion fluctuations across the interface (e). .....	154
Figure 110. (a) and (b) are scanning electron microscopy images of 1000°C sintered LLZTO made from ball milled powder (Dv50 = 238 nm) and raw powder (Dv50 = 7 μm), respectively. Diffusion flux (c/e) and advection flux (d/f) associated with particle translational motion during sintering of three particles with diameters equal to 0.6 μm (c-d) or 1.2 μm (e-f). The white arrows represent the flux vectors, with the arrow size proportional to the flux magnitude. Both diffusion and advection flux, which transport mass to the pore region in the center, increase with decreasing particle size. The scale bar in (c) also applies to (d-f). .....	156
Figure 111. (a) Solid-state battery configuration and corresponding galvanostatic charge/discharge curves for cells containing (b) LiFePO <sub>4</sub> and (c) NMC-111 cathodes.....	158
Figure 112. <sup>7</sup> Li solid-state nuclear magnetic resonance spectra of β-Li <sub>3</sub> PS <sub>4</sub> and amorphous Li <sub>3</sub> PS <sub>4</sub> +1% PEO solid electrolytes prepared through solvent-mediated routes developed in FY 2020-2021. Notably, these materials exhibit significantly different peak intensities, and thus have been linearly scaled to facilitate direct comparisons. All spectra are referenced to lithium triflate (δ = 0 ppm). .....	159
Figure 113. (a-e) Cross-sectional scanning electron microscopy images of Li@eGF films with tunable thickness from 500 nm to 20 μm. (f) Voltage-capacity profiles of Li@eGF films with different thickness, showing the capacities exhibited in them.....	161
Figure 114. High-resolution X-ray photoelectron spectroscopy Li 1s spectra of cycled Li-metal anode of Li Cu cells in DME- and HFE-based electrolytes. ....	166
Figure 115. High-resolution X-ray photoelectron spectroscopy F 1s spectra of cycled Li-metal anode of Li Cu cells in DME- and HFE-based electrolytes. ....	166
Figure 116. Typical charge/discharge curves and cycling performance of sulfur electrodes cycled in low-polysulfide-soluble electrolytes (a-b) and liquid/polymer hybrid electrolytes (c-d). (Electrode: 4 mg S/cm <sup>2</sup> , porosity <50%, and E/S = 4 μL/mg S; 0.05C for one formation cycle, then 0.1C for cycling, at room temperature). .....	168

- Figure 117.  $\text{Li}_2\text{S}$  decomposition and Li-ion diffusion barriers on surface of nickel and graphene. (a) Comparison of the  $\text{Li}_2\text{S}$  decomposition and Li-ion diffusion barriers on the surface of nickel, graphene basal plane, and graphene edge. Energy profiles for the decomposition of  $\text{Li}_2\text{S}$  cluster and Li-ion diffusion on the surface of (b) graphene edge, (c) graphene basal plane, and (d) nickel. Inset figures are top view schematic representations of the corresponding decomposition and Li-ion diffusion pathways for graphene edge, graphene basal plane, and nickel. Note: green, yellow, gray, and beige balls symbolize lithium, sulfur, nickel, and carbon atoms, respectively. .... 171
- Figure 118. Electrochemical performances for CP/Me-N-GOMC/S cathodes. (a) Cyclic voltammetry curves of the CP/Fe-N-GOMC/S electrode for initial several cycles at a scan rate of  $0.05 \text{ mV s}^{-1}$ . (b) Galvanostatic discharge-charge profiles of electrodes for the 2<sup>nd</sup> cycle at 0.2 C. (c) Experimental Nyquist plots of electrodes after initial cycle of the cells as well as the fitting results (solid lines) based on the equivalent circuit shown in the inset. (d) Cycling performances of electrodes at 0.5 C, and (e) rate capability of electrodes at various rates with a sulfur loading of  $\sim 3 \text{ mg cm}^{-2}$ . (f) Cycling performances of CP/Fe-N-GMOC/S electrodes with different sulfur loading at 1 C, and (g) the corresponding areal capacities..... 174
- Figure 119. Voltage profiles for lithium plating/stripping test by using 0.5 M LiFSI in  $\text{F}_3\text{EO}_1/\text{TTE}$  (1:5) electrolyte under various conditions: (a)  $0.5 \text{ mA/cm}^2$  current density and  $0.5 \text{ mAh/cm}^2$  deposition capacity; (b)  $1.0 \text{ mA/cm}^2$  current density and  $1.0 \text{ mAh/cm}^2$  deposition capacity; (c)  $2.0 \text{ mA/cm}^2$  current density and  $2.0 \text{ mAh/cm}^2$  deposition capacity; and (d-f) scanning electron microscopy images ( $3000\times$ , magnification) of deposited surfaces at various current density and constant  $1.0 \text{ mAh/cm}^2$  deposition capacity. .... 177
- Figure 120. (a) Formation process of PEO-supported SEI layer on the surface of Li-metal anode, by combination steps consisting of pre-GPE coating by spin coating method and pre-charging to 5 V electrochemically. (b) Schematic illustration of the role of PEO-supported SEI layer and surface characterization results of Li-metal surfaces after pre-charging step with and without pre-PG coating. (c) Voltage profiles of Li- $\text{O}_2$  battery cells with and without PEO-supported SEI layer cycling at a current density of  $0.2 \text{ mA cm}^{-2}$  under a capacity limited protocol of  $1.0 \text{ mAh cm}^{-2}$ . Cycling performance of Li- $\text{O}_2$  batteries corresponding to voltage profiles with repeated discharge and charge cycles at same testing condition. .... 182
- Figure 121. Nano-engineering strategies for creating the ultra-small wetting and de-wetting dimensionality reduced platinum catalysts on the substrate. (a) Definition of wetting and de-wetting in a typical metal-nonmetallic substrate system. (b) Formation of dimensionality reduced platinum with help of functional metal layers on a carbon black substrate for lithium oxygen battery, and the relating regular open circuit voltage (OCV) for each cell. .... 185

Figure 122. Examples of galvanostatic charge/discharge profiles of Li-O <sub>2</sub> batteries with (a) carbon black, (b) Cr/C, (c) Au/C, (d) 3D Pt/C, (e) 2D Pt/Cr/C, and (f) 0D Pt/Au/C in the voltage range of 2.2 V to 4.5 V versus Li <sup>+</sup> /Li within the fixed capacity. ....	186
Figure 123. <i>Ab initio</i> molecular dynamics simulation of Li(100) interface with DMSO/IL electrolyte with InX <sub>3</sub> molecule added to the electrolyte. (a) Initial (left) and optimized (right) structures for InI <sub>3</sub> ; arrow indicates the initial and final position of indium atom. (b) Initial (left) and optimized (right) structures for InBr <sub>3</sub> ; arrow indicates the initial and final position of indium atom. ....	188
Figure 124. <i>Ex situ</i> X-ray absorption spectroscopy of chromium (a) and selenium (b) X-ray absorption near-edge structure (XANES) spectra of NaCrSSe electrodes at various charge/discharge states, which include pristine, half-charged (HC, charged to a capacity of 70 mAh g <sup>-1</sup> ), full charged (FC, full charged to 3.3 V), half discharged (HD, discharged to a capacity of 70 mAh g <sup>-1</sup> after full charged), and full discharged (FD, full discharged to 1.5 V after full charged). ....	192
Figure 125. Cycling performance of Argonne National Laboratory red phosphorus anode at C/3. ....	195
Figure 126. P2p X-ray photoelectron spectroscopy spectra of red phosphorus anode at different charge/discharge states. ....	195
Figure 127. Average 1 <sup>st</sup> cycle Coulombic efficiency (CE) of Na <sub>0.69</sub> Ti <sub>1.827</sub> O <sub>4</sub>   Na cells with different electrolytes. All cells were cycled at current rate of C/20 (that is, 8 mA g <sup>-1</sup> , 0.012 mA cm <sup>-2</sup> ). With each electrolyte, two to three cells were tested to obtain better statistics. The error bar represents the standard deviation of the average values of CE. 'NaBr-SEI' stands for cells cycled with NaBr-coated sodium metal. The NaBr coating was created from a spontaneous chemical reaction between 1-Bromopropane and metallic sodium, following the same procedure reported in <i>Nature Communications</i> 8 (2017): 898. No noticeable improvement in 1 <sup>st</sup> cycle CE was observed with NaBr-coated sodium metal in electrolyte of 1 M NaPF <sub>6</sub> in EC/DEC. ....	198
Figure 128. Electrochemical performance of Na <sub>0.69</sub> Ti <sub>1.827</sub> O <sub>4</sub> electrodes in half-cells. (a) Typical 1 <sup>st</sup> cycle (top panel) and 2 <sup>nd</sup> cycle (bottom panel) discharge/charge profiles of Na <sub>0.69</sub> Ti <sub>1.827</sub> O <sub>4</sub> dehydrated at 120°C (yellow curve), 180°C (green curve), and 290°C (blue curve). (b) Corresponding dQ/dV plots. All cells were cycled in 1 M NaPF <sub>6</sub> in EC/DEC at current rate of C/20. ....	198
Figure 129. X-ray photoelectron spectroscopy characterization of the CEI components on Na-CNFM (NaCu <sub>1/9</sub> Ni <sub>2/9</sub> Fe <sub>1/3</sub> Mn <sub>1/3</sub> O <sub>2</sub> ) cathode electrodes after the 10 <sup>th</sup> cycles in different electrolytes. (a/d) C 1s spectra, (b/e) F 1s spectra, (c) P 2p spectra, and (f) S 2p spectra for 1 M NaPF <sub>6</sub> /EC+DMC (1:1 in weight) electrolyte (a-c) and NaFSI-TEP/TTE (1:1.5:2 in mole) electrolyte (d-f). ....	201

Figure 130. Characterization of SEI components on pristine and cycled hard carbon (HC) electrodes by X-ray photoelectron spectroscopy. (a-c) C 1s, (d-f) F 1s, (g) P 2p, (h) S 2p, and (i) N 1s XPS profiles of the pristine HC anode (a/d) and the HC anode after 20 cycles in 1 M NaPF <sub>6</sub> /EC+DMC (1:1 in weight) electrolyte (b/e/g) and NaFSI-TEP/TTE (1:1.5:2 in mole) electrolyte (c/f/h/i). .....	201
Figure 131. Close agreement in paired anti-site (PAS) defect concentration determined from X-ray (blue) and neutron (red) powder diffraction data.....	204
Figure 132. (left) Energy of paired anti-site (PAS) defect formation is found to depend on the total concentration of Ni <sup>2+</sup> in the NMC phase. (right) Predicted PAS defect composition as a function of NMC composition. For the range of experimentally measured samples (symbols), predictions are accurate within ~ 0.5% (absolute).....	204
Figure 133. (a) Solvation structure ( <sup>17</sup> O-NMR spectra) of different solvents and electrolytes with different LiFSI concentrations and TFE0 ratios. Cycling performance of Li  NMC-811 cells under (b) moderate and (c) practical conditions with different electrolytes, where the cells were cycled between 2.8-4.4 V after two formation cycles at C/10 rate.....	205
Figure 134. (a) Optical image of three liquids and their 1 M LiFSI electrolytes. (b) Single crystal of LiTf/FDMB showing Li-F interactions. For clarity, only one LiTf and one FDMB are shown.....	206
Figure 135. (a) Coulombic efficiency as a function of stacking pressure under various current densities. (b/d) Top view and cross-section view of deposited lithium morphology formed under no pressure. (c/e) Top view and cross-section view of deposited lithium morphology formed under critical pressure. The lithium in (b-e) was deposited at 2 mA/cm <sup>2</sup> for 1 hour. ....	207
Figure 136. The tortuosity of reduced graphene oxide as a lithium host has a profound impact on lithium deposition. Vertically aligned host with minimal tortuosity results in more uniform lithium deposition in the host.....	208
Figure 137. In an ether electrolyte (1 M of LiTFSI in 1:1 v/v DOL/DME with 1% LiNO <sub>3</sub> ), VGA clearly outperforms RGA and HGA due to its low tortuosity. (LiTFSI: lithium bis(trifluoromethanesulfonyl)imide; DOL: dioxalane; DME: dimethoxyethane) .....	208
Figure 138. (a) Histogram of the pore size distribution of the porous copper. (b) Tortuosity of the porous copper as a function of depth. (c) Effective surface area in the porous copper. (d) The 3D tomography of 30Arc and 20Arc with resolution of 0.7834 μm. (e) The 3D tomography of 10Arc and 30Furnace with resolution of 1.07 μm; the scale bar indicates 200 μm. ....	209
Figure 139. Cross-linking a polyacrylonitrile polymer results in a decrease in conductivity, but an increase in Li-ion transference number. ....	210

---

Figure 140. Photograph of the recorded thickness of (a) polyethylene (PE) and (b) LATP-coated PE separator by a micro-meter calliper. (c) Scanning electron microscopy image of the cross-section of the LATP-coated PE separator.....	210
Figure 141. Comparison of Tank-in-Series model and 1D model predictions at rates of 0.2C (blue), 0.5C (green), and 1C (orange) (a) with the Base Case diffusion coefficient of $1 \times 10^{-10} \text{ m}^2/\text{s}$ , and (b) with diffusion coefficient of $1 \times 10^{-11} \text{ m}^2/\text{s}$ where transport limitations are introduced and some variation is introduced at the end of discharge.....	211
Figure 142. Pair distribution function (PDF) analysis and schematic illustration of the synthetic process of CPAPN-S. (a) PDF data of sulfur and CPAPN-S. Characteristic bonds and their corresponding PDF peaks are labelled. (b) PDF data of pristine and <i>ex situ</i> CPAPN-S electrodes in the 1 <sup>st</sup> cycle, indicating that S-O, S-C, and S-S bond lengths generally increase during discharge and decrease during charge. (c) PDF data of charge-to-3V electrode overlaid on the pristine data (without offset), showing the decrease of S-O peak and increase of S-S peak after 1 <sup>st</sup> cycle. (d) A schematic illustration of the formation of chemical bonding stabilized carbon-small sulfur composite.....	212

## TABLE OF TABLES

Table 1. The key compositions of final cell, including cathode, separator, electrolyte, and anode..... 8

Table 2. Test cell numbers and sulfur loading of deliverable test cells..... 9

Table 3. Composition of PEO-POSS and POSS-PEO-POSS diblock and triblock copolymers. .... 24

Table 4. Tabulated glass chemistry for glassy solid electrolyte testing. .... 28

Table 5. Tabulated thermal properties of glassy solid electrolytes. .... 29

Table 6. Conductivity at 25°C and critical current density of the multilayer electrolyte materials. .... 61

Table 7. Summary of nudged elastic band (NEB)-computed activation energies for  
Li-ion diffusion in bulk LLZO under various strains. .... 117

Table 8. Comparison of calculated room-temperature lithium conductivity and activation energy  
for lithium transport in the bulk of Al-doped LLZO with measured values from  
two references. .... 139

Table 9. Thickness of the polymer composite membranes showing swelling with TEGDME. .... 148

## **A MESSAGE FROM THE MANAGER: ADVANCED BATTERY MATERIALS RESEARCH PROGRAM AND BATTERY500 CONSORTIUM**

In spite of the pandemic, the Advanced Battery Materials Research (BMR) and Battery500 Teams continued to advance battery science and technology. In this document, we report on the progress made from April 1, 2020, through June 30, 2020.

A few notable achievements from the BMR investigators this quarter are summarized below:

- The Virginia Commonwealth University team (P. Jena) has modeled and screened cluster-based electrolytes that display low activation energies, practical room-temperature ionic conductivities, wide electrochemical stability windows, and desirable mechanical properties. The group found that nonstoichiometric compositions of  $\text{Li}_6\text{PS}_2\text{Cl}$  containing excess lithium show 3 orders of magnitude higher room-temperature conductivity than that of the stoichiometric compositions.
- Novel characterization approaches to evaluate the variations in solid-state electrolyte electronic conductivity as a function of location as well as electrochemical cycling were developed by the Stanford University/SLAC National Acceleratory Laboratory team (Y. Cui, W. Chueh, and M. Toney).
- A series of semi-graphitic ordered mesoporous carbons with metal/nitrogen doping (Me–N-GOMCs; Me = Fe, Co, Ni, and Cu) was designed as sulfur hosts by the University of Wisconsin team (D. Qu). When these materials were embedded in the void space of carbon paper to construct a free-standing sulfur cathode ( $\sim 3 \text{ mg/cm}^2$ ), a coin cell displayed a high initial capacity of 1473 mAh/g and good cycling stability for up to 500 cycles.
- Density functional calculations were conducted by the Argonne National Laboratory (L. Curtis and A. Ngo) and University of Illinois at Chicago (A. Salehi-Khojin) team to investigate how two electrolyte additives,  $\text{InI}_3$  and  $\text{InBr}_3$ , provide a protective interphase on the lithium anode that promotes long cycle life in  $\text{Li-O}_2$  batteries. The computations reveal that the  $\text{InX}_3$  additive ( $X = \text{I, Br}$ ) can react and dissociate on the lithium surface, forming  $\text{LiX}$  interphase that protects against oxygen cross-over and other deleterious reactions.
- The Argonne National Laboratory (C. Johnson and K. Amine) team reported a low-cost, red phosphorus-based anode that can demonstrate a high specific capacity of 2000 mAh/g, with stable cycle performance and high initial Coulombic efficiency of 86% as well as thin solid-electrolyte interphase during cycling.

Highlights from the Battery500 Consortium team include the following:

### **Keystone Project 1: Materials and Interfaces**

- The Pacific Northwest National Laboratory team systematically investigated the tris(2,2,2-trifluoroethyl)orthoformate (TFEO)-based localized high concentration electrolytes (LHCEs). Formulation of  $\text{LiFSI}$ -(1.2~1.3) dimethoxyethane (DME) -2TFEO demonstrated 80% capacity retention over 200 cycles in 4.4 V  $\text{Li}||\text{NMC-811}$  cells under practical conditions.

### **Keystone Project 2: Electrode Architecture**

- Tortuosity was found to be a critical parameter affecting the morphology and electrochemical performances of hosted lithium anodes. The team at Stanford synthesized three types of hosts (vertically aligned, horizontally aligned, and random rGO electrodes) and showed that high electrode tortuosity causes locally higher current density on the top surface of electrodes, resulting in thick lithium deposition on the surface and degraded cycling performance.

### **Keystone Project 3: Cell Fabrication, Testing, and Diagnosis**

- The Pacific Northwest National Laboratory team developed a “machine learning-assisted lithium metal battery design software package.” Additional information about this tool can be found online (<https://www.pnnl.gov/technology/li-batt-design-app>).

We encourage you to follow our progress as we proceed. Our next report is expected to be available in January 2021.

Sincerely,

*Tien Q. Duong*

Tien Q. Duong  
Manager, Advanced Battery Materials Research Program & Battery500 Consortium  
Batteries & Electrification R&D  
Energy Efficiency and Renewable Energy  
U.S. Department of Energy

## TASK 1 – Liquid/Polymer Solid-State Electrolytes

### Summary and Highlights

The BMR Program goal is to develop long-life batteries superior to commercial Li-ion systems in terms of cost, vehicle range, and safety. The BMR Program addresses the fundamental problems of electrode chemical and mechanical instabilities that have slowed development of affordable, high-performance, automotive batteries. The aim is to identify electrode/electrolyte materials that yield enhanced battery performance and lead to greater acceptance of electric vehicles (EVs). Currently, the U. S. Department of Energy (DOE) Vehicle Technologies Office (VTO) supports 16 projects in the BMR Program under this Electrolytes Task. These projects can be categorized into four general topics:

- **Liquid.** The projects for liquid electrolyte (LE) aim to develop electrolyte formulations, based on fluoro-chemistries, to achieve significantly improved operating voltage, increased durability, and increased energy density of Li-ion batteries at a reasonable cost. Nonaqueous polyelectrolyte solutions with high Li<sup>+</sup> transference numbers will be developed to achieve high rate capabilities at room temperature. In addition, electrolytes with new polymer binders bearing a pentafluorophenyl group on the backbone will be designed, synthesized, and tested.
- **Polymer.** The targets of polymer electrolyte (PE) projects include inorganic/polymer and polymer/gel hybrid electrolytes that have flexibility, mechanical strength, thermal stability, high ionic conductivity, stable interfaces against lithium metal, and polysulfide-trapping capability enabling energy density Li-S batteries, with comparable cycle life.
- **Self-Forming & Self-Healing.** The self-forming, self-healing electrolyte projects are focused on developing and implementing Li-metal-based metal fluorite and metal iodide batteries, capable of energy densities > 400-500 Wh/kg and 1000 Wh/L.
- **Solid-State.** The solid-state projects are to develop high conductivities solid electrolytes (SEs) / composite SEs that are scalable, are chemically and electrochemically stable, and will enable low-cost, high-energy-density solid-state lithium batteries (SSLBs).

### Highlights

At the Daikin group (J. Sunstrom, R. Hendershot, and A. Falzone), the final report from Idaho National Laboratory (INL) outlining the results of the FY 2019 *Go/No-Go Decision* milestone were received. Cells comprised of NMC-532 / artificial graphite with the optimized fluorinated electrolyte exceeded the project's performance target of  $\geq 80\%$  capacity retention at 300 cycles when cycled at 4.6 V. Baseline cells with identical cell chemistry and hydrocarbon electrolyte fell below the 80% capacity threshold after 100 cycles. Full results from interim cell testing will be included in the FY 2020 report, along with the final project report.

The University of Washington (UW; A. Jen and J. Yang) group received official release of deliverable cell test data via an email on June 11, 2020, from INL. Overall, the improved cells possess much better performances in initial discharge capacity, cycling stability, and C-rate performance. The significantly improved cycling stability of cells is attributed to the multiple function of PENDI-350, which not only mediates transformation of soluble lithium polysulfides into insoluble polysulfides, but also traps dissolved polysulfides via strong ion-dipole interaction. The better initial discharge capacity and C-rate performances are connected to the improved ionic conductivity and electrolyte wetting. Despite these improvements, the improved cells still suffer from capacity decay and shuttle effect. A final project report has been submitted to the DOE.

At Stony Brook University (SBU; E. Takeuchi), destructive analysis of tested cells has been carried out. The evolution of the active interfaces was revealed by scanning electron microscopy (SEM) images as the LiI formed lithium and iodine and then reformed LiI. The combination of backscattered electron (BSE) images

with energy dispersive spectroscopy (EDS) proved effective in visualizing the features of the SE in the pristine and formed cells. The images provide insight into the enhanced Coulombic efficiency (CE) attained by cells with modified interfaces compared to cells with only SE and current collectors.

The University of California at Berkeley (UC Berkeley; B. McCloskey) team focused on theory and modeling to understand the issues occurring during transference number measurements, particularly deviations from expected literature results during Bruce-Vincent-type polarization experiments and the sensitivity of restricted diffusion measurements to the fitting window. In addition, they have completed a molecular dynamics (MD) study of the ion correlations and transport properties of polyelectrolytes. They find that the transference number monotonically decreases as a function of polyanion chain length, with the most drastic decreases observed at low ion concentrations.

The Stanford University (Z. Bao and Y. Cui) group carried out long-term stability of polymer coating evaluation by monitoring the evolution of the interfacial resistance over time with and without the polymer coating. They found that the presence of polymer coating significantly diminishes impedance divergence as a function of time. They also found that the polymer coating significantly enhances the lifetime of a full-cell, in which the polymer-coated thin 25- $\mu\text{m}$  Li-metal electrode ( $N = 5\text{mAh/cm}^2$ ) was paired against LiNiMnCoO<sub>2</sub> (NMC-532) cathode having capacity (P) 1.7 mAh/cm<sup>2</sup> and the batteries (N/P = 3).

The Lawrence Berkeley National Laboratory (LBNL; N. Balsara) group has completed full electrochemical characterization of hybrid organic-inorganic block copolymer electrolytes this quarter, including ionic conductivity as a function of temperature and salt concentration; diffusion coefficient, current fraction as a function of salt concentration; and thermodynamic factor and cation transference number.

The Iowa State University (ISU; S. Martin) group has demonstrated that the MOSN MGF GSEs (mixed-oxy-sulfide-nitride, mixed-glass-former glassy solid electrolyte) are stable against lithium through 100 cycles. In addition, they have optimized the film tower system by adding a conveyor assembly within the tower to allow tools to be more effectively moved from the lower zones to the upper zones. They have also used alternative oxide glasses having similar thermal and mechanical properties allowed for the testing of draw tower capabilities at lower cost by using borosilicate glasses.

The Wildcat group (K. Carroll/C. Peebles) has down-selected LATP as the ceramic ionic conductor, the composite SE additives, and the high-voltage polymer formulations for future optimization. They have also screened 70+ different Li-metal protection materials (called artificial SEIs, or ASEIs) from 14 different additive families (anhydride, carbonate, etc.) using their high-throughput (HT) platform. Their data suggest that the protective film formed from an ASEI may be more susceptible to the ASEI cation and less susceptible to the ASEI anion.

The University of Michigan (UM; J. Sakamoto) was able to manufacture thin film constructs (TFC) for delivery to the N. Dasgupta group for surface chemical analysis using X-ray photoelectron spectroscopy (XPS). Their data demonstrate that the surface of as-fabricated TFC LLZTO is clean on both the lithium anode and cathode interfaces. Because surface cleanliness directly correlates with interface resistance, these data indicate that the interface resistances should be relatively low.

The University of Maryland (UMD; C. Wang) group measured electrochemical properties of Li|Li<sub>7</sub>N<sub>2</sub>I-LiOH (coated) | Li symmetry cell. The stability of Li<sub>7</sub>N<sub>2</sub>I-LiOH electrolyte with lithium metal was also demonstrated by the galvanostatic cycling test. In addition, their modeling work showed that the critical potential for the cell will be affected by not only the Li | solid-state electrolyte (SSE) interface but also the cathode|SSE interface. To get a good capability in suppression dendrite, a stable SSE is needed.

The General Motors (GM; T. Yersak) group focused primarily on developing a baseline dataset with which to evaluate potential catholytes and hot pressing protocols. They found the following: the LiNbO<sub>3</sub> coatings are confirmed to improve the performance of test cells with  $\beta$ -Li<sub>3</sub>PS<sub>4</sub> SSE; the benefit of composite preparation by

ball milling becomes apparent at higher electrode loadings; and with a composite loading of  $46.2 \text{ mg/cm}^2$ , they achieved the target of  $> 3 \text{ mAh/cm}^2$  at a C/10 rate and room temperature. In addition, the candidate cathode they used showed very good thermal stability.

At UMD (E. Wachsman and Y. Mo), X-ray diffraction (XRD) experiments were performed on composite pellets of Ta-doped LLZO (LLZTO) and cathode materials prepared by physical mixing, mold pressing, and co-sintering at  $700^\circ\text{C}$  for 3 hours. Cathode materials tested include NMC-111,  $\text{LiMnO}_4$  (LMO),  $\text{LiNi}_{0.5}\text{Mn}_{1.5}\text{O}_4$  (LNMO), and  $\text{LiCoO}_2$  (LCO). XRD results suggest that at  $700^\circ\text{C}$ , all the cathode materials investigated react with LLZTO, with the reactivity increasing in the order of  $\text{LCO} < \text{LNMO} < \text{LMO} = \text{NMC-111}$ . This trend generally agrees with their computational studies reported last quarter showing that higher nickel content in cathodes generally leads to poor stability with garnet.

The team at University of Wisconsin at Milwaukee (UWM; D. Qu) has investigated and shown the role of trisaminocyclopropenium (TAC) cation on lithium dendrite suppression. A cation-shield mechanism is proposed. It is well established that the plating process can unavoidably generate protuberant tips on which electric charges tend to accumulate. The TAC cations can be absorbed on those tips without being reduced via electrostatic attraction. Thus, a lithiophobic protective layer can be formed due to its bulky scaffold with branched nonpolar groups. The arriving  $\text{Li}^+$  was repelled and deposited on the adjacent flat lithium surface, thus generating a dendrite-free lithium deposition.

The team at Virginia Tech (VT; L. Madsen) has investigated compatibility between the molecular ionic composite (MIC) electrolyte and Li-metal anode through cyclic voltammetry (CV) and symmetric cell cycling. Furthermore, the team has investigated the mechanisms of ion transport and the thermo-mechanical stability of the MIC electrolyte.

The team at Solid Power (P. Zhang) and UC San Diego (UCSD; S. Meng) showed that their multifunctional electrolyte materials have met the Year 1 performance targets on both the Li-ion conductivity and the critical current density (CCD) against lithium metal. They have also scaled up the SSE separator coating process at pilot scale. Furthermore, their full cell demonstrated 250 cycles at 80% capacity retention, exceeding the cycle life target in Year 1 ( $> 200$ ). The cell performance results support a *Go Decision* to continue the project.

The Pennsylvania State University (PSU; Wang) group investigated a new SE system,  $65\text{Li}_2\text{S}-65\text{Li}_2\text{S}-26\text{P}_2\text{S}_5-10\text{Li}_3\text{N}-x\text{Al}_2\text{S}_3$  (LPSNAI-x). They found  $\text{Al}_2\text{S}_3$  impurities when  $x$  is above 14. Highest ionic conductivity of above  $0.7 \text{ mS cm}^{-1}$  was achieved when  $x = 10$ . It was found that with  $\text{TiS}_2$  addition ( $\sim 0.38 \text{ wt\%}$  in the cathode) to replace SE (LPS), rate performance and sulfur utilization of sulfur cathode were greatly improved. They also optimized carbon materials for sulfur cathode.

## Task 1.1 – Advanced Lithium-Ion Battery Technology: High-Voltage Electrolyte (Joe Sunstrom, Ron Hendershot, and Alec Falzone, Daikin)

**Project Objective.** The project objective is to identify electrolyte formulations, based on fluoro-chemistries, that will allow significantly improved operating voltage, increased durability, and increased energy density of Li-ion batteries at a reasonable cost. The project seeks to understand the conditions under which the electrolyte degrades, the effect on battery performance, and solutions that can overcome current limitations of the electrolyte. Gassing in Li-ion batteries is one of the most common failure mechanisms and poses the greatest safety risk in consumer devices. This project aims to investigate gas composition as a function of cathode material, electrolyte formulation, and operating voltage, and proposes optimal cell compositions at decomposition voltages.

**Project Impact.** Developing an understanding of the operating conditions in which gases form in Li-ion batteries enables the project to propose optimized cell compositions that operate at higher voltages for a longer period. Different fluorinated electrolyte components and additives may suppress and/or eliminate gas generation at or above hypothesized decomposition voltages. To investigate these topics, it is imperative that the project utilize multiple approaches, including, but not limited to, cathode material, electrolyte composition, operating voltage, and cycle number.

**Approach.** The evolving composition of the electrolyte in the battery will be examined by various analytical instruments to study volatiles [gas chromatography – mass spectrometry / thermal conductivity detection (GC-MS/TCD)], liquid [liquid chromatography MS (LC-MS)], and solid [time-of-flight secondary ion mass spectrometry (TOF-SIMS), thermogravimetric analysis MS (TGA-MS), XPS, and auger electron spectroscopy (AES)] electrolyte decomposition products during battery operation. In the first year, the team addressed gas composition and kinetics for both hydrocarbon and fluorocarbon as a function of several charge/discharge conditions. In the second year, the project will transition into analysis of the SSE decomposition components of its tested batteries to obtain valuable information about solid electrolyte interphase (SEI) layer formation and how it manifests change in both the anode (graphite) and cathode (LCO and NMC). The third year is focused on measuring changes in the solid-state structure of the cathode following high-voltage operation. The project aims to quantify any dissolved metal ions originating from the cathode and deposited on the anode using inductively coupled plasma – mass spectrometry (ICP-MS). It will also study changes in the cathode structure using powder XRD.

**Out-Year Goals.** Work will progress toward understanding how electrolyte formulation and cell operation affect stability of transition metals (TMs) in the cathode structure. The project aims to quantify metal ions, if any, dissolved into solution as a function of operating parameters (that is, voltage, time, etc.) and electrolyte formulation. In addition, measurements will be made using powder XRD to detect changes in the crystal structure of the cathode (LCO and NMC). Understanding effects on the solid-state structure in Li-ion batteries will provide valuable information on the required cathode chemistry for increased performance at high voltage.

**Collaborations.** The project has initiated a collaboration with Dr. J. Chan (University of Texas, or UT, at Dallas) for powder XRD measurements to investigate changes in cathode structure as a function of operating conditions.

### Milestones

1. *Go/No-Go Decision:* Interim cells achieve significant improvement at 4.6 V. (Q4, FY 2019; Complete)
2. Cathode structure versus time/voltage. (Q3, FY 2020; In progress)
3. Data compilation and selection of new electrolyte composition. (Q4, FY 2020; In progress)

## Progress Report

The team received the final report from INL outlining results of the FY 2019 *Go/No-Go Milestone*. Cells comprised of NMC-532 / artificial graphite with the optimized fluorinated electrolyte exceeded the project's performance target of  $\geq 80\%$  capacity retention at 300 cycles when cycled at 4.6 V. Baseline cells with identical cell chemistry and hydrocarbon electrolyte fell below the 80% capacity threshold after 100 cycles. Full results from interim cell testing will be included in the FY 2020 report, along with the final project report.

Full experimental results were obtained from the first trial of measuring pouch cell thickness changes as a function of testing parameters. This experimental setup is depicted in Figure 1, and utilizes a pseudo-interferometer method to correlate laser position to changes in position on the z-axis (pouch cell swelling). The first trial utilized a cell chemistry of NMC-532 / artificial graphite with fluorinated electrolyte [1.2 M LiPF<sub>6</sub>, 60:20:20 ethyl methyl carbonate (EMC) : fluoroethylene carbonate (FEC) : hydrofluoroether (HFE) + 1% PS (w/w)] at 4.6 V. The cell was cycled between 3.0 V and 4.6 V at C/2, with a CC-CV (C/20) step every 10 cycles.

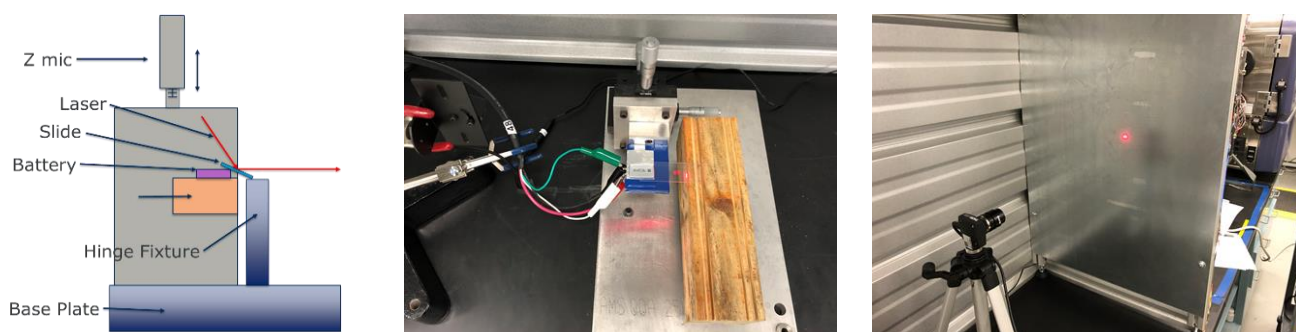


**Figure 1.** (left) Schematic of contact-less components. (center) Incident angle of laser off glass slide resting on a 200-mAh pouch cell. (right) Depiction of the time-resolved camera setup tracking the laser position throughout the duration of the experiment.

A calibration curve was generated before initializing the experiment, normalizing the starting thickness of the cell to a 0% change (3.776-mm starting thickness of cell). The largest cell thickness change was observed at cycle number 10, with an approximate 3.5% (132  $\mu\text{m}$ ) increase. The NMC-532 cell with fluorinated electrolyte exhibited  $\geq 80\%$  capacity at the conclusion of the experiment.

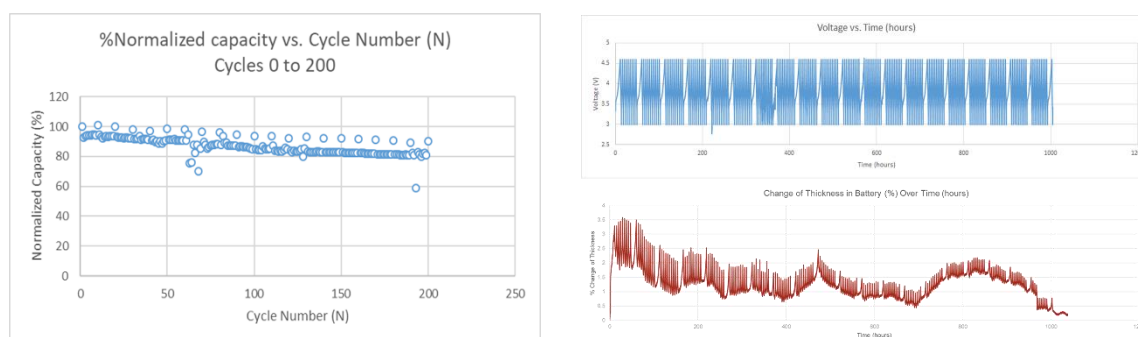


**Figure 2.** (left) Normalized discharge capacity as a function of cycle number. (right) Cell thickness change (%) as a function of state of charge.

Efforts to quantify gaseous components of pouch cells as a function of electrolyte and cell chemistry continued this quarter. Calibration curves were updated to account for increased amounts of CO<sub>2</sub> and O<sub>2</sub> observed in NMC-622 and NCA cells at 4.6 V. Pouch cells without the applied coating reported last quarter were injected for gas quantification to confirm coating effectiveness. This experimental method introduced a significant amount of N<sub>2</sub>/O<sub>2</sub> (air), further supporting the notion to coat pouch cells before quantification via GC/MS.

## Patents/Publications/Presentations

The project has no patents, publications, or presentations to report this quarter.

## Task 1.2 – Multi-Functional, Self-Healing Polyelectrolyte Gels for Long-Cycle-Life, High-Capacity Sulfur Cathodes in Lithium-Sulfur Batteries (Alex Jen and Jihui Yang, University of Washington)

**Project Objective.** The project objective is to develop self-healing and polysulfide-trapping polyelectrolyte gels containing room-temperature ionic liquid (RTIL) for the Li-S battery system. The Li-S battery design will be able to achieve gravimetric and volumetric energy densities of  $\geq 800$  Wh/kg and  $\geq 1000$  Wh/L, respectively.

**Project Impact.** The Li-S battery system is hampered by poor capacity retention, primarily caused by dissolution of polysulfide reaction intermediates in typical organic electrolytes, as well as poor electrical contact between insulating sulfur and the conductive carbon matrix. This project aims to produce a high-capacity, long-cycle-life Li-S battery system by using rational molecular design strategies to address each capacity loss mechanism directly. A long-cycle-life Li-S battery system capable of doubling Li-ion energy density would enable production of lighter, longer range EVs at a cost that is affordable to the average U. S. household.

**Approach.** The team will develop Li-S coin cells that utilize self-healing, interpenetrated ionomer gel electrolytes in both the cathode and separator. The team will synthesize necessary starting materials and fabricate components of these gels while testing their relevant electrochemical and mechanical properties. All components are combined into interpenetrating structures, which are being tested both alone and in cell configurations. Device performance data were collected and used to further optimize designs of both material and cell, culminating in an optimized Li-S battery design capable of doubling the energy density of traditional Li-ion batteries. The team has focused on (1) design and synthesis of various precursors for gel electrolytes, (2) fabrication and testing of both reference materials and novel materials made from these precursors, and (3) iterative validation and improvement of design principles through both materials and device testing.

**Out-Year Goals.** Work will progress toward developing structure-property relationships for the self-healing, interpenetrated gel ionomer electrolyte and its individual components, as well as successful incorporation of such an electrolyte into a working Li-S cell. The team plans to demonstrate significant improvements in both capacity and retention when using the project's developed materials, as compared to state-of-the-art reference systems.

**Collaborations.** This project funds work at UW. Dr. A. Jen, principal investigator (PI), focuses on design, synthesis, and testing of novel materials, as well as device-based verification of design principles. Dr. J. Yang (co-PI) focuses on optimizing device fabrication and testing, as well as investigating failure mechanisms in devices using novel materials. Pacific Northwest National Laboratory (PNNL) facilities are used for detailed material characterization study.

### Milestones

1. Provide test cells for performance evaluation at a designated DOE testing laboratory: 12 baseline cells or half cells with a minimum capacity of 10 mAh, and 12 improved cells or half cells with a minimum capacity of 10 mAh. (Q1, FY 2020; Completed)
2. Suggest test procedures for the cells/half-cells evaluation. This should include discharge/charge voltage and current limits, number of test sequences, recommended cycling temperature, or other relevant test conditions as appropriate. (Q1, FY 2020; Completed)
3. Analyze deliverable test cell performance data collected by the designated DOE testing laboratory, INL. (Q3, FY 2020; Completed)

## Progress Report

**Composition of Deliverable Cells.** The compositions of the project’s final cell design are summarized in Table 1. More specifically, the cathode layer consists of C-SH/S composite, binder, and conductive carbon [C-SH/S : binder : carbon nanotube (CNT) = 70:25:5 by weight]. The binder is formed by blending PENDI-350, poly(ethylene oxide) (PEO), and poly(vinylidene fluoride) (PVDF) in weight ratio of 2:1:1. Carbon-coated aluminum foil is used as cathode current collector. The 2032 coin-type cells were assembled. PVDF was used as binder in the control cells.

**Table 1. The key compositions of final cell, including cathode, separator, electrolyte, and anode.**

<b>Cathode</b>	C-SH/S composite (70 wt%)	Mesoporous carbon (MJ430) was modified with thiol groups to form C-SH; C-SH was then mixed with S by melt-infiltrated method to form C-SH/S composite; The weight ratio of S in C-SH/S composite was estimated as 56% by TGA
	Binder (25 wt%)	PENDI-350:PEO:PVDF = 2:1:1 (by weight)
	Conductive carbon (5 wt%)	Carbon nanotube (CNT)
<b>Separator</b>	Polypropylene (PP) Celgard2500	
<b>Electrolyte</b>	1 M lithium bis-(trifluoromethanesulfonyl)imide (LiTFSI) and 2 wt% LiNO <sub>3</sub> in 1,3-dioxolane (DOL) / 1,2-dimethoxyethane (DME) (v/v =1:1) as the electrolyte; 7 mL of electrolyte was used for 1 mg S	
<b>Anode</b>	Lithium metal (0.25 mm in thickness)	

**Suggested Testing Protocol for the Deliverable Cells.** The protocol for testing the deliverable cells with 10-mAh nominal capacity and evaluation metrics for each cell is summarized below.

### 1. Cell Components and Construction

**SS | Li Anode.** Pure lithium metal (Ø15.6 mm, MTI Corp) pressed onto a SS304 disc (Ø15.5 mm, MTI Corp).

**Electrolyte.** 1 M LiTFSI dissolved in 1,3-dioxolane (DOL, Sigma-Aldrich) and 1,2-dimethoxyethane (DME, Sigma-Aldrich) in a 1:1 volumetric ratio, with 2 wt% LiNO<sub>3</sub> (Sigma-Aldrich) added for anode protection.

**S/C Cathode (Improved).** A Ø16mm composite film of pure sulfur (powder, ≥ 99.8% trace metals basis, Sigma-Aldrich) melt-diffused into an equal or lesser weight of mesoporous carbon (MJ430, Toyo Tanso Co Ltd) which has been surface-modified with thiol functionality, held together by a novel mixture of polymer binders. The nominal capacity is 10 mAh.

**S/C Cathode (Control).** A Ø16 mm composite film of pure sulfur (powder, ≥ 99.8% trace metals basis, Sigma-Aldrich) melt-diffused into an equal or lesser weight of mesoporous carbon (MJ430, Toyo Tanso Co Ltd), held together by PVDF (MTI Corp) as a binder. The nominal capacity is 10 mAh.

**C/Al.** Carbon-coated aluminum foil (Ø16 mm, 0.018 mm thick, MTI Corp) onto which the above composite film has been uniformly coated.

**Cell Construction.** The above components are assembled into CR2032 coin cells (Hohsen Corp), with the positive terminal contacting the large cap of the cell as following:

(SS | Li Anode | Electrolyte | S/C Cathode | C/Al)

### 2. Testing Protocol

It is recommended that cells be tested promptly after they are received. Electrochemical measurements should be performed on both control Li-S Cells and improved Li-S cells using an Arbin battery testing station or similar (LAND, Maccor, etc.) at room temperature (20-30°C). For constant-current cycling tests, cells should first be discharged at a fixed current of -0.5 mA cm<sup>-2</sup> (corresponding to a C-rate of C/20) until the cells reach a lower voltage threshold of 1.8 V, followed by a rest period of 10 min. This conditioning step should be considered

the 1<sup>st</sup> cycle, after which the 2<sup>nd</sup> cycle begins. Then, the cells may be charged and discharged at fixed currents (calculated from C-rate by assuming 10 mAh nominal capacity), between upper and lower voltage limits of 2.8 V and 1.8 V for charge and discharge, respectively. A rest step of 10 minutes should occur after each charge and discharge. It is recommended that cells be tested at both C/2 ( $\pm 5 \text{ mA cm}^{-2}$ ) and C/10 ( $\pm 1 \text{ mA cm}^{-2}$ ), although other rates may be acceptable. Test schedules should include a safety limit of 50-mAh capacity during each charge step, to halt the test in the case of an internal short-circuit due to redox shuttling of lithium polysulfides. Current should not exceed  $\pm 10 \text{ mA}$ .

### 3. Evaluation Metrics

Charge and discharge capacity may be converted to aerial capacity (mAh cm<sup>-2</sup>) using cathode area (2.011 cm<sup>2</sup>) or to gravimetric specific capacity (mAh/g) using the cathode weight table provided below. CE is undefined for the 1<sup>st</sup> cycle, which consists solely of the first discharge; for the 2<sup>nd</sup> cycle and beyond, it may be evaluated as the quotient of discharge capacity over charge capacity.

**Table 2. Test cell numbers and sulfur loading of deliverable test cells.**

Cell #	S/C Cathode Weights			
	Improved		Control	
	Total (mg)	Sulfur (mg)	Total (mg)	Sulfur (mg)
1	29.15	8.37	32.15	11.93
2	31.55	9.31	32.35	12.03
3	26.98	7.52	32.35	12.03
4	33.57	10.10	32.25	11.98
5	34.46	10.45	34.11	12.89
6	32.19	9.56	31.17	11.45
7	33.87	10.22	33.13	12.41
8	28.03	7.93	32.58	12.14
9	30.33	8.83	32.02	11.87
10	31.65	9.35	31.17	11.45
11	34.02	10.28	33.23	12.46
12	34.48	10.46	28.66	10.22

**Deliverable Cell Test Performed at INL.** As described, the team has delivered 24 coin cells (12 improved cells and 12 control cells) for testing to DOE-designated INL. They received official release of deliverable cell test data via an email on June 11, 2020. Results of the test are summarized in this section.

Deliverable test cells were divided into group A (3 improved cells and 3 control cells) for cycle life test at 0.1C rate and group B (3 improved cells and 3 control cells) for conditioning and cycle capacity tests with varying C rates of 0.1C and 0.5C (1C = 1675 mAh/g). Figure 3 shows the test results in group A. The cells are denoted as AI2, AI4, AI5, AC2, AC3, and AC5; “A” refers to “group A”, “I” or “C” refers to “improved cells” or “control cells,” and the last number refers to their corresponding number listed in Table 2. As shown in Figure 3a, the initial discharge capacities of control cells (AC2 and AC5) are around 920 mAh/g and 1020 mAh/g at 0.1C rate, respectively. Because AC3 failed in the 1<sup>st</sup> cycle, there is no data point for AC3 in Figure 3. Both AC2 and AC5 decay quickly and fail after 3-7 cycles. As mentioned, control cells were fabricated using PVDF as binder lacking LiPS trapping property. The CE of AC2 and AC5 is not only unstable, but also generally lower than 75%, which suggests serious shuttle effect. On the contrary, the improved cells (AI2, AI4, and AI5) deliver initial discharge capacities around 1020-1200 mAh/g, which are 100-200 mAh/g (10-20%) higher than that of control cells. The cyclability is improved to 40 cycles for AI2. The improved cells also possess much more stable and higher CE.

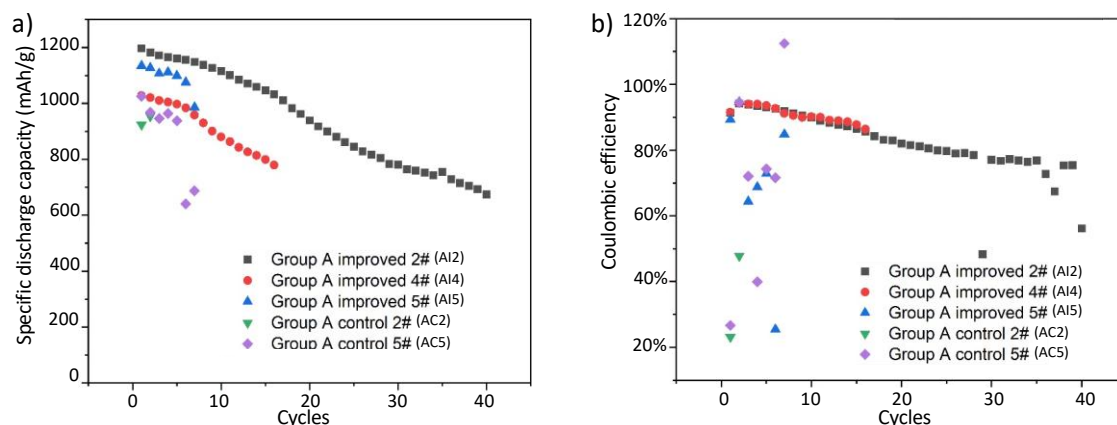


**Figure 3. Cycle capacity tests of improved and control cells in group A at 0.1C rate, including AI2 (4.67 mgS/cm<sup>2</sup>), AI4 (5.1 mgS/cm<sup>2</sup>), AI5 (5.2 mgS/cm<sup>2</sup>), AC2 (6.0 mgS/cm<sup>2</sup>), AC3 (6.0 mgS/cm<sup>2</sup>), and AC5 (6.4 mgS/cm<sup>2</sup>). (a) Specific discharge capacity and (b) Coulombic efficiency of improved and control cells.**

Figure 4 summarizes the test results of group B, including 6 cells denoted as BI7, BI11, BI12, BC7, BC8, and BC11; “B” refers to “group B”, “I” or “C” refers to “improved cells” or “control cells,” and the last number(s) refers to their corresponding number listed in Table 2. In this group, cells were tested at 0.1C rate in the first three cycles, followed by 9 cycles at 0.5C and 1 cycle at 0.1C, alternately. As shown in Figure 4a, the three control cells demonstrate similar initial discharge capacity to that of control cells in group A. However, their discharge capacities drop sharply to around 80 mAh/g at 0.5C and fail quickly. These suggest that control cells have poor C-rate performance. As for improved cells (BI7, BI12), they deliver discharge capacity around 860 mAh/g, even at 0.5C rate. When the C rate changed back to 0.1C at the 13<sup>th</sup> cycle, it still delivered discharge capacity ~ 990 mAh/g. The corresponding CE is stable and higher than 90%.

Overall, the improved cells possess much better performances in initial discharge capacity, cycling stability, and C-rate performance. The team attributes the significantly improved cycling stability of cells to the multiple function of PENDI-350, which not only mediates transformation of soluble lithium polysulfides into insoluble polysulfides, but also traps dissolved polysulfides via strong ion-dipole interaction. The better initial discharge capacity and C-rate performances contributed to the improved ionic conductivity and electrolyte wetting. Electrochemical impedance spectroscopy (EIS) test shows that the Li-ion conductivity of PENDI-350 ( $1.4 \times 10^{-2}$  mS/cm) reaches the same order of magnitude as amorphous PEO. The thiol groups surface modification of carbon also enhances the electrolyte wetting ability of cathode. All these advantages could enhance the cycling kinetics.

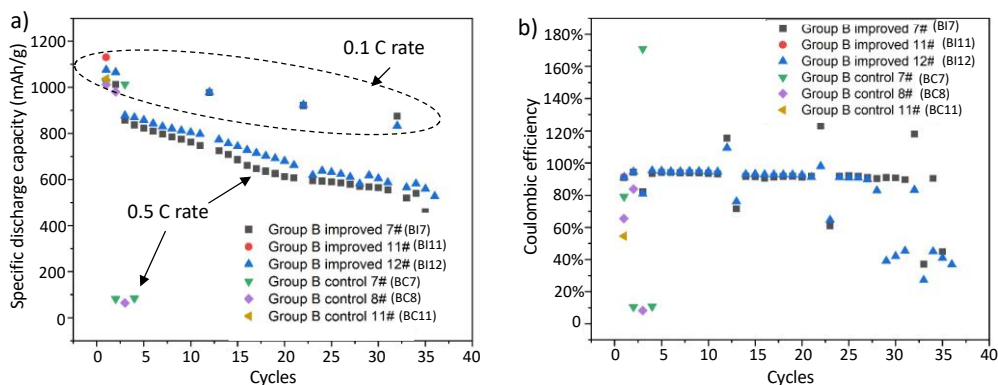


**Figure 4. Conditioning and cycle capacity tests of improved and control cells in group B at 0.1C rate, including BI7 (5.1 mgS/cm<sup>2</sup>), BI11 (5.1 mgS/cm<sup>2</sup>), BI12 (5.2 mgS/cm<sup>2</sup>), BC7 (6.2 mgS/cm<sup>2</sup>), BC8 (6.1 mgS/cm<sup>2</sup>), and BC11 (6.2 mgS/cm<sup>2</sup>). (a) Specific discharge capacity and (b) Coulombic efficiency of improved and control cells.**

Despite these improvements, the improved cells still suffer from capacity decay and shuttle effect. As discussed previously, the cracking issue has been a serious challenge for the project's PENDI binder system. With low loading ( $1.0 \text{ mg/cm}^2$ ), the cracking issue is negligible, which delivers improved cycling stability with high CE ( $> 99\%$ ). However, when the team increases sulfur loading, the problem of cathode cracking and shuttle effect is revealed. Especially when they fabricated cells with high sulfur loading ( $4.7\text{-}5.2 \text{ mg/cm}^2$ ) in Figures 3 and 4, the cathode cracking could be more prominent. Although LiPS could be transformed or trapped by PENDI, the cracks in cathode could lead to LiPS leaking into electrolyte. Therefore, to improve the design, the team needs to improve the mechanical integrity of the binder system. Two possibilities should receive attention. First, design derivative polymers with higher flexibility and molecular weight. Second, the recipe of physical blending with other binders should be optimized further.

### Conclusions

The team has delivered 24 coin cells (12 improved cells and 12 control cells) for testing to DOE-designated INL. They have received official release of deliverable cell test data from INL via an e-mail on June 11, 2020.

Overall, the improved cells exhibit much better performance in initial discharge capacity, cycling stability, and C-rate performance. The team attributes the significantly improved cycling stability of cells to the multiple function of PENDI-350, which not only mediates transformation of soluble lithium polysulfides into insoluble polysulfides, but also traps dissolved polysulfides via strong ion-dipole interaction. The better initial discharge capacity and C-rate performances are connected to the improved ionic conductivity and electrolyte wetting.

Despite these improvements, the improved cells still suffer from capacity decay and shuttle effect. The cathode cracking issue is negligible with low loading ( $1.0 \text{ mg/cm}^2$ ), which delivers improved cycling stability with high CE ( $> 99\%$ ). However, with increased sulfur loading ( $4.7\text{-}5.2 \text{ mg/cm}^2$ ) of the deliverable cells, the decay was more prominent. The team proposes two ways to further improve the mechanical integrity of the binder system. First, develop derivative polymers with higher flexibility and molecular weight. Second, optimize blends with other binders with complementary mechanical properties.

### Patents/Publications/Presentations

The project has no patents, publications, or presentations to report this quarter.

## Task 1.3 – Dual Function Solid-State Battery with Self-Forming, Self-Healing Electrolyte and Separator (Esther Takeuchi, Stony Brook University)

**Project Objective.** The project objective is to demonstrate a solid-state rechargeable battery based on a Li-metal anode and iodine cathode with a self-forming, self-healing electrolyte and separator with high gravimetric and volumetric energy density.

**Project Impact.** This program will enable demonstration of the proposed rechargeable battery with improved power capability, high energy density, and a self-forming, self-healing SSE/separator. Technical insight will be gained regarding improved conductivity of the solid LiI based electrolyte, power capability of the proposed system, the self-healing nature of the LiI layer, the nature of the electrode-electrolyte interfaces, and feasibility of the system to reach the DOE targets.

**Approach.** The proposed concept is a dual function rechargeable SSB utilizing LiI combined with silver iodide (AgI) as the electrolyte, with lithium metal (and small quantities of silver metal) as the anode and iodine as the cathode and with a self-forming, self-healing separator/electrolyte. The battery will be assembled in the discharged state, where the anode and cathode will be created during the first formation (charge) step. Initially, silver ion ( $\text{Ag}^+$ ) will diffuse toward the negative electrode and be reduced to silver metal ( $\text{Ag}^0$ ), and iodine ion ( $\text{I}^-$ ) will be oxidized to elemental iodine ( $\text{I}_2$ ) at the cathode side. As the formation of the battery continues, lithium ion ( $\text{Li}^+$ ) will form a Li-metal layer at the anode, with generation of iodine at the cathode. LiI will remain and serve as both the separator and electrolyte.

**Out-Year Goals.** This is a multi-year program where the effort is divided into three major tasks.

- Year 1 involves electrolyte preparation and characterization including preparation of SSEs and conductivity measurements.
- Year 2 will focus on cell construction and testing including both *in situ* and *ex situ* analysis.
- Year 3 will focus on cell characterization. Under the program, cycle life, efficiency, energy density, and the functional capacity of cells will be determined.

**Collaborations.** This project collaborates with A. Marschilok and K. Takeuchi of SBU.

### Milestones

1. Determine cycling performance at elevated temperature. (Q1, FY 2020; Completed)
2. Determine behavior of conductivity as a function of temperature to determine resistance as well as fundamental thermodynamic parameters of the SSEs. (Q2, FY 2020; Completed)
3. Conduct destructive analysis of tested cells. (Q3, FY 2020; Completed)
4. Perform extended cycle life testing. (Q4, FY 2020)

## Progress Report

This quarter, the milestone was to analyze cells after they have undergone formation and then have been cycled. For this set of experiments, four types of cells were explored where the interface of the SE was modified relative to the current collector. The four SEs of LiI-LiI(HPN)<sub>2</sub> cell types were: (1) SE only; (2) including lithium (Li-SE), (3) including CNT layer (SE-CNT), and (4) including lithium and CNT layers (Li-SE-CNT). Cells were charged to form the electrochemical couple Li/I. After formation, the cells were cycled over 10 or 40 cycles. Pristine and cycled cells were disassembled and used for analysis of the SE. The surface of the SE was analyzed, along with cross sections of the SE from each cell type. The analyses also focused on the areas near the interfaces of the SE. The microscopic observations provide insight into the formation and evolution of the microstructures as a result of cell formation and cycling. Additionally, the modified interfaces could be visualized through this analysis.

SEM-BSE imaging, EDS mapping, and high-resolution SEM-BSE were used to characterize pristine and cycled samples. SEM-BSE/EDS images of cross-sections of pristine SE-CNT are shown in Figure 5. As observed, a layer CNT is attached on the SE with some LiI particles integrated into the CNT layer (see

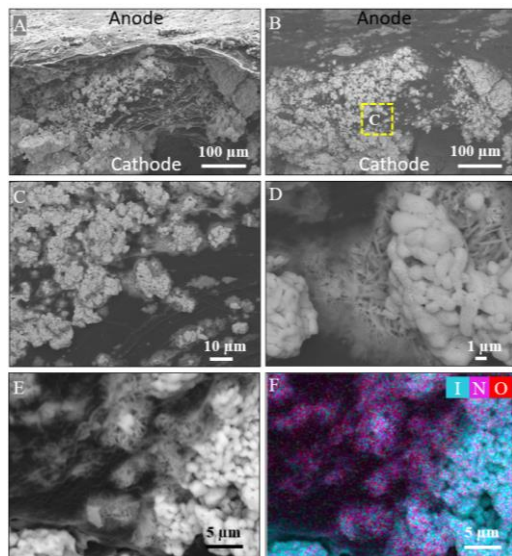


**Figure 6.** Scanning electron microscopy / energy dispersive X-ray spectroscopy (SEM-EDS) of the cross-section of cycled Li-SE. (a-b) SEM and backscattered electrons (BSE) images. (c-d) BSE from the yellow rectangle area in (b), with the bright area for LiI, grey area for LiI(HPN)<sub>2</sub>, and dark area for Li. (e-f) BSE image and EDS map, with blue for iodine, purple for nitrogen, and red for oxygen.

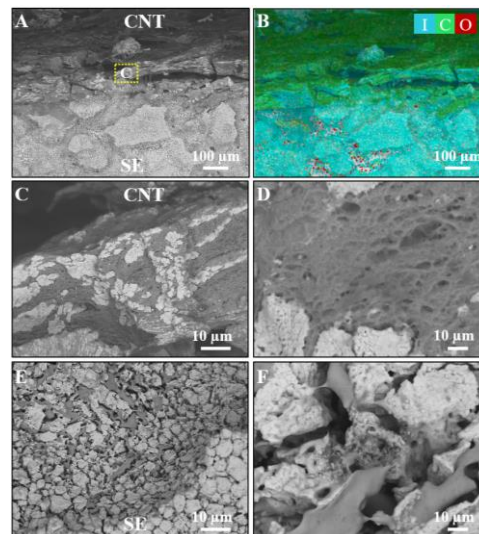


**Figure 5.** Scanning electron microscopy / energy dispersive X-ray spectroscopy (EDS) of the cross-section of pristine solid electrolyte (SE) – carbon nanotube (CNT). (a-b) Backscattered electrons (BSE) images and corresponding EDS map; blue for iodine, green for carbon, and red for oxygen. (c-d) BSE images of CNT area, with the bright area for LiI and dark area for CNT. (e-f) BSE images of LiI-LiI(HPN)<sub>2</sub> area, with bright area for LiI, and grey area for LiI(HPN)<sub>2</sub>.

Figure 5c-d). The LiI-LiI(HPN)<sub>2</sub> SE area, shown in Figure 5e-f, suggests the LiI is well dispersed, with LiI(HPN)<sub>2</sub> surrounding the LiI particles. The combination of BSE/EDS allows discrimination of the components present in the SE.

SEM-BSE/EDS images of cross-sections of cycled Li-SE in the charged state are shown in Figure 6. Figure 6a-b shows the larger view of cycled Li-SE. The magnified view of the yellow rectangle area in (b) is shown in Figure 6c-d, revealing evidence of lithium penetrating into the SE, where the bright area indicates LiI, grey area indicates LiI(HPN)<sub>2</sub>, and dark area indicates lithium. The compositions were also demonstrated by EDS mapping data (Figure 6e-f). Again, the composition of the microstructure was effectively visualized, including the aspects of a formed and cycled cell including detection of lithium metal.

SEM-BSE images of cross-section of cycled SE-CNT in charged state are shown in Figure 7. Figure 7a shows a thin layer of CNT attached on the SE surface on the cathode side. In Figure 7b-c, there is LiI particle layer on the top of the CNT layer indicating the LiI particle integration with

CNT layer. The BSE images of the anode side are shown in Figure 7d-f, where the bright area indicates LiI and the grey area indicates  $\text{LiI}(\text{HPN})_2$ . The morphology of  $\text{LiI}(\text{HPN})_2$  changed after cycling, as evidenced by a large piece of  $\text{LiI}(\text{HPN})_2$  and some phase separation from LiI (Figure 7f).

SEM-BSE images of cross-section of cycled Li-SE-CNT in charged state are shown in Figure 8. The cathode side is shown in Figure 8a-b; a layer of CNT attached on SE surface and some LiI particles integrated into the CNT layer, where the dark area indicates CNT and bright area indicates SE. The high-resolution SEM images of the CNT layer are shown in Figure 8c-d. The anode side attached with the lithium foil displayed penetration of lithium into the SE area and the morphology of  $\text{LiI}(\text{HPN})_2$  showing strip structures after cycling (Figure 8e-f).

The detailed SEM images collected over the past quarter have provided insight into the microstructure of the SE, both in the pristine state and after cycling. The evolution of the active interfaces was revealed as the LiI formed lithium and iodine and then reformed LiI. The combination of BSE-EDS proved effective in visualizing the features of the SE in the pristine and formed cells. The images provide insight into the enhanced CE attained by cells with modified interfaces compared to cells with only SE and current collectors.

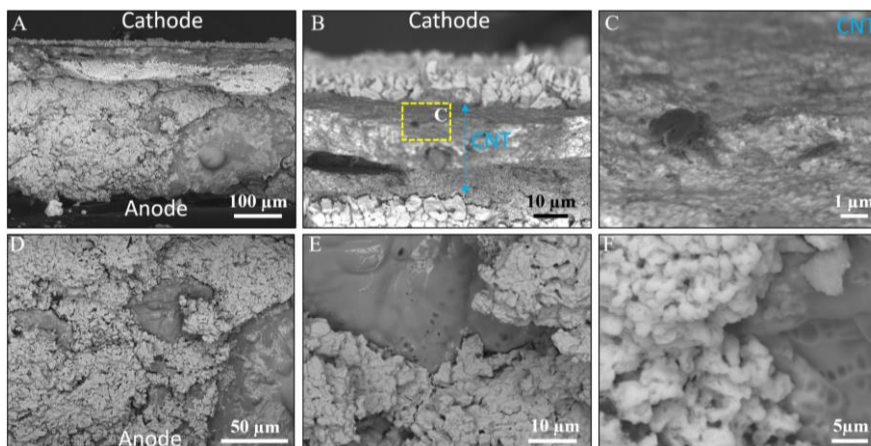


**Figure 7.** Scanning electron microscopy (SEM) images for the cross-section of cycled solid electrolyte (SE) carbon nanotube (CNT) in charged state. (a) SEM images. (b) backscattered electrons (BSE) images of cathode side with LiI and grey area for CNT. (c) High-resolution BSE images where the grey area is for CNT and the dark area for lithium. (d-e) BSE images of SE anode side; bright area is for LiI and grey area for  $\text{LiI}(\text{HPN})_2$ .

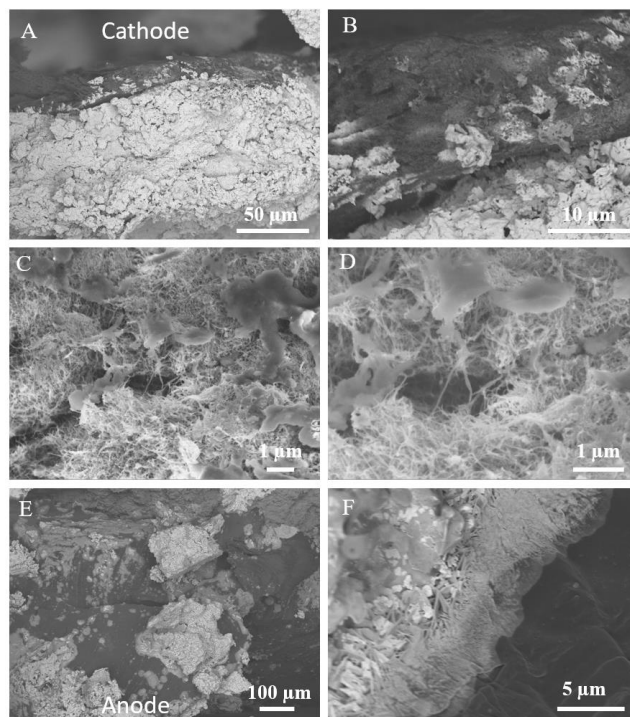


**Figure 8.** Scanning electron microscopy (SEM) images for the cross-section view of cycled lithium – solid electrolyte – carbon nanotube (Li-SE-CNT) in charged state. (a-b) Backscattered electrons (BSE) images of cycled at cathode side, where the dark area is for CNT and the bright area for lithium. (c-d) High-resolution SEM images of CNT area with lithium dendrite. (e-f) BSE images of SE anode side, with bright area for LiI, grey area for  $\text{LiI}(\text{HPN})_2$ , and dark area for lithium.

## Patents/Publications/Presentations

### Publication

- Submitted manuscript under revision.

## Task 1.4 – Characterization and Modeling of Li-Metal Batteries: Characterization of Li<sup>+</sup> Transport in Polyelectrolytes (Bryan D. McCloskey, University of California at Berkeley)

**Project Objective.** This task aims to understand lithium plating and stripping in non-traditional electrolyte systems (specifically, polyelectrolyte solutions and concentrated binary salt electrolytes) that have been proposed to reduce dendrite formation during lithium stripping and plating due to their high Li<sup>+</sup> transference numbers ( $t_+$ ). The team will develop capabilities that allow them to understand how ion dynamics in these electrolytes impact macroscale transport properties and Li-metal plating and stripping.

**Impact.** Ultimately, this task will develop an understanding of how electrolyte composition and molecular interactions can be manipulated to positively impact ion transport of potential electrolytes for Li-metal batteries. This will provide a set of general design rules for novel electrolytes enabling stable, efficient high capacity Li-metal stripping and plating.

**Approach.** To understand various aspects of lithium plating and ion transport in these systems, the team will develop novel diagnostic and computational modeling techniques. Model polyelectrolytes, with pendant triflimide anions, will be used as polyanions, as their properties can be easily tuned via changes in the polymerization chemistry. Solution parameters that can be varied for both polyelectrolyte solutions and concentrated electrolytes include solvent and salt composition, additive inclusion, and the aforementioned polymer properties, all of which can have a profound impact on electrostatic interactions between charged species in solution, as well as interfacial stability and reaction kinetics of the lithium electrode. The team will develop capabilities that allow them to understand how molecular-level ion dynamics in these electrolytes impact macroscale transport properties and Li-metal plating and stripping. These computational simulations will be validated and refined by comparing results to experimentally measured transport properties of these electrolytes. They will optimize electrochemical methods for these electrolytes to evaluate relevant transport properties under the Newman Concentrated Solution Theory framework, which has never been performed on these non-traditional electrolytes. <sup>1</sup>H and <sup>19</sup>F nuclear magnetic resonance (NMR) diffusometry will also be used to measure single-ion self diffusion coefficients without an applied electric field; solution viscosity measurements using a state-of-the-art rotating sphere viscometer can be performed under entirely air/water-free conditions. The team will develop capabilities to quantitatively understand degradation mechanisms of various electrolytes during Li-metal stripping and plating. Specifically, differential electrochemical MS will be used to study outgassing that occurs from electrolyte degradation processes.

**Out-Year Goals.** The ultimate goal of this project is to understand the influence of electrolytes with novel transport characteristics on the performance of Li-metal electrodes. Work will continue to build toward a complete understanding of Li-ion and counterion transport in polyelectrolyte solutions and concentrated electrolytes, as well as the impact of electrolyte transport properties on Li-metal uniformity during electrochemical stripping and plating. Outgassing measurements using differential electrochemical MS will be developed to further probe the interfacial reactivity of lithium metal with electrolytes created in this project.

**Collaborations.** Collaborators on this project include K. Persson (atomistic and coarse-grained modeling) and N. Balsara (electrochemical characterization of PEs), both at LBNL.

### Milestones

1. Complete study of solvent influence of transport in polysulfone-based polyelectrolyte solutions. (Q1, FY 2020; Completed)
2. Complete development and validation (using known LEs) of electrochemical transport methods. (Q2, FY 2020; Completed)

- Complete synthesis and transport characterization of model triflimide-based polyion (pTFSI) solutions in symmetric cells with Li-metal electrodes. (Q3, FY 2020; Delayed due to COVID, with expected completion in early Q1, FY 2021)
- Complete development of coarse-grained polyelectrolyte model to study effect of polyelectrolyte composition on transport of model polyelectrolyte systems. Progress measure: publish article on scaling of transport properties of polyelectrolyte solutions as a function of polymer and solvent properties. (Q4, FY 2020)

## Progress Report

This quarter, the team focused on theory and modeling to understand the issues occurring during transference number measurements, particularly deviations from expected literature results during Bruce-Vincent-type polarization experiments and the sensitivity of restricted diffusion measurements to the fitting window. To better understand the concentration gradients and electrolyte potential during these experiments, a simple one-dimensional COMSOL model was created for a lithium symmetric cell similar to those used in the project's laboratory experiments. The concentrated-solution ion transport properties of  $\text{LiPF}_6$  in EC:EMC (3:7 by wt.) were directly used from the COMSOL material library. At each lithium electrode, a film resistance was added to model the effect of interfacial resistance due to SEI formation. Values for this film resistance ( $\sim 250 \Omega \text{ cm}^2$  per electrode) were directly taken from EIS measurements on the project's typical Li|Li symmetric cells employing  $\text{LiPF}_6$  in EC:EMC electrolytes. Potentiostatic polarization experiments with a 10-mV bias were modeled for a variety of electrolyte concentrations yielding both the concentration gradient across the cell along with the corresponding LE potential difference across the cell. From this data, the team observed that only small concentration gradients are achieved at this polarization, on the order of 5 mM for a 1 M electrolyte solution, which corresponds to less than 1 mV of potential drop across the electrolyte.

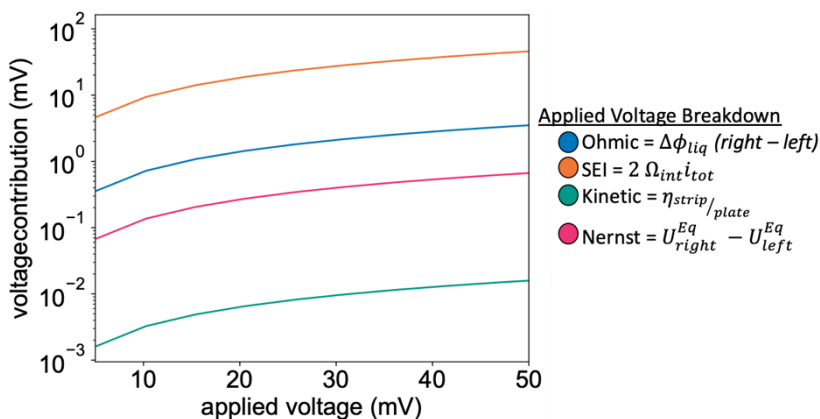


**Figure 9.** Applied voltage breakdown for 1M  $\text{LiPF}_6$  in EC:EMC (3:7 by wt.) as calculated in a lithium symmetric cell using COMSOL Multiphysics. Note the most significant contribution is from the SEI resistance (using a typical experimentally measured value), with the Nernst potential, the desired measured quantity, representing less than 2% of the applied voltage.

Looking at an applied voltage breakdown for this system, the team can clearly see the majority of the applied voltage goes into SEI, with the Nernst potential representing less than 2% of the overall applied voltage (see Figure 9). This is significant because the polarization experiments rely on the team's ability to induce a small but significant electrochemical potential gradient across the electrolyte. When the majority of polarization goes into the SEI, it is easy to understand how even small shifts in the interfacial resistance at the electrodes would mask any other phenomena in the cell. This suggests the need to reduce the contribution of the interface through either cell redesign, different

electrodes, or alternative non-electrochemical methods. Along this line, the team has started to explore using Li-Al alloys for these polarization experiments. They have initially observed that it is possible to achieve an order of magnitude lower interfacial resistance in the aluminum cells; however, the team has not yet been able to achieve sufficiently stable electrode potentials over the course of full polarization experiments.

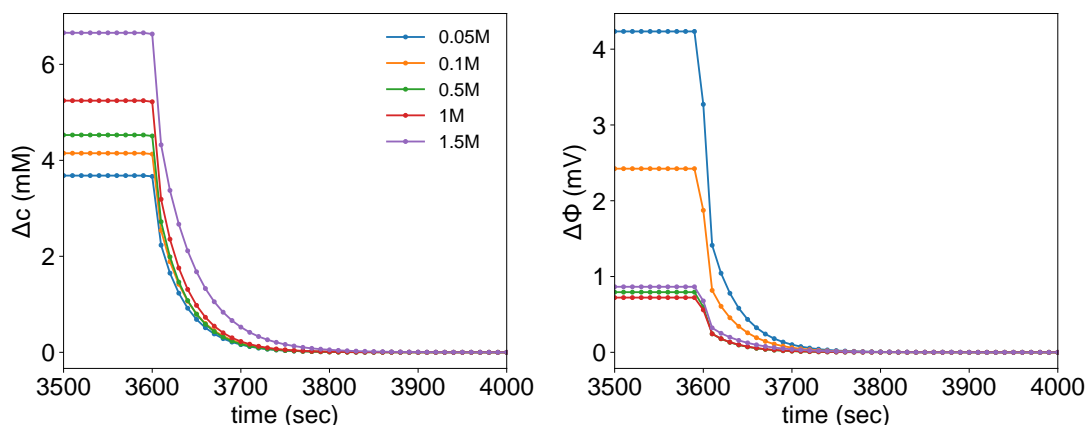


Figure 10. Concentration gradient ( $\Delta c$ ) and electrolyte potential ( $\Delta\phi$ ) relaxation across a 250- $\mu\text{m}$  lithium symmetric cell after 1 hour of polarization at 10 mV for a range of  $\text{LiPF}_6$  in EC:EMC (3:7) concentrations as modeled in COMSOL Multiphysics.

Additionally, this COMSOL model has provided important insight into the issues with fitting window for restricted diffusion experiments. After polarizing a cell at 10 mV for 1 hour and allowing the cell to relax at open circuit voltage (OCV), the team can see that the concentration profile is almost completely relaxed within 2 minutes of stopping polarization (see Figure 10). This suggests that much of the change in OCV that the team sees at longer time scales could be due to SEI formation on freshly plated lithium and surface corrosion, not concentration relaxation. This again highlights the importance of experimental design with polarizations large enough to induce a sufficiently large concentration gradient to have sufficient signal, but small enough to allow the approximation of local zero-order concentration dependence for transport coefficients.

Last quarter, the team reported on the development of a coarse-grained model to study polyelectrolyte transport using MD simulations. This quarter, they have completed a rigorous characterization of the ion correlations and transport properties of these systems. They find that the transference number monotonically decreases as a function of polyanion chain length (Figure 11), with the most drastic decreases observed at low ion concentrations. They may rationalize this trend as follows. On the one hand, longer chains yield lower polymer self-diffusion coefficients such that each chain moves more slowly; this trend alone would give higher cation transference numbers as chain length increases. However, longer chains also carry much more charge. The latter effect outweighs the former such that longer chains contribute substantially more to the conductivity, decreasing the cation transference number. These findings suggest that instead of oligomeric, unentangled polyelectrolytes, it may be possible to create more promising high transference number electrolyte systems using entangled or cross-linked chains that more effectively immobilize the polymer chains.

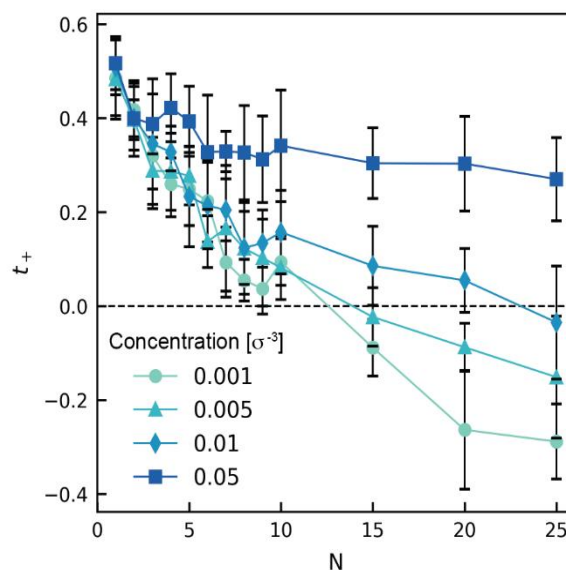


Figure 11. Cation transference number as a function of polyanion chain length at four concentrations, computed using coarse-grained molecular dynamics simulations.

## Patents/Publications/Presentations

The project has no patents, publications, or presentations to report this quarter.

## Task 1.5 – Advanced Polymer Materials for Batteries (Zhenan Bao and Yi Cui, Stanford University)

**Project Objective.** This project will develop new polymer materials for batteries. The team will develop polymer coatings with specific mechanical properties that can accommodate the volume expansion and contraction of the Li-metal anode associated with deposition and stripping (charging and discharging).

**Project Impact.** The cycling stability and CE of Li-metal electrodes will be increased by implementation of a polymer-based protective layer that functions as an artificial SEI with desired properties. The improved performance will enable further development toward practical utilization of Li-metal anodes with higher cycling efficiency and less susceptibility to dendrite-based failure.

**Approach.** The project uses soft polymer coatings with dynamic crosslinking to give the resulting polymers liquid-like rheological properties and stretchable and self-healing properties. In previous work, the project has shown that such coatings resulted in uniform deposition/stripping of lithium metal and improved cycling stability of Li-metal electrodes. To understand the design rules for effective polymer coatings, the team chose a few representative polymers to systematically understand structure property relationships. Here, the team investigates the correlation between surface energy of the polymer and exchange current for lithium deposition.

**Out-Year Goals.** Work will progress toward the correlation between dielectric constant and exchange current. These findings will enable further understanding and development of various polymer coatings for protecting Li-metal anodes.

**Collaborations.** This quarter, the team is collaborating with J. Qin at Stanford University.

### Milestones

1. Analyze the solvation structure and lithium diffusivity of polymer/electrolyte using NMR, Fourier transform infrared (FTIR) spectroscopy, electrochemical tests, and molecular simulations. (Q1, FY 2020; Completed)
2. Evaluate the polymer basic cycling performance: 0.5 and 1 mA/cm<sup>2</sup> conditions in Li|Li and Li|Cu cells using carbonate electrolyte. (Q2, FY 2020; Completed)
3. Self-healing polymer coated Li||NMC battery: Stable cycling at C/3 rate for 150 cycles using 15  $\mu$ l/mAh electrolyte. (Q3, FY 2020; Completed)
4. Self-healing polymer coated Li||NMC battery: Stable cycling at C/3 rate for at least 50 cycles using 50- $\mu$ m lithium. (Q4, FY 2020)

## Progress Report

### Introduction

Li-metal anode suffers from several instabilities during electrodeposition process in the battery charging. Specifically, lithium deposition leads to inhomogeneous coverage on the electrode substrate, resulting in concentration of electric field at the tip of these deposits, ultimately resulting in dendritic growth that shorts the battery. The high surface area metal deposition also causes faster parasitic reactions between the lithium metal and organic electrolyte that is responsible for the rapid fade of battery capacity. According to conventional understanding, the primary sources of instabilities in electrodeposition are diffusion limitations in ion transport processes both in the bulk electrolyte and at the electrode-electrolyte interfaces. Consequently, many theoretical efforts have focused on modeling dendritic growth in a purely diffusion limited condition by varying the transport properties like ion conductivity, on relative mobility of anions and cations (transference number), and on studying their effect on electrolyte modulus or electrode geometry. Likewise, several experimental efforts have reported improved electrodeposition stability with electrolytes with high transference number, conductivity, or modulus. While the ion transport and mechanics are important determinants of morphological evolution of the metal electrode, other coupled parameters like electrochemical kinetics and electrostatic potential landscape can play a critical role. For example, several experimental findings have reported observation of fractal structures during electrodeposition of metallic lithium, even at rates much below the diffusion limited current density. This further indicates that transport parameters in the electrolyte may not be the sole determinant of morphological stability. The relative effect of the electrochemical kinetics and ion transport is particularly important considering the metal electrode does not have a smooth surface, which is aggravated even at earlier stages of deposition. The physical perturbations on the metal surface result in abrupt enhancement of local electric field, causing the ions to be preferentially directed toward the dendritic tips, ultimately leading to unstable growth. In addition, a major challenge in understanding this phenomenon is that the transport and kinetics essentially rely on the same physical factors as ion concentration, viscosity, and temperature, among others. Here, the team leverages ultrafast scanning voltammetry and pulse-field gradient NMR to decouple the effects of kinetics and transport, respectively. Based on these analyses, they design a polymer interface that stabilizes electrodeposition by maintaining a uniform ion flux to the electrode. Subsequently, they intend to utilize the polymer interface for improving Li-metal battery cycling both in Li||Cu and Li||NMC configurations.

### Polymer Coating Design

On the basis of the previously mentioned theoretical understanding, the team proposes a design strategy of incorporating an ionic polymer coating at the electrode-electrolyte interface that can enable interfacial ion transport, while reducing the charge transfer kinetics. The chemical design of the polymer network is shown in Figure 12a. Specifically, perfluoropolyether-dimethacrylate (PFPE-DMA) is used as polymer network backbone, pentaerythritol-tetrakis(3-mercaptopropionate) (PETMP) as the crosslinker, and lithium-styrene-trifluoromethanesulfonyl-imide (Li-STFSI) is utilized as salt linker in different ratios. The PFPE polymer is known to be resistive to chemical corruptions, while the salt molecules are incorporated to facilitate ion transport. The variation in the salt content in the polymer is characterized using NMR and FTIR. Figure 12b shows the varying  $^1\text{H}$  NMR peak intensities of the polymers for the specific methyl groups labeled in Figure 12a, where it is seen that as linkable Li-STFSI is increased in the feed, the immobilized salt content in the polymer network is progressively higher. The team further analyzed the IR-spectra of the ionic polymer networks, where they observe that on crosslinking, the representing vibrational mode of the thiol group ( $-\text{SH}$ ) at  $2550\text{cm}^{-1}$  disappears for all the polymers synthesized here. Thus, the team can conclusively say that all the PETMP linkers are reacted. Also, the vibration modes of the double bonds ( $1650\text{cm}^{-1}$ ) in the styrene molecule present in the Li-STFSI monomers were compared for different cases, and it is confirmed that increasing the Li-STFSI in the feed indeed leads to stronger intensity of this peak. Thus, the team confirms being able to systematically vary immobilized salt content in the polymer network that can ultimately lead to fundamental understanding of the effect of ionic polymers in stabilizing electrodeposition.

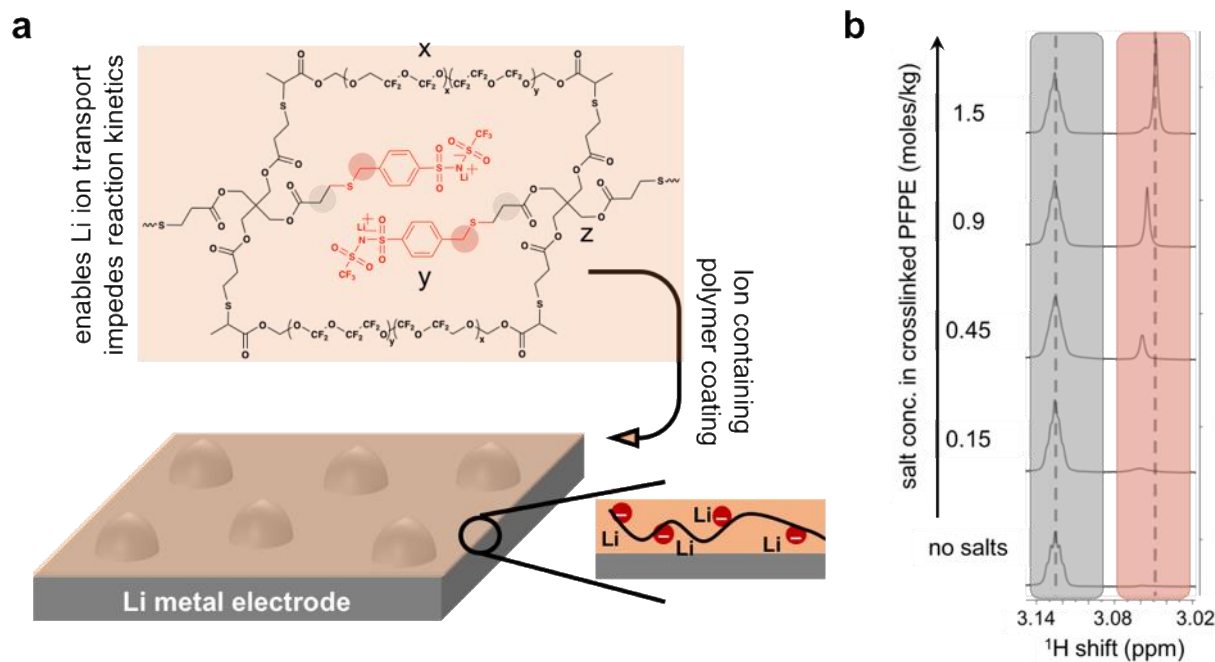
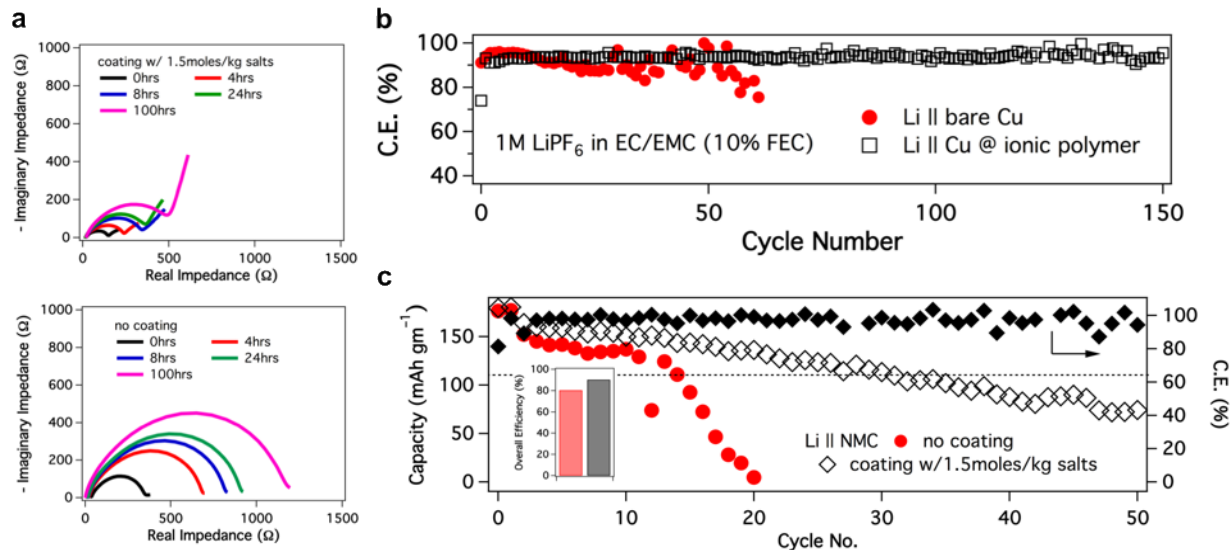


Figure 12. Polymer coating on Li-metal electrode. (a) Schematic showing the structure of ionic polymer coated on the Li-metal electrode. The ionic polymer comprises of x: perfluoropolyether-dimethacrylate (PFPE-DMA) backbone, y: pentaerythritol tetrakis(3-mercaptopropionate) or PETMP crosslinker, and z: (4 styrenesulfonyl) (trifluoromethanesulfonyl) imide (STFSI-Li) monomeric salts. The PFPE polymer acts as blocking agents for the liquid electrolyte, while the STFSI anions provide Li-ion transport pathways. (b) Comparison of peak heights obtained from  $^1\text{H}$  NMR measurements showing the relative content of the methyl groups in the polymer backbone and the tethered anions (spectra referenced to residual protons in  $\text{CD}_3\text{OD}$ ). The NMR trend follows the trend of varying salt moieties in the polymer backbone.

## Electrochemical Analysis

The long-term stability of polymer coating was evaluated by monitoring the evolution of the interfacial resistance over time with and without the polymer coating. Specifically, the team built symmetric lithium cells using the LE of 1 M  $\text{LiPF}_6$  in ethylene carbonate (EC) / EMC with 10% FEC and measured the interfacial resistance growth over time, using impedance spectroscopy. Figure 13a shows that the Nyquist diagrams from impedance measurements in symmetric lithium cells with and without the ionic polymer coating (1.5 moles/kg of grafted salts) using the same electrolyte. Clearly, the presence of polymer coating significantly diminishes impedance divergence as a function of time. At the end of 100 hours of rest, the cells without the coating have over two-times interfacial resistance than that of polymer-coated case, implying that the polymers are successful in blocking electrolyte access without significantly hindering ion transport. The cycling stability of the ionic polymer coatings in Li||Cu configuration was analyzed using the same electrolyte of 1 M  $\text{LiPF}_6$  in EC/EMC with 10% FEC. The CE comparison of the control (bare electrode) and polymer coating is presented in Figure 13b. It is seen that the ionic polymer coating shows improved performance for at least 150 cycles in comparison to the control that fails at about 50 cycles. Finally, the polymer-coated thin 25- $\mu\text{m}$  Li-metal electrode ( $N = 5\text{mAh}/\text{cm}^2$ ) was paired against LiNiMnCoO<sub>2</sub> (NMC-532) cathode having capacity ( $P$ ) 1.7  $\text{mAh}/\text{cm}^2$ , and the batteries ( $N/P = 3$ ) were cycled using the electrolyte 1 M  $\text{LiPF}_6$  in EC/EMC with 10% FEC. The corresponding capacity and CE for the two different cases (with and without polymer coating) are plotted in Figure 13c, while the overall efficiency, measured with the formula,  $C.E. = 100(1 - N/n \times P)$ , where  $n$  is the cycle number until 80% fade, is plotted as bar chart in the inset. The team observes that the polymer coating significantly enhances the lifetime of the full cell, in agreement with the findings from the reported electrochemical and electrodeposition results.



**Figure 13. Stability with carbonate-based electrolytes:** (a) Nyquist diagrams of symmetric lithium cells obtained using impedance spectroscopy measurement with and without the ionic polymer coating on the lithium. The different results were obtained after varying rest times of the batteries. (b) Cycling stability of lithium versus copper cells, where the copper electrodes were either bare or coated with ionic polymers containing 1.5 moles/kg of grafted salts. The bare electrode fails in 50 cycles, while that with coating showed enhanced stability. (c) Li||NMC full-cell cycling using 25  $\mu\text{m}$  lithium and 1.7  $\text{mAh}/\text{cm}^2$  NMC-532, such that the anode (N) to cathode capacity (P) ratio is 3:1. The lithium metal utilized either bare or coated with the ionic polymer (1.5 moles/kg of salts). The inset shows the comparison of the overall efficiency obtained using the formula:  $(1 - N/(n \times P))100\%$ . The electrolyte in all the subparts was 1 M  $\text{LiPF}_6$  in EC/EMC with 10% FEC.

## Patents/Publications/Presentations

### Patent

- Cui, Y., Z. Bao, Z. Yu, S. Choudhury, and H. Wang. Liquid and Solid Electrolytes with Special Li-F Solvation Structure Enabling Practical Li-Metal Batteries. U. S. provisional patent filed.

### Publications

- Mackanic, D. G., T-H. Chang, X. Huang, Y. Cui, and Z. Bao. "Stretchable Electrochemical Energy Storage Devices." *Chemical Society Reviews* (2020). doi: 10.1039/D0CS00035C.
- Mackanic, D. G., M. Kao, and Z. Bao. "Enabling Deformable and Stretchable Batteries." *Advanced Energy Materials* (2020). doi: 10.1002/aenm.202001424.
- Yu, Z., H. Wang, X. Kong, W. Huang, Y. Tsao, D. G. Mackanic, K. Wang, X. Wang, W. Huang, S. Choudhury, Y. Zheng, C. Amanchukwu, S. T. Hung, Y. Ma, E. G. Lomeli, J. Qin, Y. Cui, and Z. Bao. "Molecular Design for Electrolyte Solvents Enabling Energy-Dense and Long-Cycling Lithium Metal Batteries." *Nature Energy* (2020). doi: 10.1038/s41560-020-0634-5.

## Task 1.6 – Improving the Stability of Lithium-Metal Anodes and Inorganic-Organic Solid Electrolytes (Nitash Balsara, Lawrence Berkeley National Laboratory)

**Project Objective.** The project objective is to establish a new hybrid electrolyte that will be stable against cells with a Li-metal anode.

**Project Impact.** PEs offer increased stability in lithium batteries in comparison to more widely used LEs. Nanostructured electrolytes containing both soft, ion-conducting domains and rigid, nonconducting domains offer the opportunity to tune both mechanical and electrical properties separately. Such electrolytes are conveniently made by block copolymer self-assembly. Most of the block copolymer electrolytes studied thus far comprise organic polymer chains for both the conducting and rigid domains. The team hopes to synthesize new electrolytes that simultaneously have high transport properties and have greater stability against lithium in comparison to organic diblock copolymers.

**Approach.** First, the team synthesizes hybrid diblock copolymers by incorporating monomers that contain an inorganic component. Then, electrolytes are prepared by mixing these diblock copolymers with salt. Electrochemical and mechanical characterization of these materials is performed before carrying out cycling X-ray tomography (XRT) experiments. The combination of these approaches enables rational design of materials that exhibit improved stability against lithium metal.

**Out-Year Goals.** The project will synthesize a new hybrid electrolyte that is designed to be stable against lithium metal. The material is a block copolymer wherein acryloisobutyl polyhedral oligomeric silsesquioxane (POSS) is covalently bonded to the chain. The second block is a conventional PE, PEO. Electrochemical characterization of this polymer will include measurement of all transport properties including conductivity, diffusion coefficient, and the transference number. The stability against lithium metal will be evaluated by CV, while its applications as an electrolyte will be evaluated and visualized using cycling XRT experiments on symmetric Li-hybrid-Li cells.

**Collaborations.** There are no active collaborations this quarter.

### Milestones

1. Synthesize a series of POSS-containing block copolymer electrolytes for electrochemical studies. (Q1, FY 2020; Completed)
2. Create impurity-free lithium layers. (Q2, FY 2020; Completed)
3. Complete electrochemical characterization of POSS-containing block copolymer electrolytes. (Q3, FY 2020; Completed)
4. Provide cycling data for at least two POSS-containing block copolymer electrolytes. (Q4, FY 2020)

## Progress Report

Full electrochemical characterization of hybrid organic-inorganic block copolymer electrolytes was completed this quarter. The compositions of the PEO-b-POSS (PEO-POSS) diblock and POSS-b-PEO-b-POSS (POSS-PEO-POSS) triblock copolymers used in this study are given in Table 3. All copolymers in the study have similar volume fraction of the conductive block, between 0.72 to 0.76. Electrolytes are prepared by mixing PEO-POSS or POSS-PEO-POSS with LiTFSI.

**Table 3. Composition of PEO-POSS and POSS-PEO-POSS diblock and triblock copolymers.**

PEO-POSS/ POSS-PEO- POSS	Structure	$M_{PEO}$ (kg mol <sup>-1</sup> )	$M_{POSS}$ (kg mol <sup>-1</sup> )
(5-2)	Diblock	5	1.86
(10-4)	Diblock	10	3.72
(5-35-5)	Triblock	35	10

Ionic conductivity is a complex function of both morphology of nanostructured block copolymers as well as chain length. The team posits that the PEO phase is ionically conductive, while the POSS phase offers mechanical strength to the electrolyte and is entirely nonconductive. Ionic conductivity of PEO-POSS, POSS-PEO-POSS/LiTFSI mixtures is demonstrated in Figure 14. Figure 14a shows POSS-PEO-POSS(5-35-5) ionic conductivity as a function of temperature alongside PEO(35)<sup>[1]</sup> and poly(styrene)-b-poly(ethylene oxide)-b-poly(styrene) (SEOS)(5-35-5)<sup>[1]</sup> of comparable molecular weights at a salt concentration of  $r = [Li]/[EO] = 0.04$  to 0.05. Conductivity of the hybrid organic-inorganic triblock copolymer is similar to the all-organic triblock copolymer, and exhibits a comparable trend with temperature above the melting transition of PEO (~ 55°C). PEO-POSS(5-2), PEO-POSS(10-4), and POSS-PEO-POSS(5-35-5) ionic conductivity is plotted as a function of salt concentration and compared to PEO(10) at 90°C in Figure 14b. The PEO domain is amorphous at this temperature. The three hybrid organic-inorganic PEs also exhibit a similar trend, with a maximum in ionic conductivity in the proximity of  $r = 0.08$ . All block copolymers in the study exhibit ionic conductivity lower than that of the homopolymer. PEO-POSS(5-2), the lowest molecular weight copolymer, exhibits ionic conductivity below that of POSS-PEO-POSS(5-35-5) and PEO-POSS(10-4). This indicates that ionic conductivity in POSS-containing block copolymers increases with overall molecular weight.

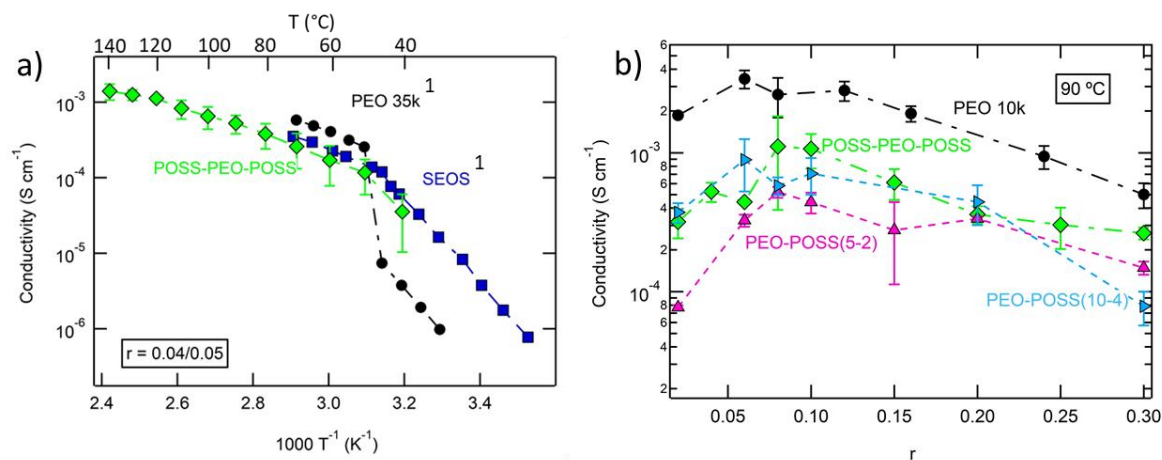


**Figure 14. Ionic conductivity of PEO-POSS, POSS-PEO-POSS/LiTFSI mixtures. (a) POSS-PEO-POSS(5-35-5) ionic conductivity is plotted as a function of temperature alongside PEO(35)<sup>[1]</sup> and SEOS(5-35-5)<sup>[1]</sup> of comparable molecular weights at a salt concentration of  $r = [Li]/[EO] = 0.04$  to 0.05. (b) PEO-POSS(5-2), PEO-POSS(10-4), and POSS-PEO-POSS(5-35-5) ionic conductivity is plotted as a function of salt concentration and compared to PEO(10) at 90°C.**

Complete electrochemical characterization allows for the prediction of salt concentration gradients across a battery electrolyte during polarization. Ideally, the electrolyte will have small salt concentration and potential gradients within the electrolyte at large current densities. Predicting the magnitude of these gradients in an electrolyte requires knowledge of two or more transport coefficients in addition to the ionic conductivity. Complete electrochemical characterization was carried out in PEO-POSS(5-2). The diffusion coefficient ( $D$ ) and cation current fraction ( $\rho_{+SS}$ ) calculated using ideal, dilute solution theory, are demonstrated in Figure 15 and compared to an all organic analogous diblock copolymer, poly(styrene)-*b*-poly(ethylene oxide) (SEO) and PEO<sup>[2]</sup> at 90°C. All three copolymers exhibit similar  $\rho_{+SS}$  and exhibit a similar trend with salt concentration. However,  $D$ , shown in Figure 15b, is about 2 orders of magnitude higher in PEO-POSS(5-2) than the other two polymers and exhibits weak salt concentration dependence over the salt concentration range.

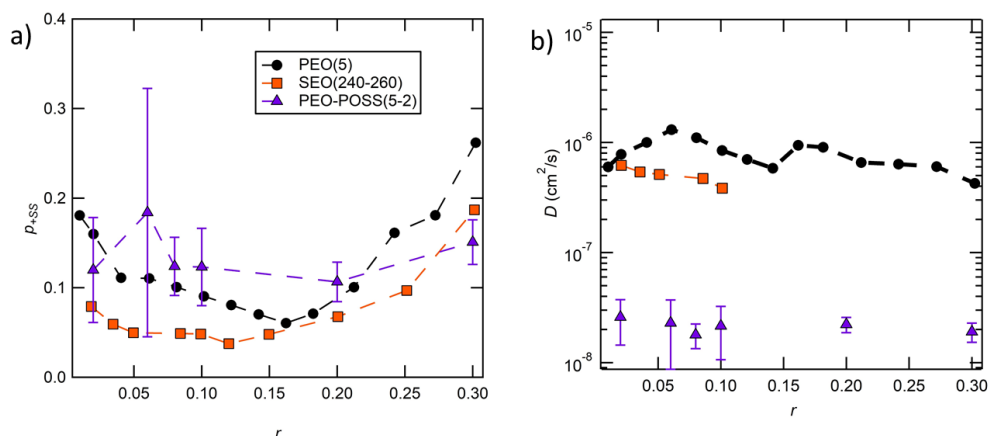


Figure 15. Electrochemical characterization of PEO-POSS, PEO<sup>[2]</sup>, and SEO<sup>[2]</sup>. (a) Diffusion coefficient ( $D$ ). (b) Current fraction ( $\rho_{+SS}$ ) as a function of salt concentration,  $r$  at 90°C.

The thermodynamic factor ( $T_f$ ),  $1 + \text{dln}\gamma/\text{dln}m$ , is calculated using the OCV and the anion current fraction according to reference 2, where  $m$  is molality of salt and  $\gamma$  is the mean molal activity coefficient of the salt.  $T_f$  of PEO-POSS(5-2) is shown in Figure 16a, and increases with salt concentration. A similar trend is exhibited with PEO homopolymer,<sup>[2]</sup> indicating that PEO-POSS/LiTFSI can be treated as a 2-component system. For an ideal system,  $T_f$  should be close to 1, indicating PEO-POSS is far from ideal.<sup>[3]</sup>

Figure 16b demonstrates the full transference number,  $t_{+,Ne}$  of lamellar PEO-POSS(5-2) alongside lamellar SEO of various molecular weights.<sup>[3]</sup> The two diblock copolymers exhibit  $t_{+,Ne}$  between 0.20 and 0.70. While PEO-POSS exhibits a maximum at  $r = 0.08$ , SEO exhibits a maximum at  $r = 0.30$ . The study results show that addition of an inorganic moiety to an organic, conductive, polymer chain does not drastically decrease  $t_{+,Ne}$ .

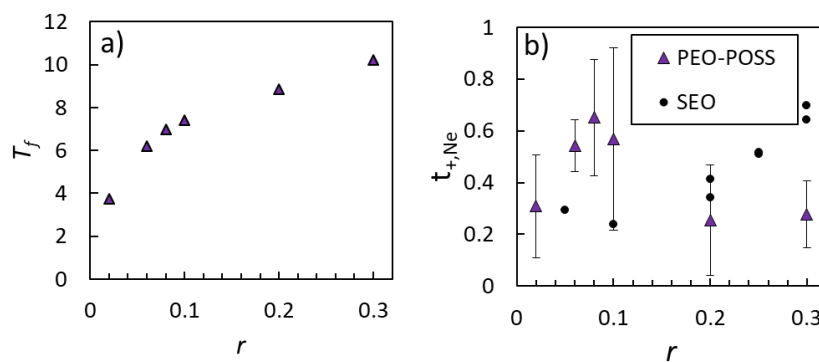


Figure 16. (a) Thermodynamic factor ( $T_f$ ) and (b) cation transference number ( $t_{+,Ne}$ ) in PEO-POSS(5-2) and lamellar SEO<sup>[3]</sup> of varying molecular weights as a function of salt concentration,  $r$ , at 90°C.

## References

- [1] Bouchet, R., T. N. T. Phan, E. Beaudoin, D. Devaux, P. Davidson, D. Bertin, and R. Denoyel. *Macromolecules* 47, no. 8 (2014): 2659–2665.
- [2] Villaluenga, I., D. Pesko, K. Timachova, Z. Feng, J. Newman, V. Srinivasan, and N. Balsara. “Negative Stefan-Maxwell Diffusion Coefficients and Complete Electrochemical Transport Characterization of Homopolymer and Block Copolymer Electrolytes.” *Journal of the Electrochemical Society* 165, no. 11 (2018): 2766–2773.
- [3] Galluzzo, M. D., W. S. Loo, A. A. Wang, A. Walton, J. A. Maslyn, and N. P. Balsara. “Measurement of Three Transport Coefficients and the Thermodynamic Factor in Block Copolymer Electrolytes with Different Morphologies.” *The Journal of Physical Chemistry B* 124, no. 5 (2020): 921–935.

**Patents/Publications/Presentations**

## Publications

- Chakraborty, S., X. Jiang, Z. Hoffman, G. K. Sethi, N. P. Balsara, and I. Villaluenga. “Reversible Changes in the Grain Structure and Conductivity in a Block Copolymer Electrolyte.” *Macromolecules* (2020).
- Maslyn, J. A., K. D. McEntush, K. J. Harry, L. Frenck, W. S. Loo, D. Y. Parkinson, and N. P. Balsara. “Preferential Stripping of a Lithium Protrusion Resulting in Recovery of a Planar Electrode.” *Journal of The Electrochemical Society* 167, no. 10 (2020): 100553.

## Task 1.7 – Development of Thin, Robust, Lithium-Impenetrable, High-Conductivity, Electrochemically Stable, Scalable, and Low-Cost Glassy Solid Electrolytes for Solid-State Lithium Batteries (Steve Martin, Iowa State University of Science and Technology)

**Project Objective.** The objective of this project is to develop new Li<sup>+</sup>-conducting mixed-oxy-sulfide-nitride (MOSN) glassy solid electrolytes (GSEs) that are impermeable to lithium dendrites, have high conductivities, are scalable through low-cost glass manufacturing, are chemically and electrochemically stable, and will enable low-cost, high-energy-density SSLBs. The SSLBs constructed from these new GSEs will meet and exceed all program objectives: useable specific energy @ C/3  $\geq$  350 Wh/kg, calendar life 15 years, cycle life (C/3 deep discharge with < 20% energy fade) 1,000, and cost  $\leq$  \$100/kWh.

**Project Impact.** This project will enable the team to demonstrate that (1) thin MOSN GSE films yield superior performance in a much safer, lower-cost, and Li-dendrite impenetrable form and (2) high rate and long cycle life can be achieved in SSLBs using thin-film MOSN GSEs. The new GSEs in SSLBs are anticipated to increase the energy density (anode basis) from  $\sim$  300 mAh/g to  $\sim$  4,000 mAh/g, enabling replacement of internal combustion engines in both light and heavy duty vehicles. Each 20% reduction in the  $\sim$  1.6 billion liters of gasoline used per day in the United States would reduce CO<sub>2</sub> emissions by  $\sim$  4 billion kg or  $2 \times 10^{12}$  l of CO<sub>2</sub> per day. The team will also increase scientific and engineering knowledge of thin-film GSEs in SSLBs.

**Approach.** The MOSN mixed-glass-former (MGF) glasses used for the GSEs in this project have been developed in previous work to have the necessary thermal stability and high ionic conductivity for successful use as a drawn-film electrolyte. In this project, the glass chemistry will be tuned for even more desirable properties, by investigating structure-property relationships and testing variations in glass chemistry.

**Out-Year Goals.** Work will progress toward developing a glass capable of being drawn to 100-micron thickness, while having high conductivity and electrochemical stability and good cycling ability.

**Collaborations.** There are no active collaborations this quarter.

### Milestones

1. Preform redraw capability to form 5-m ribbons verified. (Q1, FY 2020; Completed)
2. Accomplish: MOSN MGF GSEs are thermally stable between -20°C and 100°C, have a Li<sup>+</sup> ion conductivity  $> 1$  mS/cm at 25°C, have a Li<sup>+</sup> ion area specific resistance (ASR) of  $\leq 100$  Ohm-cm<sup>2</sup>, have an electronic ASR of  $> 0.1$  M Ohm-cm<sup>2</sup>, are electrochemically stable between 0 and 4.5 V versus Li/Li<sup>+</sup>, and have no more than 1 wt% weight change in 45% relative humidity (RH) air. (Q2, FY 2020; Completed)
3. Accomplish: MOSN MGF GSE are stable against lithium through 100 cycles. (Q3, FY 2020; Completed)
4. *Go/No Go Decision:* MOSN MGF GSE is chemically stable and resistant to crystallization. Analysis indicates technical approach capable of achieving performance targets. (Q4, FY 2020)

## Progress Report

### Development of Optimized High Li<sup>+</sup> Ion Conductivity MOSN MGF GSEs

Table 4. Tabulated glass chemistry for glassy solid electrolyte testing.

Sample ID	Compositional Formula
<b>ISU 3</b>	0.55 Li <sub>2</sub> S + 0.35 SiS <sub>2</sub> + 0.1 LiPO <sub>3</sub>
<b>ISU 4</b>	0.55 Li <sub>2</sub> S + 0.35 SiS <sub>2</sub> + 0.07 LiPO <sub>3</sub> + 0.03 LiPO <sub>2.5</sub> N <sub>0.33</sub>
<b>SLiP 3</b>	0.6 Li <sub>2</sub> S + 0.3 SiS <sub>2</sub> + 0.1 LiPO <sub>3</sub>
<b>SLiP 5</b>	0.6 Li <sub>2</sub> S + 0.25 SiS <sub>2</sub> + 0.15 LiPO <sub>3</sub>

#### *Thermal Properties*

All of the GSEs listed in Table 4 have achieved the milestone 1.1a and are thermally stable within the described region of -20 to 100°C. As demonstrated in Figure 17, no thermal events occur from -20°C to 100°C. These values are tabulated in Table 5.

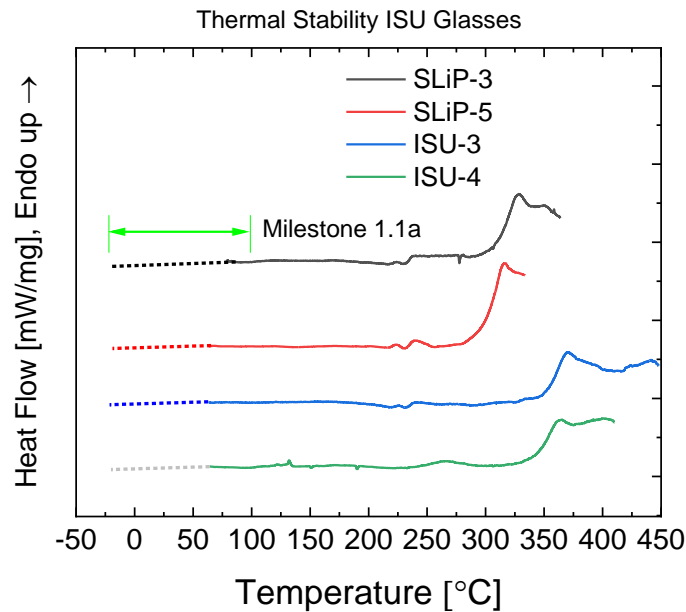


Figure 17. Thermal stability of ISU glasses as shown via differential scanning calorimetry (DSC) thermograms for selected ISU glassy solid electrolytes (GSEs). All of these GSEs are thermally stable from -20°C to 100°C.

Table 5. Tabulated thermal properties of glassy solid electrolytes.

Sample ID	Thermally Stable (-20°C and 100°C)	Upper Useful Temperature Limit of the Glass, Softening Point(°C)
<b>ISU 3</b>	Yes	345
<b>ISU 4</b>	Yes	350
<b>SLiP 3</b>	Yes	305
<b>SLiP 5</b>	Yes	295

### *Ionic Conductivity > 1 mS/cm at 25°C*

The temperature-dependent Li<sup>+</sup> ion conductivity of the ISU GSEs has been measured with impedance spectroscopy. It can be seen in Figure 18 that GSE SLIP-3 has a 25°C Li<sup>+</sup> ion conductivity of 1.06 mS/cm ± 0.4 mS/cm. The team will continue to optimize this GSE composition to improve all of its thermal, chemical, and electrochemical properties.

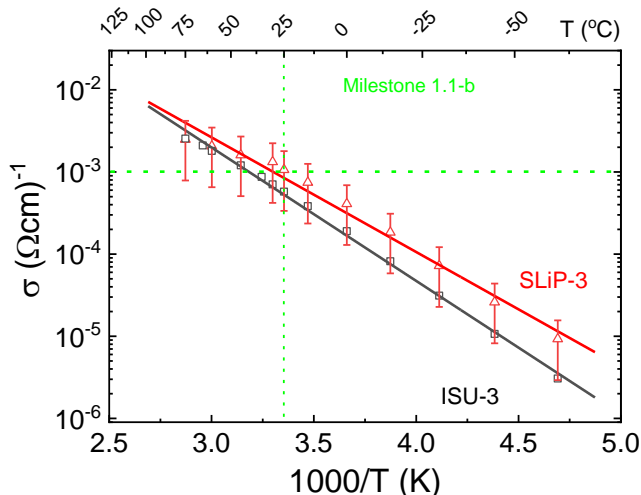


Figure 18. Arrhenius plot comparing the temperature dependent ionic conductivity for two ISU glassy solid electrolytes (GSEs), SLIP-3 and ISU-3. These data show that SLIP-3 exceeds the Milestone 1.1b value of 1 mS/cm.

### *Material Stability – Electrochemically Stable between 0 and 4.5 V versus Li/Li<sup>+</sup>*

The team used impedance spectroscopy to determine the stability of the GSE in contact with lithium metal, as shown in Figure 19. The Nyquist plot of the pure sulfide (left) shows an unstable / chemically active interface, which grows continuously with time. The mixed anion glass, ISU-4 (right), has been shown to demonstrate a stable, self-passivating interface in contact with lithium metal.

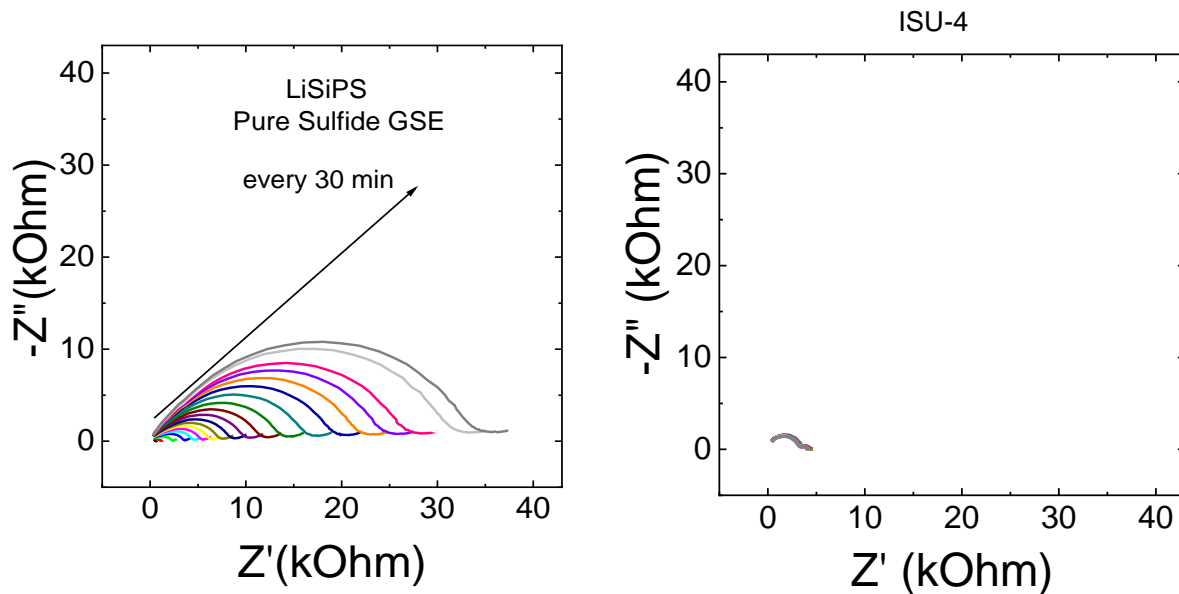


Figure 19. Complex plane plots of lithium metal | glassy solid electrolyte (GSE) | lithium metal symmetric cells as a function of time up to 10 hours for a reactive pure sulfide glass (left) whose impedance grows strongly with time and for a mixed-oxy-sulfide-nitride (MOSN) glass (right) whose impedance remains small for the same period of time, indicating that this MOSN GSE, ISU-4, is stable in contact with lithium metals.

The team used CV to test the oxidative stability of the MOS and MOSN MGF glassy electrolytes. For CV experiments, coin cells are assembled using stainless-steel blocking electrode // GSE // Li-metal non-blocking electrode architecture. Figure 20 shows the CV scans for ISU-4 with and without LiPON addition. No major anodic or cathodic peaks can be seen in the samples of ISU-4 with and without LiPON additions. There is a minor peak present around 1.5-2.5 V, which is most likely attributable to S-S bond oxidation. As further CV cycles are run on the same sample, the anodic current tends to increase more in the sample without LiPON doping, as shown in Figure 21, indicating that nitrogen does help to stabilize the Li-metal – GSE interface. On preliminary analysis, it is believed that the  $\text{Li}_3\text{PS}_4$  short range order structures are unstable in the host glass, leading to this increase in anodic current. This growth in anodic current follows a linear trend for both the base MOS glass and the nitrogen-doped MOSN glass, with the slope of the MOS glass being more than five times larger than the slope of the MOSN glass. The lack of major peaks indicates that both the host glass and its nitrogen-doped analogue are both electrochemically stable within the potential window of 0-5 V versus  $\text{Li}/\text{Li}^+$ , exceeding the milestone potential window of 0-4.5 V versus  $\text{Li}/\text{Li}^+$ .

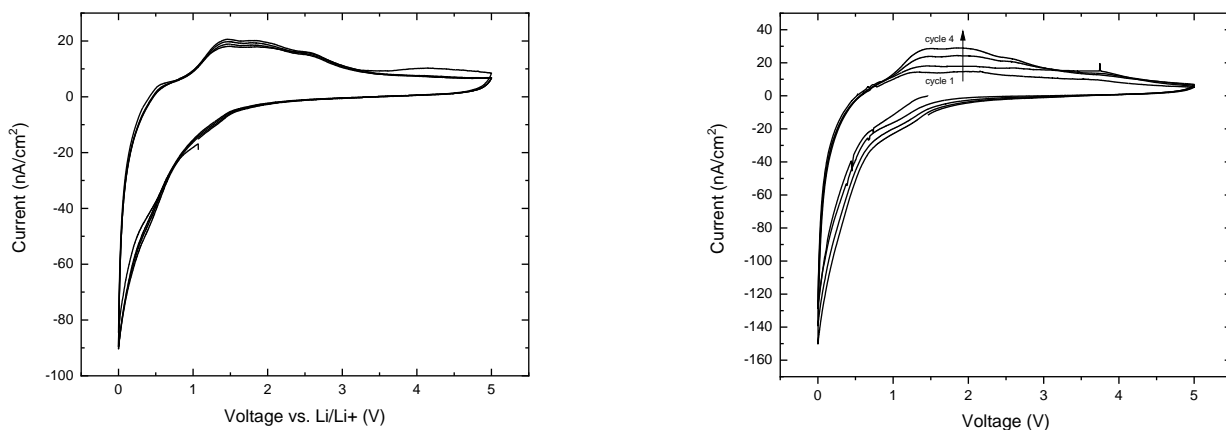


Figure 20. Cyclic voltammetry plots of stable ISU-4 mixed-oxy-sulfide-nitride (MOSN) glassy solid electrolyte (GSE) with a maximum oxidative current of  $20.6 \text{ nA/cm}^2$  (active area:  $0.3563 \text{ cm}^2$ , average thickness:  $1.076 \text{ mm}$ ) and right ISU-4 MOS GSE with a maximum oxidative current of  $29.0 \text{ nA/cm}^2$  (active area:  $0.7126 \text{ cm}^2$ ).

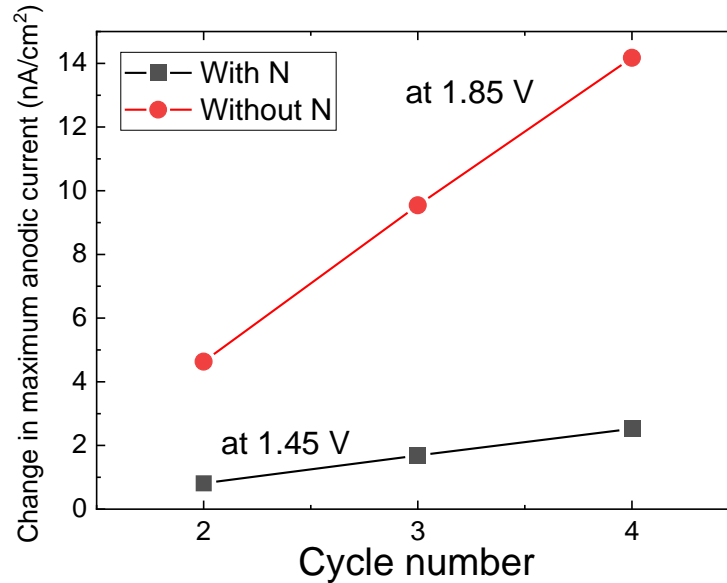


Figure 21. Change in peak anodic current with respect to peak anodic current of the 1<sup>st</sup> cycle ( $i_1 - i_c$ ).

#### Chemically Stable (No More than 1 wt% Weight Change in 45% RH Air)

Figure 22 shows a TGA thermogram of a typical pure sulfide glass that reacts immediately with humid air, whereas the MOSN GSE ISU-4 remains stable for periods of multiple hours in contact with humid air.

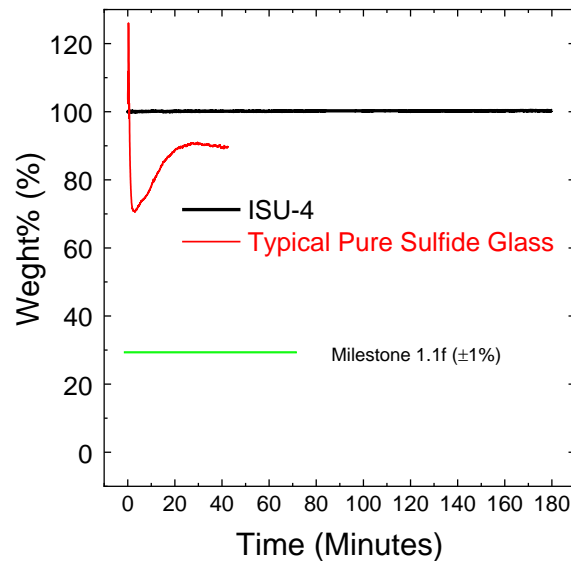


Figure 22. Thermogravimetric analysis (TGA) results for a typically sulfide glass, compared to the mixed-oxy-sulfide-nitride (MOSN) glassy solid electrolyte (GSE) ISU-4.

#### Development of Micro-Sheet Glass Ribbon Processing Facility

- Design, development, and installation of the preform redraw facility inside a high-quality glove box capable of drawing long, thin ribbons of MOSN MGF GSE compositions that are at least 5-m long, averaging 5 cm in width, and are 100- $\mu$ m or less in thickness.

This quarter, the team has optimized the film tower system by adding (1) a conveyor assembly within the tower to allow tools to be more effectively moved from the lower zones to the upper zones of the box, (2) a scaffolding assembly to allow safe usage of all gloves, and (3) a waste collection system for excess glass material. It was found that when using larger and heavier preform bars, the grips originally used proved insufficient. To alleviate this, the grips were modified from a two-grip system to a three-grip trident. Additionally, the grips were extended in length to allow for the preforms to be fully lowered into the furnace heating zone, allowing more of the base preform to be used in drawing. These changes have significantly increased capabilities and were necessary to reach the achieved values.



Figure 23. (a-c) External view of draw tower assembly and scaffolding. (d) Preform grip assembly.

### Develop Processing Conditions Micro-Sheet Ribbons of MOSN MGF GSEs

- Initiate optimization of draw conditions for optimized oxide GSEs  $< 500 \mu\text{m}$ .
- Initiate optimization of draw conditions for optimized MOS MGF GSEs  $< 200 \mu\text{m}$ .

This quarter, the team has used alternative oxide glasses having similar thermal and mechanical properties allowed for the testing of draw tower capabilities at lower cost by using borosilicate glasses. Utilizing these borosilicate glasses, films have been consistently drawn to thicknesses less than  $40 \mu\text{m}$ , widths over 5 cm, and

lengths over 5 m. These values have met or exceeded all milestones. Tests using lithium oxide glasses as well as sodium mixed oxy-sulfide glasses indicate that the results found using the borosilicate glasses will be reproducible in many other glass compositions including MOSN MGF GSEs.

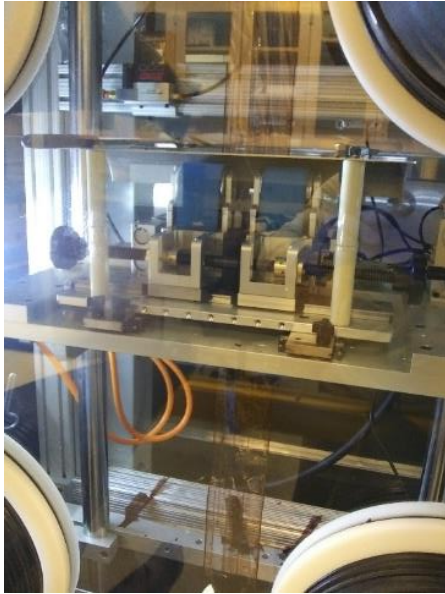


Figure 24. Consistent 20- $\mu$ m film being drawn.

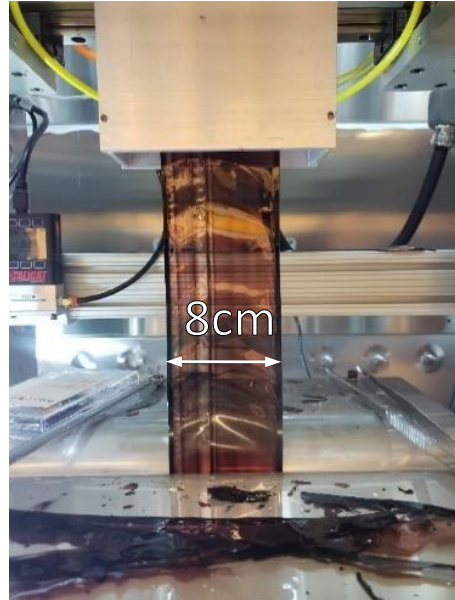


Figure 25. Picture of a consistent 8-cm wide by 40- $\mu$ m thick film being drawn.



Figure 26. Mn-doped borosilicate glass preform prior to drawing. The  $MnO_2$  doping gives the glass a strong color that allows it to be easily visualized, even at 20- $\mu$ m thick. This glass is used as glass typical of the thermal properties of GSEs, but it is more easily handled to enable faster optimization of the draw conditions.



Figure 27. Flexible 20- $\mu$ m film folded over in fingers, which demonstrates that these GSEs can be handled and will be able to be rolled up into long length spools.

## Patents/Publications/Presentations

### Publications

- Zhao, R., G. Hu, S. Kmiec, R. Gebhardt, A. Whale, and S. W. Martin. “A New Amorphous Oxy-Sulfide Solid Electrolyte Material: Anion Exchange, Electrochemical Properties, and Lithium Dendrite Suppression via *In Situ* Interfacial Modification.” *ACS Applied Materials and Interfaces* (am-2020-09420a); submitted May 23, 2020.
- S. Kmiec, J. Lovi, A. Joyce, D. Bayko, and S. W. Martin. “Anomalously Strong Viscosity Behavior in Mixed Oxy-Sulfide  $\text{Na}_4\text{P}_2\text{S}_7\text{O}_x$  Invert Glasses.” *Journal of Non-Crystalline Solids* (NOC-D-20-00706); submitted May 18, 2020.
- Joyce, A., S. Kmiec, and S. W. Martin. “Glass Transition Temperature Studies of Planetary Ball Milled  $\text{Na}_4\text{P}_2\text{S}_{7-x}\text{O}_x$ ,  $0 \leq x \leq 7$ , Oxy-Thio Phosphate Glasses.” *Journal of Non-Crystalline Solids* (NOC-D-20-00826); submitted June 11, 2020.
- Kim, K-H., and S. W. Martin. “A Study on the Improved Structure and Properties of Cation and Anion Double Doped  $\text{Li}_{10}[\text{Sn}_y\text{Si}_{1-y}]\text{P}_2\text{S}_{12-x}\text{O}_x$  Solid Electrolytes.” *Chemistry of Materials* (cm-2020-02499d); submitted June 15, 2020.

## Task 1.8 – Composite Solid Ion Conductor with Engineered Lithium Interface (Kyler Carroll and Cam Peebles, Wildcat Discovery Technologies)

**Project Objective.** In this project, Wildcat seeks to perform focused, fundamental research and development on composite polymer/ceramic electrolytes and for the protection of Li-metal anodes to develop an all-solid-state Li-metal battery that achieves DOE requirements for performance that enables potential commercialization of this technology. Wildcat will leverage its HT battery platform to explore a broad composite electrolyte compositional space. Additionally, the HT platform will allow the team to screen hundreds of inorganic and organic coatings for Li-metal protection and translate the best results to all solid cells.

**Project Impact.** Successful widespread commercialization of EVs is contingent on developing safe high-energy-density batteries capable of long cycle life. Lithium metal affords the highest theoretical capacity (3,860 mAh/g) and lowest electrochemical potential (-3.04 V versus SHE), which offers the highest specific energy density of anode materials today. However, significant progress toward the passivation of lithium metal must occur before the energy density benefit can be realized. The intrinsic high reactivity between lithium metal with conventional Li-ion electrolytes (organic carbonate-based solvents) makes it extremely difficult to overcome these problems. The proposed composite polymer/ceramic electrolyte and a protected Li-metal anode will enable an all-solid-state Li-metal battery. It is expected that the outcomes from this effort will deliver a safe all-solid-state Li-metal pouch cell with over 350 Wh/kg and over 1,000 cycles (C/3) with the cost estimate below \$100/kWh.

**Approach.** The project approach involves (1) identifying a suitable combination of solid ion conductor, polymer, and additive that minimizes overall interfacial impedance between the PE and solid ion conductor, and (2) identification of stable Li-metal protection agent or combination of agents that shows enhanced cycling performance (relative to a non-protected system) using the down-selected cell architectures.

**Out-Year Goals.** The out-year goals involve screening hundreds of additive, polymer, and solid ion conductor combinations using a HT trilayer cell architecture developed during method development phase. Based on the best combinations, Wildcat will develop a composite polymer/ceramic electrolyte where the Li-ion conductivity is occurring at the ceramic phases of the composite. Additionally, the team will screen hundreds of Li-metal protection agents using the designed HT cell architecture with the goal of identifying those that offer highest stability.

**Collaborations.** All project tasks will be performed at Wildcat Discovery Technologies.

### Milestones

1. Establish baseline performance. (Q1, FY 2020; Completed)
2. Complete synthesis of ceramic ion conductors. (Q2, FY 2020; Completed)
3. Perform down-selection of best ceramic ion conductors for further optimization. (Q3, FY 2020; Completed)
4. Perform down-selection of best composite SE additives for further optimization. (Q4, FY 2020; Completed)
5. Perform down-selection of best high-voltage polymer formulations for further optimization. (Q4, FY 2020; Completed)
6. Lithium ion conductivity is occurring at the ceramic phase of the composite. Technical progress is acceptable by measurements of ionic conductivity, shear modulus, and film thickness measurements. Analysis of technical results indicates that performance targets are achievable. (Q4, FY 2020; Completed)

## Progress Report

This quarter, Wildcat utilized its HT platform to test hundreds of additives belonging to various families with different functionalization groups to find hits that reduced the interfacial impedance between the ceramic and the PE in the tri-layer cell setup. Based on the most promising candidates, the team then took those additives and added them to make a composite ceramic/polymer SE and had shown an improvement in ionic conductivity versus that of a pure PE. Significant progress was made, and Wildcat has successfully completed all scheduled milestones.

### Down Selection of Best Composite SE Additives

Figure 28a shows an overview plot of the several additive families tested at room temperature. During three quarters, more than 5200 EIS measurements were taken. As can be seen in Figure 28, several hits show low interfacial impedance, suggesting that resistance between the ceramic LATP and PEO polymer was reduced or eliminated. Figure 28b-c shows a selected set of results where several families have low interfacial impedance and higher tri-layer conductivities when compared to the control. Of the best hits, Additive Families A, C, and D show the lowest interfacial impedance of all systems tested.

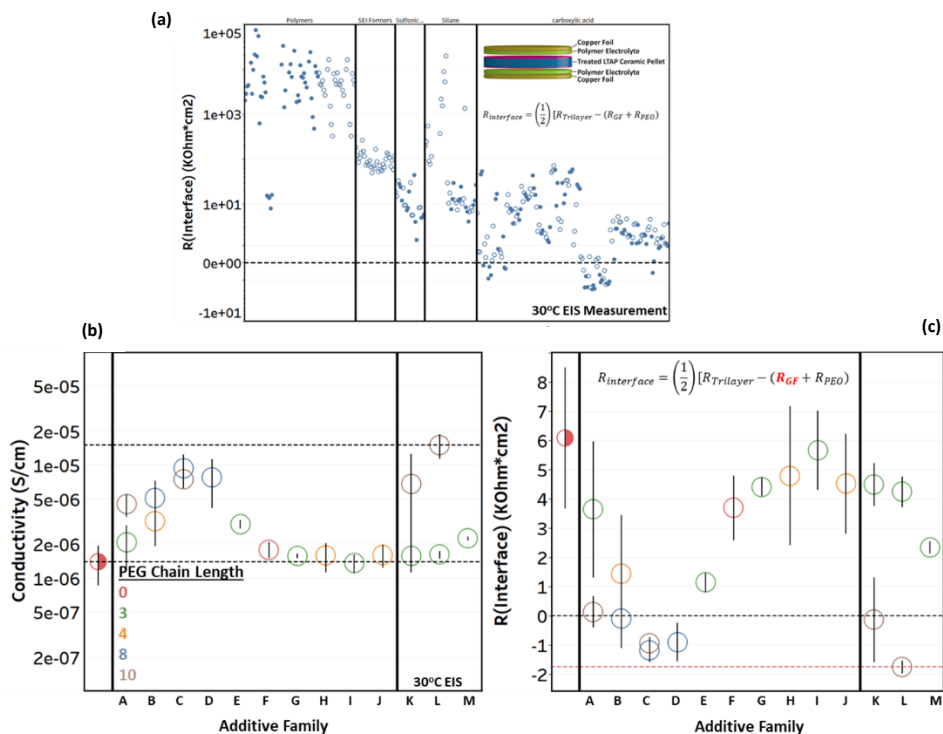


**Figure 28. (a) Additive screening using the Wildcat high-throughput tri-layer cell geometry. More than 5200 electrochemical impedance spectroscopy measurements ran during the past three quarters. (b/c) Best hit families that show lowest interfacial impedance in tri-layer cell geometry. The baseline system is shown in the left-most panels of (b/c).**

The next step of the process is to verify that the additives will translate from the tri-layer geometry to a composite polymer/ceramic electrolyte film. Additive Family C was chosen as the preliminary additive to test in a ceramic/polymer composite. The team tested the additive in two forms: one where the additive was simply added to the slurry of the PEO, ceramic, salt, and solvent and then cast to make the composite electrolyte, and the second where the additive was first functionalized onto the surface of the LATP ceramic, then mixed with PEO, salt, and solvent. Figure 29 shows the preliminary results with 10 wt% LATP for both the functionalized and non-functionalized composites. One can see that the additive increases the conductivity of the composite PEO/ceramic over no additive. This result is significant, as it shows that the interfacial impedance between the PEO and ceramic is indeed lowered, resulting in Li-ion conductivity moving through the ceramic phase. While

exciting, much work is needed to improve the % ceramic filler in the composite. The targeted % ceramic will be greater than 60 wt% and will require tuning many variables. However, the team believes this challenge can be addressed utilizing the Wildcat HT platform.

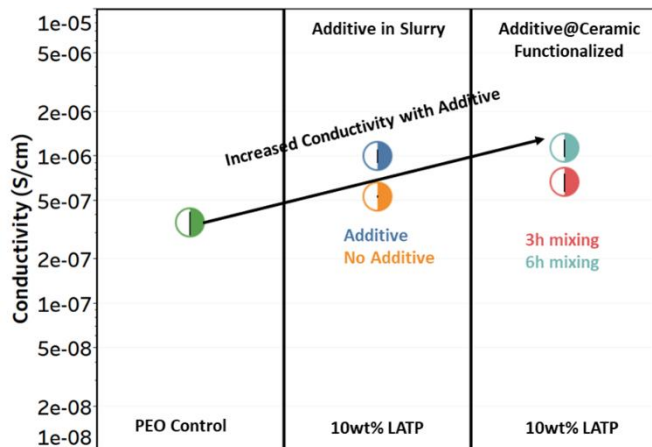


Figure 29. Results of the PEO/ceramic composite with and without the additive C. These results show that having the additive in the composite improves ionic conductivity.

### Protected Li-Metal Additive Testing

This quarter, Wildcat screened 70+ different Li-metal protection materials (called artificial SEIs, or ASEIs) from 14 additive families (anhydride, carbonate, etc.) using the HT platform. Using Li/Li symmetric cells with thin lithium metal and a small volume of carbonate-based electrolyte, the goal is to see an increase in cycle life when the lithium metal is treated with an ASEI. Figure 30a shows the voltage profile of a Li/Li cell with non-treated lithium metal (baseline system) utilizing a current density of 1.0 mA/cm<sup>2</sup> for 1 hour plating and stripping. The performance indicator for this cell format is called ‘Cumulative Capacity Plated’ and measures how much lithium is plated from one electrode to another; the project’s baseline system plates an average of 23 mAh/cm<sup>2</sup> before cell failure. In Figure 30b, the team demonstrates that through HT screening, many ASEIs were found that increased the cycle life of the baseline system. As shown, each additive family had different percentages of materials that enhanced the baseline performance. For instance, of all the triflate (Tf)-based ASEIs tested, only one outperformed the baseline system. On the other hand, numerous nitrate- and chloride-based ASEIs behaved better than the baseline system.

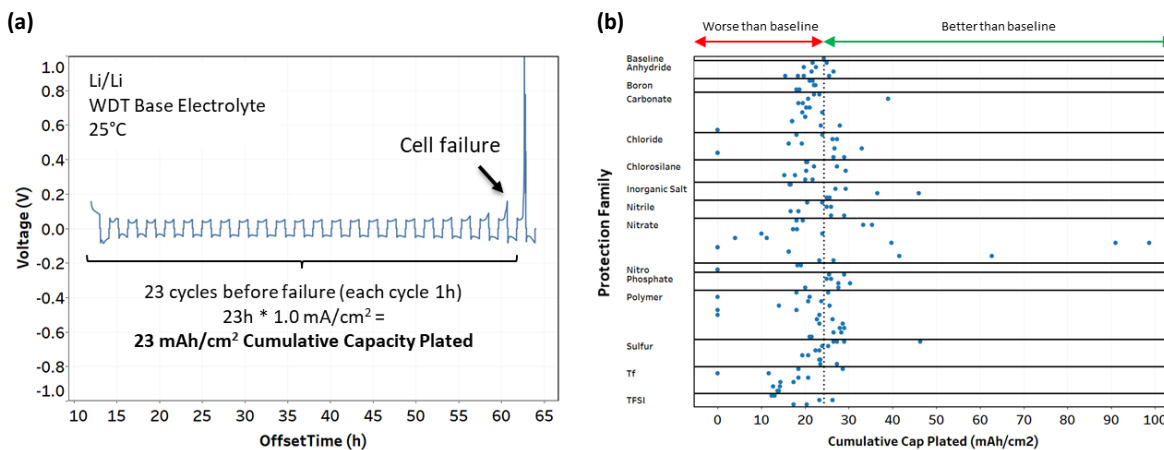


Figure 30. (a) Baseline system (no Li-metal protection) performance in Li/Li symmetric cell showing the point of cell failure (marked with arrow). The cumulative capacity plated is calculated from cycle life (h) and plating current (mA). (b) Li-metal protection screening using the Wildcat high-throughput Li/Li cell platform showing 160+ protection layers. The baseline system is visualized with a dotted line.

Figure 31a shows the voltage profile of the baseline system and three select ASEI systems in the Li/Li symmetric cell format (the current density is 1.0 mA/cm<sup>2</sup>, and each plating/stripping cycle is 1 h). From this plot, it is easy to see the performance benefit of the three ASEIs shown. To learn more about the ASEI systems, the team employs sporadic design of experiments to look for structure-activity relationships between ASEIs. In Figure 31b, the performance of 17 ASEIs comprised of five anions and four cations in Li/Li symmetric cells is shown (for instance, ASEI 1-A is comprised of a cation and an anion in its chemical structure). There are several take away messages from this data, with highlights shown below:

- Cation B shows similar performance regardless of anion and additive concentration (wt%). This suggests that the protective film that forms on the lithium metal is similar between these ASEI systems.
- Cation D shows an inability to cycle for Anions 1 and 2, but can cycle (albeit poorly) for Anions 4 and 5. This suggests that while some Anions do not pair well with this Cation (resulting in an inhibitive protective film), other Anions participate in the ASEI protective film and allow cycling to occur.
- Generally, the order of performance is Cation A > Cation B > Cation C ≥ Cation D. This suggests that the protective film formed from an ASEI may be more susceptible to the ASEI Cation and less susceptible to the ASEI Anion.

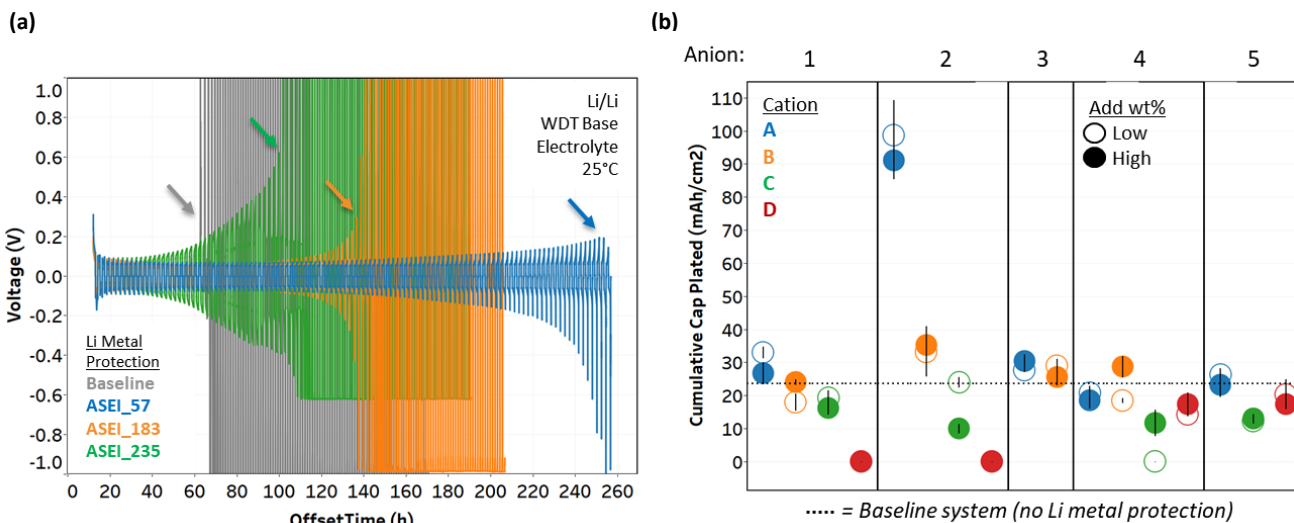


Figure 31. (a) Li/Li symmetric cells showing the point of cell failure (marked with arrows) for the baseline system and selected Li-metal protection artificial SEIs (ASEIs) found via screening. (b) Cumulative capacity plated (mAh/cm<sup>2</sup>) for 17 different ASEIs screened having similar cations and anions to see relative differences in Li/Li cell performance.

In the next step, the team plans to take ASEIs that showed beneficial performance on their own and pair them with other ASEIs so that a synergistic effect may be observed. For instance, if an ASEI that the team hypothesizes to form a more elastic layer on the Li-metal surface performed well, they would pair it with an ASEI that they hypothesize to form a more rigid mechanical layer. In this manner the ASEI that the team applies to the Li-metal surface would have characteristics that comprise both elasticity and mechanical strength.

## Patents/Publications/Presentations

The project has no patents, publications, or presentations to report this quarter.

## Task 1.9 – Physical and Mechano-Electrochemical Phenomena of Thin-Film Lithium-Ceramic Electrolyte Constructs

(Jeff Sakamoto, University of Michigan)

**Project Objective.** While a small number of SEs exhibit high ionic conductivity ( $\sim 1 \text{ mS cm}$  at 298 K), few are stable against lithium metal. The garnet-type SE, based on the nominal formula  $\text{Li}_7\text{La}_3\text{Zr}_2\text{O}_{12}$  (LLZO), is unique in that it is a fast ion conductor and—as demonstrated in the team’s recent project (DE-EE-00006821)—is stable against lithium. Moreover, the team’s former project successfully demonstrated a decrease in Li-LLZO interface resistance from 12,000 to 2 Ohms  $\text{cm}^2$  and stable cycling at 1 mA  $\text{cm}^2$  for 100 cycles ( $\pm 15 \mu\text{m}$  lithium per cycle). Although the past project demonstrated that LLZO is a viable SE for enabling batteries using metallic lithium, the studies used thick pellets (1 mm) and thick anodes ( $\sim 500 \mu\text{m}$ ). The goal of this project is to acquire a deep fundamental understanding of the physical and mechano-electrochemical phenomena that control the performance of cells consisting of thin LLZO ( $\sim 10 \mu\text{m}$ ), thin lithium anodes ( $\sim 20 \mu\text{m}$ ), and thin solid-state composite cathodes.

**Project Impact.** If successful, the project will gain knowledge to guide closely related commercialization efforts to scale the production of LLZO-based SSBs.

**Approach.** The team believes that to achieve a step increase in technology readiness level (TRL), the same performance characteristics previously shown should be demonstrated in technologically relevant cells, for example, thin LLZO and thin lithium.

**Out-Year Goals.** The out-year goals involve the following: custom thin-film construct development, preliminary cycling studies, Vis cell development, lithium cycling, and polymer gel electrolyte screening.

**Collaborations.** This project collaborates with Professors N. Dasgupta and D. Siegel of UM, Mechanical Engineering.

### Milestones

1. Thin film LLZO integration. (Q1-Q2, FY 2020; Completed / Q4, FY 2020; In progress)
2. Long-term cycling stability. (Q2, FY 2020; Completed / Q4, FY 2020; In progress)
3. Mechanics of the Li-LLZO interface. (Q3, FY 2020; In progress)
4. Stability and kinetics of the LLZO-electrolyte interface. (Q4, FY 2020; In progress)

## Progress Report

### Mechanics of the Li-LLZO Interface

The goal of this quarter’s milestone was to measure the charge-coupled devices (CCDs) of TFCs. Some of the data was acquired and is being analyzed. Because the laboratories were inaccessible for April and May, progress toward this quarter’s milestone was slowed. However, the Sakamoto group was able to manufacture TFCs for delivery to the N. Dasgupta group for surface chemical analysis using XPS (Figure 32). The XPS of as-fabricated TFC indicated the LLZTO surface was relatively clean and consistent through the top ~ 100 nm. There was likely some lithium carbonate on the surface; however, it was only about 10-nm thick. After sputtering beneath 10 nm, the LLZTO composition was relatively constant. These analyses demonstrate that the surface of as-fabricated TFC LLZTO is clean on both the lithium anode and cathode interfaces. Because surface cleanliness directly correlates with interface resistance, these data indicate the interface resistances should be relatively low.

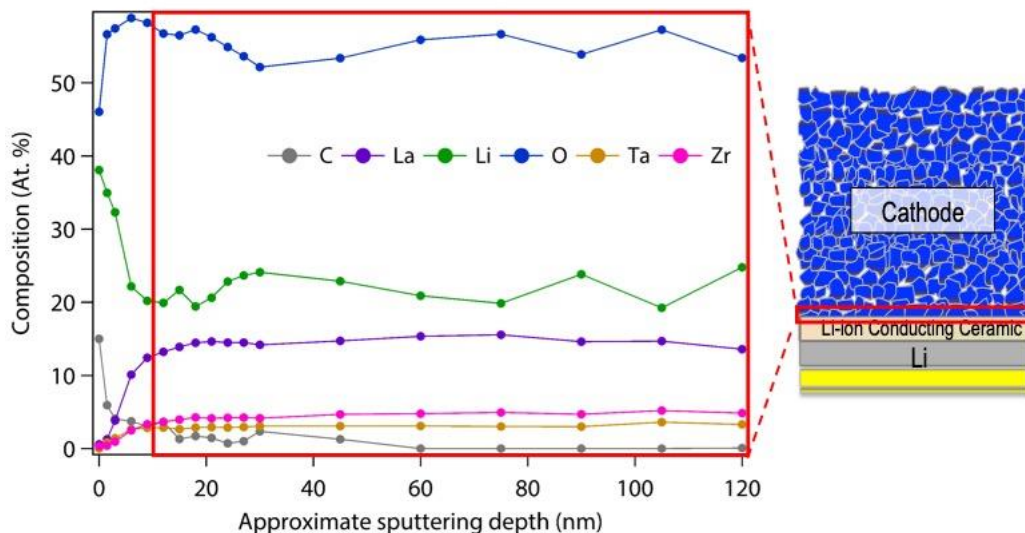


Figure 32. X-ray photoelectron surface analysis of as-densified thin-film construct LLZTO.

## Patents/Publications/Presentations

The project has no patents, publications, or presentations to report this quarter.

## Task 1.10 – Lithium Dendrite-Free $\text{Li}_7\text{N}_2\text{I-LiOH}$ Solid Electrolytes for High-Energy Lithium Batteries (Chunsheng Wang, University of Maryland)

**Project Objective.** The objective of this project is to research, develop, and test Li-metal-based batteries that implement solid Li-ion conductors (LICs) equipped with  $\text{Li}_7\text{N}_2\text{I-LiOH}$  SE capable of achieving cell performance of 350 Wh/Kg energy density for 1000 cycle life with a cost of  $\leq \$100/\text{kWh}$ .

**Project Impact.** Lithium dendrite growth during charge/discharge cycles limits the use of all-solid-state batteries (ASSBs). A criterion for lithium dendrite suppression that is developed through systematical investigation on thermodynamics and kinetics of lithium dendrite growth will guide the electrolyte design.  $\text{Li}_7\text{N}_2\text{I-LiOH}$  and  $\text{Li}_3\text{YCl}_6$  SE with high ionic conductivity and low electronic conductivity will be used to validate the criterion for lithium dendrite suppression, to achieve the project objective.

**Approach.** The team will establish the relationship among interface energy, lithium plating/stripping overpotential, interface resistance, SE stability with lithium, and CCD. The dendrite suppression criterion will be developed based on the relationship. The dendrite suppression capability for the  $\text{Li}_7\text{N}_2\text{I-LiOH}$  pellet will be evaluated by testing the CCD.

**Out-Year Goals.** In year one, the project will synthesize, modify, and optimize the  $\text{Li}_7\text{N}_2\text{I-LiOH}$  and  $\text{Li}_3\text{YCl}_6$  electrolytes, and  $\text{Li}_7\text{N}_2\text{I-LiOH/Li}_3\text{YCl}_6$  bi-layered electrolytes to achieve a high ionic conductivity to  $> 5 \times 10^{-4} \text{ S/cm}$  CCD of  $> 3.0 \text{ mA/cm}^2$  at a capacity of  $> 3.0 \text{ mAh/cm}^2$ . The team will focus on enhancing the CE for lithium anode to  $> 99\%$ . The CE of the SE is a powerful indicator of electrolyte stability and lithium dendrite growth.

**Collaborations.** There are no reported collaborations this quarter.

### Milestones

1. Synthesis of  $\text{Li}_7\text{N}_2\text{I-LiOH}$  and  $\text{Li}_3\text{YCl}_6$  electrolytes with high ionic conductivity. (Q1, FY 2020; Completed, December 31, 2019)
2. Electrochemical property of  $\text{Li}_7\text{N}_2\text{I-LiOH}$  and  $\text{Li}_7\text{N}_2\text{I-LiOH/Li}_3\text{YCl}_6$  bi-layer film. (Q2, FY 2020; Completed)
3. Lithium dendrite suppression capability. (Q3, FY 2020; In progress)
4. High CE for lithium plating/stripping. (Q4, FY 2020)

## Progress Report

### Reduction of Li/Li<sub>7</sub>N<sub>2</sub>I-LiOH Interface Resistance

The Li<sub>7</sub>N<sub>2</sub>I-LiOH is thermodynamically stable with lithium and has high interface energy, which causes large interfacial resistance. As shown in Figure , metallic lithium was melted in a stainless-steel container on a hot plate at 250°C for 10 minutes in a glovebox filled with pure argon. A drop of molten lithium was added on the surface of the heated Li<sub>7</sub>N<sub>2</sub>I-LiOH pellet. Molten metallic lithium is not wetted with Li<sub>7</sub>N<sub>2</sub>I-LiOH pellet surface, exhibiting a large contact angle. By surface coating, the contact angle of lithium on Li<sub>7</sub>N<sub>2</sub>I-LiOH pellet surface becomes smaller.

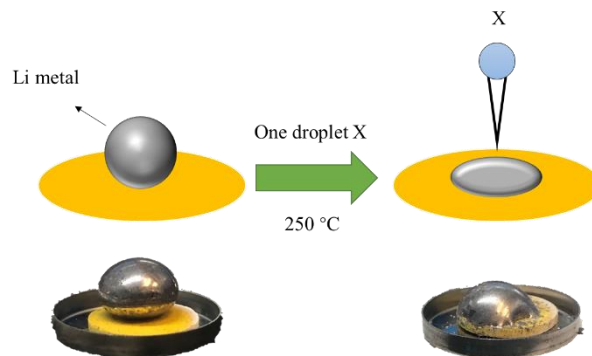


Figure 33. Scheme and digital picture of molten metal lithium on Li<sub>7</sub>N<sub>2</sub>I-LiOH pellet surface with and without surface treatment.

### Li|Li<sub>7</sub>N<sub>2</sub>I-LiOH|Li Symmetry Cell

The Li|Li<sub>7</sub>N<sub>2</sub>I-LiOH|Li cell was assembled by attaching molten lithium on both sides of SE pellet as shown in Figure 34.



Figure 34. Digital picture for the process of assembling Li|Li<sub>7</sub>N<sub>2</sub>I-LiOH|Li cell.

The interface resistance of Li/Li<sub>7</sub>N<sub>2</sub>I-LiOH/Li was measured using EIS at room temperature in the frequency range of 0.1–1 × 10<sup>6</sup> Hz. Figure 35 shows the EIS plots of the Li/Li<sub>7</sub>N<sub>2</sub>I-LiOH/Li at room temperature. The EIS plot consists of a huge semicircle in the high frequency region, followed by a small semicircle in the low frequency region. The large semicircle at high frequency could be assigned to the bulk and grain boundary (GB) resistance in the electrolyte, which is estimated to be ~ 1900 Ω cm<sup>2</sup>, by fitting the equivalent circuit in Figure 35. The semicircle in the low frequency region was contributed by the interfacial resistance, which is estimated to be 150 Ω cm<sup>2</sup>. The bulk and GB resistance is consistent with the resistance measured using Au|Li<sub>7</sub>N<sub>2</sub>I-LiOH|Au blocking electrode. The interfacial resistance of 150 Ω cm<sup>2</sup> is still high; however, it can be further reduced by the optimization of surface coating.

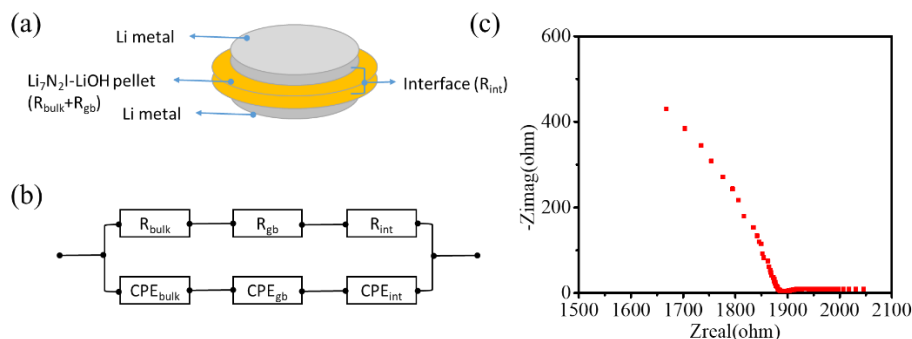


**Figure 35. (a) Schematic of the all-solid-state Li|Li<sub>7</sub>N<sub>2</sub>I-LiOH|Li cell. (b) Equivalent circuit for fitting the electrochemical impedance spectroscopy (EIS) data of the Li|Li<sub>7</sub>N<sub>2</sub>I-LiOH|Li cell. (c) EIS data Li|Li<sub>7</sub>N<sub>2</sub>I-LiOH|Li cell at room temperature.**

The CCD was measured at room temperature and 80°C. Figure 36 shows the voltage profiles of Li|Li<sub>7</sub>N<sub>2</sub>I-LiOH|Li cell with a step-increased current density and a fixed lithium plating/stripping time of 0.5 hour at room temperature (Figure 36a) and at 80°C (Figure 36b). The lithium plating/stripping overpotential increases with the increase of the current density. In the room temperature, a sudden voltage drop was observed at the 10<sup>th</sup> cycle as the current density increased to 0.2 mA/cm<sup>2</sup> because of the dendrite penetration through the SSE. Therefore, the CCD of Li<sub>7</sub>N<sub>2</sub>I-LiOH electrolyte at room temperature is 0.2 mA/cm<sup>2</sup>. The low CCD is probably due to high overpotential of > 0.22 V induced by a relatively low conductivity of the Li<sub>7</sub>N<sub>2</sub>I-LiOH electrolyte and the high contact resistance between lithium and the Li<sub>7</sub>N<sub>2</sub>I-LiOH electrolyte. However, the overpotential of 2.2 V for short-circuit of Li<sub>7</sub>N<sub>2</sub>I-LiOH electrolyte is still higher than that (0.1 V) for LPS. The team also measured the DC cycling of Li |Li<sub>7</sub>N<sub>2</sub>I-LiOH|Li cell at 80°C at a constant capacity of 0.025 mAh/cm<sup>2</sup>, as shown in Figure 36b. The results show that even at the current density of 1.0 mA/cm<sup>2</sup>, no sudden voltage drop can be found. This can be attributed to the high ionic conductivity of the Li<sub>7</sub>N<sub>2</sub>I-LiOH electrolyte at the higher temperature and the low capacity that avoids the large volume change during cycling. The team will further optimize the room-temperature ionic conductivity of the pellet and enhance the Li|Li<sub>7</sub>N<sub>2</sub>I-LiOH interface by better interfacial engineering.

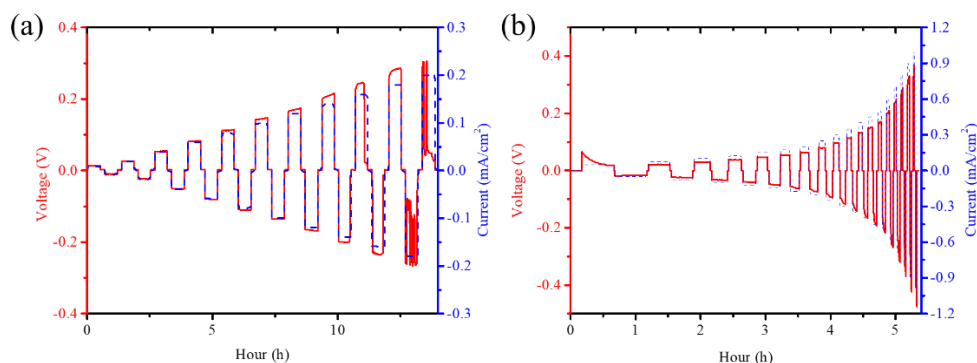


**Figure 36. (a) Lithium plating/stripping of Li|Li<sub>7</sub>N<sub>2</sub>I-LiOH|Li cell at room temperature with step increased current density from 0.01 to 0.2 mA/cm<sup>2</sup> at an incremental step of 0.02 mA/cm<sup>2</sup>. (b) Lithium plating/stripping of Li|Li<sub>7</sub>N<sub>2</sub>I-LiOH|Li cell at 80°C with increased current, but fixed capacity of 0.025 mAh/cm<sup>2</sup>.**

The stability of Li<sub>7</sub>N<sub>2</sub>I-LiOH electrolyte with lithium metal was also demonstrated by the galvanostatic cycling test. As shown in Figure 37, the Li|Li<sub>7</sub>N<sub>2</sub>I-LiOH|Li cell was able to cycle stably with a current density of 0.1 mA cm<sup>-2</sup> for more than 35 hours / 70 cycles without short circuit. The stable cycling stability is attributed to the thermodynamic stability of Li<sub>7</sub>N<sub>2</sub>I-LiOH electrolyte with lithium.

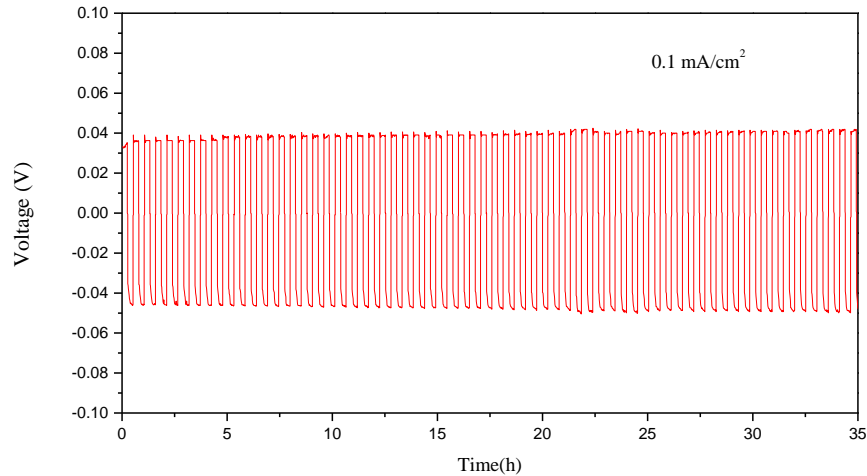


Figure 37. Lithium plating/stripping of Li|Li<sub>7</sub>N<sub>2</sub>|LiOH|Li cell at 80°C with current density of 0.1 mA/cm<sup>2</sup> and capacity of 0.05 mAh/cm<sup>2</sup>.

### Modeling for the Dendrite Formation Mechanism in Unstable Electrolytes

To model the dendrite formation mechanism in unstable electrolytes, the team carried out electrochemical analysis based on the thermodynamic equilibrium process. Using the model as shown in Figure 38, they formulated the dendrite formation criterion in unstable electrolytes against lithium metal.

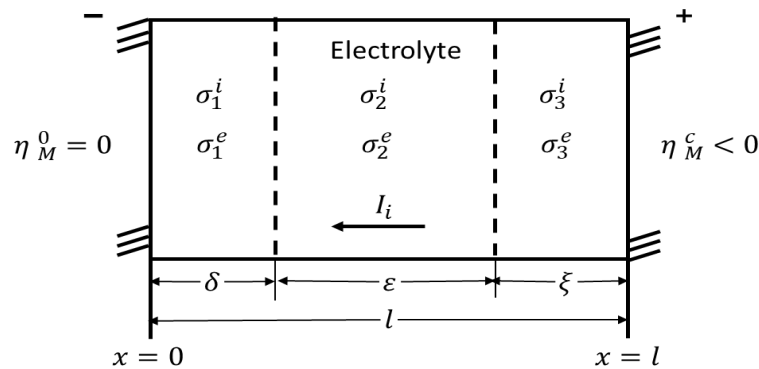


Figure 38. Geometry of the cell and its corresponding parameters.

Consider a simple ionic solid where the conduction cations have a charge of +1, giving the equilibrium reaction:



Assume that one particle current is independent of the other's gradient in chemical potential. Transport in such a solid can be described by

$$I_i = -\frac{\sigma_i \nabla \eta_i}{F} \quad (2)$$

and

$$I_e = \frac{\sigma_e \nabla \eta_e}{F} \quad (3)$$

$I_e$  flows in a direction opposite to  $I_i$ . Ionic conductivity ( $\sigma_i$ ) and electronic conductivity ( $\sigma_e$ ) are defined under Ohmic current flow. Hence, the electrochemical potential gradients of the ions and the electrons,  $\nabla \eta_i$  and  $\nabla \eta_e$ , relate simply to their respective current densities  $I_i$  and  $I_e$ .  $F$  is Faraday's constant. The electrolyte with its

electrode is shown in Figure 38. In the steady state, the total ionic and electronic currents are constant, so that:

$$I = I_i + I_e \quad (4)$$

Since  $I$ ,  $I_i$ , and  $I_e$  are constants everywhere in the electrolyte, thus:

$$\frac{1}{x} \int_0^x \left( \frac{\sigma^i \nabla \eta_i}{F} \right) dx = \frac{1}{l} \int_0^l \left( \frac{\sigma^i \nabla \eta_i}{F} \right) dx \quad (5)$$

Assuming that the conductivities are constant in each region and the cross-coefficients between  $\sigma_i$  and  $\sigma_e$  are omitted, thus the geometry shown in Figure 38:

$$\frac{1}{\delta} \int_0^\delta (\sigma_1^i \nabla \eta_i / F) dx = \frac{1}{l} \left[ \int_0^\delta (\sigma_1^i \nabla \eta_i / F) dx + \int_\delta^{\delta+\varepsilon} (\sigma_2^i \nabla \eta_i / F) dx + \int_{\delta+\varepsilon}^{\delta+\varepsilon+\xi} (\sigma_3^i \nabla \eta_i / F) dx \right] \quad (6)$$

it follows

$$\left( \frac{l}{\delta} - 1 \right) \int_0^\delta \sigma_1^i \nabla \eta_i dx = \int_\delta^{\delta+\varepsilon} \sigma_2^i \nabla \eta_i dx + \int_{\delta+\varepsilon}^{\delta+\varepsilon+\xi} \sigma_3^i \nabla \eta_i dx \quad (7)$$

Based on some basic electrochemical principles and reasonable assumption, the team can get

$$\frac{\Delta \eta_M^\delta}{F} = \frac{A \left[ \frac{\Delta \eta_M^c}{F} + \frac{\sigma_2^i}{\sigma_3^i} V_T \right]}{1 + A} \quad (8)$$

According to the Equation 8, the team can find the critical potential for the cell will be affected by not only the Li|SSE interface, but also the cathode|SSE interface. To get a good capability in suppression dendrite, a stable SSE is needed. If unstable, the interphase should have high ionic conductivity and low electronic conductivity.

### Patents/Publications/Presentations

The project has no patents, publications, or presentations to report this quarter.

## Task 1.11 – Hot Pressing of Reinforced Lithium-NMC All-Solid-State Batteries with Sulfide Glass Electrolyte (Thomas Yersak, General Motors)

**Project Objective.** The objective of this project is to research, develop, and test Li-NMC ASSBs capable of achieving program performance metrics by implementing sulfide glass SSEs and hot press processing in a dry room environment. The performance of ASSBs with sulfide SSEs is limited because they are essentially green tapes with up to 20% porosity. In composite cathodes, the porosity limits energy density and power, while porosity in the separator acts as a conduit for Li-metal deposits if cycling conditions (that is, C-rate, operating temperature, and pressure) are not strictly controlled. The goal of the project is to demonstrate that the hot pressing method and appropriately formulated sulfide glass SSEs can eliminate porosity to enable Li-NMC ASSBs with energy density of  $\geq 350$  Wh/kg.

**Project Impact.** The hot press processing method and appropriately formulated sulfide glass SSEs may enable Li-NMC ASSBs with improved energy density  $> 350$  Wh/kg. The GM processing technology depends on heating a sulfide glass SSE above its glass transition temperature,  $T_g$ , at which point it can consolidate via viscoplastic flow. In the composite cathode, hot pressing provides liquid-like contact between the NMC cathode and SSE to increase energy density and power by enabling thick composite cathodes with high active material loading. Furthermore, cathode-supported sulfide glass separators can be made dense and thin by hot pressing. A dense separator enables the robust use of a Li-metal anode because lithium deposits may be more effectively blocked, preventing cell shorting.

**Approach.** The sulfide SSE used in the composite cathode, otherwise known as the catholyte, will dictate the processing specifications for ASSB hot pressing. Thermal stability can be achieved by NMC passivation and proper catholyte formulation. This project will systematically evaluate different NMC coatings, catholyte formulations, and hot-press processing specifications (that is, temperature, time, and pressure). The performance of hot-pressed ASSBs will be compared to green baseline ASSBs and hot-pressed control ASSBs consisting of the  $\beta$ -Li<sub>3</sub>PS<sub>4</sub> and Li<sub>6</sub>PS<sub>5</sub>Cl model SSEs. Electron microscopy will be employed to understand interfacial phenomena and track composite cathode microstructure before and after hot pressing.

**Out-Year Goals.** In the second year of this project, a sulfide glass SSE will be formulated specifically for use as the separator. The separator glass SSE formulation will be designed to achieve full densification under the hot-press processing specifications determined for the catholyte. Separator glass formulation design will also consider cathodic stability, moisture stability, and ionic conductivity. Once a system of separator glass SSE and catholyte has been determined, the third year of the project will demonstrate hot-pressed full cells at the coin-cell and single-layer pouch cell levels, which meet program target performance metrics.

**Collaborations.** GM will lead this project with no subrecipients.

### Milestones

1. Establish protective coating on cathode: select best coating method and coating chemistry. Confirm conformality of coating using microscopy. (Q2, FY 2020; Completed)
2. Develop suitable baseline system with reversible capacity of  $\sim 120$  mAh/g. (Q3, FY 2020; Completed)
3. Determine parameters required to prepare cathode samples via focused ion beam (FIB)/SEM lift-out and to analyze samples via high-resolution transmission electron microscopy (HRTEM). (Q4, FY 2020; In progress)
4. Demonstrate hot-pressed cathode with reversible capacity of 120 mAh/g. Analysis indicates technical approach capable of achieving performance targets. (Q1 FY 2021; In progress)

## Progress Report

Work this quarter focused primarily on efforts to develop a baseline dataset with which to evaluate potential catholytes and hot pressing protocols. The work to establish a baseline dataset may be broken into three distinct tasks, namely, NCM coating, composite electrode homogeneity, and electrode thickness. The project's baselining work utilizes the BMR model SSE  $\beta$ -Li<sub>3</sub>PS<sub>4</sub>, and the team expects that their dataset may help inform the work of other groups in the program. In addition to collecting a baseline dataset, they have also begun work to evaluate potential catholyte candidates, with preliminary results reported here.

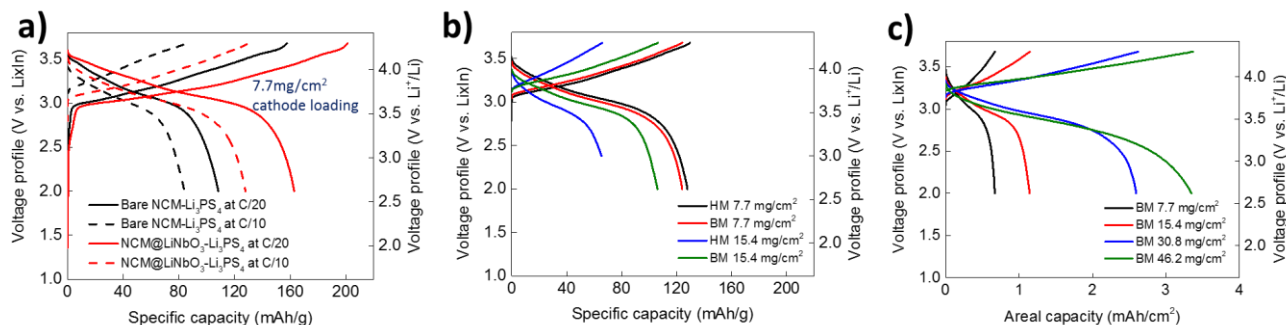


**Figure 39.** The preparation of a baseline dataset utilizes composite electrodes that are a 7:3 (w/w) mixture of NCM-851505 and  $\beta$ -Li<sub>3</sub>PS<sub>4</sub>. (a) 1<sup>st</sup> and 10<sup>th</sup> cycle voltage profiles of test cells confirming that a LiNbO<sub>3</sub> coating on NCM improves performance. (b) 10<sup>th</sup> cycle voltage profiles of test cells showing that preparation of composite electrodes by ball milling (BM) instead of hand mixing (HM) improves performance. The improvement is only noticeable at higher loading (15.4 mg/cm<sup>2</sup>). (c) 10<sup>th</sup> cycle voltage profiles of test cells with electrode loadings of 7.7 (black), 15.4 (red), 30.8 (blue), and 46.2 (green) mg/cm<sup>2</sup>. The cell with 46.2 mg/cm<sup>2</sup> electrode loading delivers an areal capacity of > 3 mAh/cm<sup>2</sup>.

The first task of the baseline work focuses on completion of previous reporting period activities, namely, the application and testing of protective coatings on NCM-851505. Of the three target coatings [LiNbO<sub>3</sub>, Li<sub>3</sub>PO<sub>4</sub>, and Li<sub>2</sub>O-ZrO<sub>2</sub> (LZO)], in-house LiNbO<sub>3</sub> coatings will be carried into future work. Differential scanning calorimetry (DSC) screening of 7:3 (w/w) NCM and  $\beta$ -Li<sub>3</sub>PS<sub>4</sub> composites show that all coatings impart similar thermal stability to the composite. The onset of a first exothermic feature (data not shown) was approximately 325°C, 350°C, 351°C, and 354°C for bare NCM, NCM@LZO, NCM@Li<sub>3</sub>PO<sub>4</sub>, and NCM@LiNbO<sub>3</sub>, respectively. Figure 39a presents the 1<sup>st</sup> cycle voltage profiles for test cells made with bare NCM (black) and NCM@LiNbO<sub>3</sub> (red). The cell with bare NCM has a 1<sup>st</sup> cycle CE of 68.7% and a discharge capacity of 108.3 mAh/g, while the cell with NCM@LiNbO<sub>3</sub> has a 1<sup>st</sup> cycle CE of 80.9% and discharge capacity of 162.8 mAh/g. As expected, the LiNbO<sub>3</sub> coatings are confirmed to improve performance of test cells with  $\beta$ -Li<sub>3</sub>PS<sub>4</sub> SSE.

The second task focuses on establishing composite electrode homogeneity. Typically, academic-scale composite electrodes are prepared by hand mixing. However, aggregated SSE particles are difficult to disperse completely by hand mixing, which leads to sample-to-sample variation that increases experimental error. Electrode heterogeneity may also reduce rate performance of test cells by impeding Li<sup>+</sup> transport due to increased impedance. Better dispersion of NCM and SSE particles was accomplished by ambient planetary ball milling (Fritsch P7). Figure 39b provides voltage profiles for test cells with composite electrodes prepared by either hand mixing (HM) or planetary ball milling (BM). The composite electrodes were 7:3 (w/w) NCM@LiNbO<sub>3</sub> and  $\beta$ -Li<sub>3</sub>PS<sub>4</sub>. At a low loading that is typical for academic studies (7.7 mg/cm<sup>2</sup>), there is little difference between the HM and the BM composites, with both cells delivering a 10<sup>th</sup> cycle capacity of ~ 125 mAh/g. However, when the composite loading is doubled to 15.4 mg/cm<sup>2</sup>, the BM composite delivers a 10<sup>th</sup> cycle capacity of 106 mAh/g, which is 39% greater than that of the HM composite. At a C/10 rate, the benefit of composite preparation by BM only becomes apparent at higher electrode loadings.

Heterogeneity of HM and BM composites was quantified by analysis of backscatter SEM images (not shown) of composite cathode cross sections. To quantify cathode homogeneity, image processing was used to calculate particle size distribution (PSD) and average nearest neighbor distance (NND).<sup>[2]</sup> The HM composite had a SSE PSD of 110.1  $\mu\text{m}^2$  and an average NND of 6.5  $\mu\text{m}$ , while the BM composite had a SSE PSD of 52.9  $\mu\text{m}^2$  and an average NND of 9.12  $\mu\text{m}$ . A shorter NND for the HM composite indicates that  $\beta\text{-Li}_3\text{PS}_4$  particles are aggregated and that the aggregations are close to each other.

Having established the need to prepare composite electrodes by BM, the third task was to build a baseline dataset of cells with thick cathodes. Thick is defined here as delivering areal capacities equivalent to state-of-the-art Li-ion cells ( $> 3 \text{ mAh/cm}^2$ ). As stated, typical academic SSB test cells have thin cathodes with  $< 1 \text{ mAh/cm}^2$  areal capacity. It is the team's expectation that consolidation of composite cathodes by hot pressing will most benefit cells with thick electrodes. Figure 39c provides the 10<sup>th</sup> cycle voltage profiles for test cells with 7:3 (w/w) NCM@LiNbO<sub>3</sub> and  $\beta\text{-Li}_3\text{PS}_4$  composite electrodes of various thicknesses. With a composite loading of 46.2  $\text{mg/cm}^2$ , the team was able to achieve the target of  $> 3 \text{ mAh/cm}^2$  at a C/10 rate and room temperature.

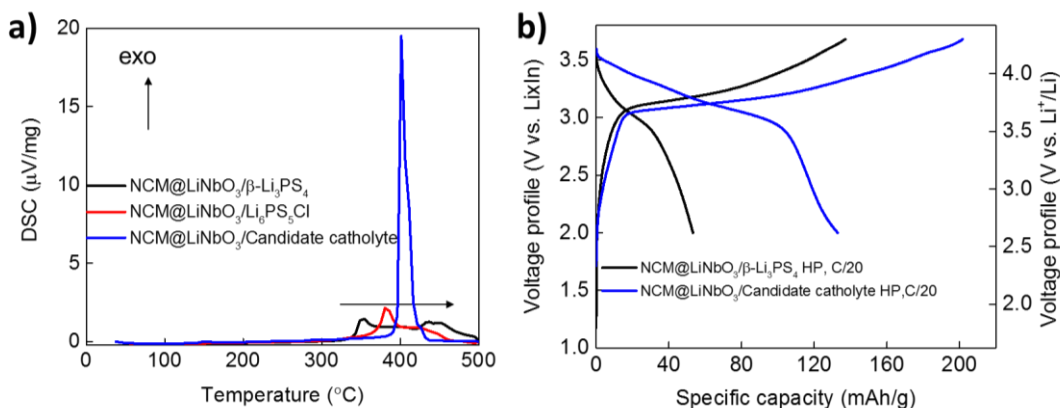


**Figure 40. Preliminary data on the evaluation of a candidate catholyte for hot pressing. (a) Differential scanning calorimetry (DSC) scans for 7:3 (w/w) composites of NCM@LiNbO<sub>3</sub> with either  $\beta\text{-Li}_3\text{PS}_4$ ,  $\text{Li}_6\text{PS}_5\text{Cl}$ , or a candidate catholyte. The onset temperature of an exothermic feature is highest for the candidate catholyte suggesting that it has superior thermal stability. (b) First cycle voltage profiles for hot pressed test cells with 7:3 (w/w) composite cathodes of NCM@LiNbO<sub>3</sub> and either  $\beta\text{-Li}_3\text{PS}_4$  (black) or the candidate catholyte (blue).**

Having established the appropriate baseline, work has commenced on evaluation of candidate catholytes for hot pressing. Prior to the project's work, DSC had been only used to measure the thermal stability of charged NCM composites.<sup>[2]</sup> Last quarter, the team developed DSC as a means to measure the thermal stability of discharged cathode composites to quickly and systematically evaluate catholyte compositions before assembly of test cells. Here, they show that DSC results can predict the outcome of SSB hot pressing. Figure 40a details the DSC scans of 7:3 (w/w) composites of NCM@LiNbO<sub>3</sub> and either  $\beta\text{-Li}_3\text{PS}_4$ ,  $\text{Li}_6\text{PS}_5\text{Cl}$ , or a candidate catholyte. The thermal stability of each composite may be quantified by assessing the onset temperature of the first exothermic feature. The onset temperatures were 300 $^{\circ}\text{C}$ , 325 $^{\circ}\text{C}$ , and 380 $^{\circ}\text{C}$  for the composites with  $\beta\text{-Li}_3\text{PS}_4$ ,  $\text{Li}_6\text{PS}_5\text{Cl}$ , and the candidate catholyte, respectively. Based on the onset temperature, the candidate catholyte was predicted to be the most thermally stable. Figure 40b shows the 1<sup>st</sup> cycle voltage profiles for hot-pressed cells with 7:3 (w/w) composites of NCM@LiNbO<sub>3</sub> and either  $\beta\text{-Li}_3\text{PS}_4$  (black) or the candidate catholyte (blue). The cell with  $\beta\text{-Li}_3\text{PS}_4$  has a 1<sup>st</sup> cycle CE of 38.7% and a discharge capacity of only 53 mAh/g, while the cell with the candidate catholyte has a 1<sup>st</sup> cycle CE of 65.8% and discharge capacity of 132.4 mAh/g. Current work aims to understand the fundamental mechanisms for the improved thermal stability of the candidate catholyte and to systematically evaluate a range of candidate catholytes using DSC.

#### References

- [1] Louis, P., et al. *Metallurgical and Materials Transactions A* 26 (1995): 1449–1456.
- [2] Tsukasaki, H., et al. *Journal of Power Sources* 367 (2017): 42–48.

## Patents/Publications/Presentations

The project has no patents, publications, or presentations to report this quarter.

## Task 1.12 – Low Impedance Cathode/Electrolyte Interfaces for High-Energy-Density Solid-State Batteries (Eric Wachsman and Yifei Mo, University of Maryland)

**Project Objective.** The project objective is to research, develop, and test Li-metal-based batteries that implement solid LICs equipped with NMC cathodes integrated into the Li-metal/LLZ ( $\text{Li}_7\text{La}_3\text{Zr}_2\text{O}_{12}$ ) tri-layer architecture. Specifically, the team will achieve the following: (1) identify and demonstrate interfacial layers to achieve low-impedance and stable NMC/LLZ interfaces; (2) develop novel processing techniques to fabricate NMC/LLZ composite cathodes with low interfacial resistance; and (3) enable high-performance ASSBs with an energy density of 450 Wh/kg and 1400 Wh/L and negligible degradation for 500 cycles.

**Project Impact.** Instability or high resistance at the interface of high-energy cathode materials with Li-garnet SEs limits the high-energy-density all-solid-state lithium battery. This project will lead to a fundamental understanding of solid-electrolyte/solid-cathode interfaces and a unique and transformative LLZ framework to enable high-energy-density, safe Li-metal batteries approaching ~ 400 Wh/kg.

**Approach.** In this new EERE project, the team will build on their demonstrated expertise with garnet electrolytes and ASSB cells to accomplish the following: (1) engineer interfaces to overcome high NMC/LLZ interfacial impedance and interfacial degradation; (2) develop processing and fabrication techniques to achieve high-loading NMC/LLZ composite cathodes with low resistance and high cyclability; and (3) integrate the NMC/LLZ cathodes into all-solid-state Li-metal/LLZ cells to achieve high-energy-density batteries.

**Out-Year Goals.** The project will solve the current challenges of integrating garnet SE with a cathode to achieve a high-performance ASSB using a high-energy-density Li-metal anode. The resultant high energy density and stability using both high-energy-density Li-metal anodes and NMC cathodes will open new applications in portable electronics, EVs, and beyond.

**Collaborations.** This project funds work at UMD. Dr. E. Wachsman (PI) will have management responsibility and will lead experimental efforts including garnet synthesis, interface processing, cell fabrication, and testing. Dr. Y. Mo (Co-PI) will lead the computational efforts on understanding the stability between garnet and cathode and on identifying promising coating materials. No collaborations are reported this quarter.

### Milestones

1. Computationally determine interfacial stability between LLZ SEs and NMC cathode. (Q2, FY 2020; Completed)
2. Determine thermochemical stability between LLZ and infiltrated NMC. (Q3, FY 2020; In progress)
3. Computationally determine the mechanism of interfacial stabilization between LLZ and NMC through coating layers. (Q3, FY 2020; In progress)
4. *Go/No-Go Decision:* Computationally determine appropriate compositions to stabilize the LLZ-NMC interface. Achieve design capable of meeting performance requirements. (Q4, FY 2020)

NOTE: The campus was closed for three months, and thus experimental results were limited.

## Progress Report

XRD experiments were performed on composite pellets of Ta-doped LLZO (LLZTO) and cathode materials prepared by physical mixing, mold pressing, and co-sintering at 700°C for 3 hours. Cathode materials tested include NMC-111,  $\text{LiMnO}_4$  (LMO),  $\text{LiNi}_{0.5}\text{Mn}_{1.5}\text{O}_4$  (LNMO), and  $\text{LiCoO}_2$  (LCO). The weight ratio of LLZTO and the cathode material in each pellet is 1:1.

XRD results suggest that at 700°C all the cathode materials investigated react with LLZTO, with the reactivity increasing in the order of  $\text{LCO} < \text{LNMO} < \text{LMO} = \text{NMC-111}$  (Figure 41). This trend generally agrees with the project's computational studies reported last quarter showing that higher nickel content in cathodes generally leads to poor stability with garnet. The reaction products, for example,  $\text{Li}_2\text{MnO}_3$  and  $\text{La}_2\text{Zr}_2\text{O}_7$ , between LLZTO and NMC-111 detected by XRD have also been predicted by the previous computational studies. These consistent results demonstrate the efficacy of combining computation with experiment in facilitating understanding on garnet/cathode interfacial stability. The team will proceed next to extend the experiment to include NMC in other compositions and LLZTO/cathode reactivities at other temperatures in the range of 600-1100°C to eventually complete their experimental investigation on determining thermochemical stability between LLZ and infiltrated NMC.

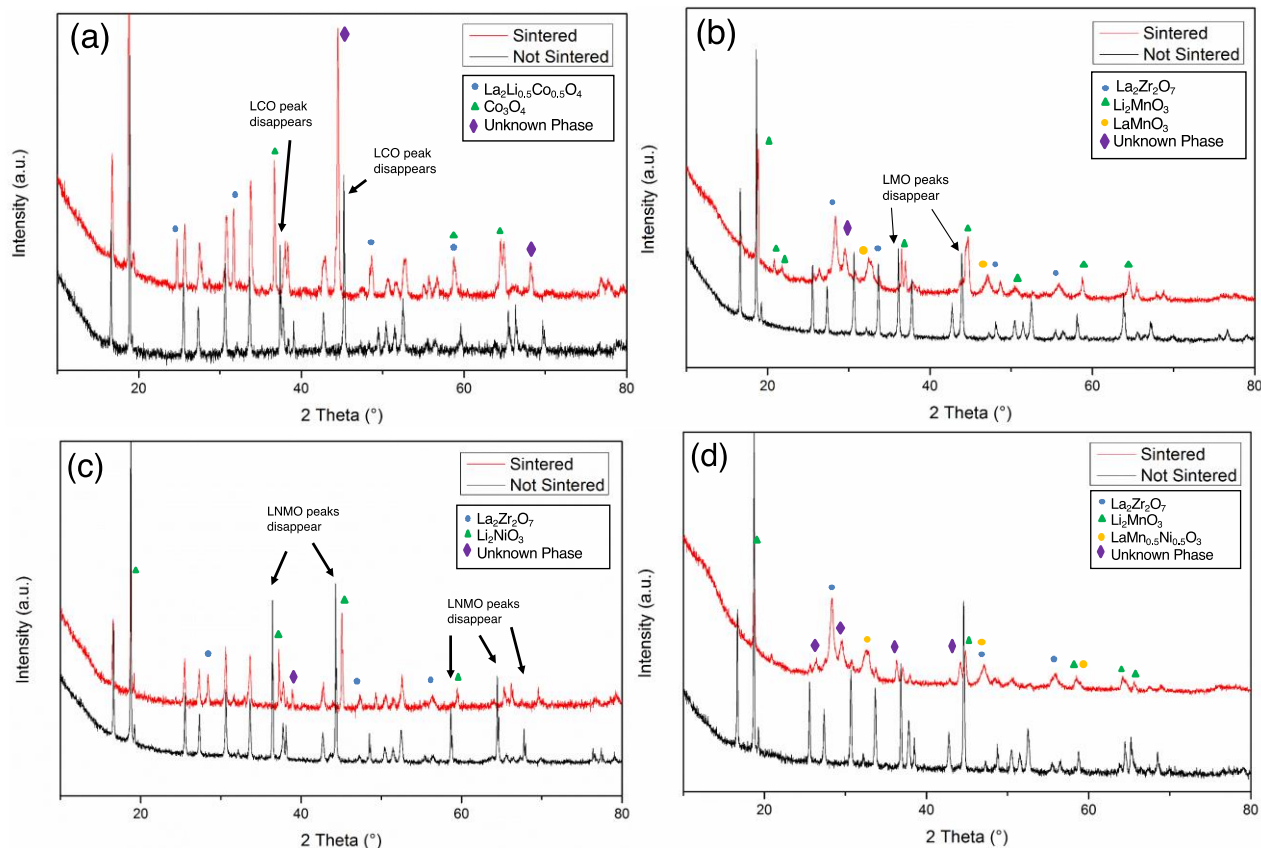


Figure 41. X-ray diffraction patterns of LLZTO and 50/50 w/w mixtures with various cathode materials before and after co-sintering at 700°C. Cathode material for each figure is (a) LCO, (b) LMO, (c) LNMO, and (d) NMC-111.

## Patents/Publications/Presentations

The project has no patents, publications, or presentations to report this quarter.

## Task 1.13 – Developing an *In Situ* Formed Dynamic Protection Layer to Mitigate Lithium Interface Shifting: Preventing Dendrite Formation on Metallic Lithium Surface to Facilitate Long Cycle Life of Lithium Solid-State Batteries (Deyang Qu, University of Wisconsin Milwaukee)

**Project Objective.** The objective of this project is to research, develop, and test Li-metal-based batteries that implement solid LICs equipped with a formed dynamic protection layer. The proposed project aims to enable safe, long-cycle lithium anodes to achieve cell performance targets of 400 Wh/Kg, over 100 cycles, with 15-year shelf life and < \$100/KWh cost.

**Project Impact.** Project efforts are to contribute an in-depth understanding of the lithium interface and dendrite growth prevention to the field of Li-metal batteries, which will pave the way for eventual development of high-energy-density, low-cost, and long-lasting lithium batteries. This advancement could be a crucial selling point for the greater adoption of EVs. This project will make possible the translation of fundamental research into practical implementation of high-energy lithium anodes, enabling eventual achievement of cell performance targets.

**Approach.** The novelty of this approach is that the team intends to mitigate the dendrite problem by creating a dynamic protection layer during the interface shift to prevent dendrite formation throughout battery operation.

**Out-Year Goals.** The project has three out-year goals: (1) *in situ* diagnostic tools are fully functional; (2) potential candidates for Li-anode modifications are identified; and (3) synthesis routes are designed.

**Collaborations.** The PI is the Johnson Control Endowed Chair Professor, who has close and frequent collaboration with Johnson Controls' scientists and engineers. The collaboration enables the team to validate the outcomes of fundamental research in pilot-scale cells. The PI also has been working closely with top scientists at Argonne National Laboratory (ANL), Brookhaven National Laboratory (BNL), LBNL, and PNNL and with U. S. industrial collaborators, for example, GM, Millipore Sigma, and Clarios. In addition, the team works with international collaborators in China, Japan, and South Korea. These collaborations will be strengthened and expanded to give this project a vision with both today's state-of-the-art technology and tomorrow's technology in development, while incorporating feed-back from the material designers and synthesizers upstream, as well as from the industrial end users downstream.

### Milestones

1. *Baseline.* Conduct literature review and establish baseline for proposed technologies. (Q1, FY 2020; Completed)
2. *Fully functional fixtures and setups.* *In situ* electrochemical-optical and *in situ* electrochemical-MS cells capable of observing dendrite growth and detecting gas generation in real time. (Q1, FY 2020; Completed)
3. *Coating methods.* Physical requirements of each coating technique and adaption of different coating methods for various coating materials based on their properties are identified. (Q2, FY 2020; Completed)
4. *N-type polymer compounds.* N-doped polymer compounds are synthesized. (Q3, FY 2020; Completed)
5. *In situ* diagnostic tools capable of investigating a coated lithium electrode / projected cell performance. Various selected materials can be coated on a lithium surface forming an artificial layer before cell assembly. The dendrite growth and gassing of the coated electrode can be investigated in real-time during cell operation with *in situ* diagnostic tools. Analysis indicates technical approach capable of achieving performance targets. (Q4, FY 2020; In progress)

## Progress Report

This quarter has been challenging. Due to the pandemic of COVID-19, the PI's research labs in the university were closed in mid-March and are only partially accessible now. However, the team still managed to complete the third milestone of FY 2020. Assuming the labs are open by the end of June, they will accomplish all of the fiscal year milestones. Based on results of the previous two quarters, they continue to develop engineering processes to create dynamic interfacial layers on metallic lithium anodes, which could suppress dendrite growth and create dynamic interface between lithium and a SSE.

An organic cation, trisaminocyclopropenium (TAC), was tested to suppress dendrite growth on a metallic lithium anode. During the lithium plating process, TAC cations with aliphatic chains can form a positively charged electrostatic shield around lithium protrusions, repelling the approaching  $\text{Li}^+$  and thereby attaining a more uniform plating. A two-times-longer cycle life of 300 hours at  $1 \text{ mA cm}^{-2}$  is achieved in a Li||Li symmetric cell in comparison with the control. Eventually, the TAC molecular will be polymerized by attaching to a backbone or distributed in a polymer matrix. The objective is to form a dynamic interface between the lithium anode and the SSE.

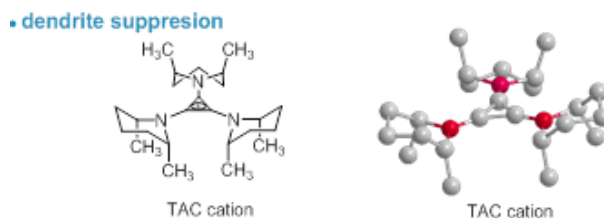


Figure 42. Molecular structure of trisaminocyclopropenium (TAC).

To investigate the role of TAC cation on dendrite suppression, the polarization profiles of Li||Li symmetric cells were 1<sup>st</sup> cycled at  $1 \text{ mA cm}^{-2}$  rate for 1-hour duration. As displayed in Figure 43a, the cell with TAC performs significantly better than the baseline. In a baseline cell, CE dropped below 90% after 49 cycles, while an average CE of 97% was preserved with TAC throughout 135 cycles (Figure 43b). The *in situ* optical microscopic images were compared under a harsh lithium plating condition of  $4.0 \text{ mA cm}^{-2}$ . As displayed in Figure 43d, highly dendritic and mossy lithium formed after 15 minutes in the baseline electrolyte and evolved into filament morphology after 60 minutes. These dead lithium can lead to a poor CE and an increased cell impedance. In contrast, a relatively uniform lithium deposition was observed in the TAC electrolyte throughout the test.

A cation-shield mechanism is proposed and illustrated in Figure 43e. It is well established that the plating process can unavoidably generate protuberant tips on which electric charges tend to accumulate. The TAC cations can be absorbed on those tips without being reduced via electrostatic attraction. Thus, a lithiophobic protective layer can be formed due to its bulky scaffold with branched nonpolar groups. The arriving  $\text{Li}^+$  was repelled and deposited on the adjacent flat lithium surface, thus generating a dendrite-free lithium deposition.

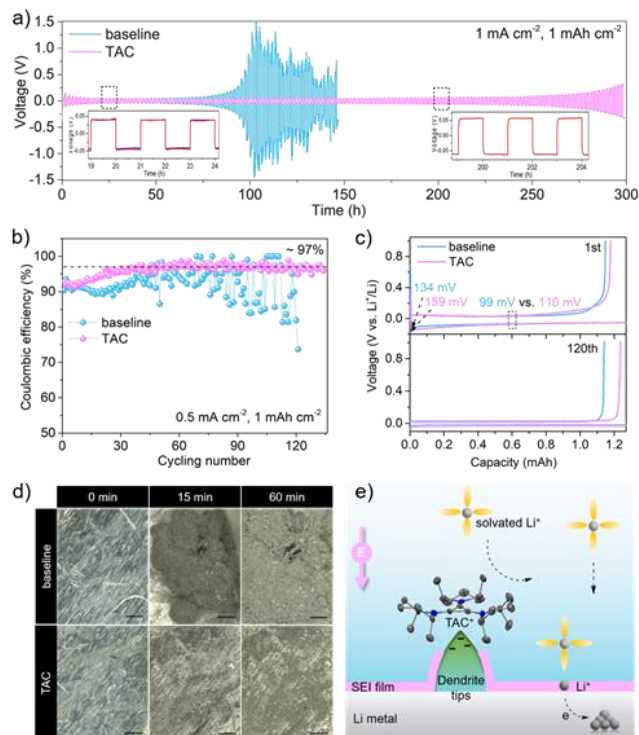


Figure 43. Electrochemical performance of lithium plating/stripping in trisaminocyclopropenium (TAC) electrolyte. (a) Voltage profiles of Li||Li symmetric cells cycling at  $1 \text{ mA cm}^{-2}$ ,  $1 \text{ mAh cm}^{-2}$ . (b) Coulombic efficiencies of Li||Cu asymmetric cells cycling at  $0.5 \text{ mA cm}^{-2}$ ,  $1 \text{ mAh cm}^{-2}$ . (c) Voltage profiles of Li||Cu cell at 1<sup>st</sup> and 120<sup>th</sup> cycles. (d) *In situ* optical microscopic images during lithium plating process at  $4 \text{ mA cm}^{-2}$ , scale bar  $200 \mu\text{m}$ . (e) Schematic illustration of a cation-shield mechanism. Note: The TAC is not drawn to scale. The manuscript is under review.

## Patents/Publications/Presentations

The project has no patents, publications, or presentations to report this quarter.

## Task 1.14 – Molecular Ionic Composites: A New Class of Polymer Electrolytes to Enable All-Solid-State and High-Voltage Lithium Batteries (Louis Madsen, Virginia Polytechnic Institute and State University)

**Project Objective.** Based on a newly discovered class of solid PE materials, that is, molecular ionic composites (MICs), the overall objective is to develop solid-state lithium conductors targeted for use in transportation applications. MICs form a mechanically stiff, electrochemically stable, and thermally stable matrix. Specific objectives include the following: (1) development of robust MIC electrolyte thin films (~ 20  $\mu\text{m}$ ) to serve as simultaneous nonflammable separators and dendrite-blocking  $\text{Li}^+$  conductors, (2) electrochemical quantification of key performance metrics including electrolyte stability, interfacial reactions, and suitability/compatibility with a range of electrode materials, and (3) comprehensive investigation of ion transport mechanisms and electrode-electrolyte interfacial reactivity under practical operating conditions using NMR and synchrotron X-ray analyses.

**Project Impact.** Commercialization of Li-metal SSBs is hampered by lack of a functional nonflammable SE that can provide high ionic conductivity, wide electrochemical window, favorable mechanical properties to inhibit lithium dendritic growth, and low interfacial resistance. The tunable MIC materials platform has potential to fulfill these requirements with relatively simple fabrication techniques, and thus shows promise for enabling nonflammable SSBs that can be optimized for low cost and high energy density.

**Approach.** MICs rely on a unique polymer that is similar to Kevlar® in its strength, stiffness, and thermal stability, but with densely spaced ionic groups that serve to form an electrostatic network that permeates mobile ions in the MIC. The team can tailor the ion concentrations and types to yield MIC electrolyte films that are electrochemically compatible with Li-metal anode as well as a range of high-voltage layered cathodes. They are searching the composition space of lithium salts, electrochemically compatible ionic liquids, and polymer (PBDT) molecular weight to determine best composition windows for MIC electrolytes. The team is also investigating best methods for casting thin films in terms of temperature, solvent/evaporation conditions, and control over the initial liquid crystalline gel formation point. Concurrently, they are testing MIC films in various electrochemical cells, quantifying transport and structural/morphology parameters with NMR and X-ray techniques, and measuring key mechanical (dynamic mechanical thermal analysis, stress-strain) and thermal (DSC, TGA) properties.

**Out-Year Goals.** This year, the team is focused on understanding evolution of structure and morphology during the film casting process to optimize this process and obtain thin MIC electrolyte films. As part of the team's electrolyte optimization, they are determining the composition windows that yield fast  $\text{Li}^+$  conduction, mechanical stability, and electrochemical compatibility with lithium metal and selected cathode materials. They will develop robust electrolyte films and an array of testing schemes (that is, electrochemical, thermal, mechanical, NMR, and X-ray) to sensibly feedback on film composition and fabrication.

**Collaborations.** The team is beginning collaboration with T. J. Dingemans' group at University of North Carolina (UNC) Chapel Hill in which they are forming composites based on PBDT polymer and carbon materials such as graphene oxide, and are beginning to develop charged rigid-rod polymers building on PBDT. The team is exploring shear rheology and broadband dielectric spectroscopy collaboration with Prof. R. H. Colby at PSU. They are starting collaboration with D. Nordlund at SLAC National Accelerator Laboratory (SLAC) to conduct synchrotron X-ray studies on MIC films.

### Milestones

1. Determine synthetic conditions for 100- $\mu\text{m}$  thick electrolyte. (Q1, FY 2020; Completed)
2. Development of the baseline Li-ion loading and chemical composition. (Q2, FY 2020; Completed)

3. Establish basic electrochemical, thermal, and mechanical testing protocols for SEs and battery cells. (Q3, FY 2020; In progress)
4. Down-select film fabrication method (drop casting or spray deposition). (Q3/Q4, FY 2020; In progress)
5. Determine optimal synthetic conditions, Li-ion loading, and chemical composition. (Q3/Q4, FY 2020; In progress)
6. Determine the parameter spaces for film formation and develop a design capable of meeting performance requirements for film casting process. (Q4, FY 2020; In progress)

## Progress Report

This period, the team has investigated compatibility between the MIC electrolyte and Li-metal anode through CV and symmetric cell cycling. Furthermore, they have investigated the mechanisms of ion transport and the thermo-mechanical stability of the MIC electrolyte.

The team analyzed formation of the SEI layer between MIC membrane and lithium metal through CV characterization. Comparisons among CV curves for the MIC membrane and a LE composed of LiTFSI and Pyr<sub>14</sub>TFSI (Figure 44) strongly indicate that side reactions come predominantly from the ionic liquid. In addition, reduction of TFSI<sup>-</sup> against lithium metal forms a stable SEI layer between the MIC membrane and lithium metal.

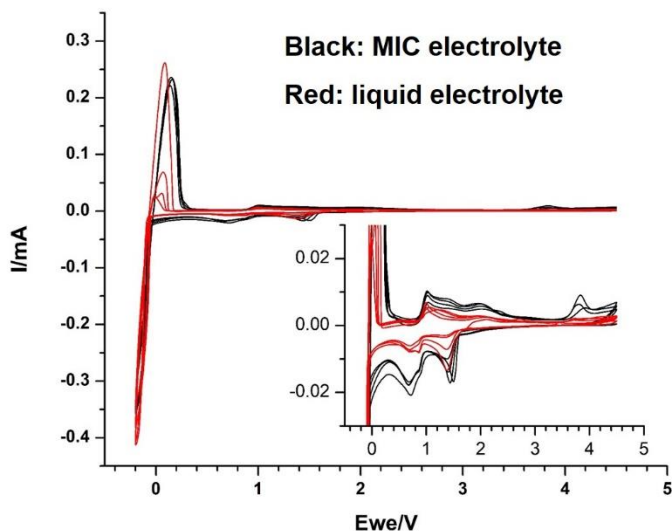
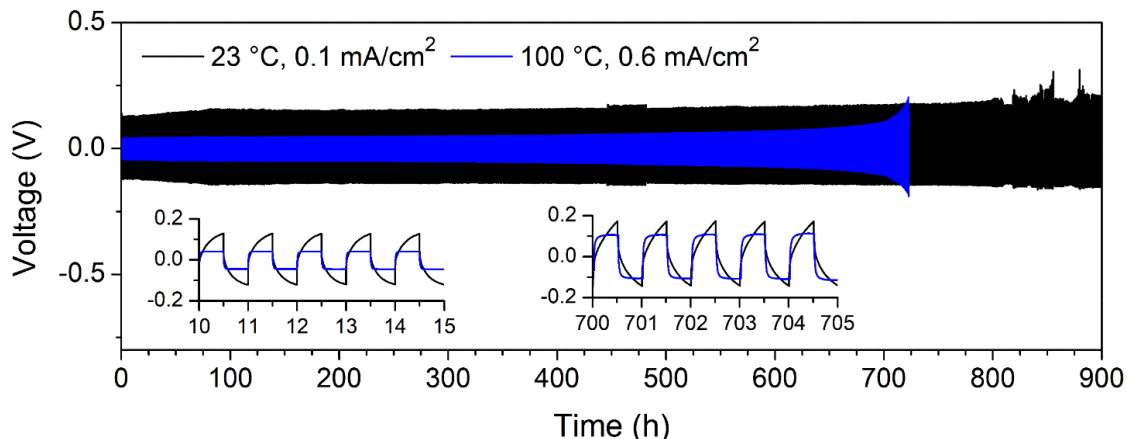


Figure 44. Cyclic voltammetry (CV) of the molecular ionic composite (MIC) electrolyte membrane and a liquid electrolyte (LE) composed of LiTFSI and Pyr<sub>14</sub>TFSI in a 1:8 mass ratio. These CV measurements were recorded at room temperature using stainless steel as working electrode and lithium metal as counter and reference electrode with a scan rate of 0.1 mV s<sup>-1</sup>. The main peak near 0 V corresponds to lithium plating and stripping. The reductive peaks at 0.7 V and 1.5 V and oxidative peaks at 1.0 V and 2.0 V appear both in the MIC membrane and in the LE, suggesting they are caused by the ionic liquid. An oxidative peak at 3.9 V is evident only in the MIC membrane, indicating it is caused by either the polymer or an impurity.

The team has also tested long-term compatibility of the MIC membrane electrolyte against lithium metal. This long-term test was conducted using lithium symmetric cells, with cell voltage monitored during multiple stripping-plating cycles. Figure 45 shows the voltage profiles for Li/MIC/Li symmetric cells cycled at 23°C and 100°C, in which the cells lasted for 800 and 700 hours, respectively, before cell failure. This result demonstrates that the MIC material is stable against lithium not only at room temperature, but up to at least 100°C. This is exciting because for many electrolyte systems their side reactions with Li-metal anode become more aggressive with increasing temperature, leading to rapid electrolyte consumption, SEI formation, and cell failure. This finding suggests that lithium batteries built using this MIC electrolyte can potentially work over a wide temperature range, which is crucial for applications such as EVs where a cooling system is conventionally needed to maintain the temperature of the battery package within a restricted range.



**Figure 45.** Voltage profiles of lithium / molecular ionic composites (MIC) / lithium symmetric cells cycled at 23°C using a current density of 0.1 mA/cm<sup>2</sup> and 100°C using a current density of 0.6 mA/cm<sup>2</sup>. The cells lasted for 800 and 700 hours, respectively, under these two conditions before cell failure, indicating durable compatibility between the MIC material and lithium metal over a wide temperature range.

The team has also continued exploration of ion transport properties this period. The Li-ion transference number of the MIC membrane is measured (via the dc polarization method) to be 0.12 (Figure 46a). To further investigate the mechanism of ion transport, dielectric relaxation spectra (DRS) have been analyzed and the  $\alpha$ -segmental relaxation of the membrane has been identified from the frequency dependence of the imaginary dielectric modulus (Figure 46c). The frequency of  $\alpha$ -relaxation increases with temperature. The Arrhenius plot of this modulus relaxation frequency versus temperature (Figure 46d) shows that this relaxation is associated with the glass transition of the ionic liquid and salt in the membrane. The transport of ionic species in the membrane is thus decoupled from the glass transition (segmental dynamics) of the polymer, leading to the high ionic conductivity of the MIC. The team has also studied the thermo-mechanical stability of the MIC membrane via oscillatory shear rheology. As shown in Figure 46b, the shear storage modulus ( $G'$ ) of the MIC electrolyte demonstrates only a slight decay from 16.2 MPa at 25°C to 10.5 MPa at 200°C, demonstrating that the MIC remains solid up to 200°C.

The MIC electrolyte has shown promising properties in terms of Li|Li cycling performance. As part of the project goals, the team will assemble MIC-based full cell batteries with various cathodes, thus motivating an exploration of the stability of the MIC electrolyte against layered cathodes. If there is any side reaction between the MIC electrolyte and the layered oxide cathode, the surface chemistry of the layered oxide cathode will be modified, such as lowering the TM oxidation states. Characterizing the surface chemistry of layered oxides is easier than characterizing the MIC electrolyte, so the team has studied how the surface chemistry of layered oxides may be influenced by contact with the MIC electrolyte. To mimic the chemical stability of the MIC against a given cathode, the team has used electrochemically delithiated NMC to produce a highly oxidized cathode (that is, high nickel oxidation state) (Figure 47a). Then, the electrochemically delithiated NMC electrode was cut into three pieces. The first piece was stored in an argon glove box at room temperature. The second piece was sealed in argon and stored at 60°C. The third piece was in physical contact with MIC film under high pressure and stored at 60°C. After one month, examination by nickel L-edge soft X-ray absorption spectroscopy (XAS) of the three electrodes (Figure 47b) showed minimal difference under the various storage conditions. This suggests that the MIC electrolyte shows high stability against layered oxide cathodes even in the charged state. This result is consistent with the robust oxidative stability of the MIC electrolyte as previously reported.

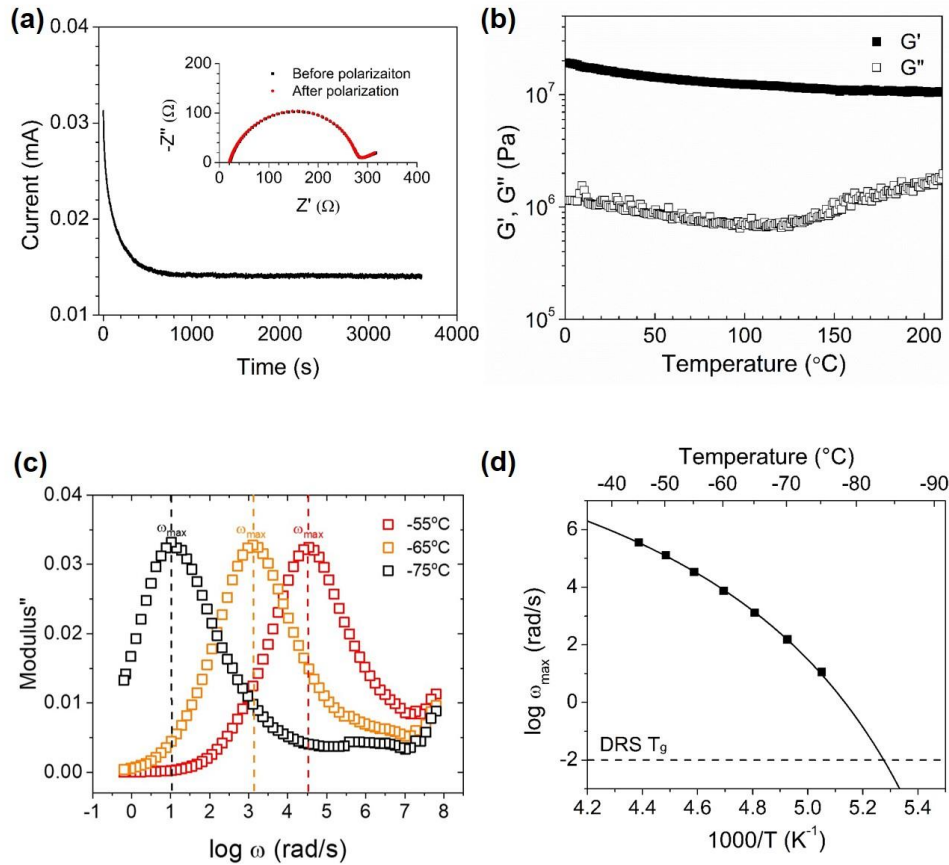


Figure 46. (a) Li-ion transference number measurement of the molecular ionic composite (MIC) electrolyte through the dc polarization technique. Inset is the impedance spectrum before and after polarization. (b) Temperature dependence of the shear storage and loss moduli ( $G'$  and  $G''$ ) at heating rate =  $5^{\circ}\text{C min}^{-1}$ . (c) Frequency dependence of imaginary modulus ( $M''$ ) at varying temperature. The main peak is the  $\alpha$  relaxation, and the minor peak at higher frequency is the  $\beta$  relaxation. (d) Temperature dependence of the  $\alpha$  relaxation frequency ( $\omega_{\text{max}}$ ) of the MIC electrolyte.

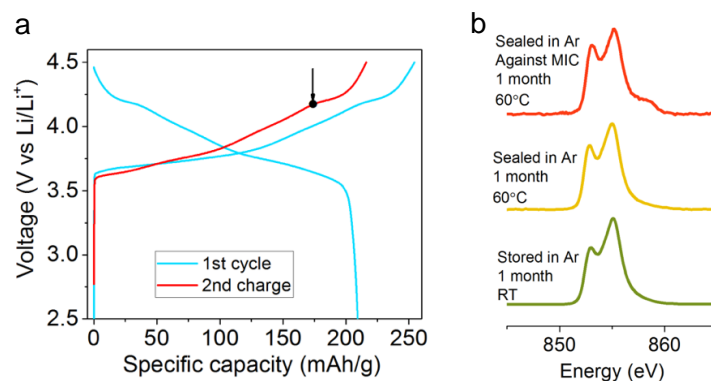


Figure 47. (a) Charge/discharge profiles of a cell containing NMC as the cathode, 1 M  $\text{LiPF}_6$  in EC/EMC with 2 v.% VC as the electrolyte, and lithium metal as the anode, the cell was cycled at C/10 within 2.5–4.5 V in the 1<sup>st</sup> cycle and then stopped at the charge 4.2 V. This charged cathode then serves as a testing platform to evaluate the stability of the MIC electrolyte. (b) The nickel L3-edge soft X-ray absorption spectra in the total electron yield mode of the NMC-811 electrode (charged to 4.2 V) after storing under various conditions. These spectra show that the MIC electrolyte is stable against layered cathodes.

## Patents/Publications/Presentations

The project has no patents, publications, or presentations to report this quarter.

## Task 1.15 – All-Solid-State Batteries Enabled by Multifunctional Electrolyte Materials (Pu Zhang, Solid Power Inc)

**Project Objective.** The project objective is to develop Li-metal SSBs enabled by multifunctional SSEs for EV application. The ultimate goal is scalable production of large-format ASSBs able to deliver  $\geq 350$  Wh/kg specific energy,  $\geq 1000$  cycle life, and  $\leq \$100/\text{kWh}$  cost.

**Project Impact.** The project impact is enabling scalable production of large format all-solid batteries required by the vehicle market and building domestic battery manufacturers as leaders in the global vehicle ASSB production. The proposed technology will address key limitations of state-of-the-art lithium batteries to meet DOE EV battery targets and accelerate their adoption as large-format EV batteries for sustainable transportation technology.

**Approach.** The project will develop a high-performance Li-metal solid-state cell enabled by a multifunctional SSE. The new SSE will: (1) have high conductivity (up to  $10 \text{ mS/cm}$ ), (2) be stable against lithium metal and high-voltage cathode (0-4.5 V), (3) promote uniform lithium plating (enabling  $> 2\text{C}$  charge rate), and (4) be compatible with large-scale manufacturing processes. The specific cell chemistry to be demonstrated will be the SSE with Li-metal anode and high-nickel-content Li-metal oxide cathode. The solid-state cell will be assembled by scalable roll-to-roll processes developed by Solid Power.

**Out-Year Goals.** In Year 1, multifunctional SSE will be developed with lithium ionic conductivity of  $\geq 3 \times 10^{-3} \text{ S/cm}$ . CCD of  $\geq 6 \text{ mA/cm}^2$  will be achieved in a symmetric lithium cell. The SSE design concept will be proven by demonstrating cycle life of  $\geq 200$  in a full cell. In Year 2, SSE material will be optimized with lithium ionic conductivity of  $\geq 5 \times 10^{-3} \text{ S/cm}$ . Scalable cell assembly processes will be developed. Cycle life of  $\geq 500$  will be demonstrated in a full cell. In Year 3, large-format solid-state cells ( $> 2\text{Ah}$ ) will be assembled/tested to meet the final goal:  $\geq 350 \text{ Wh/kg}$ ,  $\geq 1000$  cycles, and  $\leq \$100/\text{kWh}$  cost.

**Collaborations.** The proposed team consists of Solid Power and subcontractor UCSD. Solid Power (PI: Dr. P. Zhang) will develop the multifunctional SSE and other cell components, assemble cells, and conduct cell tests. UCSD (PI: Prof. S. Meng) will carry out material characterization by using advanced techniques such as XPS, Cryo-STEM imaging, Cryo-STEM EDX, electron energy loss spectroscopy (EELS), and cryo-FIB milling. The UCSD team seeks to quantify the kinetics and evolution of each contributing factor and its impact on battery performance.

### Milestones

1. Secure precursors and equipment. (Q1, FY 2020; Completed, December 31, 2019)
2. Down-select cathode materials. (Q2, FY 2020; Completed, December 31, 2019)
3. Cathode loading  $\geq 3.5 \text{ mAh/cm}^2$ . (Q3, FY 2020; Completed, March 31, 2020)
4. SSE ionic conductivity  $\geq 3 \text{ mS/cm}$ . (Q4, FY 2020; Completed, March 31, 2020)
5. SSE critical current density  $\geq 6 \text{ mA/cm}^2$ . (Q4, FY 2020; Completed, June 30, 2020)
6. Cell cycle life  $\geq 200$ . (Q4, FY 2020; Completed, July 15, 2020)

## Progress Report

### SSE Powder Development

The Solid Power halogenated LPS material was used as a starting point.  $\text{Li}_2\text{S}$ ,  $\text{P}_2\text{S}_5$ , a halogen and other selected dopants were ball-milled to form glassy sulfide electrolytes by using a mechanical ball mill. A subsequent heat-treatment was conducted to obtain glass-ceramic SEs. This quarter, the multifunctional electrolyte materials have met the Year 1 performance targets on both Li-ion conductivity and critical current density against lithium metal. The parameters are in Table 6.

Table 6. Conductivity at 25°C and critical current density of the multilayer electrolyte materials.

Parameters	Year 1 Target	Current Status
Li-Ion Conductivity (S/cm)	$\geq 3 \times 10^{-3}$	$\geq 4 \times 10^{-3}$
Critical Current Density (mA/cm <sup>2</sup> )	$\geq 6.0$	$\geq 6.0$

### SSE Separator Development

This quarter, they have scaled up the SSE separator coating process at pilot scale. A separator slurry was prepared by mixing the SSE powder, a binder, and a solvent by using a Ross high-shear mixer. Slurry viscosity was controlled by 1000 – 2000 cPs (at 100 s<sup>-1</sup> shear rate). The slurry was then cast on a carrier film by using a pilot scale slot-die coater. The separator can be used as a stand-alone film after a calendaring process. The separator also can be directly laminated to a cathode before assembling it into a solid-state cell. The separator thickness ranged from 40 to 100 μm. Figure 48 shows the slot-die coated separator film and the flexibility of a free-standing film.

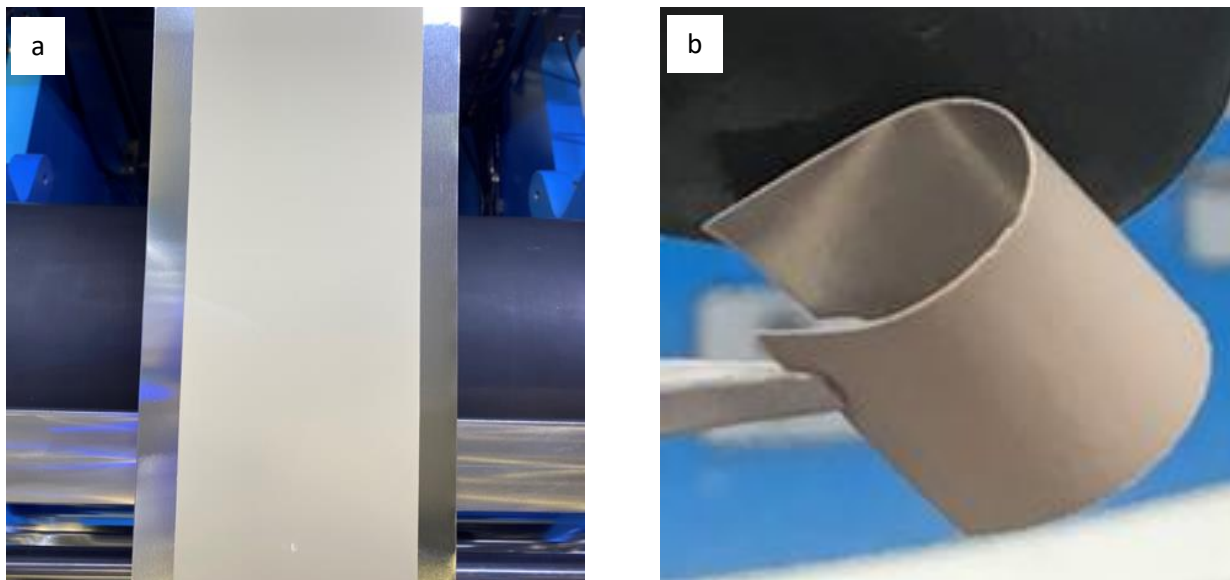


Figure 48. (a) Separator film coated by a slot-die coater. (b) Flexibility of the separator.

## Full Cell Demonstration

This quarter, the team has assembled a single-layer pouch cell (at 6 mAh) for the performance demonstration. The cell contained a NMC-622 composite cathode (at 3 mAh/cm<sup>2</sup>), a thin Li-metal foil anode, and the SSE separator. The cell is designed to deliver a specific energy of 300 Wh/kg if scaled to 20 Ah. When cycled at C/5 - C/5, 2.8 - 4.2 V, and 70°C, the cell demonstrates 250 cycles at 80% capacity retention (Figure 49), exceeding the cycle life target in Year 1 (> 200). The cell performance results support a *Go* decision to continue the project.

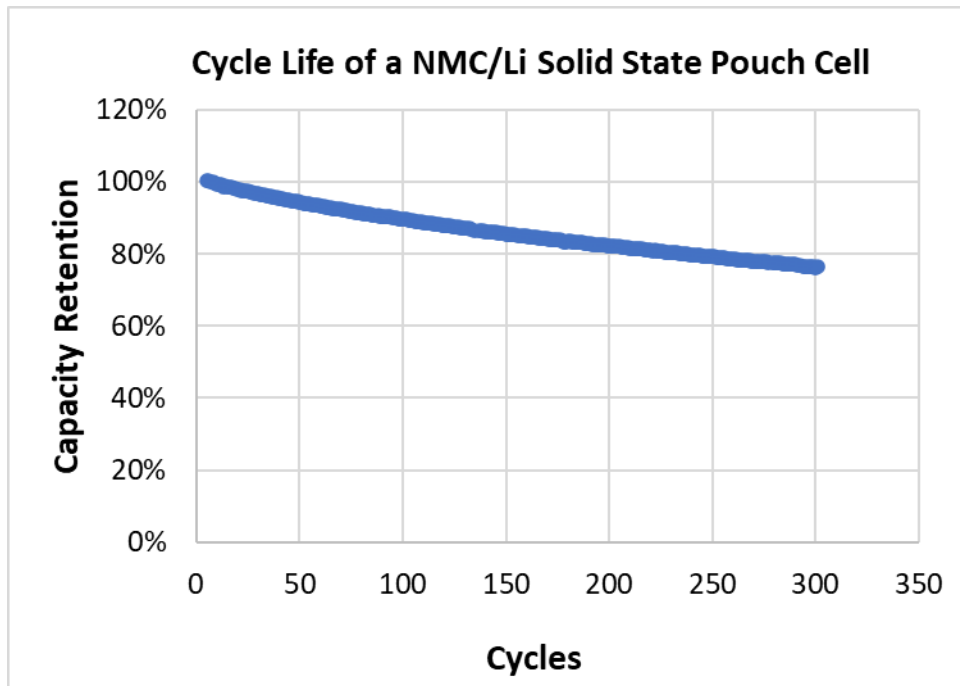


Figure 49. Cycle life of an NMC/Li-metal solid-state pouch cell with the multifunctional solid-state electrolyte.

## Patents/Publications/Presentations

The project has no patents, publications, or presentations to report this quarter.

## Task 1.16 – Developing Materials for High-Energy-Density Solid-State Lithium-Sulfur Batteries (Donghai Wang, Pennsylvania State University)

**Project Objective.** The project objectives are to develop materials involving advanced S-C composite materials, solid additives, and sulfide-based SSEs, and to acquire knowledge for Li-S ASSBs. Li-S ASSBs with large areal sulfur loading ( $\geq 5 \text{ mg cm}^{-2}$ ) and high sulfur content ( $\geq 50 \text{ wt\%}$  in cathode), pairing with lithium or lithium alloy anode, will deliver a high initial specific capacity of over  $1200 \text{ mAh g}^{-1}$  at high charge/discharge rate ( $> 0.3 \text{ C}$ ) for 500 cycles with over 80% capacity retention.

**Project Impact.** This project aims to develop new materials to enable Li-S ASSBs with high energy density, excellent cycling stability, and good rate performance, and thus to build knowledge for fabrication of prototype Li-S ASSBs batteries. Specifically, the developed new materials will greatly increase the specific capacity of sulfur and sulfur utilization at high areal sulfur loading, alleviate the interfacial problem between S-C composite and SSE within sulfur cathode, boost Li-ion conductivity, and improve moisture stability of glass and glass-ceramic sulfide-based SSE. Meeting the technical targets will potentially promote development of high-energy-density Li-S ASSBs and their practical application in EVs and plug-in hybrid EVs (PHEVs), and reduce petroleum consumption in the transportation sector by helping battery-powered vehicles become more accepted by consumers as a reliable source of transportation.

**Approach.** The project goal will be accomplished through developing new materials, together with in-depth characterization of sulfur cathode. Specifically, approaches to realize the project objectives include: (1) development of new carbon material with unique structure, high surface area, and large pore volume; (2) development of new S-C materials to facilitate electron/ion transport; (3) development of novel additives to tune interfacial behavior among components in the cathode; (4) development and optimization of new SSE through cation and anion doping with superior properties such as high ionic conductivity, good moisture, and stability; and (5) diagnostics, characterization, and cell tests on the developed new material or advanced sulfur cathode.

**Out-Year Goals.** The out-year goals are as follows: (1) develop new S-C materials, new cathode additives, and cation-doped SEs (ionic conductivity above  $2 \text{ mS cm}^{-1}$  at room temperature), (2) conduct characterization and performance tests on both material and electrode levels. The *Go/No-Go Decision* will be demonstration of all-solid-state sulfur cathode with over  $1000 \text{ mAh g}^{-1}$  discharge capacity at  $0.3 \text{ C}$  discharge rate and  $50 \text{ wt\%}$  sulfur content for 50 cycles at  $60^\circ\text{C}$ .

**Collaborations.** There are no active collaborations.

### Milestones

1. Demonstrate sulfur cathode with above  $800 \text{ mAh g}^{-1}$  capacity at  $0.1 \text{ C}$  at  $60^\circ\text{C}$ . (Q1, FY 2020; Completed, December 31, 2019)
2. Demonstrate sulfur cathode  $> 1000 \text{ mAh g}^{-1}$  using new solid additives or developed new electrolyte ( $> 1 \text{ mS cm}^{-1}$ , at  $25^\circ\text{C}$ ). (Q2, FY 2020; Completed, March 31, 2020)
3. Demonstrate sulfur cathode with  $> 1000 \text{ mAh g}^{-1}$  using optimized carbon materials. (Q3, FY 2020; Completed, June 30, 2020)
4. Demonstrate sulfur cathode with  $> 1000 \text{ mAh g}^{-1}$  at  $0.3 \text{ C}$  for 50 cycles at  $60^\circ\text{C}$ . (Q4, FY 2020; In progress)

## Progress Report

This quarter, the team continued work on developing new SE introducing nitrogen and aluminum in the basic  $\text{Li}_2\text{S-P}_2\text{S}_5$  SE system. They were investigating a new SE system,  $65\text{Li}_2\text{S-}65\text{Li}_2\text{S-}26\text{P}_2\text{S}_5\text{-}10\text{Li}_3\text{N-xAl}_2\text{S}_3$  (LPSNAI-x). The glass-type SE was synthesized by conventional ball milling approach. The XRD spectra of the synthesized material is depicted in Figure 50a. Peaks representing  $\text{Al}_2\text{S}_3$  are observed only when x is above 14. For the other compositions, no crystalline peaks are observed. The ionic conductivity of the synthesized glass-type SE at 25°C is summarized in Figure 50b. Highest ionic conductivity of above  $0.7 \text{ mS cm}^{-1}$  is achieved when  $x = 10$ . When x is above 14, significant ionic conductivity decay is observed due to the  $\text{Al}_2\text{S}_3$  residuals. Next quarter, the team will try to anneal the samples at high temperature to synthesize glass-ceramic SEs and evaluate their ionic conductivity.

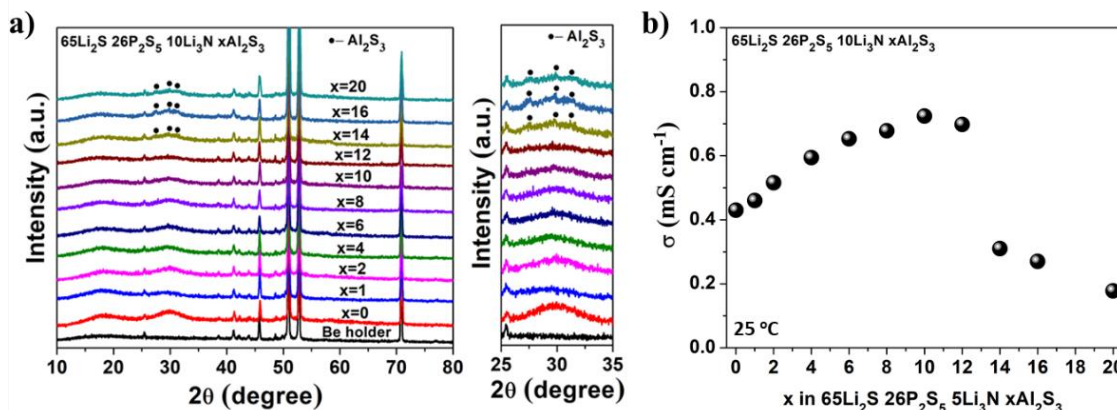


Figure 50. (a) X-ray diffraction spectra. (b) Ionic conductivity at 25°C and activation energy of various  $65\text{Li}_2\text{S-}65\text{Li}_2\text{S-}26\text{P}_2\text{S}_5\text{-}10\text{Li}_3\text{N-xAl}_2\text{S}_3$  (LPSNAI-x) glass-type solid electrolyte ( $x = 0 - 20$ ).

The team also continued investigating inorganic solid additives,  $\text{TiS}_2$ . The rate performance of the prepared sulfur cathode with  $\text{TiS}_2$  additives is shown in Figure 51. It was found that with  $\text{TiS}_2$  addition ( $\sim 0.38 \text{ wt\%}$  in the cathode) to replace SE (LPS), rate performance and sulfur utilization of sulfur cathode was greatly improved. At 0.1 C, specific capacity of sulfur cathode could be increased from around  $1200 \text{ mAh g}^{-1}$  to  $1400 \text{ mAh g}^{-1}$  with the help of  $\text{TiS}_2$  addition. The results for sulfur cathode without  $\text{TiS}_2$  addition were reported during the first quarter. The sulfur content of the cathode is around 39 wt%, and the test was performed at 60°C using  $75\text{Li}_2\text{S-}25\text{P}_2\text{S}_5$  (LPS) glass type SE. The team is trying to increase sulfur content in the cathode, investigate fundamental working mechanism of  $\text{TiS}_2$ , and identify other inorganic solid additives for future study.

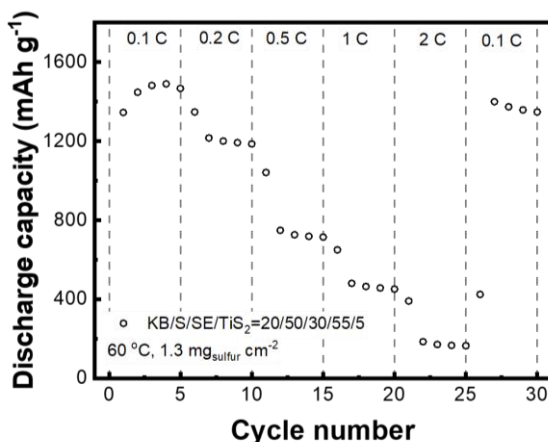


Figure 51. Rate performance of sulfur cathode with  $\text{TiS}_2$  additive.

Besides synthesizing new SEs, the team also optimized carbon materials for sulfur cathode (carbon : sulfur : solid electrolyte = 20 : 50 : 30, weight ratio) and optimized cathode preparation parameters. Various commercial carbon additives, including Super-C carbon, Ketjen Black EC-600J (KB), carbon nanofiber and other carbon materials have been tested. It was found that sulfur cathode using KB showed best electrochemical performance, with the best result summarized in Figure 52. The prepared sulfur cathode was paired with Li-In alloy and cycled between 0.8 V to 2.5 V at 60°C. LPS glass type SE prepared by wet ball milling approach was used as SE. Initial discharge specific capacity of the cathode at 0.1 C could reach around 1470 mAh g<sup>-1</sup>. Even at 0.5 C, the discharge capacity could reach over 880 mAh g<sup>-1</sup>. Such superior performance meets the target for this quarter and also meets the proposed milestone for optimizing carbon material for all-solid-state sulfur cathode.

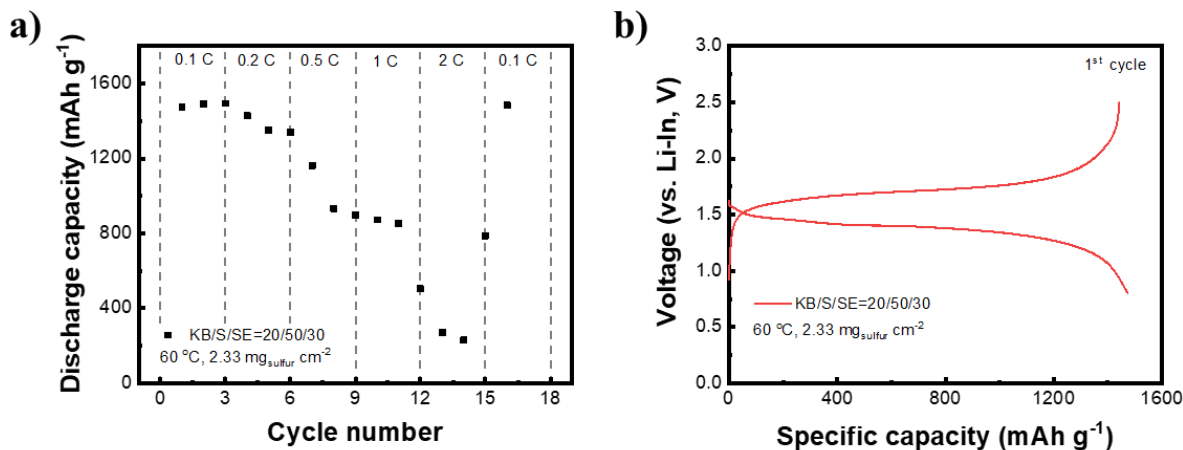


Figure 52. (a) Rate performance and (b) corresponding voltage profile at 1<sup>st</sup> cycle of sulfur cathode using Ketjen Black EC-600J (KB) as carbon additive.

## Patents/Publications/Presentations

The project has no patents, publications, or presentations to report this quarter.

## TASK 2 – DIAGNOSTICS

### Summary and Highlights

To meet the goals of the VTO programs on next-generation EVs, low-cost and abuse-tolerant batteries with higher energy density, higher power density, better safety, and longer lifetimes are needed. In pursuit of these goals, high cell operating voltages and demanding cycling conditions are used, which leads to unprecedented chemical and mechanical instabilities in cell components. Successful implementation of promising electrode materials (such as silicon anode and high-voltage cathodes) and new cell chemistry (such as high-energy Li-metal cells combined with SSEs) requires better understanding of fundamental processes, especially those at the interface/interphase of both anode and cathode. Identifying and understanding structure-property-electrochemical performance relationships in materials and various failure modes in cell chemistry are therefore more pressing than ever, not only in guiding battery development activities but also the scale-up efforts needed for commercialization.

Task 2 takes on these challenges by combining model systems, *ex situ*, *in situ*, and *operando* approaches, with an array of state-of-the-art analytical and computational tools. Numerous subtasks are tackling the chemical processes and reactions at the electrode/electrolyte interfaces in Li-metal batteries. Researchers at LBNL use surface- and bulk-sensitive techniques, including FTIR, attenuated total reflectance (ATR)-FTIR, near-field infrared (IR) and Raman spectroscopy/microscopy, and scanning probe microscopy (SPM) to characterize changes in materials and the physio-chemical phenomena occurring at the interface of Li-metal electrode. GM is developing *in situ* diagnostic techniques, including atomic force microscopy (AFM), nano-indentor, dilatometer, and stress-sensor, to be combined with atomic/continuum modeling schemes to investigate the coupled mechanical/chemical degradation of the SEI layer as well as the microstructural evolution at the interface/interphase of Li-metal anode. ANL aims to develop high-conductivity ceramic electrolytes through cation doping and identify mechanistic barriers that limit the chemical/mechanical/electrochemical durability of the solid/solid interfaces. University of Houston (UH) is developing multidimensional diagnostic tools, including FIB-SEM, TOF-SIMS, and in-SEM nanoindentation, to probe structural, chemical, and mechanical evolution at the interfaces of SSLBs. At LBNL, model systems of electrode, SSE, and their interfaces with well-defined physical attributes are being developed and used for advanced diagnostic and mechanistic studies at both bulk and single-particle levels. These controlled studies remove the ambiguity in correlating a material's physical properties and reaction mechanisms to its performance and stability, which is critical for further optimization. Subtasks at BNL and PNNL focus on the understanding of fading mechanisms in electrode materials, with the help of synchrotron-based X-ray techniques (diffraction and hard/soft X-ray absorption) at BNL and HRTEM / scanning transmission electron microscopy (STEM) and related spectroscopy techniques at PNNL. The final subtask at Stanford/SLAC develops and utilizes an integrated X-ray characterization toolkit to investigate and generate insights on SSBs, by tracking the evolution of nanoscale chemistry as well as structure, microstructure, and transport properties. The diagnostics team not only produces a wealth of knowledge that is key to development of next-generation batteries, it also advances analytical techniques and instrumentation that have a far-reaching effect on material and device development in various fields.

**Highlights.** The highlights for this quarter are as follows:

- Stanford University/SLAC National Accelerator Laboratory (Y. Cui / W. Chueh / M. Toney) team developed characterization approaches to evaluate the variations in SSE electronic conductivity as a function of location as well as electrochemical cycling.
- The UH (Y. Yao) group developed an air-free transfer vessel equipped with a cell testing platform suitable for *in situ* measurements carried out in various analytical instruments.

## Task 2.1 – Characterization and Modeling of Li-Metal Batteries: Model-System Synthesis and Advanced Characterization (Guoying Chen, Lawrence Berkeley National Laboratory)

**Project Objective.** This project will use a rational, non-empirical approach to design and develop SSE materials and interfaces for next-generation Li-metal batteries. Combining a suite of advanced diagnostic techniques with carefully prepared model-system samples, the project will perform systematic studies to achieve the following goals: (1) obtain understanding on the role of SSE grain and GBs on ion conduction and dendrite formation, (2) obtain fundamental knowledge on rate- and stability-limiting properties and processes in SSEs when used in Li-metal batteries, (3) investigate the reactivities between SSE and electrodes and gain insights on the dynamic evolution of the interfaces, and (4) design and synthesize improved SSE materials and interfaces for safer and more stable high-energy Li-metal batteries.

**Impact.** The project will focus on fundamental understanding of SSE and relevant interfaces to enable its use in Li-metal batteries. Knowledge gathered from model-system based studies will guide the design and engineering of advanced materials and interfaces. The use of the non-empirical, rational-design approach will develop high-energy battery systems with improved commercial viability.

**Approach.** The project will combine model-system synthesis and advanced diagnostic studies to investigate ion conduction and interfacial chemistry of SSE in Li-metal batteries. Single crystalline, polycrystalline, and amorphous model SSE samples with various grain and GB properties will be synthesized. Model interfaces between the SSE and electrodes with controlled properties will also be developed. Both bulk-level and single-grain level characterization will be performed. Global properties and performance of the samples will be established from the bulk analyses, while the single-grain-based studies will utilize time- and spatially-resolved analytical techniques to probe the intrinsic redox transformation processes and failure mechanisms under battery operating conditions.

**Out-Year Goals.** In the out-years, the project will deliver fundamental knowledge on the role of SSE microstructure in Li<sup>+</sup> conduction and lithium dendrite formation/propagation. Insights on performance-limiting physical properties and phase transition mechanisms as well as dynamic evolution of SSE/electrode interfaces will be obtained. Mitigating approaches, such as use of surface coating or “buffer layer” in stabilizing SSE/electrode interfaces, will be evaluated. Further, advanced SSE materials and interfaces for improved high-energy Li-metal batteries will be designed and synthesized.

**Collaborations.** This project collaborates with the following PIs: G. Ceder, K. Persson, M. Doeff, B. McCloskey, R. Kostecki, and R. Prasher (LBNL); W. Yang (Advanced Light Source, ALS); D. Nordlund and Y. Liu (Stanford Synchrotron Radiation Lightsource, SSRL); C. Wang (PNNL); and J. Nanda (Oak Ridge National Laboratory, ORNL).

### Milestones

1. Develop model systems suitable for studying the impact of SSE grain and GBs in Li-metal based batteries. (Q1, FY 2020; Completed)
2. Synthesize model SSE samples with various grain and GB characteristics. (Q2, FY 2020; Completed)
3. Advanced diagnostic studies of SSE model samples at both particle-level and bulk-sample level. (Q3, FY 2020; On schedule)
4. Obtain understanding on SSE grain and GB chemistry, properties, and their effect on ion conduction and dendrite formation. (Q4, FY 2020; On schedule)

## Progress Report

To get a better understanding on the role of SSE grains, GB chemistry, and properties in ion conduction and interfacial behavior, synthesis and evaluation of SSE model systems continued this quarter. Halide SSEs with a general formula of  $\text{Li}_3\text{MX}_6$  ( $\text{M} = \text{Sc}, \text{Y}, \text{In}, \text{Er}; \text{X} = \text{Cl}, \text{Br}$ ) were recently shown to have a very high room-temperature ionic conductivity of up to  $10^{-2}$  S/cm, a wide electrochemical stability window of up to 6 V, and good stability toward oxide cathode materials. Compared to the sulfide SSEs such as  $\text{Li}_3\text{PS}_4$  (LPS), the halides are generally more stable toward air exposure as well as high-voltage conditions at the cathode. On the other hand, halide SSEs have higher ionic conductivities, and they are much softer compared to the oxide SSEs such as LLZO.

Here, the feasibility of synthesizing one of the most promising halide SSEs in the class,  $\text{Li}_3\text{InCl}_6$ , with different grain morphology and properties was evaluated. As shown in Figure 53a, in  $\text{InCl}_3$  chloride anions form a closed packed O3 lattice and occupy the octahedral sites. In  $\text{Li}_3\text{InCl}_6$ ,

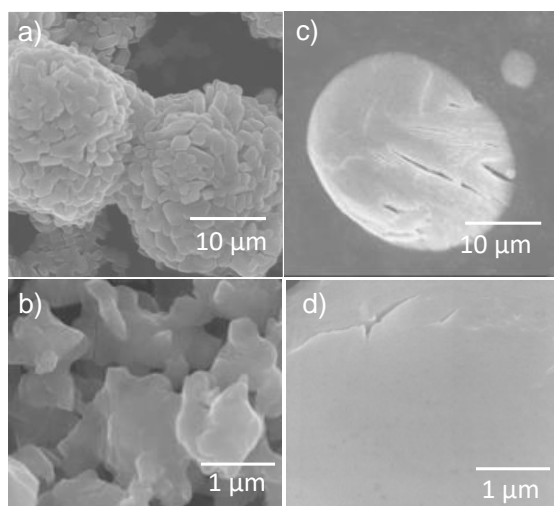


**Figure 54.** Scanning electron microscopy images of secondary-particle  $\text{Li}_3\text{InCl}_6$  sample (a/b) and single-grain  $\text{Li}_3\text{InCl}_6$  sample (c/d) synthesized by mechanical ball milling.

obtained values are slightly higher in the single-grain sample, at approximately  $2.8 \times 10^{-4}$  S/cm as compared to  $2.5 \times 10^{-4}$  S/cm for the secondary-particle sample.

It is well-known that in softer sulfide SSEs such as LPS, crystallinity often plays a critical role in  $\text{Li}^+$  transport, largely due to the effect of chemical bonding and atomic arrangements on ion mobility. Here, the synthesized secondary-particle  $\text{Li}_3\text{InCl}_6$  sample was further annealed in a vacuum-sealed quartz ampoule at  $300^\circ\text{C}$  for 6 hours. Even at the relatively low heating temperature, annealing largely fuses the primary

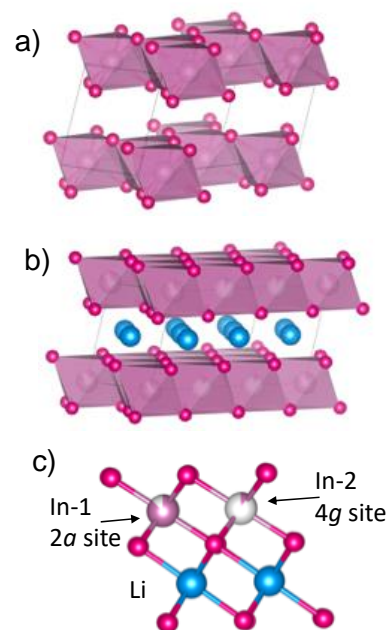


**Figure 53.** Crystal structure of (a)  $\text{InCl}_3$  and (b)  $\text{Li}_3\text{InCl}_6$ . (c) Atomic arrangement of indium and chlorine in  $\text{Li}_3\text{InCl}_6$ .

$\text{Li}^+$  cations are located at the octahedral sites to form the layered  $C/2m$ -like structure with distinct lithium layers (blue color, Figure 53b). Most  $\text{In}^{3+}$  cations are located at the  $2a$  sites,

with the rest at the  $4g$  sites (Figure 53c). By simply adjusting high-energy ball milling time, glassy  $\text{Li}_3\text{InCl}_6$  with the same average size of  $\sim 20 \mu\text{m}$ , but two types of grain morphologies, was synthesized. Secondary particles composed of sub-micron primary particles and distinct GBs (Figure 54a-b) were obtained after 36 hours, while large single grains in the absence of clear GBs (Figure 54c-d) were obtained after 24 hours. Room-temperature ionic conductivities of the  $\text{Li}_3\text{InCl}_6$  samples were measured by using stainless-steel (SS) blocking electrodes in EIS. The

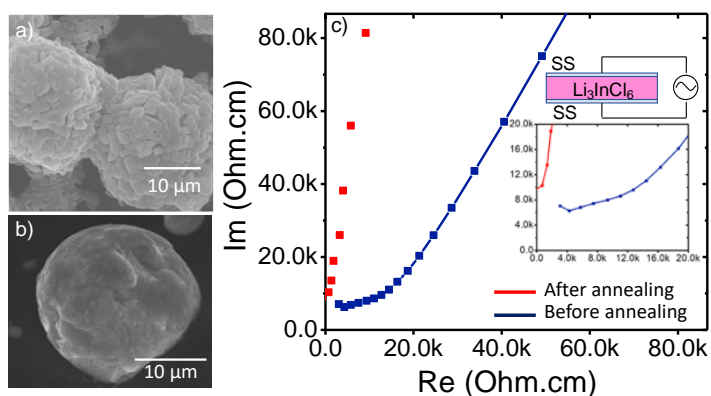


**Figure 55.** Scanning electron microscopy images of secondary-particle  $\text{Li}_3\text{InCl}_6$  sample before (a) and after (b) annealing. (c) Comparison of electrochemical impedance spectroscopy Nyquist plots of the samples.

particles within the grains and increases sample crystallinity, as shown in the SEM images before (Figure 55a) and after (Figure 55b) annealing. Comparison on Nyquist plots obtained from blocking-electrode EIS measurements are also shown in Figure 55c. The room-temperature conductivity of the secondary-particle  $\text{Li}_3\text{InCl}_6$  sample increased from  $2.5 \times 10^{-4}$  to  $1.5 \times 10^{-3}$  S/cm after annealing, suggesting the significant role of crystallinity and GBs in Li-ion conduction in halide SSEs.

## Patents/Publications/Presentations

### Publications

- Chen, D., J. Wu, J. K. Papp, B. D. McCloskey, W. Yang, and G. Chen. “Role of Redox-Inactive Transition-Metals in the Behavior of Cation-Disordered Rocksalt Cathodes.” *Small* 2000656 (2020). doi: 10.1002/sml.202000656.
- Zou, L., Y. He, Z. Liu, H. Jia, J. Zhu, J. Zheng, G. Wang, X. Li, J. Xiao, J. Liu, J-G. Zhang, G. Chen, and C. Wang. “Unlocking the Passivation Nature of the Cathode-Air Interfacial Reactions in Lithium-Ion Batteries.” *Nature Communications* (2020). doi: 10.1038/s41467-020-17050-6.
- Ahn, J., D. Chen, and G. Chen. “A Fluorination Method for Improving Cation-Disordered Rocksalt Cathode Performance.” *Advanced Energy Materials* (2020). Accepted.
- Zhu, J., S. Sharifi-Asl, J. C. Garcia, H. H. Iddir, J. R. Croy, R. Shahbazian-Yassar, and G. Chen. “Atomic-Level Understanding of Surface Reconstruction Based on  $\text{Li}[\text{Ni}_x\text{Mn}_y\text{Co}_{1-x-y}]\text{O}_2$  Single-Crystal Studies.” *ACS Applied Energy Materials* (2020). doi: 10.1021/acsaem.0c00411.
- Garcia, J. C., J. Bareño, G. Chen, J. R. Croy and H. Iddir. “Facet-Dependent Surface Reconstruction and Cation Segregation in Layered  $\text{Li}(\text{Ni}_{1-x-y}\text{Mn}_x\text{Co}_y)\text{O}_2$  (NMC) Cathode Materials.” (2020). Submitted.

## Task 2.2 – Interfacial Processes – Diagnostics (Robert Kostecki, Lawrence Berkeley National Laboratory)

**Project Objective.** The objective of the proposed research is to establish specific design rules toward the next generation of low impedance Li-metal rechargeable batteries that are capable of performing 1000 deep discharge cycles at CE > 99.9% and suppress lithium dendrites formation at high current densities (> 2 mA/cm<sup>2</sup>). This project aims at the following: (1) establishing general rules between Li<sup>+</sup> transport properties in novel liquid/solid electrolytes, and (2) determining the mechanism of the SEI layer (re)formation. The other goal is development and application of far- and near-field optical probes and synchrotron-based advanced X-ray techniques to obtain insight into the mechanism of Li<sup>+</sup> transport and interfacial reactions in lithium/liquid model systems. Through an integrated synthesis, characterization, and electrochemistry effort, this project aims to develop a better understanding of lithium / liquid electrolyte interface so that rational decisions can be made as to their further development into commercially viable Li-metal cells.

**Project Impact.** Chemical instability and high impedance at the interface of Li-metal electrodes limits electrochemical performance of high-energy-density batteries. A better understanding of the underlying principles that govern these phenomena is inextricably linked with successful implementation of high-energy-density materials in Li-metal-based cells for PHEVs and EVs. New state-of-the-art techniques to identify, characterize, and monitor changes in materials structure and composition that take place during battery operation and/or storage will be developed and made available to the Program participants. The proposed work constitutes an integral part of the concerted effort within the BMR Program, and it supports development of new electrode materials for high-energy, Li-metal-based rechargeable cells.

**Approach.** The pristine and cycled composite electrode and model thin-film electrodes will be probed using various surface- and bulk-sensitive techniques, including FTIR, ATR-FTIR, near-field IR and Raman spectroscopy/microscopy, and SPM to identify and characterize changes in materials structure and composition. Novel *in situ* / *ex situ* far- and near-field optical multi-functional probes in combination with standard electrochemical and analytical techniques are developed to unveil the structure and reactivity at interfaces and interphases that determine materials electrochemical performance and failure modes.

**Out-Year Goals.** In the out-years, the project aims to achieve the following: (1) understand factors that control performance and degradation processes, (2) unveil structure and reactivity at hidden or buried interfaces and interphases that determine electrochemical performance and failure modes, and (3) propose effective remedies to address inadequate Li-metal-based battery calendar/cycle lifetimes for PHEV and EV applications.

**Collaborations.** The diagnostic studies will be carried out in sync with other diagnosticians (G. Chen, B. McCloskey, R. Prasher, and L-W. Wang) and theory and computational scientists (G. Ceder and K. Persson).

### Milestones

1. Develop novel experimental approach(es) suitable for studying Li/electrolyte interfaces. (Q1, FY 2020; Completed)
2. Manufacture model thin-film lithium model electrodes for *ex situ* and *in situ* fundamental studies of Li/electrolyte interfaces. (Q2, FY 2020; In progress)
3. Characterize chemistry of Li/electrolyte with *ex situ* near-field IR, XAS, and XPS. (Q3, FY 2020; In progress)
4. Gain preliminary insights into SEI composition and reaction pathways for baseline electrolytes. Propose first approximative reaction scheme. (Q4, FY 2020; In progress)

## Progress Report

This quarter, the team enclosed the state-of-the-art near-field Fourier transform infrared nanospectroscopy (nano-FTIR) system within a custom-built glovebox atop a floating optical table. While the table works to suppress vibrations to maximize nano-FTIR signal-to-noise, the enclosure supports pressure differential purging to establish either nitrogen or argon atmospheres that enable nano-FTIR measurements of air sensitive Li-rich samples. The environment inside the enclosure has proven to be free enough of moisture to allow high-quality nano-FTIR measurements of a model graphene-SSE interface with nanoscale resolution. The model solid-state full cell device consists of graphene on SSE on lithium (which operates as a counter electrode and lithium provider during electrochemical processes, as well as a physical support for the SSE). This novel and unique experimental setup provides a pathway for *in situ* nondestructive nanoscale chemical identification of materials that exist at (within) the electrode/electrolyte interface (interphase). The team notes in passing that this method is compatible for both SSE and gel state electrolytes.

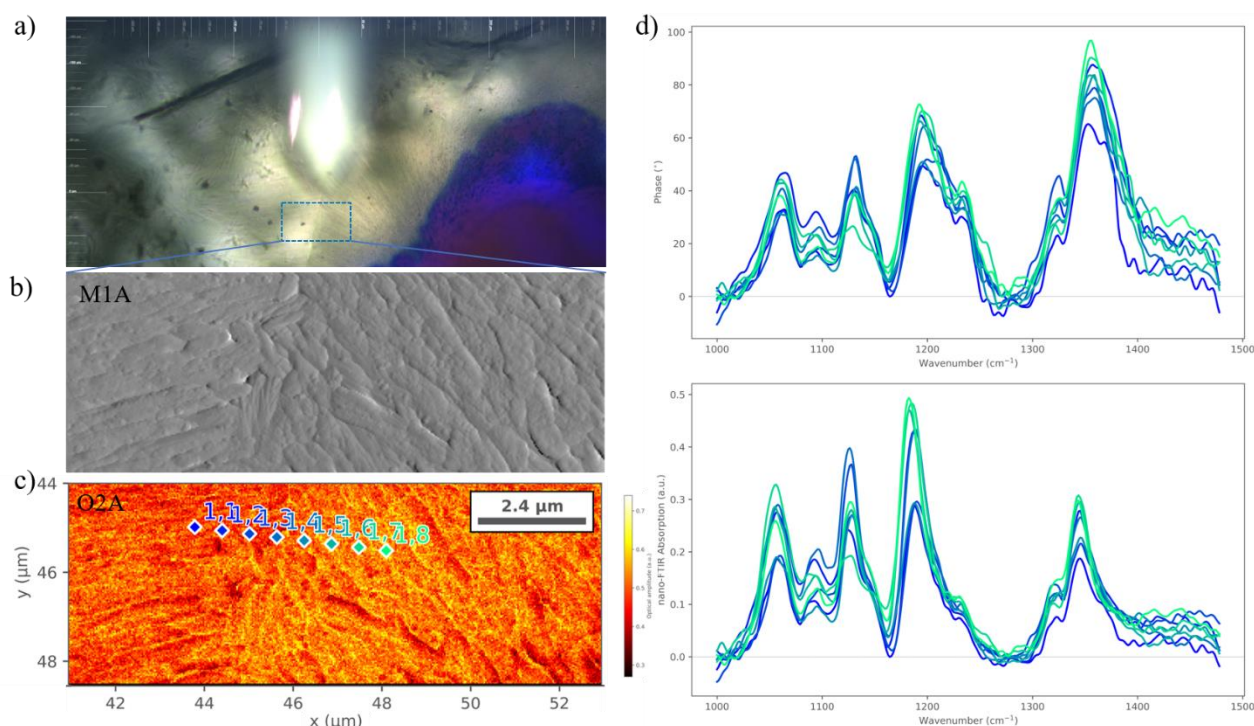


**Figure 56.** (a) Optical image of the top of the solid-state full cell device. The blue inset highlights the spatial region to be studied, which has both exposed solid-state electrolyte (SSE) (PEO+ LiTFSI mixtures at EO/Li ratios of 10:1) on the left and graphene-capped SSE on the right. (b) Topography data collected within the blue inset in panel (a). (c) White light infrared imaging (second harmonic of the optical amplitude) collected simultaneously with the data in panel (b). The brighter region on the right-hand side is graphene-capped SSE. (d) Spatially dependent nano-FTIR spectra whose color coordinates to the similarly colored diamonds in varied spatial locations displayed in panel (c).

Figure 56a shows an optical image of a selected area that highlights the boundary between the exposed SSE and graphene window. The former appears lighter and is located in the left-hand side of the inset blue box, while the latter appears darker and is in the right-hand side. Blue ink was used as a visual marker to locate the area of interest in low magnification. The representative topography data (Figure 56b) provides an image of the boundary region. Analysis of the infrared amplitude image (Figure 56c) reveals that the graphene window region yields a 7% greater infrared response in comparison to the exposed SSE region. This is likely due to the relative increase in electrical conductivity. Spatially dependent nano-FTIR measurements (Figure 56c-d) reveal intensity differences due to nanoscale spatial inhomogeneities in the SSE mixture. Future work will focus on other *in situ* characterizations under varied electrochemical states. This work concludes efforts toward Milestone 4.

## Patents/Publications/Presentations

The project has no patents, publications, or presentations to report this quarter.

## Task 2.3 – Advanced *In Situ* Diagnostic Techniques for Battery Materials (Xiao-Qing Yang and Seong-Min Bak, Brookhaven National Laboratory)

**Project Objective.** The primary objective of this project is to develop new advanced *in situ* material characterization techniques and to apply these techniques to support development of new cathode and anode materials with high energy and power density, low cost, good abuse tolerance, and long calendar and cycle life for beyond Li-ion battery systems to power PHEVs and battery electric vehicles (BEVs). The diagnostic studies will focus on issues relating to capacity retention, thermal stability, cycle life, and rate capability of beyond Li-ion battery systems.

**Project Impact.** The VTO Multi-Year Program Plan describes the goals for battery: “Specifically, lower-cost, abuse-tolerant batteries with higher energy density, higher power, better low-temperature operation, and longer lifetimes are needed for development of the next-generation of HEVs, PHEVs, and EVs.” The knowledge gained from diagnostic studies through this project will help U. S. industries develop new materials and processes for next-generation Li-ion batteries in the effort to reach these VTO goals.

**Approach.** This project will use the combined synchrotron-based *in situ* X-ray techniques (XRD; and hard and soft XAS) with other imaging and spectroscopic tools such as HRTEM and MS to study the mechanisms governing performance of electrode materials.

**Out-Year Goals.** In the out years, the project will complete development of diagnostic techniques using X-ray pair distribution function (*x*-PDF), XRD, and XAS combined with neutron diffraction and neutron PDF (*n*-PDF), as well as STEM imaging and transmission X-ray microscopy (TXM) for cathode materials studies. It will then apply these techniques to study the structural changes of various new cathode and anode materials.

**Collaborations.** The BNL team will work closely with material synthesis groups at ANL (Drs. Y. Shin and K. Amine) for the high-energy composite, at PNNL for the S-based cathode and Li-metal anode materials, and with ORNL on neutron scatterings. This project will also collaborate with industrial partners at GM and Johnson Controls, as well as with international collaborators.

### Milestones

1. Complete the first-stage development of diagnostic techniques to study and improve performance of high-energy-density Li-ion batteries and Li/S batteries. (Q1, FY 2020; Completed)
2. Complete hard XRF imaging on the concentration gradient Ni-rich NCM cathode particles in a noninvasive manner with 3D reconstructed images through tomography scans to study the 3D nickel, cobalt, and manganese elemental distribution from surface to the bulk. (Q2, FY 2020; Completed)
3. Complete hard X-ray absorption spectroscopy (hXAS) and soft XAS (sXAS) on the concentration gradient Ni-rich NCM cathode particles to study the valence state changes of nickel, cobalt, and manganese at the surface and bulk. (Q3, FY 2020; Completed)
4. Complete spatially resolved XAS at sulfur K-edge and imaging of sulfur-based chemical species using XRF on the Li-metal anode in a cycled high-energy Li/S pouch cell. (Q4, FY 2020; In progress)

## Progress Report

This quarter, the third milestone was completed, and progress on other milestones was made. BNL has been focusing on developing new diagnostic techniques to study and provide valuable information for improving performance of high-energy-density Li-ion batteries and Li/S batteries. The BNL team has applied advanced hXAS and sXAS on concentration gradient Ni-rich NCM (CG-NCM) cathode particles to study valence state changes of nickel, cobalt, and manganese at surface and bulk caused by multiple cycling. No noticeable differences were observed in spectra both of nickel and manganese K-edge hXAS after different numbers of cycles (Figure 57a), indicating the averaged valence state of nickel and manganese at the same state of charge (SOC) was not changed much by cycling for both normal and CG-NCM-622. The total electron yield (TEY) of nickel and manganese L-edge sXAS representing surface valence state and partial fluorescence yield (PFY) spectra reflecting bulk valence state of nickel and manganese are shown in Figure 57b. The TEY spectra show clear cycling induced changes, while the PFY spectra show no cycling induced changes, as similarly observed in hXAS spectra. More quantitative comparisons using linear combination fitting (LCF) of the sXAS spectra are shown in Figure 57c-d. Gradual reduction of surface Ni to  $\text{Ni}^{2+}$  was observed in the normal NMC-622. It is commonly believed that the surface structural degradation is associated with formation and propagation of inactive rock-salt structured NiO from the surface to bulk. In contrast, the level of surface nickel valence state in the CG-NMC-622 shows a gradual increase, rather than decrease, indicating the electrochemically active  $\text{Ni}^{3+}$  contribution was increased and reached to the average valence state (*ca.*  $\text{Ni}^{2.7+}$ ) of the bulk (Figure 57c). This result originates from the valence state change of surface manganese. The LCF fit of TEY spectra for manganese L-edge reveals that the surface manganese was reduced from 4+ to 2+ in both normal and CG NMC cathode (Figure 57d). Due to the large portion of surface manganese content in the shell of CG-NMC-622 (surface shell composition: NMC-442), manganese reduction from  $\text{Mn}^{4+}$  to  $\text{Mn}^{2+}$  leads to the increase of nickel valence state to keep the charge neutrality. In contrast, the effect of manganese reduction is much smaller in the normal NMC-622 cathode, due to the low content of manganese at the surface. This result demonstrates that the Mn-rich surface of CG-NMC-622 could suppress formation of the inactive NiO phase with  $\text{Ni}^{2+}$  at the surface and improve cycle performance.

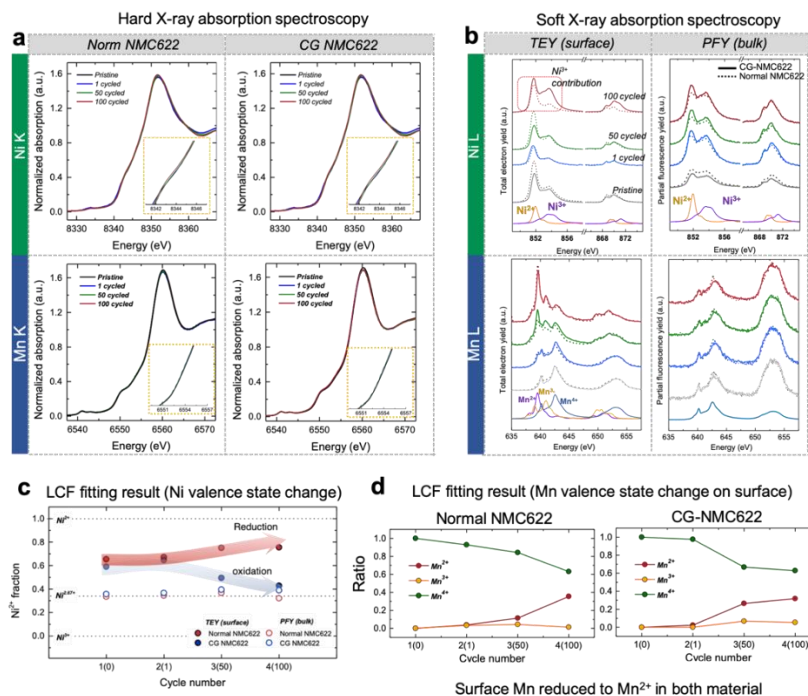


**Figure 57.** (a) Nickel and manganese K-edge hard X-ray absorption spectroscopy (hXAS) spectra. (b) Total electron yield (TEY) and partial fluorescence yield (PFY) of nickel and manganese L-edge soft X-ray absorption spectroscopy (sXAS). (c) Linear combination fitting (LCF) results for TEY and PFY of nickel L-edge spectra. (d) LCF results for TEY of manganese L-edge spectra.

## Patents/Publications/Presentations

### Publications

- Jiang, Q., P. Xiong, J. Liu, Z. Xie, Q. Wang, X-Q. Yang, E. Hu,\* Y. Cao, J. Sun, Y. Xu,\* and L. Chen.\* “A Redox-Active 2D Metal-Organic Framework for Efficient Lithium Storage with Extraordinary High Capacity.” *Angewandte Chemie* 132 (2020): 5311–5315. Publication Date (Web): March 23, 2020.
- Cui, C., X. Fan, X. Zhou, J. Chen, Q. Wang, L. Ma, C. Yang, E. Hu, X-Q. Yang, and C. Wang. “Structure and Interface Design Enable Stable Li-Rich Cathode.” *Journal of the American Chemical Society* 142, no. 19 (2020): 8918–8927. doi: 10.1021/jacs.0c02302. Publication Date (Web): April 22, 2020.
- Wang, X., X. Fan, X. Yu, S. Bak, Z. Shadik, I. Waluyo, A. Hunt, S. D. Senanayake, H. Li, L. Chen, C. Wang, R. Xiao, E. Hu, and X-Q. Yang. “The Role of Electron Localization on Covalency and Electrochemical Properties of Lithium-Ion Battery Cathode Materials.” *Advanced Functional Materials*. doi: 10.1002/adfm.202001633. Publication Date (Web): May 13, 2020.
- Luo, C., E. Hu, K. J. Gaskell, X. Fan, T. Gao, C. Cui, S. Ghose, X-Q. Yang, and C. Wang. “A Chemically Stabilized Sulfur Cathode for Lean Electrolyte Lithium Sulfur Batteries.” *Proceedings of the National Academy of Sciences of the United States of America (PNAS)* 117, no. 26 (2020): 14712–14720. doi: 10.1073/pnas.2006301117. Publication Date (Web): June 17, 2020.
- Li, Z., A. Li, H. Zhang, R. Lin, T. Jin, Q. Cheng, X. Xiao, W-K. Lee, M. Ge, H. Zhang, A. Zangiabadi, I. Waluyod, A. Hunt, H. Zhai, J. J. Borovilas, P. Wang, X-Q. Yang, X. Chun, and Y. Yang. “Interfacial Engineering for Stabilizing Polymer Electrolytes with 4V Cathodes in Lithium Metal Batteries at Elevated Temperature.” *Nano Energy* 72 (2020): 104665. doi: 10.1016/j.nanoen.2020.104655. Publication Date (Web): June 2020.

### Presentation

- The Minerals, Metals, and Materials Society (TMS) Annual Meeting, San Diego, California (February 24, 2020): “Multi-Modal and Multi-Length-Scale Characterization of Composition Graded Ni-Rich Layered Oxide Cathode Materials”; S-M. Bak,\* Y. Shin, and X-Q. Yang. Invited.

## Task 2.4 – Probing Interfacial Processes Controlled Electrode Stability in Rechargeable Batteries (Chongmin Wang, Pacific Northwest National Laboratory)

**Project Objective.** The main objective of the proposed research is to explore interfacial phenomena in rechargeable Li-ion batteries of both solid-state and LE configuration, to identify the critical parameters that control the stability of interface and electrodes as well as SE. The outcome will be establishing correlations between structural-chemical evolution of active components of batteries and their properties. These correlations will provide insight and guidance to battery materials development groups for developing high-performance battery materials.

**Project Impact.** The proposed characterization work focuses on atomic-level structural and chemical analysis and direct correlation with battery fading properties. The work can be directly used to guide design of electrode materials with tailored microstructure and chemistry for enhanced properties of increasing the energy density of Li-ion batteries and to accelerate market acceptance of EVs, especially for PHEVs as required by the EV Everywhere Grand Challenge.

**Approach.** The project will use integrated advanced microscopic and spectroscopic techniques, including *in situ* S/TEM and *ex situ* S/TEM, environmental S/TEM, cryo-electron microscopy, and *in situ* liquid SIMS to directly probe the structural and chemical information during lithium deposition and stripping. Cryo-S/TEM with analytical tools, such as EDS and EELS, will be used to gain chemical and electronic structural information at the interface between lithium metal and electrolyte of both solid-state and liquid configuration, which will allow direct correlation between the morphology and chemistry. STEM – high-angle annular dark-field (HAADF) atomic-level imaging and EDS/EELS will be used to probe the interface and bulk lattice stability. The work will be in close collaboration with the battery development group within the BMR and U. S.–Germany Collaboration on Energy Storage.

**Out-Year-Goals.** This project has the following out-year goals:

- Atomic-level multi-scale *ex situ* / *in situ* and *operando* TEM and cryo-TEM investigation of failure mechanisms of energy-storage materials and devices; develop fundamental understanding of electrochemical energy-storage processes and kinetics of electrodes.
- Develop new *in situ* TEM capability for probing challenging questions related to energy storage technology.

**Collaborations.** This project collaborates with G. Chen (LBNL); J. Nanda (ORNL); K. Amine (ANL); D. Wang (PSU); A. Manthiram (UT Austin); W. Tong (LBNL); Y. Cui (Stanford University); J. Zhang (PNNL); J. Liu (PNNL); W. Xu (PNNL); X. Jie (PNNL); D. Lu (PNNL); X. Xiao (GM); S. Meng (UCSD); and M. S. Whittingham (State University of New York at Binghamton).

### Milestones

1. Integrate AFM cantilever into TEM column to *in situ* measure lithium dendrite growth force. (Q1, FY 2020; Completed)
2. Identify correlation of SEI structure and chemistry with electrolyte composition and electrochemical operating condition. (Q2, FY 2020; Completed)
3. Establish molecular signature of SEI formation process. (Q3, FY 2020; Completed)
4. Establish cathode stability in solid-state configuration. (Q4, FY 2020)

## Progress Report

A fundamental understanding of SEI is of paramount importance for controlling cycling performance of rechargeable Li-metal batteries. The structural and chemical evolution of SEI with respect to electrochemical operating condition remains barely established. Here, the team develops a unique method for imaging the evolution of SEI formed on the copper foil under sweeping electrochemical potential. They explore the fundamental mechanism of how the SEI evolves both structurally and compositionally on the positive potential change during the 1<sup>st</sup> charging cycle of batteries and compare the SEI formed on the lithium metal below overpotential.

The team combines advantages of cryo-TEM (high spatial resolution) and XPS (high chemical sensitivity) techniques to characterize the detailed structural and chemical evolutions of electrochemically formed SEI layers in the vinylene carbonate (VC)-free and VC-containing electrolytes, to establish correlation between the electrochemical potential and the VC additive induced SEI structural and chemical variations, as schematically shown in Figure 58.

As representatively shown in Figure 59, the team reveals that the SEI formed in the electrolyte of LiPF<sub>6</sub>/EC-EMC without VC additive is monolithic amorphous layer at the cut-off voltage of 1.0 V, and it changes to amorphous layer embedded with Li<sub>2</sub>O particles at 0 V. The SEI formed in the VC-containing electrolyte maintains amorphous layer embedded with Li<sub>2</sub>O particles from 1.0 V to 0 V. The SEI formed in VC-free electrolyte is thinner than that in VC-containing electrolyte at 1.0 V and then increases rapidly as the voltage decreases. The team directly reveals that the surface structure of copper foil (GB and twin boundary) influences the SEI formation process via regulating charge distribution. In addition, the SEIs formed on the surfaces of copper foil and lithium metal are different in composition. Associated with the localized charge modulation by the surface topographic feature and defects in the copper foil, the SEI layer shows direct spatial correlation with these structural defects in the copper. In addition, on

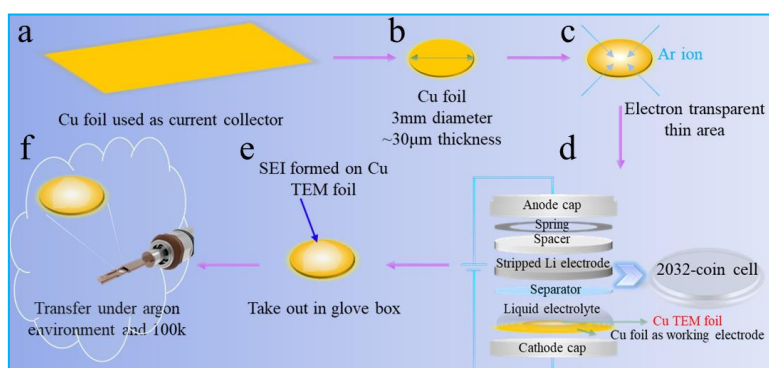


**Figure 58.** Schematic diagram of preserving and stabilizing SEI formed on copper current collector by cryo-TEM. (a) Commercial copper foil as current collector. (b) Copper foil with 3-mm diameter prepared from copper foil. (c) TEM copper foil prepared by precision ion polishing system. (d) Assembling TEM foil into coin cell. (e) Retrieved TEM copper foil from the coin cell in an argon-filled glovebox. (f) The TEM copper foil with SEI formed on is sealed in argon environment, plunged into liquid nitrogen, and then transferred to the cryo-TEM holder.

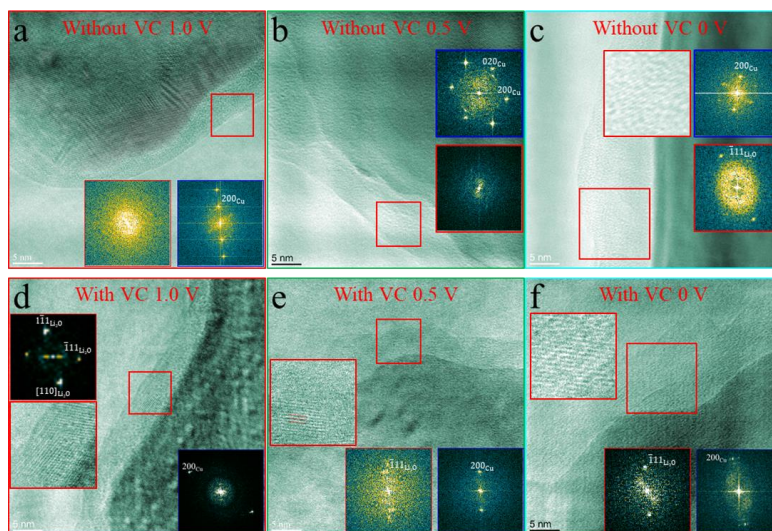


**Figure 59.** High-resolution transmission electron microscopy (HR-TEM) micrographs of SEI formed on TEM copper foil in the electrolytes without/with 5% vinylene carbonate (VC) additive. (a-c) High-magnification images of the SEI formed on TEM copper foil at different cut-off voltages of 1.0 V, 0.5 V, and 0 V in the electrolyte without VC additive. (d-f) High-magnification images of the SEI formed on TEM copper foil at different cut-off voltages of 1.0 V, 0.5 V, and 0 V in the electrolyte with VC additive. Insets: Fast Fourier transform patterns from SEI (red) and copper foil (blue).

lithium deposition, the SEI formed on the lithium metal has similar thickness with, but different composition from, the SEI formed on the copper foil at 0 V.

The results establish the correlation between the electrochemical potential and the structure of SEI layer formed on the copper foil in the electrolytes without/with VC additive, giving a complete picture of electrochemical SEI formation process. The team believes that these results will be critical for development of rationally designed SEI through electrolyte engineering for enhanced cycling stability of lithium metal.

## Patents/Publications/Presentations

### Publications

- Xu, Y., H. Wu, H. Jia, M. H. Engelhard, J-G. Zhang, W. Xu, and C. Wang. “Sweeping Potential Regulated Structural and Chemical Evolution of Solid-Electrolyte Interphase on Cu and Li as Revealed by Cryo-TEM.” *Nano Energy* 76 (2020): 105040.
- Zhou, Y., M. Su, X. Yu, Y. Zhang, J-G. Wang, X. Ren, R. Cao, W. Xu, D. R. Baer, Y. Du, O. Borodin, Y. Wang, X-L. Wang, K. Xu, Z. Xu, C. Wang, and Z. Zhu. “Real-Time Mass Spectrometric Characterization of the Solid–Electrolyte Interphase of a Lithium-Ion Battery.” *Nature Nanotechnology* 15 (2020): 224–230.
- Le, P. M. L., T. D. Vo, H. Pan, Y. Jin, Y. He, X. Cao, H. V. Nguyen, M. H. Engelhard, C. Wang, J. Xiao, and J-G. Zhang. “Excellent Cycling Stability of Sodium Anode Enabled by a Stable Solid Electrolyte Interphase Formed in Ether-Based Electrolytes.” *Advanced Functional Materials* (2020): 2001151.

## Task 2.5 – Integrated Atomic-, Meso-, and Micro-Scale Diagnostics of Solid-State Batteries (Yi Cui, William Chueh, and Michael Toney; Stanford University / SLAC National Accelerator Laboratory)

**Project Objective.** By developing a characterization toolkit that tackles length scales (Å to mm), cell pressure (1-100 bars), and dynamics (during synthesis, fabrication, and cycling), the project aims to generate insights to engineer SSBs for deployment in EVs. This interdisciplinary team aims to achieve this objective by merging a broad range of characterization approaches as well as modeling to track the evolution of nanoscale chemistry and structure, microstructure, and transport.

**Project Impact.** The project will have an impact in several areas: (1) accelerate rational design of coatings and artificial SEIs in SSBs; (2) inhibit the root causes leading to cell shorting, and enable high current cycling; (3) accelerate design of cathode coating and composite electrode architectures; and (4) reduce degradation and variability during SSB manufacturing via composition and surface engineering.

**Approach.** The project has a multi-fold approach that will encompass the following: (1) resolve nanoscale structure and chemistry of SEIs via cryo-TEM; (2) track SE and lithium microstructure evolution in 3D via X-ray micro and diffraction tomography; (3) visualize nanoscale ionic and electronic transport at GBs via conducting AFM; (4) map current distribution in cathodes via scanning transmission X-ray microscopy (STXM); and (5) monitor nanoscale SE evolution with gas impurity via *in situ* environmental TEM (E-TEM).

**Out-Year Goals.** The project will develop an integrated characterization toolkit to characterize SSBs within a single cycle and over hundreds of cycles, spanning a wide range of relevant length scales.

**Collaborations.** Project collaborations include work with SSRL, ALS, and Advanced Photon Source (APS) synchrotron light sources.

### Milestones

1. Design, build, and test *operando* SSB cell for depth-resolved XAS. (Q1, FY 2020; Completed)
2. Record micro-tomograms of Li/SE/Li half cells for 10 cycling conditions. (Q2, FY 2020; Completed)
3. Record DC conducting AFM map of pristine SEs. (Q3, FY 2020)
4. Prepare X-ray transparent cathode / SE by cryo-sectioning. (Q4, FY 2020)

## Progress Report

Electronic conduction in SEs has been suggested as failure mechanism, as it can lead to internal lithium deposition within the SE. For LLZO and LPS, the macroscopic electronic conductivity in as-synthesized pellets is negligibly small, typically about 5-7 orders of magnitude lower than the ionic conductivity. Therefore, it is difficult to imagine that such small conductivity could lead to short circuiting in SSBs. Here, the key assumption is that electronic conductivity is fixed and also homogenous. The team is developing several characterization approaches to test the validity of this assumption.

First, the team is examining the hypothesis that electronic conductivity is heterogenous. This quarter, they have demonstrated the conducting AFM is an effective tool to study local electronic conduction on LLZO. Specifically, they carried out a two-electrode measurement (in which one electrode is the conducting AFM tip) on a fractured LLZO surface in an argon glovebox. Atmosphere control is crucial since the formation of highly insulating lithium carbonate and other phases will mask the electronic conductivity in the SE. They have successfully recorded electronic conductance map on LLZO surface and are working on performing the same measurement on LPS, achieving the third quarter milestone.

Second, the team is examining the hypothesis that electronic conductivity is fixed. Specifically, there are evidences in literature indicating that electronic conductivity increases on cycling, presumably due to preferential reduction of the SE as lithium activity is lowered during lithium plating. To examine the electronic conduction, the team carries out Hebb-Wagner blocking electrode measurement on cycled LLZO and LPS. The SEs are exposed to different cycling conditions (cutoff voltages, in particular) and then the electronic conductivity is measured. Preliminary results show that the electronic conductivity can increase one to two orders of magnitude after cycling. Systematic experiments are being carried out to understand the evolution of electronic conductivity with cycling conditions.

## Patents/Publications/Presentations

The project has no patents, publications, or presentations to report this quarter.

## Task 2.6 – Investigating the Stability of Solid/Solid Interface (Zonghai Chen, Argonne National Laboratory)

**Project Objective.** The project objective is to characterize the physical/chemical properties of species at the solid/solid interfaces and to fundamentally understand the critical issues that limit the mechanical, chemical, and electrochemical stability of solid/solid interfaces at the cathode and the anode.

**Project Impact.** The project will lead to several areas of impact: (1) to generate knowledge that supports the rational design of materials and process development; (2) to establish structure-properties relationship of the interface; and (3) to understand the formation mechanism of lithium dendrite and to predict potential solutions.

**Approach.** The project approach is multi-fold: (1) understanding the physics behind the transformation between the low conductivity phase and the high conductivity phase; (2) investigating the bonding strength of the cathode/electrolyte interface using model systems; and (3) developing electrolytes with high ionic conductivity and good bonding to cathodes through cation doping.

**Out-Year Goals.** The project has the following out-year goals:

- Developing synchrotron-based diagnosis tools to investigate physical/chemical properties of solid/solid interface.
- Identifying mechanistic barriers that limit the chemical/mechanical/electrochemical durability of solid/solid interface.
- Developing model systems to validate the failure mechanism of solid/solid interface.

**Collaborations.** The project collaborates with Dr. A. Ngo (ANL), Dr. L. A. Curtiss (ANL), Dr. V. Srinivasan (ANL), Dr. Y. Ren (ANL), Dr. J. Libera (ANL), Dr. T. Li (Northern Illinois University), Dr. F. Wang (BNL), Dr. X. H. Xiao (BNL), and Dr. D. Chen (UH).

### Milestones

1. Forming model Ta-LLZO/NMC-622 interface for physical diagnosis. (Q1, FY 2020; Completed)
2. Investigating the interaction between Ta-LLZO and NMC-622 at the interface on cycling. (Q2, FY 2020; Completed)
3. Investigating the chemical reactions of Ta-LLZO at the reducing environment. (Q3, FY 2020; In progress)
4. Investigating the chemical/mechanical stability of Li/Ta-LLZO interface. (Q4, FY 2020; In progress)

## Progress Report

This quarter, a limited amount of effort was made to fabricate Ta-doped LLZO (Ta-LLZO) pallets for assembling model cells for diagnosis. To achieve this, a hot press was used to densify the Ta-LLZO powder into a dense and solid pallet (see Figure 60a). On both sides of the pallet, the surface layer was contaminated by the graphitic material migrated from the graphite punch die used for hot press. This layer of contamination can be easily burned off at above 700°C. However, the SEM image of the cross section clearly shows a multiple layer structure for the Ta-LLZO pallet (see Figure 60b). The center part of the pallet is composed of highly crystallized and densely packed particles; the outer layers on both sides are covered by a layer of less crystallized material. A clear interface was observed between the core part and the outer layers; the thickness of the outer layers is about 50  $\mu\text{m}$ . The high temperature process at 700°C did not eliminate these outer layers. Instead, the thickness of the outer layers increases with the thermal processing time. This confirms that the outer layer is not the graphitic contamination, but rather is something from the side reaction of Ta-LLZO.

To identify the species in the core part, as well as in the outer layers, a focused X-ray beam was used to scan the sample in the thickness direction, and the collected XRD patterns are shown in Figure 60c. It clearly shows that the structure of the outer layers is substantially different from what is in the core part; the thickness of the outer layers is about 60  $\mu\text{m}$ , consistent with the SEM observation. A Rietveld Refinement was conducted to quantitatively analyze the XRD data. It was revealed that the core part of the LLZO pallet is a cubic LLZO phase, while the outer layers are dominated by  $\text{La}_2\text{Zr}_2\text{O}_7$  (LZO) with a small fraction of  $\text{La}_2\text{O}_3$  (see Figure 60d). In addition, the concentration profile analysis also shows a clear negative correlation between the content of LLZO and the content of LZO. It implies that the outer layers are the side products of the decomposition of LLZO during hot pressure, which can be rooted to either the thermal decomposition of LLZO at 1000°C, or extraction of  $\text{Li}_2\text{O}$  by porous graphite of the punch die set. To focus on the diagnosis effort, a simple mechanical polishing was deployed to get rid of the outer layer, and the core piece will be used as the SSE to investigate the interface issues in the following effort.

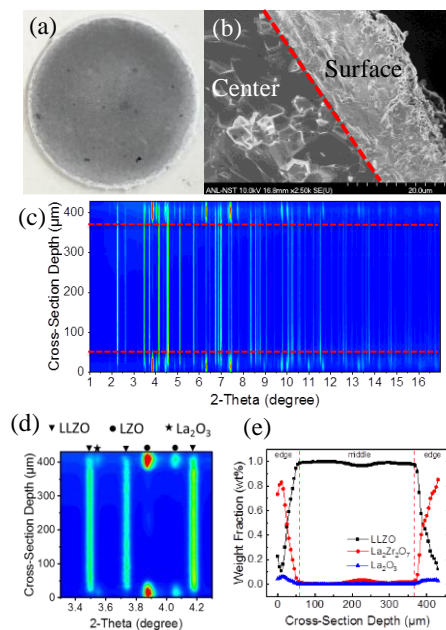


**Figure 60.** (a) Digital image of a Ta-LLZO pallet fabricated by hot pressing. (b) Scanning electron microscopy image of the hot pressed Ta-LLZO pallet showing a clear contrast between the core part and the outer layers. (c) Space resolved high-energy X-ray diffraction (HEXRD) patterns showing the phase evolution along the thickness direction. (d) Zoomed view of HEXRD patterns. (e) Evolution of concentration profiles for different species in the thickness direction of Ta-LLZO pallet.

## Patents/Publications/Presentations

The project has no patents, publications, or presentations to report this quarter.

## Task 2.7 – Fundamental Understanding of Interfacial Phenomena in Solid-State Batteries (Xingcheng Xiao, General Motors)

**Project Objective.** The project objective is to develop a comprehensive set of *in situ* diagnostic techniques combined with atomic/continuum modeling schemes to investigate and understand the coupled mechanical/chemical degradation associated with dynamic interfacial phenomena in SSBs. Specifically, *in situ* observations and characterizations of lithium plating-stripping processes, lithium dendrite formation, interphase formation, and the induced interfacial stresses, as well as the mechanical and electrochemical properties of interfaces and interphases, are paramount. The study will provide useful guidelines for optimizing cell structure design and engineering interfaces and interphases to enable SSBs.

**Project Impact.** The project will provide fundamental understanding of the dynamic interfacial phenomena and the coupled mechanical and chemical degradation. In addition, it will establish a critical guideline to design safe and durable SSBs with energy density > 500 wh/kg for EV applications.

**Approach.** The multiscale *in situ* diagnostic tools, including AFM, nanoindentation, dilatometer, stress sensors, and pressure cells, will be used to investigate mechanical behavior and microstructure evolution at interface/interphase during lithium plating and stripping. The information (along with Li-ion transport properties and microstructure evolution obtained using the advanced spectroscopic ellipsometry, and *in situ* TEM) will be correlated with electrochemical performance toward high cycle efficiency and dendrite-free SSBs. The goal of this understanding is to develop strategies for surface and interface engineering, apply them to commercially available SEs (including powder, pellets, and foils), and assemble SSBs for further validation and optimization, eventually extending cycle life for EV application.

**Out-Year Goals.** The project seeks to develop SSB model systems to capture critical mechanical properties and probe the coupled mechanical-chemical degradation by further developing comprehensive *in situ* diagnostic tools. All results obtained from these *in situ* studies, combined with advanced postmortem analysis and modeling, will be correlated with the cycling stability of SSBs. The *in situ* tools developed will be applied to the following two periods to deeply understand the coupled mechanical and chemical degradation of interface/interphase.

**Collaborations.** The co-PIs involved in experiments and simulation will be as follows: Profs. B. W. Sheldon (Brown University), Y-T. Cheng and A. Seo (University of Kentucky), Y. Qi (Michigan State), and Dr. Q. Zhang (GM).

### Milestones

1. Thin-film electrode system for different *in situ* electrochemical tests developed. (Q1, FY 2020; Completed)
2. Thin-film SE system established with the comparable ionic conductivity reported in the literature. (Q2, FY 2020; Ongoing)
3. *In situ* electrochemical-mechanical tools established. (Q3, FY 2020; Ongoing)
4. A rank of the interfacial adhesion between SE and electrodes determined. (Q4, FY 2020)

## Progress Report

### Proof-of-Concept Experiment

A proof-of-concept experiment was carried out to investigate the evolving stress when using garnet-based LLZO SE. The measured bending prior to the short-circuiting event indicates that the stress measured by multi-beam optical stress sensor (MOSS) is about three orders of magnitude higher than that of the growth stress in plated lithium metal. Furthermore, post-mortem images indicate that Li-metal plates not only in the Cu/LLZO interface, but also in the bulk of the SE. Hence, the team hypothesizes that these large stresses are largely contributed from the lithium metal penetration through the stiff ceramic SE.

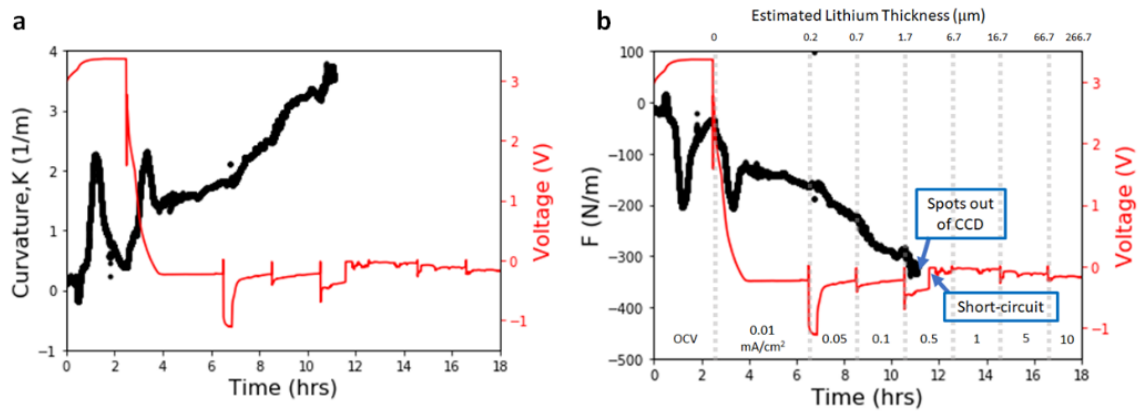


Figure 61. (a) Curvature and voltage versus time measured by multi-beam optical stress sensor (MOSS) using LLZO solid electrolyte. (b) Membrane force  $F$  and measured voltage versus time.

As shown in Figure 61b, an increase in compressive stress was observed prior to possible short-circuit feature in voltage profile. The stress values prior to short-circuiting are at around -150 MPa, which will need further analysis to evaluate. The large stress values the team observed cannot be explained solely by the growth stress in lithium metal, which was previously reported to be around 0.2 MPa. The stresses the team measured that are three orders of magnitude higher than the growth stress in lithium metal are most likely contributed by the stiff SE prior to short-circuiting.

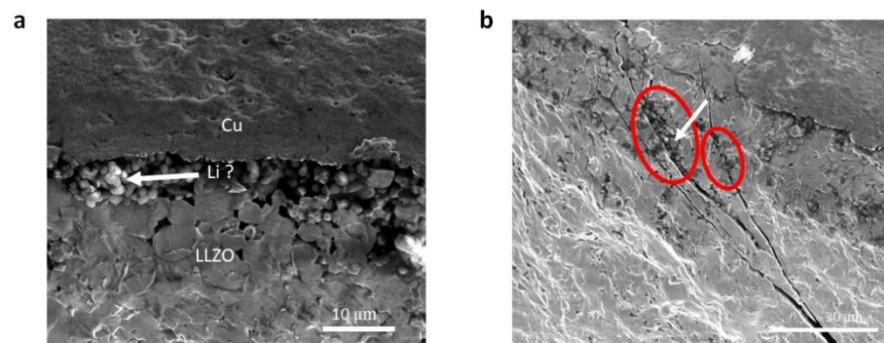


Figure 62. (a) Cross-sectional image of a fractured surface (near copper side) after short circuiting. (b) Lithium metal penetration through the LLZO solid electrolyte along the grain boundary.

After the short-circuiting event, the LLZO pallet was fractured and imaged using SEM. As shown in Figure 62a-b, plating of lithium metal was observed both in Cu/LLZO interface and along the LLZO GB. These post-mortem images will be essential in building the valid model that can describe the bending measurement accurately.

For future work, reproducibility of this experiment needs to be improved by controlling the surface reflectivity of the current collector during plating. Additionally, the effects of current density and relaxation behavior during OCV will be investigated to decouple the contributions from plated lithium metal and the LLZO. Improved model is required to interpret the measured bending accurately. Nonetheless, the results shown above demonstrate a proof-of-concept, in which the team measured bending of the LLZO/Li-metal electrode.

### DFT Calculations

The team conducted DFT calculations to understand the root cause behind lithiophilicity and lithiophobicity of Li(001)/Li<sub>2</sub>O(110) and Li(001)/LiF(001) interfaces, respectively. The former interface draws lithium atom to the interface to fill the vacancy, while the latter repels the lithium diffusion to the interface. The Li(001)/Li<sub>2</sub>PO<sub>2</sub>N(010) (representing LiPON) interface was also studied for its lithiophilic tendency.

Charge density difference and planar averaged charge density difference were studied, as shown in Figure 63a, to investigate the origin of the lithiophilicity and lithiophobicity of Li(001)/Li<sub>2</sub>O(110) and Li(001)/LiF(001) interfaces. On formation of the interfaces, the planar charge density difference normal to the interface shows that electron transfers from SEI materials to the interfaces and more electron density is localized at the Li(001)/Li<sub>2</sub>O(110) interface than at the Li(001)/LiF(001) interface. The high electron location at the interface will attract Li-ion toward the interface and create a stronger interfacial adhesion, consistent with the definition of lithiophilic Li(001)/Li<sub>2</sub>O(110) interface. The rectangular lithium pattern at the Li(001)/Li<sub>2</sub>O(110) interface created a spot with wider Li-Li spacing to localize electrons, while the lithium pattern at the Li/LiF interface may be too tight to localize any electron, as shown by the charge density difference at the interface plane in Figure 63b. Therefore, more electron density can accumulate at the Li(001)/Li<sub>2</sub>O(110) interface, making it lithiophilic and vice versa. Such observation was tested on Li(001)/Li<sub>2</sub>PO<sub>2</sub>N(010) interface. The Li<sub>2</sub>PO<sub>2</sub>N (010) surface has a centered rectangular pattern with the 1Li-under-coordinated O to O spacing in the range of 3.14-4.16 Å. The resulting Li-Li spacing on the surface is in the range of 3.57-4.00 Å. By observing the structure, it is suggested that considerable electron density can be seen in the Li-Li spot, which is proven by charge density difference, as shown in Figure 63b. Li(001)/Li<sub>2</sub>PO<sub>2</sub>N(010) is supposed to be lithiophilic, and the calculation regarding lithium vacancy formation energy at the interface is running to further prove the lithiophilicity of such interface.

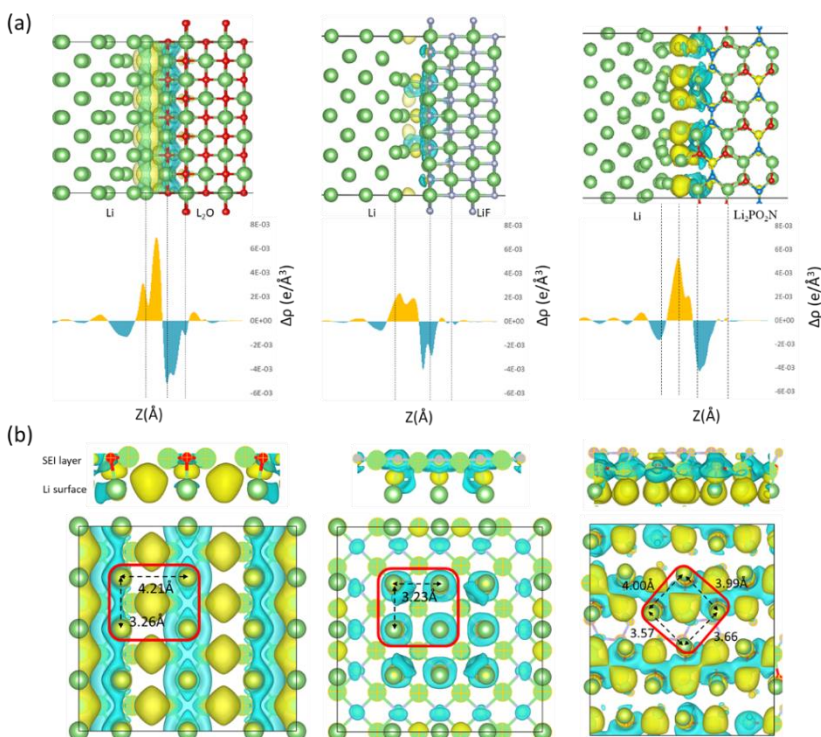


Figure 63. (a) Charge density difference,  $\Delta\rho = \rho_{\text{Li-coating}} - \rho_{\text{Li-coating}}$ , (upper panel) and planar-averaged charge density difference (lower panel) of Li(001)/Li<sub>2</sub>O(110)(left), Li(001)/LiF(001)(middle), and Li(001)/Li<sub>2</sub>PO<sub>2</sub>N(010)(right) interfaces; (b) Cross-view (bottom) and side view (side) of charge density difference of Li(001)/Li<sub>2</sub>O(110)(left), Li(001)/LiF(001)(middle), and Li(001)/Li<sub>2</sub>PO<sub>2</sub>N(010)(right) interfaces. Note: The yellow region corresponds to charge accumulation, and the blue region corresponds to charge depletion. Oxygen in red, lithium in green, fluorine in grey, nickel in blue, and sulfur in yellow. The atoms with a cross indicate the atoms of Li<sub>2</sub>O, LiF, and Li<sub>2</sub>PO<sub>2</sub>N.

## Patents/Publications/Presentations

The project has no patents, publications, or presentations to report this quarter.

## Task 2.8 – Multidimensional Diagnostics of the Interface Evolutions in Solid-State Lithium Batteries (Yan Yao, University of Houston)

**Project Objective.** The project objective is to develop a platform combining FIB-SEM tomography, TOF-SIMS, and in-SEM nanoindentation-based stiffness mapping for structural, chemical, and mechanical characterizations in SSLBs. Assessment of the influence of cell design and testing conditions (external pressure, current density, temperature) on the evolutions of interfaces will be performed.

**Project Impact.** The consolidated *in situ* structural–chemical–mechanical diagnostic platform established in this project will provide unprecedented insights into the failure mechanisms of SSLBs.

**Approach.** Space- and time-resolved structural, chemical, and mechanical characterizations of the cathode–electrolyte and anode–electrolyte interfaces will be performed on all-solid-state lithium batteries using FIB-SEM, TOF-SIMS, and in-SEM nanoindentation. Tasks include the following: (1) development of solid-state cell thin stacks and test-cell configurations that are suitable for *in situ* characterizations; (2) quantitative characterization and *in situ* tracking of interfacial voids formation within composite cathode and electrolyte layer; (3) identification and *in situ* tracking of the chemical composition, spatial distribution, and mechanical properties of electrolyte decomposition products at the lithium- and cathode-electrolyte interfaces; and (4) visualization, chemo-mechanical properties detection, and *in situ* tracking of lithium dendrites grown within the SE layer.

**Out-Year Goals.** In the out years, the project will develop thin-stack solid-state cells, micro-cells, in-SEM nanoindentation, and testing protocols. The correlation between structural evolution, electrolyte decomposition, and interfacial resistance increase will be investigated.

**Collaborations.** The UH team (Drs. Y. Yao, Z. Fan, Y. Liang) works closely with the Rice University team (Drs. J. Lou and H. Guo).

### Milestones

1. Thin-cell stack development. (Q2, FY 2020; Completed, March 31, 2020)
2. Micro-cell development. (Q3, FY 2020; Completed, June 30, 2020)
3. Nano-cell development. (Q4, FY 2020; Postponed to FY 2021)
4. Composition and spatial distribution study. (M 3.1 moved up; Q4, FY 2021; In progress)
5. Cell optimization and electrochemical benchmarking. (Q4, FY 2020; In progress)

Note: Because of the difficulty in accessing the clean room facility at Rice due to the COVID-19 pandemic, the PI postponed milestone 3 (as it requires significant clean room access) and moved up milestone 4. These changes will improve work efficiency and minimize health risks.

## Progress Report

This quarter, the team optimized thin-format all-solid-state cells to demonstrate electrochemical performance in line with that in bulk-type cells. One key improvement came from optimizing slurry formulations used for tape-casting thin cathode and electrolyte layers. Slurries used in fabrication of component layers are unique in that they are consisted of highly

polar ionic sulfides that do not blend well in nonpolar dispersant, but dissolve in and/or react with polar ones. The team's early attempts to make thin layers often resulted in notable uniformity and defects (Figure 64a). They have experimented a limited range of binders, dispersants, and solid contents and have found a strong correlation of the film quality on these variables. Thin films fabricated with the latest slurries show no apparent defects (Figure 64b). Thin cells thus fabricated are showing improved electrochemical performance and, more importantly, much improved reproducibility and consistency.

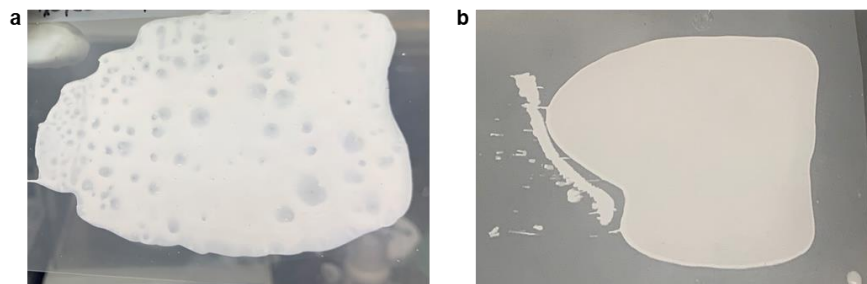


Figure 64. Solid-state electrolyte thin films tape-cast with slurries based on (a) less-optimized and (b) improved formulations.

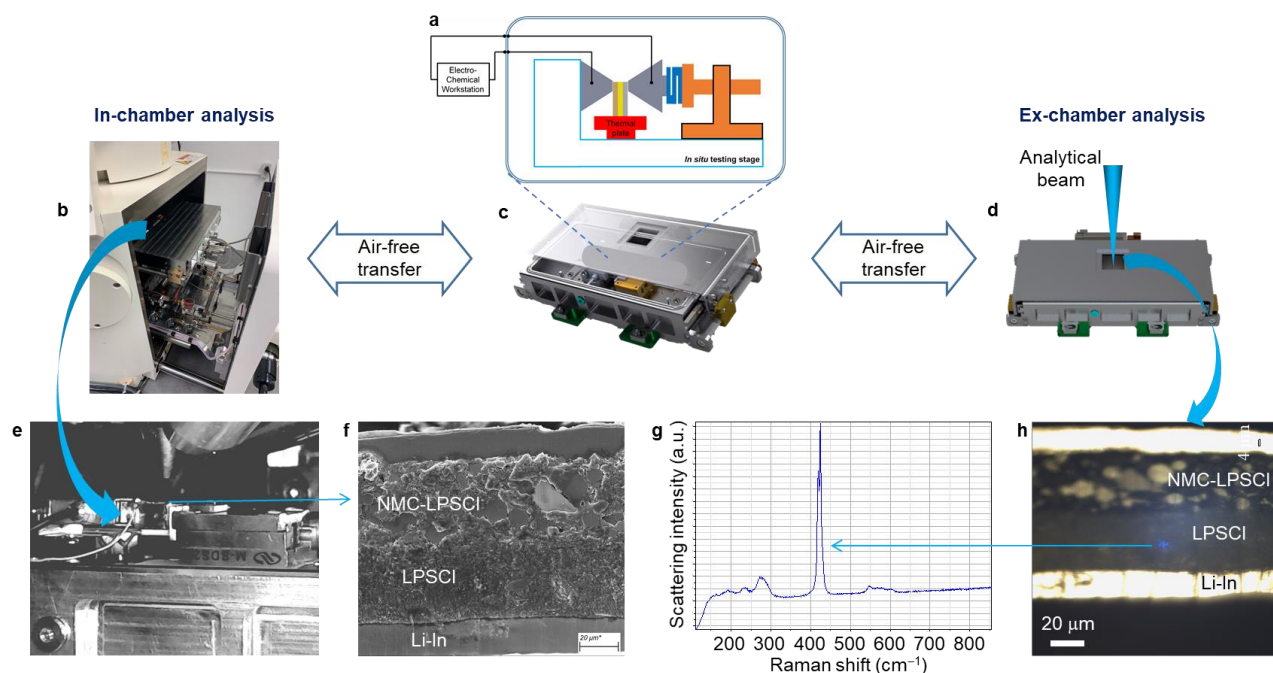


Figure 65. Design and applications of an air-free transfer vessel with an *in situ* cell test platform built-in. (a) Cell test platform equipped with micro-cell mount, heater, pressure applicator, and sensor. (b) Installation of the vessel in instruments where characterizations are performed inside a chamber [for example, focused ion beam/scanning electron microscopy (SEM)]. (c) Vessel remains closed when used with (d) instruments without a chamber (for example, laser-based spectrometers); analytical beams come in through a window in the vessel. (e) The cover of the vessel opens up, revealing the test platform and lifting up toward the electron gun. (f) SEM image of the cross-section of a thin-format cell obtained using the vessel. (g) Raman spectrum of the LPSCI electrolyte obtained using the vessel. (h) Optical image of the cross-section of a thin-format cell obtained with a Raman spectrometer using the vessel.

*Operando* characterization of micro-cells requires transferring a cell fabricated in a glove box to various analytical instruments without exposure to the air. Conventional transfer vessels for sample transferring are typically designed for use with a specific instrument, thus lacking the flexibility needed in this project for

different instruments. Some diagnostic devices do not have suitable transfer vessel options available. Therefore, an air-free transfer vessel has been developed to complement the project's micro-cell characterizations.

Figure 65 details the design and application of the transfer vessel. At the heart of the hermetically sealable vessel (Figure 65c) sits a cell test platform (Figure 65a). The cell test platform is equipped with a micro-cell mount where electrochemical tests are performed *in situ*. Heating and pressure applying/sensing modules are integrated in the platform. The air-tight vessel design allows transfer of the test platform, on which an air-sensitive all-solid-state cell is mounted, between different analytical instruments. For characterizations performed inside a chamber, such as FIB techniques, the vessel is installed into the chamber with the cover closed (Figure 65b). Once desirable atmosphere inside the chamber is reached, the cover of the vessel opens up via an electrically controlled motor. The test platform is lifted to an adjustable height according to the requirement of the measurement (Figure 65e). Here, the team shows an example of SEM observation of the cross-section of an NMC/LPSCI/Li-In thin-format cell mounted on the platform (Figure 65f). For characterizations performed without a chamber, such as laser-based spectroscopy, the vessel is used directly with the cover closed. A window on top of the test platform allows analytical laser beams to strike through (Figure 65d). Here, an example of Raman spectroscopy measurement of the same thin-format cell used for SEM observation is presented. The optical image of the same area from the Raman spectrometer appears identical to the SEM image (Figure 65h). Raman spectra of the electrolyte layer reveal the characteristic peak attributable to the  $PS_x$  polyhedra (Figure 65g). The results indicate the efficacy of the vessel in isolating the test platform from ambient atmosphere without interfering analytical beams and signal collection.

The test platform for micro-cell tests is being optimized to deliver electrochemical performance akin to regular bulk cells. Figure 66 shows an NMC/LPSCI/Li-In micro-cell tested on the platform within the transfer vessel. The first discharge capacity approaches 200 mAh/g (based on the weight of NMC), which is comparable to results from bulk cells. Initial efficiency, cycling stability, and rate capability are areas to be improved.

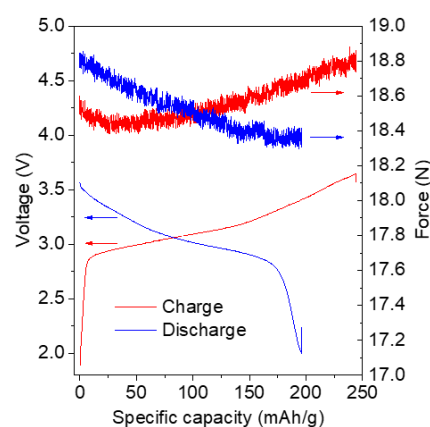


Figure 66. Voltage profile and pressure change of an NMC/LPSCI/Li-In micro-cell tested in the transfer vessel.

## Patents/Publications/Presentations

### Patent

- Fan, Z. An *In Situ* Electrochemical Testing Stage and *In Situ* Analysis Method. UH ID (2020-048), US Provisional Application 63036110; filed on June 28, 2020.

### Publication

- Ai, Q., Q. Fang, J. Liang, X. Xu, T. Zhai, G. Gao, H. Guo, G. Han, L. Ci, and J. Lou. "Lithium-Conducting Covalent-Organic-Frameworks as Artificial Solid-Electrolyte-Interphase on Silicon Anode for High Performance Lithium Ion Batteries." *Nano Energy* 72 (2020): 104657.

## TASK 3 – MODELING

### Summary and Highlights

Achieving the performance, life, and cost targets outlined by VTO will require moving to next-generation chemistries, such as higher capacity Li-ion intercalation cathodes, silicon and other alloy-based anodes, Li-metal anode, and sulfur cathodes. However, numerous problems plague development of these systems, from material-level challenges in ensuring reversibility to electrode-level issues in accommodating volume changes, to cell-level challenges in preventing cross talk between the electrodes. In this task, a mathematical perspective is applied to these challenges to provide an understanding of the underlying phenomenon and to suggest solutions that can be implemented by the material synthesis and electrode architecture groups.

The effort spans multiple length scales, from *ab initio* methods to continuum-scale techniques. Models are combined with experiments, and extensive collaborations are established with experimental groups to ensure that the predictions match reality. Efforts also focus on obtaining parameters needed for the models, either from lower-length scale methods or from experiments. Projects also emphasize pushing the boundaries of the modeling techniques used to ensure that the task stays at the cutting edge.

A major focus of the effort is around Li-metal-based SSBs. While these chemistries hold promise, numerous challenges such as reactivity, conductivity, and mechanical stability prevent their commercialization. Mathematical models are ideal to provide the guidance and insights needed to solve these issues.

In the area of Li-metal anodes, the focus is on understanding how materials can be designed to prevent dendrite growth using continuum modeling approaches, combined with calculations on mobility in solid conductors. The results are used to guide materials development by providing the properties needed to prevent dendrites while also achieving the energy and power goals. Models examine the role of the SEI on the morphology of the dendrite and describe the mechanical-electrochemical coupled effects that are critical for dendrite formation. Finally, efforts are focused on discovery of new solid ion conductors with properties that far exceed existing materials. The focus is on using these models as a guide before embarking on extensive experimentation.

Lithium metal with SEs will be paired with cathode materials, often intercalative in nature. Models are being developed to examine the solid-cathode interface in Li-metal based systems, where side reactions and interface debonding issues are known to limit cycling. These models are being used to understand how to prevent chemo-mechanical failure at the interface. Coatings, an effective strategy for high-voltage operation, are being explored with the aim of providing a rational design approach for new coating materials. In addition, focus is paid to porous electrodes with cathode particles to predict the impact of heterogeneities on electrode behavior.

**Highlight.** Jena and coworkers have modeled and screened cluster-based SEs that have low activation energies, practical room-temperature ionic conductivities, wide electrochemical stability windows, and desired mechanical properties. Numerous materials are being examined using MD to calculate conductivities at different temperatures. The group found that nonstoichiometric compositions, with lithium excess, can show remarkable conductivities compared to the stoichiometric compositions, based on  $\text{Li}_6\text{PS}_5\text{Cl}$ . The group found some materials that show 3 to 5 orders of magnitude higher conductivity compared to the stoichiometric variation, higher than previously known nonstoichiometric compositions.

## Task 3.1 – Characterization and Modeling of Li-Metal Batteries: First-Principles Modeling and Machine Learning (Kristin Persson, Lawrence Berkeley National Laboratory)

**Project Objective.** This project supports VTO programmatic goals by developing next-generation, high-energy cathode materials and enabling stable cathode operation at high voltages through target particle morphology design, functional coatings, and rational design of electrolytes. The end-of-project goals include the following: (1) understanding of the factors that govern charge transport in nonaqueous, superconcentrated LEs, (2) critical surface and coating design and optimization strategies that will improve cycling of Li-ion battery cathodes by reducing cathode degradation from oxygen loss, and (3) simulation and ML of the early formation of the SEI on Li-metal electrodes.

**Project Impact.** This project is aimed at providing fundamental insights into the atomistic mechanisms underlying surface reactivity and performance of Li-ion cathode materials and electrolytes with the ultimate goal to suggest improvement strategies, such as coatings, surface protection, novel electrolyte formulations, and particle morphology design. Transport modes as a function of solvent and salt concentrations will be clarified, and a data-driven reaction network framework will be designed and implemented to predict early SEI formation on lithium metal.

**Approach.** First-principles calculations, both static and dynamic approaches, are used to model SSE material thermodynamics and kinetics. LEs are modeled through coupled classical MD and first-principles methods to accurately capture solvation structure as well as reactivity of the liquid system. The reaction network is built on large-scale first-principles data, using graph theory and machine learning (ML) models.

**Out-Year Goals.** Electrolyte work will be aimed toward understanding the atomistic interactions underlying performance of lithium electrolytes, specifically elucidating conductivity (as a function of salt concentration) and impact on the charge transport mechanisms at play. Amorphous coatings will be evaluated based on ionic transport metrics and thermodynamic stability. The reaction network will be tested against known interfacial species forming on lithium metal in LiPF<sub>6</sub>/EC electrolytes.

**Collaborations.** This project is highly collaborative between BMR PIs G. Chen (LBNL), G. Ceder (UC Berkeley), and R. Kostecki (ANL). Improved coating formulations will be examined by Chen and Ceder, and interfacial reactivity insights corroborated by Kostecki.

### Milestones

1. Obtain desirable chemical and structural traits of amorphous cathode coatings. (Q1, FY 2020; Completed, December 2019)
2. Identify the lithium diffusion bottlenecks in two known coating materials. (Q2, FY 2020; Completed)
3. Quantify the conduction mechanisms in superconcentrated LiPF<sub>6</sub>/PC. (Q3, FY 2020; Completed)
4. Preliminary insights into the SEI composition and reaction pathways for baseline electrolytes. First approximative reaction scheme proposed. (Q4, FY 2020; In progress)

## Progress Report

The current BMR project is aimed to obtain desirable chemical and structural traits of commonly used amorphous cathode coatings such as  $\text{Al}_2\text{O}_3$  and  $\text{ZnO}$ . The team uses *ab initio* molecular dynamics (AIMD) simulations to model  $\text{Li}^+$  and  $\text{O}^{2-}$  self-diffusion in amorphous  $\text{Al}_2\text{O}_3$  and  $\text{ZnO}$ . Within each diffusion trajectory, they extract vibrational motion at fixed sites and translational motion between two sites. For these separate motions, they characterize the changes in local coordination environments as a function of  $\text{Li}^+$  concentration during the ionic diffusion by calculating the number of nearest neighbors.

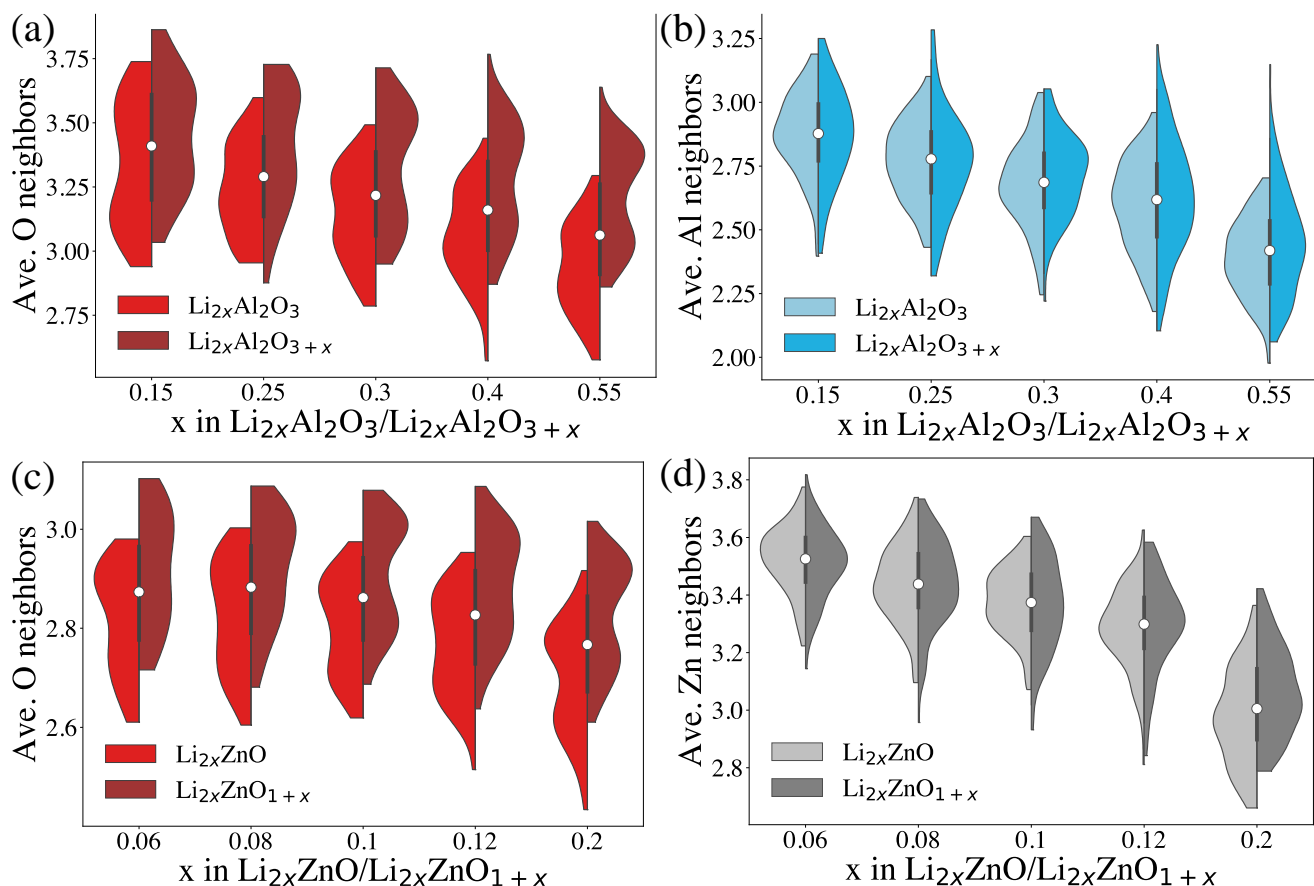


**Figure 67.** Averaged number of  $\text{O}^{2-}$  neighbors during  $\text{Li}^+$  diffusion (a/c) and averaged number of  $\text{Al}^{3+}$  and  $\text{Zn}^{2+}$  neighbors during  $\text{O}^{2-}$  diffusion (b/d) for amorphous  $\text{Al}_2\text{O}_3$  and  $\text{ZnO}$  at 2000 K for 40 ps.

In Figure 67, the average number of  $\text{O}^{2-}$  neighbors during  $\text{Li}^+$  diffusion and the average number of  $\text{Al}^{3+}/\text{Zn}^{2+}$  neighbors during  $\text{O}^{2-}$  diffusion for  $\text{Li}_{2x}\text{Al}_2\text{O}_3/\text{Li}_{2x}\text{Al}_2\text{O}_{3+x}$  and  $\text{Li}_{2x}\text{ZnO}/\text{Li}_{2x}\text{ZnO}_{1+x}$  at 2000 K for 40 ps are plotted as a function of  $\text{Li}^+$  concentration. The changes in coordination environments during vibrational and translational motions are particularly noticeable for  $\text{Li}^+$  diffusion, which are represented by the two bumps in Figure 67a-b. There are more  $\text{O}^{2-}$  neighbors during vibrational motions than during translational motions, which implies that  $\text{Li}^+$  is trapped at its local equilibrium site by the neighboring  $\text{O}^{2-}$  ions, and its translation to another vibration site is initiated by the Li-O bond breaking/formation process. In addition, the team observes a decrease in the  $\text{O}^{2-}$  coordination number during  $\text{Li}^+$  diffusion and similarly, a decrease of  $\text{Al}^{3+}$  ( $\text{Zn}^{2+}$ ) neighbors during  $\text{O}^{2-}$  diffusion, as a function of increasing  $\text{Li}^+$  concentration. This implies that a higher  $\text{Li}^+$  content can increase both  $\text{Li}^+$  (desirable) and  $\text{O}^{2-}$  mobility (not desirable) in amorphous structures. In addition, the number of  $\text{O}^{2-}$  neighbors during  $\text{Li}^+$  diffusion in  $\text{ZnO}$  is smaller than that in  $\text{Al}_2\text{O}_3$ , consistent with a higher  $\text{Li}^+$  diffusivity in  $\text{ZnO}$ . On the other hand, in  $\text{ZnO}$ , the  $\text{O}^{2-}$  ion exhibits a higher coordination number to  $\text{Zn}^{2+}$  neighbors as

compared to  $\text{Al}^{3+}$  in  $\text{Al}_2\text{O}_3$ . However, the Al-O bond is stronger than the Zn-O bond such that the bond-breaking process necessary for translation is less favorable in  $\text{Al}_2\text{O}_3$  as compared to ZnO. Therefore, the  $\text{O}^{2-}$  diffusivity is limited by both the cation coordination number and the cation-oxygen bond strength.

### Patents/Publications/Presentations

#### Publication

- Cheng, J., E. Sivonxay, and K. A. Persson. “Evaluation of Amorphous Oxide Coatings for High-Voltage Li-ion Battery Applications using a First-Principles Framework.” *ACS Applied Materials & Interfaces*. Accepted.

## Task 3.2 – Understanding and Strategies for Controlled Interfacial Phenomena in Lithium-Ion Batteries and Beyond (Perla Balbuena and Jorge Seminario, Texas A&M University; Partha Mukherjee, Purdue University)

**Project Objective.** The project objective is to evaluate and characterize interfacial phenomena in lithiated silicon and Li-metal anodes and to develop guidelines for potential solutions leading to controlled reactivity at electrode/electrolyte interfaces of rechargeable batteries using advanced modeling techniques based on first principles.

**Project Impact.** Understanding SEI growth on constantly evolving silicon surfaces and on highly reactive Li-metal surfaces is expected to allow definition of the electrolyte properties required in high-performance cells. Strategies to control the silicon anode instability and pulverization issues and the well-known safety and short effective lifetimes of Li-metal anodes will be developed by tuning the electrolyte composition, structure, dynamic, and stability, as well as that of the electrode morphology and interactions with the electrolyte, based on multiple characterizations of interfacial phenomena.

**Approach.** A comprehensive multi-scale modeling approach, including first-principles *ab initio* static and dynamics, classical MD, and coarse-grained mesoscopic models, will focus on the roles of the electrolyte's chemical, structural, and dynamical properties and of the electrode micro- and nano- structure on the formation and evolution of the SEI layer and the associated electrochemical performance on silicon and on Li-metal anodes.

**Out-Year Goals.** Work will progress toward characterizing lithiation and SEI formation at silicon surfaces as well as the subsequent cracking and reforming events under the most realistic modeling conditions. Similarly, the project will investigate electrolyte effects on reactivity and dendrite formation in Li-metal surfaces. The project aims to capture how the chemistry of the various electrolyte components (mainly liquids, but also solid polymers and gels) affects the main issues that influence the electrode performance.

**Collaborations.** This project funds work at Texas A&M University (TAMU) and Purdue University. The team has collaborated with Prof. G. Somorjai (UC Berkeley), Prof. S. Yassar (University of Illinois at Chicago, or UIC), and Dr. V. Murugesan (PNNL).

### Milestones

1. Complete thermal and chemical/electrochemical analysis of dendrite growth. (Q1, FY 2020; Completed)
2. Complete analysis regarding SEI formation and electrodeposition processes. (Q2, FY 2020; Completed)
3. Complete studies on cationic additive effect on electrodeposition. (Q3, FY 2020; Completed)
4. Complete mesoscale investigation on external field effects on electrodeposition. (Q4, FY 2020)

## Progress Report

### Effects of Cationic Additive on Lithium Nucleation

In single-metal batteries, three fundamental mechanisms govern the morphological evolution of the dendrite at the anode-electrolyte interface. These mechanisms involve the following: transport of cations in the electrolyte, reduction of cations, and surface self-diffusion of the deposited metal atom(s). On the other hand, when a cationic additive reduces simultaneously at the growth front, the underlying mechanisms are more complex. A multi-component diffusion takes place in the electrolyte, and two cations can possibly undergo reduction at the reaction front. The presence of a binary metal deposit also results in several pathways of surface self-diffusion of deposited atoms. To understand the formation of a binary electrodeposit and investigate its potential to enable a stable morphology, the team develops a coarse-grained mesoscale model capable of capturing the dynamic evolution of the co-electrodeposit morphology and composition.

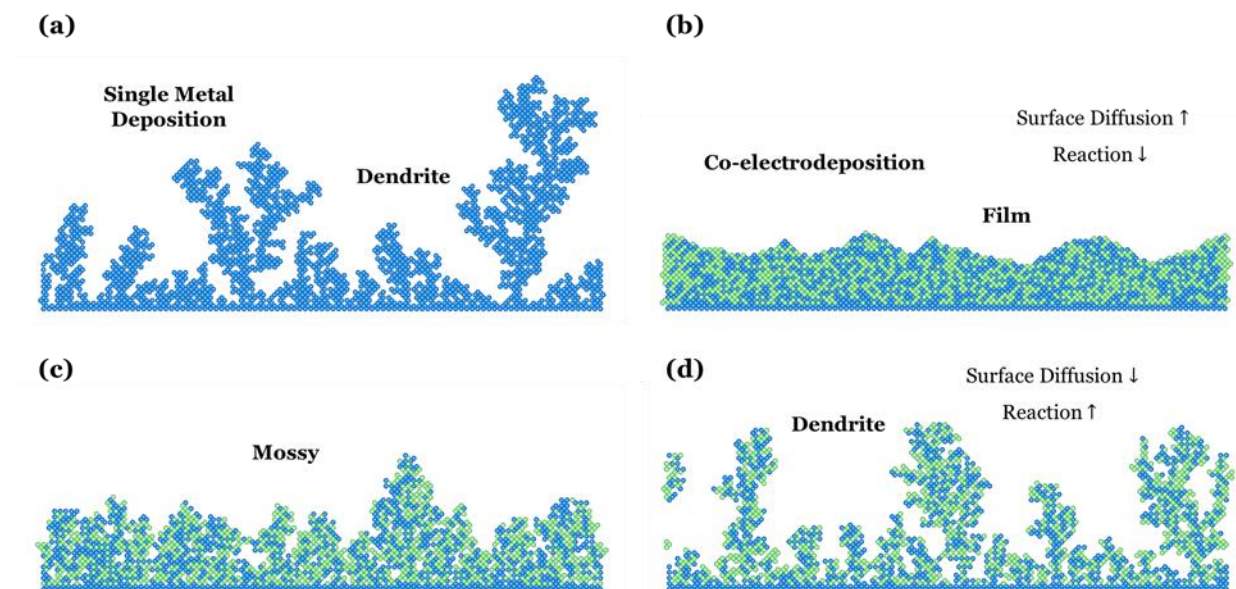


Figure 68. (a) Representative illustration of a dendritic morphology formed for single metal electrodeposition. Co-electrodeposition morphologies exhibiting (b) film-type, (c) mossy, and (d) dendritic features depending on the surface diffusion barrier of the deposited atom and the electrochemical reaction rate. An increase in the porosity and number of branches is observed with an increase in the surface diffusion barrier (that is, decrease in surface diffusion rate) and an increase in the reaction rate.

A representative dendrite morphology formed in case of a single metal deposition is shown in Figure 68a. Figure 68b shows the obtained morphology for fixed reaction rate and surface diffusion barrier  $E_a = 0.1$  eV. This low surface diffusion barrier enables facile migration of the deposited atoms, and results in relaxation of the metal surface. The film-type morphology formed is highly dense and devoid of any pore spaces and branched structures. Increasing the surface diffusion barrier ( $E_a = 0.5$  eV) and reaction rate  $\sim 33\%$  higher results in a transition from a film-type to mossy morphology (Figure 68c). Due to the reduced surface migration the porosity increases and branch-like structures are formed. An even higher surface diffusion barrier ( $E_a = 0.9$  eV) and extremely high reaction rate ( $> 4$  times higher than the initial) prevent any surface relaxation of the morphology and result in deposition of atoms on top of each other to form a dendritic structure (Figure 68d). The additive can compensate for lack of the lithium migration capability to fill the vacancies and enable formation of a dense, compact morphology. Therefore, choosing a simultaneously reducing additive metal with a low self-diffusion barrier height (manganese, sodium, potassium, and zinc) is crucial for development of dendrite-free metal anodes.

## Patents/Publications/Presentations

### Publications

- Vishnugopi, B. S., F. Hao, A. Verma, and P. P. Mukherjee. “Surface Diffusion Manifestation in Electrodeposition of Metal Anodes.” *Physical Chemistry Chemical Physics* 22 (2020): 11286–11295.
- Ponce, V., and J. M. Seminario. “Lithiation of Sulfur-Graphene Compounds Using Reactive Force-Field Molecular Dynamics Simulations.” *Journal of the Electrochemical Society* 167 (2020): 100555.

### Presentation

- DOE VTO Annual Merit Review, virtual presentation, bat 329\_p (June 1–4, 2020): “Understanding and Strategies for Controlled Interfacial Phenomena in Lithium-Ion Batteries and Beyond”; P. B. Balbuena.

### Task 3.3 – Electrode Materials Design and Failure Prediction (Venkat Srinivasan, Argonne National Laboratory)

**Project Objective.** The main project objective is to develop computational models for understanding the various degradation mechanisms for next-generation Li-ion batteries. This year's goal is to use the continuum-based mathematical model to (1) investigate interfacial stability between electrodes and ceramic-based SSEs, and (2) experimentally measure and understand the impedance observed at the cathode/SSE interface. Ceramic-based SSEs are expected to enable high-energy-density and liquid-free, safe, next-generation Li-ion batteries. Li-metal anodes should be incorporated due to their substantially larger specific capacity, as compared to present day graphite-based anodes. During deposition, lithium dendrite growth through the SSEs, and subsequent short circuit, has been a major issue, limiting successful implementation of SSEs. Similarly, on the cathode side, diffusion of TMs into the SSEs, along with delamination between cathode and SSE, leads to increased interfacial resistance. The developed computational model will be used to investigate the impact of microstructural (grain size), physical (mechanical stiffness), and transport (conductivity) properties of the SSE on the overall interfacial degradation observed at both the cathode and anode sides. Due to the SOC-dependent electrochemical and mechanical properties of the cathode, an attempt will be made to experimentally measure the SOC-dependent impedance at the cathode/SSE interface. The main focus will be to elucidate interfacial issues, observed at both anode and cathode sides, and to devise strategies to enable successful implementation of SSE in next-generation Li-ion batteries.

**Project Impact.** Findings from this research will give a better understanding of the factors, at the cathode/SSE interface, limiting the cycle life of SE-based Li-ion batteries. These results will help to enable incorporation of cathode particles within SSEs.

**Project Approach.** The approach used here is to develop mesoscale models, based on continuum modeling, to describe the critical processes in the materials, and combining them with electrochemical, microscopic, and spectroscopic data to ensure parameter estimation and model validation. The model is then used to provide insights on impact of material properties on performance and life and as guidance for design of new materials.

**Out-Year Goals.** At the end of this project, a computational framework will be presented that is capable of estimating delamination and impedance at cathode/SSE interface.

**Collaborations.** This project collaborates with L. A. Curtiss, A. T. Ngo, and C. M. Phatak at ANL.

#### Milestones

1. Elucidate the difference in delamination mechanisms for NMC/LLZO- and LCO/LLZO- type cathode/SEIs. (Q1, FY 2019; Completed)
2. *Go/No-Go Decision:* Investigate impact of exchange current density on delamination-induced capacity fade. If effect is minor, use experimentally observed exchange current values. Otherwise, use value obtained from DFT calculations. (Q2, FY 2020; Completed)
3. Develop continuum model for charge transport and mechanical degradation incorporating an interphase layer between LLZO electrolyte and NMC cathode. (Q3, FY 2020; Completed)
4. Gain understanding of growth rate of electrodepositing lithium nuclei. (Q4, FY 2020; In progress)

## Progress Report

**Develop Continuum Model for Charge Transport and Mechanical Degradation Incorporating an Interphase Layer between LLZO Electrolyte and NMC Cathode.** It has been demonstrated in earlier quarters that substantial detachment occurs between the NMC cathodes and LLZO SEs during operation, which leads to loss of electrochemically active surface area, and subsequent increase in interfacial charge transport resistance. It has been argued that incorporation of interphase layers, such as LBO ( $\text{Li}_3\text{BO}_3$ ) and/or LBCO ( $\text{Li}_3\text{BO}_3\text{-Li}_2\text{CO}_3$ ), can substantially help to mitigate the interfacial resistance growth. It has been experimentally demonstrated that LBCO can prevent the inter-diffusion of TM ions from the cathode to the electrolyte, and vice versa, during synthesis as well as charge-discharge operation. Impact of LBCO coating layers on the extent of interfacial delamination has not been investigated. This quarter, the team implemented an LBCO interphase layer between the NMC cathode and LLZO SEs. Single ion conduction behavior has been assumed within the LBCO interphase layers. Conductivity of LBCO has also been assumed to be two orders of magnitude smaller than the conductivity of LLZO ceramic SEs. Exchange current densities at NMC/LBCO and LBCO/LLZO interface have been assumed to be same as the NMC/LLZO interfacial region. Fracture energies at the NMC/LBCO and LBCO/LLZO interface have also been assumed to be three times and two times larger than the NMC/LLZO interface, respectively. These magnitudes of fracture energies have been obtained from the atomistic calculations. Figure 69a-b demonstrates the NMC/LBCO/LLZO cathode/interphase-layer/SE microstructure with two different thicknesses of the interphase layer, 5 nm and 25 nm, respectively. The extent of fractional delamination with and without the LBCO interphase layer is shown in Figure 69c.

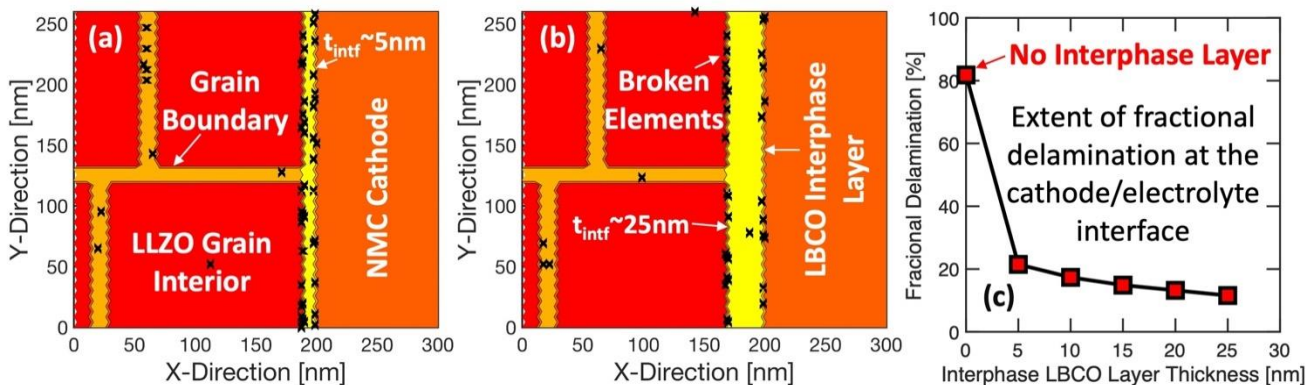


**Figure 69.** (a) NMC/LLZO cathode electrolyte microstructure with a 5-nm thick LBCO interphase layer in between. (b) NMC/LBCO/LLZO cathode/interphase-layer/electrolyte microstructure with thickness of interphase layer being 25 nm. (c) Evolution of fractional delamination with increasing thickness of the LBCO interphase layer. Addition of interphase layer helps to minimize the delamination.

The voltage versus capacity performance curves, with and without LBCO interphase layers, are shown in Figure 70a. The discharge capacities obtained with different thicknesses of the interphase layers are shown in Figure 70b. It is evident that addition of LBCO helps to improve discharge capacity and also increases interphase resistance. Incorporation of LBCO completes the milestone for this quarter.

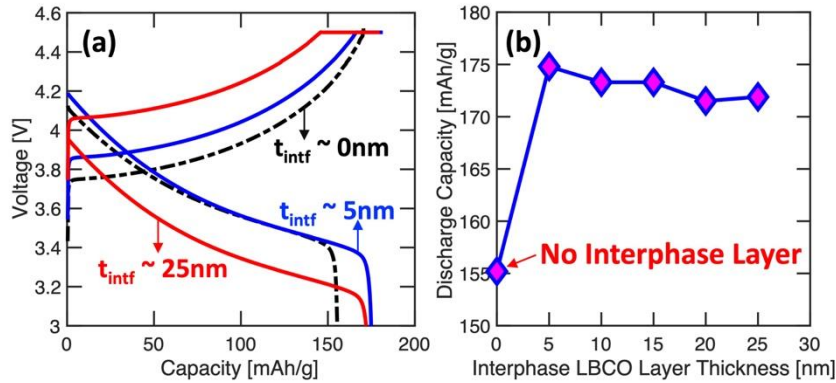


Figure 70. (a) Voltage versus capacity performance curves with interphase layer thickness 0 nm (black dashed line), 5 nm (blue line), and 25 nm (red line). (b) Discharge capacity with increasing thickness of the interphase layer. Addition of interphase layer helps to minimize delamination and enhances discharge capacity. Increasing thickness of interphase layer also increases the ohmic resistance.

## Patents/Publications/Presentations

### Publication

- Barai, P., A. Ngo, B. Narayanan, K. Higa, L. A. Curtiss, and V. Srinivasan. "The Role of Local Inhomogeneities on Dendrite Growth in LLZO-Based Solid Electrolytes." *Journal of the Electrochemical Society* 167 (2020): 100537.

## Task 3.4 – Dendrite Growth Morphology Modeling in Liquid and Solid Electrolytes (Yue Qi, Michigan State University)

**Project Objective.** The project goal is to develop a validated model to predict lithium dendrite morphology evolution in both liquid and solid electrolytes during electrodeposition and stripping to accelerate the adoption of Li-metal electrodes in current and emerging battery technologies. To achieve this goal, the project has four objectives: (1) formulate a general framework that captures the electrochemical-mechanical driving forces for lithium morphology evolution; (2) consider the role of the nm-thin SEI in LEs as well as the microstructures of  $\mu\text{m}$ -thick SEs for lithium morphology evolution; (3) connect micron-scale phase-field models and atomic-scale DFT-based simulations via parameter- and relationship-passing to predict lithium dendrite nucleation and growth kinetics and morphology; and (4) validate the key input parameters and main conclusions of the multi-scale model as new capabilities are being developed step-by-step.

**Project Impact.** This atomically informed, fully coupled, electrochemical-mechanical dendrite morphology evolution model will allow the project to design the desired properties of artificial SEI coatings, the microstructure of SE materials, and the corresponding battery operating conditions, so as to avoid dendrite growth during cycling. It will accelerate design of durable and safe lithium anodes for Li-S, Li-air, and all-solid Li-ion batteries. Thus, it directly impacts such emerging technologies that aim to meet the DOE target of the high-energy-density battery cells ( $> 350 \text{ Wh/kg}$ ) for EV applications and to push the cost below  $\$100/\text{kWh}_{\text{use}}$ .

**Approach.** A multi-scale model approach is taken to connect micron-scale phase-field models and atomic-scale DFT-based simulations via parameter- and relationship-passing.

**Out-Year Goals.** The second-year goal is to establish the model to simulate metallic lithium precipitation in SEs while further developing understanding of lithium dendrite growth in LEs. To reach this goal, mechanical and electrochemical driving forces for lithium dendrite growth in SEs will be coupled in phase-field model, while DFT is used to address the lithium plating tendency in various SEs and coating materials. Validation of the model will come from experiments to correlate the distinctive transport properties of artificial SEI layers with their impact on lithium dendrite morphology.

**Collaborations.** This project collaborates with UMD, Sandia National Laboratories (SNL), PNNL, University of Arkansas, and UH.

### Milestones

1. Determine the effect of multi-component SEI layer on dendrite morphology in a LE. (Q4, FY 2019; Completed)

## Progress Report

### DFT Prediction of the Effect of GBs in SEI

One key inhomogeneity in the SEI is the GBs. A systematic study of the electronic properties of GBs was conducted via DFT calculations. Previously ordered coherent GB structures, including tilt and twist GBs, have been studied. All the GBs reduced the bandgaps, and the tilt GBs reduced the bandgaps to a larger extent than the twist GBs. This quarter, the electronic properties of experimentally observed disordered/amorphous GB structures were investigated.

The GB region of a LiF twist  $\Sigma 3$  (111)/[111] GB was melted at 3000 K for 10 ps with a time step of 1fs using NVT AIMD simulations to generate an amorphous GB region. Figure 71 compared the density of states (DOS) of ordered and amorphous GBs with the same grain orientations. Due to the randomly distributed atoms, the electronic states in both the valence and conduction bands were split, and the GB bandgap decreased from 8.58 eV (in the bulk) to 4.96 eV. Two unoccupied states were lower than the  $\text{Li}^+/\text{Li}^0$  depositing potential level, suggesting they can be occupied on contact with lithium to facilitate lithium plating. So, the amorphous GBs will deteriorate the SEI passivation by trapping electrons in the GB regions, which can reduce Li-ions inside of SEI and prompt the lithium dendrite growth. The structural analysis showed more under-coordinated atoms in the amorphous GB than the twist and tilt LiF  $\Sigma 3$  GBs. These results suggest that well-ordered, coherent GBs are preferred to design a fully electronically passivating SEI.

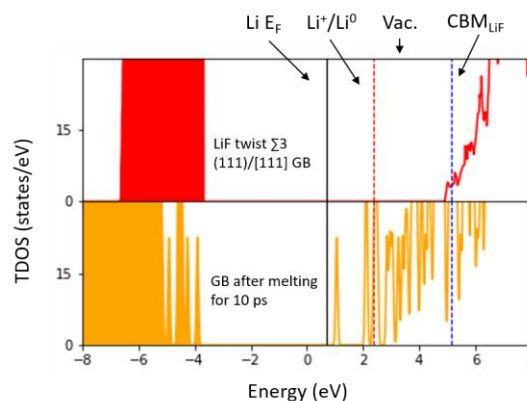


Figure 71. Amorphous grain boundaries (GBs) have even lower band gap than ordered GBs, and can trap electrons.

### Phase Field Model to Reveal Impact of SEI on Dendrite Morphology in LE

By varying exchange current, transport property of SEI (Figure 72a-d) introducing porous structure (Figure 72e-h) and cracks (Figure 72i-j) in SEI, and comparing SEI/Li interfacial adhesion properties (Figure 72k-l), the team has elucidated the impact of these factors on lithium plating morphology. The most effective method to achieve a smooth plating surface, similar to that observed in magnesium plating, as shown in Figure 72c/d, is reducing the intrinsic exchange current,  $I_0$ . This can be achieved by increasing de-solvation energy and/or increasing solvation shell size via electrolyte design, following the atomistic informed Butler-Volmer equation the team developed. Another method to change interface kinetics is to design a porous SEI with a high-zeta-potential sponge to change concentration and current density profiles, which enabled dendrite-free plating/stripping of lithium (Figure 72e-h). Other structural failures such as crack and delamination promoted dendrite growth.

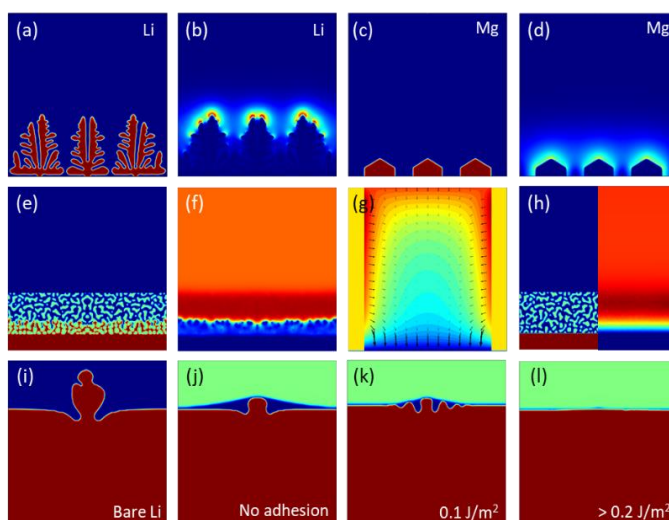


Figure 72. Phase-field simulations on (a-d) lithium and magnesium plating morphologies using implicit SEI model. (e-h) Lithium dendrite suppression by  $\text{Li}^+$ -affinity porous media at anode. (i-l) Lithium metal/coating interfacial adhesion impact on electrodeposition.

## Patents/Publications/Presentations

The project has no patents, publications, or presentations to report this quarter.

## Task 3.5 – Modeling of Amorphous Solid-State Conductors (Gerbrand Ceder, University of California Berkeley)

**Project Objective.** SSEs are promising to achieve high energy density. The project objective is to determine the design principles needed to create SSEs with high Li-ion conductivity while also achieving stability against common Li-ion cathodes and Li-metal anodes.

**Project Impact.** The project will lead to understanding the factors that control Li-ion motion in crystalline and amorphous solids and will develop strategies to create stable interfaces against lithium metal and high-voltage cathode materials. The understanding of such processes is necessary to determine design principles to develop reliable ASSBs.

### Approach.

HT computation method is used to screen suitable SE with high electrochemical stability and high ionic conductivity, by incorporating Nudged Elastic Band (NEB) and an AIMD method. Meanwhile, DFT is used to calculate bulk elastic constants of materials, surface energies, and interface decohesion energies of GBs. Thermodynamic interface stability is assessed from *ab initio* computed grand potential phase diagrams in which the lithium voltage can be controlled. Kinetic limits for SE decomposition are assessed by topotactic lithium insertion and removal from the SE.

**Out-Year Goals.** Future goals include the following: (1) gain insight into what creates high Li-ion conduction in sulfide and oxide solids, and (2) develop stable, processable solid-state conductors that can be applied in ASSBs.

**Collaborations.** There are no collaborative activities this quarter.

### Milestones

1. Modeling of the  $\text{Li}_2\text{S}-\text{P}_2\text{S}_5$  ground state phase diagram for SSEs: solid phases correctly modeled. (Q1, FY 2020; Completed)
2. Modeling of LPS lithium mobility in amorphous state with variations of  $\text{PS}_4$  structural units. (Q2, FY 2020; Completed)
3. Develop model for the lithium conductivity in amorphous sulfide solids. (Q3, FY 2020; Completed)
4. Modeling of the full finite temperature L-S-P phase diagram to understand metastability of the highly conducting solids. (Q4, FY 2020)

## Progress Report

In trying to understand lithium conductivity in solids, the team recently extended work<sup>[1]</sup> to investigate the kinetic pathways in lithium titanate ( $\text{Li}_4\text{Ti}_5\text{O}_{12}$ ), a high-rate anode exhibiting extraordinary rate capability seemingly inconsistent with its two-phase reaction. The team believes that even though it is an anode material, this type of metastable spinel can be a promising SSE, and thus understanding the origin of its high rate is critical. Using first-principles calculations and the NEB method, they identified and explored the energetics of and migration in representative low-energy intermediate  $\text{Li}_{4+x}\text{Ti}_5\text{O}_{12}$  configurations. In these intermediate configurations, they discovered a large amount of highly distorted face-sharing lithium that are involved in distinct  $\text{Li}^+$  ion migration pathways with substantially lower activation energy than the pathways in the end members. Figure 73a shows the energy profile of the pathways in  $\text{Li}_{4+\delta}\text{Ti}_5\text{O}_{12}$  (green),  $\text{Li}_{5+\delta}\text{Ti}_5\text{O}_{12}$  (red), and  $\text{Li}_{7+\delta}\text{Ti}_5\text{O}_{12}$  (blue) as a function of distance along the paths. The activation energies of  $\text{Li}^+$  ion migration in the lowest energy  $\text{Li}_4\text{Ti}_5\text{O}_{12}$ , and  $\text{Li}_5\text{Ti}_5\text{O}_{12}$  and  $\text{Li}_7\text{Ti}_5\text{O}_{12}$  configurations are  $\sim 343$ ,  $\sim 216$ , and  $\sim 455$  meV, respectively. Steps a-g in Figure 73b illustrate an example migration pathway in one representative metastable  $\text{Li}_{5+\delta}\text{Ti}_5\text{O}_{12}$  configuration. The black arrows show the migration direction of each step. The purple-colored face indicates the three-coordinated oxygen face through which the  $\text{Li}^+$  ions can migrate from a  $\text{Li}(8a)$  tetrahedron to a  $\text{Li}(16c)$  octahedron.

In general, the  $\text{Li}^+$ -ion diffusion pathway involves lithium hopping from face-sharing tetrahedral (octahedral) lithium sites to octahedral (tetrahedral) lithium sites (Figure 73b). Along this path, although face-sharing  $\text{Li}^+$  ions change position, the number of face-sharing  $\text{Li}^+$  ions (three to four) remains nearly constant in the  $\text{Li}_4\text{Ti}_5\text{O}_{12}$  (always two) and  $\text{Li}_5\text{Ti}_5\text{O}_{12}$  (from three to four to three) pathways. As a result, there is no abrupt increase of the energy of the system. In the higher-energy pathway in  $\text{Li}_7\text{Ti}_5\text{O}_{12}$ , however, the number of face-sharing  $\text{Li}^+$ -ions changes substantially

from zero to two and back to zero. The low migration barrier for  $\text{Li}^+$  ions in the LTO system can be attributed to two important factors. The first factor is that the number of face-sharing lithium polyhedra is smaller in the transition state (when the migrating  $\text{Li}^+$  ions are in the triangular face in Figure 73b) than in the initial and final states within each step [for example, there are three instances of face-sharing in states *a* and *b* (marked in Figure 73), but only two between *a* and *b*]. The reduction in  $\text{Li}^+ - \text{Li}^+$  repulsion in the transition state is likely to lower the activation barrier. For the second factor, because local distortion helps to reduce the effective coordination number of lithium, the change in lithium coordination is minimized during  $\text{Li}^+$ -ion migration through the three-coordinated oxygen face, further lowering the activation barrier. Both factors minimize changes in the energy, resulting in a relatively flat energy landscape along the migration path. These results show that the improved kinetics at higher rate in LTO result from the increased amount of face-sharing  $\text{Li}^+$ , and thus mobile carriers, and from the more highly distorted lithium polyhedra seen in the high-energy  $\text{Li}_{4+x}\text{Ti}_5\text{O}_{12}$  configurations accessible at high rates. This conclusion is supported by *operando* lithium K-edge electron energy-loss spectroscopy (Li-EELS) showing high intensities of signal associated with distorted face-sharing lithium in the intermediate compositions during charge and discharge at high rates.

### Reference

- [1] Zhang, W., D. H. Seo, T. Chen, L. Wu, M. Topsakal, Y. Zhu, D. Lu, G. Ceder, and F. Wang. “Kinetic Pathways of Ionic Transport in Fast-Charging Lithium Titanate.” *Science* 367, issue 6481 (2020): 1030–1034.

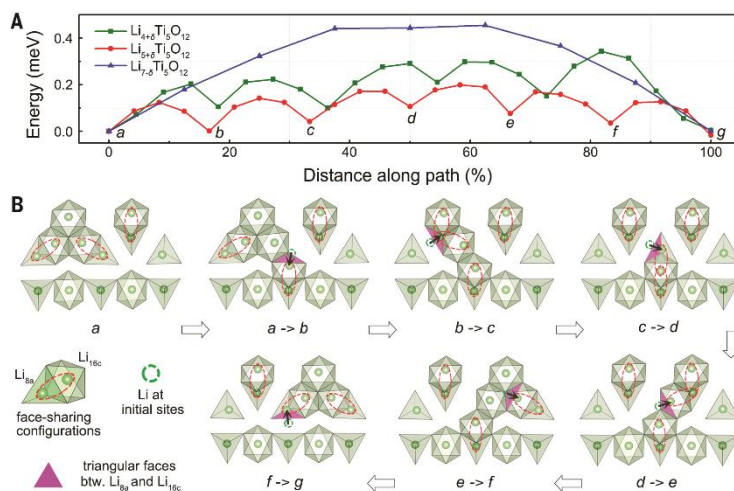


**Figure 73.  $\text{Li}^+$ -ion migration pathways and corresponding energy barriers in the intermediates.**

## Patents/Publications/Presentations

### Publications

- Zhang, W., D. H. Seo, T. Chen, L. Wu, M. Topsakal, Y. Zhu, D. Lu, G. Ceder, and F. Wang. “Kinetic Pathways of Ionic Transport in Fast-Charging Lithium Titanate.” *Science* 367, issue 6481 (2020): 1030–1034.
- Ji, H., J. Wu, Z. Cai, J. Liu, D. H. Kwon, H. Kim...and M. Balasubramanian. “Ultrahigh Power and Energy Density in Partially Ordered Lithium-Ion Cathode Materials.” *Nature Energy* 5, no. 3 (2020): 213–221.

## Task 3.6 – Characterization and Modeling of Li-Metal Batteries: Force Field Theory and Lithium-Sulfur Battery Simulations (Lin-Wang Wang, Lawrence Berkeley National Laboratory)

**Project Objective.** The project objective is to develop force field based on *ab initio* calculations to study Li-S cathode and lithium LE. It also includes designs for Li-S cathode systems for high gravimetric and volumetric capacities. Lithium diffusion in both LE in a confined space, and in Li-S cathode systems, is a main focus of this subtask. To enable calculation of large systems, machine learning force field (ML-FF) trained on *ab initio* calculation data will also be developed. The success of this new approach will greatly expand the capability of theoretical simulation for battery systems. ML-FF can also be used in combination with traditional classical force field to deal with the nonreactive parts of the system.

**Project Impact.** Making the Li-S battery a commercial reality will have a major impact on society and also help to realize the VTO goal of 500 km per charge for EV. However, the nature of chemical reaction makes it different from the traditional intercalation-based Li-ion battery. The molecular nature of  $\text{Li}_2\text{S}_n$  also allows solvation in the electrolyte. To address these problems, it is essential to have fundamental studies and understandings of the underlying mechanisms. Theoretical simulations can play an important role in discovering and designing new cathode materials. However, traditional *ab initio* calculations are limited by their computational size, while the classical force field simulations are limited by their accuracy and the lack of adequate force field. The development of ML-FF can overcome these problems by bridging the size gap between the *ab initio* simulation and the real systems that need to be studied.

**Approach.** ML-FF will be developed by first running *ab initio* simulations, which can generate hundreds of thousands of data sets. The project has a unique capability of decomposing the total energy of a DFT calculation into the energy of each atom. Compared to conventional DFT calculations, this increases the number of data by hundreds of times, an important requirement for ML model training. The dependence of the atomic energy to the local atomic bonding environment will be captured using ML methods. Three ML approaches will be: linear fitting, neural network (NN) model, and Gaussian process regression (GPR) model. The team will compare the efficacies of these models. Meanwhile, they will also deal with the long-range Coulomb interactions existing in the electrolyte system and the ionic species in LE. The idea is to first fit the charge density of the system, and remove the long-range electrostatic energy before the fitting of the local energy on each atom. The team will also design new Li-S and Na-S cathode materials. In particular, they will design an amorphous Li-S mixture, with other materials such as CNT, black carbon, or electric conductive 2D materials).

**Out-Year Goals.** In outgoing years, the project will further develop computational methods for more accurate entropy and interaction energy calculations for the electrolyte, as well as for Li-S cathode systems.

**Collaborations.** The project will collaborate with G. Liu and Y. Cui for cathode design. It has also collaborated with Prof. F. Pan of Beijing University for lithium battery research in general.

### Milestones

1. New Li-S design, mixing Li-S with CNT for an ultrafine mixture. (Q1, FY 2020; Partially completed)
2. Lithium charge density fitting in electrolyte, to fit the long-range Coulomb interaction. (Q2, FY 2020; Initiated)
3. Incorporation of Coulomb interaction in the local energy calculation; ML-FF fitting. (Q3, FY 2020)
4. Further study of Li-S cathode with polymer, to study electric conductivity in such a system. (Q4, FY 2020)

## Progress Report

The team initiated a new project to investigate the formation mechanism of SEI via the fixed-potential method (grand canonical calculations). In this method, the total number of electrons in the system was floated to match the given electrode Fermi energy automatically to mimic the realistic experimental processes. As the fixed-potential method is not a mature method, the team has conducted initial testing to confirm whether it can be used for SEI simulation. Figure 74 illustrates effects of positions and potentials to the total charge of PF6 cluster (neutral is 37). Here, the SCF calculation (without geometry relaxation) is performed to get basic information. Under low and medium potential (-3.5 V, and -2.5 V), the total number of electrons of PF6 is 37.8, 38, and 38 for 2 Å, 7 Å, and 11 Å, respectively. These results are consistent with common chemical knowledge.

However, at high potential (-1.5 V), the total electrons of lithium increase to 48.9. Based on vacuum potential analysis in Z direction, the team finds a concave peak in the middle region of periodic lithium slab. This concave peak corresponds to an abnormal charge accumulation of PF6. The team has increased the dielectric constant in the solvent model, and increased the vacuum region in Z direction to avoid the charge accumulation. They are still analyzing the results and testing different aspects of the fixed-potential method.

They have also investigated the dissolution behavior of lithium from the Li(111) surface under different potential based on geometry optimization. Under high potential (-2.00 V), the top layer of lithium split into two floated layers of lithium on the Li(111) surface. At this stage, the team can consider this splitting phenomenon as a surface reconstruction. The lithium in the floated layers is still charge neutral. As they decrease the potential to -2.50 V, no significant structure changes are found except that the floated layers of lithium shift slightly away from surface. The lithium in the top layer lost electrons partially (range from +0.26 to +0.45). When decreasing the potential further to -3.00 V, the top layer lithium dissolved into the solvent completely, and the charge state of these lithium is +1. This trend is consistent with the experimental trend of lithium dissolution under different potential. Following this work, the team will optimize parameters to make the dissolution potential of lithium at exactly experimental value. They will also investigate the floated lithium layer in more detail.

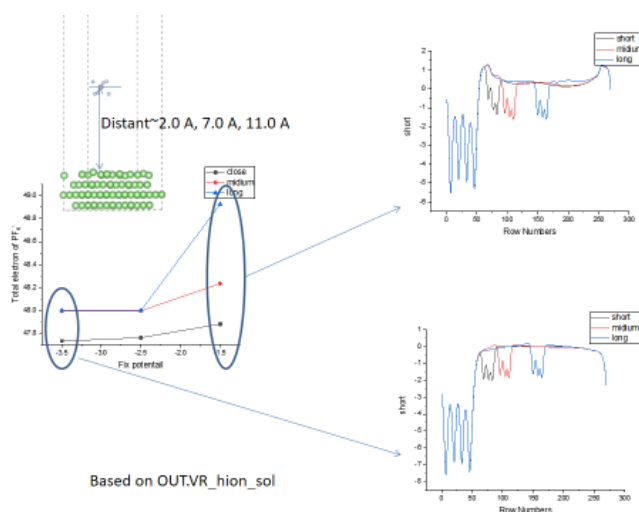


Figure 74. The charge status of PF6 at different positions and under different potential.

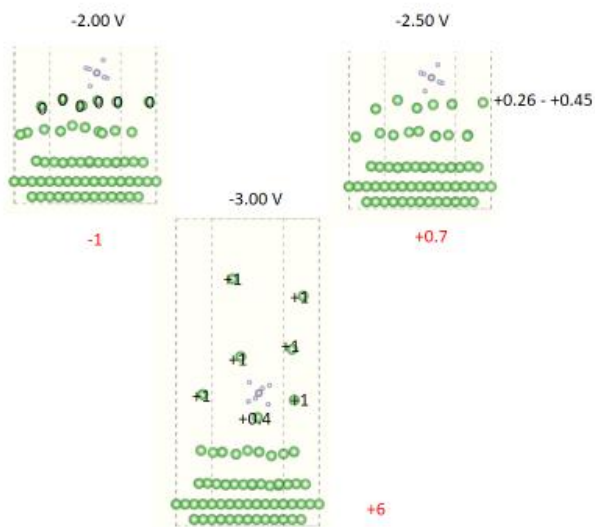


Figure 75. The dissolution behavior of lithium from the Li(111) surface under different potential.

## Patents/Publications/Presentations

The project has no patents, publications, or presentations to report this quarter.

## Task 3.7 – *In Situ* and *Operando* Thermal Diagnostics of Buried Interfaces in Beyond Lithium-Ion Cells (Ravi Prasher, Lawrence Berkeley National Laboratory)

**Project Objective.** Transport at various interfaces in *beyond lithium ion* cells will play a major role in electrochemical performance and reliability. It has not yet been possible to thermally profile a Li-metal cell during operation to provide a spatially resolved map of thermal transport properties throughout the cell. The objective of this research is to create a metrology capable of spatially resolved *in operando* thermal property profiling, and then relate thermal property to the quality of electrodes and interfaces, and use the developed thermal metrology to understand electrochemical processes in Li-metal batteries such as dendrite growth, interface kinetics, and ionic transport.

**Project Impact.** Characterizing electrochemical processes in Li-metal cells such as lithium deposition and dendrite growth at interfaces is of great significance for understanding and enhancing their electrochemical performance and reliability. *In situ* and *operando* 3-omega micro thermal sensors can provide significant information regarding the impact of buried interfaces as a function of time, material, voltage, current, and temperature, etc. Therefore, it is important to develop *operando* 3-omega micro thermal sensors and develop models relating those signals to electrochemical performance for *beyond lithium ion* cells. The physics-based model relating thermal and electrochemical properties based on these measurements can facilitate future design of Li-metal batteries.

**Approach.** To accomplish project goals, the team will utilize an in-house adapted 3-omega technique to probe thermal properties of a Li-metal cell while it is in operation, without affecting the operation of the cell. The 3-omega sensors will be deposited and fabricated on Li-metal cells based on previous learning on 3-omega sensor fabrication. The characteristic depth of the thermally probed region is defined by the wave's "thermal penetration depth,"  $\delta_p = \sqrt{D/2\omega}$ , where D is the sample's thermal diffusivity, and  $2\omega$  is the heating frequency of the thermal wave. By depositing the project's  $3\omega$  sensors on the battery's outer surface and adjusting  $\omega$ , the team controls  $\delta_p$  to span the full range from the top to the bottom layer, thereby noninvasively probing the thermal transport in subsurface layers and interfaces within the bulk of the battery. Thermal transport can be related to quality of the interface. By doing concurrent thermal transport and electrochemical performance measurements, the team plans to relate thermal transport to electrochemical performance. As frequency based thermal measurement techniques provide excellent spatial resolution within the cell, the team also plans to study heat generation at the electrolyte – Li-metal interface and relate the thermal signals to the interface kinetics and ionic transport. The frequency dependence of heat generated due to transport resistance is different from that due to kinetic resistance. The team plans to utilize this difference to separate the contributions of kinetic and transport resistance at the interface, which will enable understanding of interface kinetics and transport at the Li-metal – SSE interface.

**Out-Year Goals.** In outgoing years, the project will design, build, and implement the adapted 3-omega metrology to examine thermal properties and a general frequency dependent thermal metrology to examine heat generation. This will involve developing and testing the metrology itself along with accompanying theory, designing compatible battery samples, and applying the technique to live cells. The team will measure thermal transport properties of battery materials provided by collaborators. Combined with the electrochemical performance measurement, this will provide significant information relating the thermal signal to the electrochemical process.

**Collaborations.** This project collaborates with two LBNL groups: V. Battaglia's for cell assembly for 3-omega studies, and R. Kostecki's for pristine battery active material growths for studies of thermal signals related to electrochemical process.

## Milestones

1. Design pristine samples to be compatible with 3-omega and ambient environments. (Q1, FY 2020; Completed)
2. Perform sensitivity analysis and pristine sample design optimization to maximize measurement sensitivity to thermal interfaces. (Q2, FY 2020; Completed)
3. Fabrication of bi-layer pristine samples to experimentally isolate different kinds of interfaces. (Q3, FY 2020; Completed)
4. Thermal measurements of battery composites made from various materials. (Q4, FY 2020; In progress)

## Progress Report

The Prasher group is building *operando*  $3\omega$  micro thermal sensors and developing models relating thermal signals to electrochemical performance for *beyond lithium ion* cells. The anode-side  $3\omega$  sensor will be used to probe thermal properties of Li-metal anode and related interfaces. The group is also developing a general frequency-based thermal metrology to probe the interface kinetics and transport.

During the first quarter, the team had performed sensitivity analysis for the anode-side  $3\omega$  measurement of thermal properties of Li-metal anode and interfaces and proposed that they would use the thermal interface resistance as a measure of morphology of the lithium at the interface. In the second quarter, they had developed the  $3\omega$  sensors for the symmetric cells (Figure 76a) and had obtained the thermal properties of the electrolyte (LLZO) using  $3\omega$ . The specific heat and thermal conductivity of LLZO were determined to be 500 J/kg-K and 1.33 W/m-K, respectively.

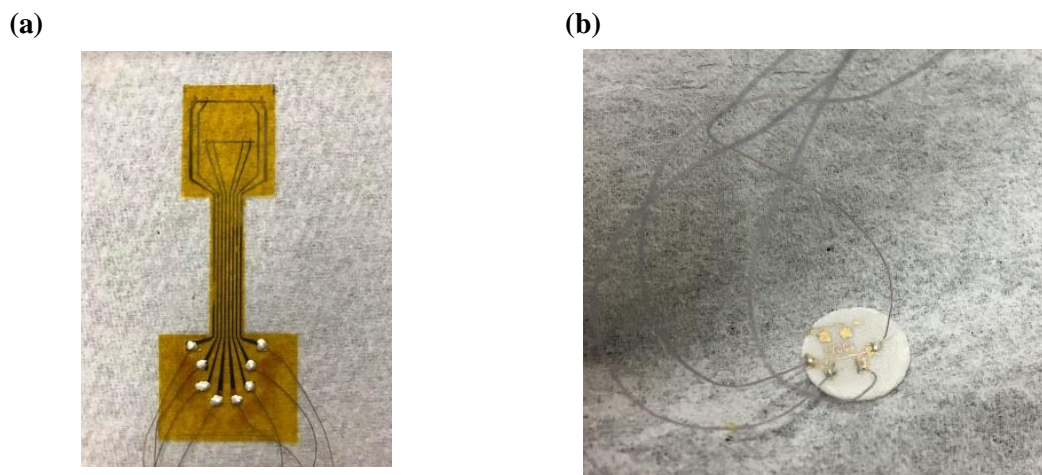


Figure 76. (a)  $3\omega$  sensor used for anode of the lithium symmetric cell. (b) LLZO pellet with a  $3\omega$  sensor.

This quarter, the team has assembled the lithium symmetric solid-state cells with  $3\omega$  sensors, which we will be able to cycle and conduct  $3\omega$  measurements simultaneously to extract the anode-electrolyte thermal interface resistance and track its evolution as a function of the number of cycles. The cells assembled are circular and have a diameter of 15 mm. They consist of 1-mm thick LLZO pellets (similar to the one shown in Figure 76b), 200- $\mu\text{m}$  thick Li-metal anode on both sides of the electrolyte, and 20- $\mu\text{m}$  thick current collectors, with a  $3\omega$  sensor attached to one of the current collectors. The assembled cell, with different layers and the  $3\omega$  sensor on the current collector, is shown in Figure 77. The  $3\omega$  sensor was attached to the copper current collector using an epoxy (SU-8). To form the assembly, the different layers were sandwiched together and heated to the melting

point of the lithium (180.5°C). Both sides of the electrolyte and the side of the current collector adjacent to lithium were pre-coated with 20 nm of gold to facilitate lithium wetting and adhesion. Next quarter, the team will cycle these cells and perform  $3\omega$  measurements. Doing so, they will study how the thermal interface resistance varies with the numbers of cycles and relate the change in the interface resistance with the morphological changes at the interface. Additionally, they will vary the surface roughness (polishing) of the LLZO pellets and will also assemble cells without the gold coating to study the effects of the electrolyte surface roughness and the lithium adhesion on the interface resistance.

The team is also developing a frequency-based study of thermal signatures in Li-metal batteries to noninvasively probe the kinetics and transport at the Li-metal-SSE interface and the ionic transport in the electrolyte. As mentioned in last quarter's report, the heat generated at the  $4\omega$  and the  $2\omega$  frequencies contains the kinetic and the charge transport information, respectively; by performing a frequency sweep to vary the thermal penetration depth, they will in principle be able to isolate the location of the origin of the  $4\omega$  and the  $2\omega$  signatures, thereby noninvasively probing the kinetics and transport at the interfaces and the electrolyte. This quarter, the team completed developing a full-scale combined electrochemical and thermal model that includes the effect of the applied frequency on the current distribution (capacitive versus reactive), heat generation ( $4\omega$ ,  $2\omega$ , and  $1\omega$  signatures), and the temperature rise at the sensors. To do so, they combined frequency analysis of heat generation with the Feldman analysis of frequency dependent temperature rise. With this combined electrochemical-thermal model, the team performed a sensitivity analysis of the thermal signatures of the kinetic, transport, and capacitive processes in the interfaces and the electrolyte. The results are presented in Figure 78. Of particular interest are the electrolyte transport resistance and the exchange current densities (related to the kinetic overpotential) at the interfaces. As seen in Figure 78, the thermal signature (frequency dependent temperature rise) due to the electrolyte resistance is exclusively sensitive at low frequencies for both the  $2\omega$ -in phase and the  $2\omega$ -out of phase signals. Similarly, the temperature rise due to the exchange current density for a particular interface is exclusively sensitive at high frequencies for both the  $4\omega$ -in phase and the  $4\omega$ -out of phase signals. Therefore, by utilizing the fact that the thermal signatures from the different electrochemical processes occurring at different locations in the cell are selectively sensitive at different frequencies (and harmonics of the frequencies), the team will be able to noninvasively probe those electrochemical processes in the cell with an external thermal sensor.



Figure 77. Assembled lithium symmetric cell with a  $3\omega$  sensor.

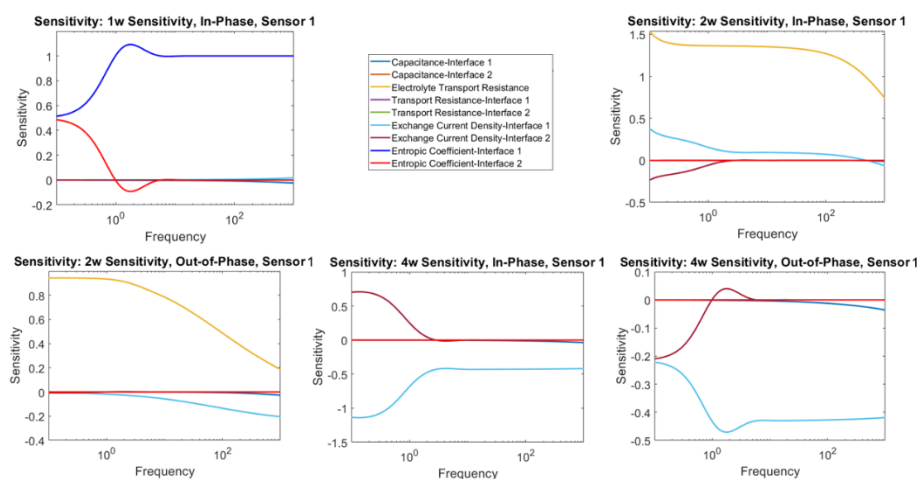


Figure 78. Sensitivity of the temperature rise at different harmonics of the applied charging frequency ( $1\omega$ ,  $2\omega$ , and  $4\omega$ ) due to different electrochemical processes at the interfaces and the electrolyte. The  $2\omega$  temperature rise (both in-phase and out-of-phase) at low frequencies is the most sensitive to the ionic transport resistance in the electrolyte. The  $4\omega$  temperature rise (both in-phase and out-of-phase) at high frequencies is the most sensitive to the kinetics at the interface (exchange current density).

## Patents/Publications/Presentations

The project has no patents, publications, or presentations to report this quarter.

## Task 3.8 – Multi-Scale Modeling of Solid-State Electrolytes for Next-Generation Lithium Batteries (Anh Ngo, Larry A. Curtiss, and Venkat Srinivasan, Argonne National Laboratory)

**Project Objective.** This project is part of a multi-scale modeling effort to obtain an in-depth understanding of the interaction of the electrode and the SE aimed at developing highly efficient SSE batteries for vehicle applications. Input parameters needed for mesoscale (continuum) level calculations are being obtained from atomistic calculations including DFT and classical MD simulations. This atomistic input will enable a multi-scale computational procedure for SSEs that is capable of successfully capturing the physicochemical aspects during charge and discharge process including lithium transport mechanisms, interfacial phenomena during the insertion and extraction of lithium ions, and mechanical deformation of SSE.

**Project Impact.** A major safety concern experienced with commercially available Li-ion batteries under some scenarios is leakage of the LE, which can potentially catch fire. Replacement of the LE is necessary to decrease the fire hazard and improve safety associated with present-day Li-ion batteries. In addition, use of SEs provides a path to prevent dendrites in Li-metal anodes, thereby leading to batteries with significantly higher energy density. The impact of this project will be to help in development of good SSEs as a replacement for the commercially used organic LEs to improve safety and energy density in Li-ion batteries.

**Approach.** Parameters needed for mesoscale modeling of grain interior (GI), GB, and electrode-electrolyte interface will be calculated by DFT-based calculations along with Monte Carlo (MC) and MD simulations. The calculations will be used to determine properties of the electrode with the SE as well as in GB regions of the SE. This will include calculations of structure, stability, ionic conductivity, Young's modulus, fracture toughness, exchange current density, and other properties.

**Out-Year Goals.** The out-year goals of this work are to calculate other properties such as fracture toughness and include other SSEs and coatings in the multi-scale modeling.

**Collaborations.** This project collaborates with Y. Cui at Stanford.

### Milestones

1. Determine the most stable interface between LLZO SE and lithium borate carbonate (LBCO) coating material. Calculate the activation energy barrier between LLZO and LBCO coating materials. (Q1, FY 2020; Completed)
2. Determine the most stable interface between NMC cathode and LBCO coating material, and calculate the activation energy barrier. (Q2, FY 2020; Completed)
3. Evaluate the exchange current density associated with charge transfer from LBCO coating to NMC cathode and LLZO SE. (Q3, FY 2020; Completed)
4. Incorporate the information obtained from the atomistic calculations into the mesoscale model, and predict the impact of coating on performance. (Q4, FY 2020; Initiated)

## Progress Report

Use of ceramic SEs to create ASSBs can enable the use of lithium metal by preventing propagation of lithium dendrites, thus enhancing safety and decreasing capacity fade. The interfaces between the cathode and SE must be stable to enable the use of these materials in batteries. Multi-scale modeling can provide insight into the mechanism for dendrite growth and other instabilities for guidance into how to prevent them. Mesoscale (continuum) modeling requires atomistic-level input from theory or experiment to accurately capture physicochemical aspects during charge and discharge processes.

LBCO is an interesting compound that can be used as a coating material for stabilizing the cathode/SE interface. The chemical composition of LBCO is given as  $\text{Li}_{2.3}\text{B}_{0.3}\text{C}_{0.7}\text{O}_3$ , and it is manufactured either by a solid-state reaction between  $\text{Li}_3\text{BO}_3$  and  $\text{Li}_2\text{CO}_3$ , or by ALD techniques that lead to formation of amorphous LBCO. In general, LBCO demonstrates decent ionic conductivity, around  $10^{-5}$  S/cm, single-ion-conducting behavior, very high electrochemical stability with lithium ( $\sim 0.1$  V – 6 V), and extremely low interfacial impedance against lithium, around  $5 \Omega\text{-cm}^2$ . All these properties indicate that incorporation of a thin layer of LBCO between the cathode and LLZO SE may not hamper the electrochemical performance substantially. LBCO is a better choice as a cathode coating material than LBO, because LBCO demonstrates higher ionic conductivity than LBO. Lithium carbonate can form on top of LLZO and cathode particles due to reaction with moisture and carbon dioxide from air. It is well known that  $\text{Li}_2\text{CO}_3$  demonstrates very high resistance to transport of lithium. LBCO can easily form a solid solution with  $\text{Li}_2\text{CO}_3$  due to the iso-structural lattice configuration and can remove the resistive lithium-carbonate layer from the surface of the cathode and electrolyte particles, and effectively reduce the interfacial impedance. However, the Li-ion transport mechanism between LLZO/LBCO and LBCO/cathode is not well understood. Delamination between the cathode and SE, and subsequent capacity fade, have been reported with LBCO as the coating material. Hence, further study is required to better understand the interfacial properties of LBCO with the cathode and SE materials.

Even under equilibrium conditions (zero applied overpotential), a current of certain magnitude flows between electrode and electrolyte. The anodic and cathodic component of this current is equal in magnitude, and they cancel each other, resulting in zero net current flow between the electrode and electrolyte. The magnitude of this current that flows under equilibrium condition is known as the exchange current density. This quantity is very important in batteries material research in the sense that it provides a measure of the reaction kinetics occurring at the interface of two different materials. A higher magnitude of exchange current density indicates that the reaction at the interface is kinetically favorable, whereas a smaller magnitude of exchange current density denotes the necessity to apply a large overpotential for the particular interfacial reaction to occur.

For an electrode and SSE interface, the magnitude of exchange current density ( $i_0$ ) can be given as:

$$i_0 = Fk_{ref} \cdot \left( \bar{k}_c \cdot c_{\text{Li}^+} \cdot (c_{\text{Li,max}} - c_{\text{Li}}) \right)^{\alpha_a} \cdot (\bar{k}_a \cdot c_{\text{Li}})^{\alpha_c}$$

where,  $\bar{k}_a = \nu \exp\left(-\frac{\Delta G}{k_B T}\right)$ , and  $\bar{k}_c = \nu \exp\left(-\frac{\Delta G}{k_B T}\right) / c_{\text{Li,max}}$  (1)

Here, F indicates Faraday's constant,  $c_{\text{Li}^+}$  stands for Li-ion concentration within the electrolyte,  $\alpha_a$  is the cathodic component of transfer coefficient (assumed to be 0.5 in the present research),  $\nu$  is the reaction rate pre-factor,  $\Delta G$  indicates thermodynamic energy barrier at equilibrium,  $k_B$  is the Boltzmann's constant, and T denotes temperature in Kelvin scale. Among all the parameters and constants mentioned here,  $\Delta G$  and  $\nu$  can be extracted directly from the AIMD calculations, and Li-ion concentration within the electrolyte can be estimated from lower length scale analysis.

This quarter, the team focused on LLZO/LBCO and LBCO/cathode materials to try to understand the charge transfer process between those interfaces. The calculations were carried out with the PBE functional and a plane wave basis. Both GGA and GGA+U calculations were performed. The stability of the interfaces was investigated first with AIMD simulations. All production runs of the AIMD trajectories were obtained after

10 ps of thermal equilibration At  $T = 300$  K. The magnitude of the pre-factor  $k_0$  can be extracted from AIMD calculations that depends on the attempt frequency  $\nu = \frac{1}{2\pi} \sqrt{\frac{k}{m}}$ , where  $k$  is spring constant and  $m$  is the mass of the Li-diffused atom. Using GGA+U calculations, the team obtains  $\nu = 1.33 \times 10^3$  m/s and  $\nu = 1.23 \times 10^3$  m/s for the LBCO/NMC and LLZO/LBCO interfaces, respectively.

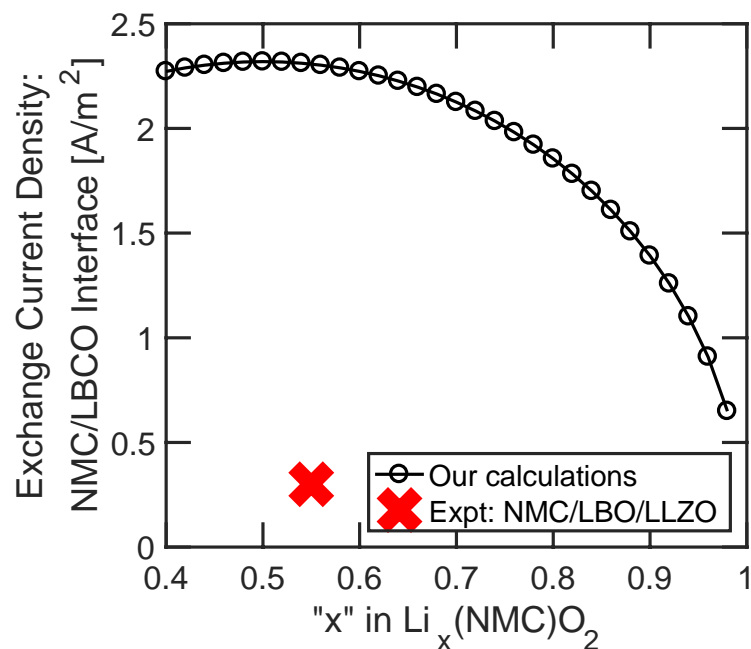


Figure 79. The magnitude of NMC/LBCO exchange current density as a function of the NMC Li-ion concentration.  $\Delta G$  and  $\nu$  can be extracted directly from the *ab initio* molecular dynamics calculations.

## Patents/Publications/Presentations

### Publication

- Barai, P., A. Ngo, B. Narayanan, K. Higa, L. A. Curtiss, and V. Srinivasan. "The Role of Local Inhomogeneities on Dendrite Growth in LLZO-Based Solid Electrolytes." *Journal of the Electrochemical Society* 167 (2020): 100537.

## Task 3.9 – Integrated Multi-Scale Modeling for Design of Robust 3D Solid-State Lithium Batteries (Brandon Wood, Lawrence Livermore National Laboratory)

**Project Objective.** This project will develop a multi-scale, multi-physics modeling framework for probing the effects of materials microstructure and device architecture on ion transport within 3D ceramic SSB materials, with the goal of enhancing performance and reliability. The project has three primary objectives: (1) integrate multi-physics and multi-scale model components; (2) understand interface- and microstructure-derived limitations on ion transport; and (3) derive key structure-performance relations for enabling future optimization.

**Project Impact.** This project will lead to understanding interfacial losses and instabilities that impede performance and promote failure of SSBs. The multi-scale and multi-physics modeling framework developed in this work will address shortcomings of existing modeling strategies that either lack coupling of the multi-physics nature of various processes active in 3D batteries or fail to incorporate processes at different length scales to understand function. Ultimately, the tools and understanding generated by this project can be utilized to realize optimization of interface-dominated 3D batteries.

**Approach.** The project approach integrates simulations at three scales to predict ion transport limitations within the ceramic SSE LLZO, as well as across the interface between LLZO and  $\text{LiCoO}_2$  (LCO) cathodes. A particular focus is on understanding the effects of microstructures and architectures resulting from processing of 3D SSBs as well as their mechanical and chemical evolution at different stages of cycling. First-principles and classical MD simulations are used to compute fundamental Li-ion diffusion within bulk SE and cathode materials, along/across GBs of the electrolyte, and along/across electrolyte/cathode interfaces. Next, phase-field simulations are used to generate digital representation of realistic microstructures of the materials, which are combined with the atomistic simulation results to parameterize mesoscale effective property calculations and to establish microstructure-property relationships for ion transport. Finally, these relationships inform a cell-level macroscopic electro-chemo-mechanical modeling framework, which can be used to optimize performance of ceramic 3D SSLBs based on LLZO SEs.

**Out-Year Goals.** Future activities will focus on refining the project's atomistic interface models for improved fidelity of ion transport simulations across cathode-electrolyte interfaces. The team will also work with collaboration partners to reconstruct microstructures of 3D-printed materials and apply them to determine effective stresses and ion transport through the polycrystalline materials. They will also further develop and validate the EIS models for connection to macroscale observables.

**Collaborations.** This project collaborates with Dr. N. Adelstein from San Francisco State University (SFSU) on atomistic diffusion modeling, and Dr. Ye from LLNL on 3D printing of SSB materials. They also partner with Drs. T. Danner and A. Latz from Deutsches Zentrum für Luft- und Raumfahrt (DLR) on impedance modeling and electrochemomechanical interface models, with Dr. E. Ivers-Tiffée from Karlsruhe Institute of Technology (KIT) on impedance spectroscopy of SSEs, with Dr. P. Zapol from ANL on modeling of solute segregation in LLZO, and with Prof. D. Fattakhova-Rohlfing from Forschungszentrum Jülich (FZJ) and Prof. E. Wachsman from UMD on controlled synthesis of LLZO with varying densities and microstructures as part of the U. S.–Germany partnership on SSB research.

### Milestones

1. Construct models of solid-solid LCO/LLZO interface. (Q1, FY 2020; Completed)
2. Perform phase-field simulation to reproduce 3D-printed microstructure of LLZO and LCO. (Q2, FY 2020; Completed)

3. Perform AIMD of LCO/LLZO interface model to determine interdiffusion. (Q3, FY 2020; In progress)
4. Quantify threshold grain/pore size that eliminates Griffith-criterion hotspots based on computed internal stress in polycrystalline LLZO. (Q4, FY 2020; In progress)

## Progress Report

**Atomistic Modeling of Strain-Dependent Li-ion Diffusion in Bulk LLZO.** The team carried out a series of calculations to quantify how Li-ion transport is affected by strain, which is important for quantifying implications of cycling strain during lithiation and delithiation. They previously used NEB to examine the role of Li-ion vacancies in affecting the diffusion behavior of nearby lithium ions. They considered three distinct Li-ion diffusion mechanisms: single-ion hopping and concerted motions involving dimers and trimers. When lithium ions fully occupy their lattice positions in LLZO, the activation energies for diffusion are around 0.15 eV (shown in Table 7, with zero strain). When a single Li-ion vacancy is introduced along the diffusion pathways, the activation energies increase to  $\sim 0.3 - 0.5$  eV. Under strain, variations in activation energies range between 40 meV/% (hydrostatic strain) and 100 meV/% (uniaxial strain). A key conclusion is that different Li-ion diffusion mechanisms respond to strain differently (Table 7), which implies that the diffusion mechanism may change under various local cycling strains.

Although these simple NEB calculations survey how individual Li-ion diffusion mechanisms depend on local strains, in practice, Li-ion diffusion is determined by an ensemble average of all mechanisms. It is therefore important to extract the collective “average” activation energies that describe the overall impact of cycling strain. Hence, this quarter the team performed AIMD simulations to obtain the “average” Li-ion diffusion coefficients in bulk crystalline LLZO and at GBs (estimated using an amorphous model). From AIMD, Li-ion diffusion coefficient can be estimated as the slope of mean square displacement (MSD), as shown in Figure 80. To ensure convergence of the MSD plots, they are performing longer AIMD runs to reach at least 20 ps, at which point they will extract Li-ion diffusion coefficients in various structure models and compute the overall activation energies via Arrhenius analysis.

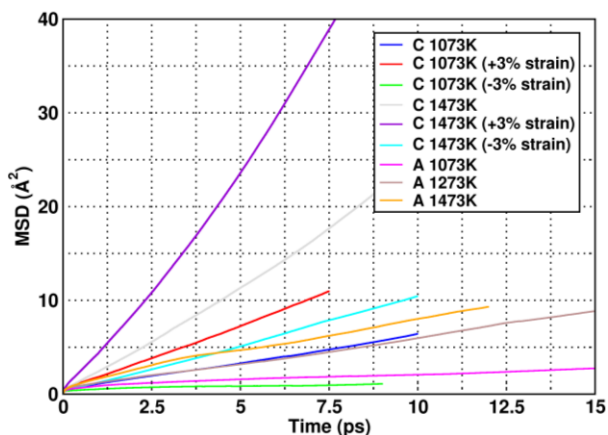


Figure 80. Mean square displacement (MSD) of Li-ion in various LLZO structure models from *ab initio* molecular dynamics. “C” and “A” refer to crystalline and amorphous LLZO structures.

**Atomistic Modeling of LLZO/LCO Interfaces.** Last quarter, the team performed high-temperature AIMD simulations to probe the interfacial structures of LLZO/LCO. This quarter, they have started to examine Li-ion diffusion through these disordered interface models. Figure 81 shows a snapshot of the LLZO/LCO interface from AIMD, along with a zoom-in to show one of the identified Li-ion diffusion pathways across the interface. Cobalt and lanthanum interdiffusion is observed across the LLZO/LCO interfaces, in particular at Li-poor regions. The activation energy associated with Li-ion diffusion along the diffusion pathway identified in Figure 81 is found to be  $\sim 0.82$  eV, which is significantly higher than the values in bulk LLZO and LCO. The team is conducting NEB calculations to obtain the activation energies for all Li-ion diffusion pathways across both the Li-rich and Li-poor LLZO/LCO interfaces. Results will be discussed in the next report. Eventually, these parameters will be combined with the strain studies in the project’s continuum model, and the approach will be validated and supported by activities being pursued through VTO U.S.-Germany collaboration.

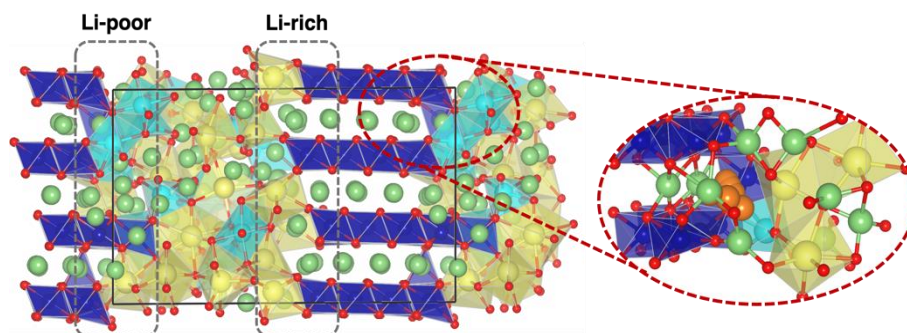
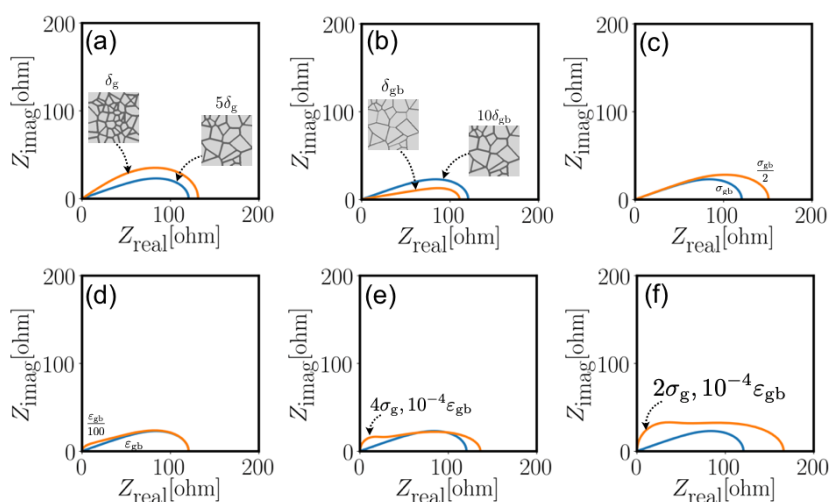


Figure 81. Snapshot of the LLZO(001)/LCO(100) interface from *ab initio* molecular dynamics. Lithium, lanthanum, zirconium, oxygen, and cobalt atoms are green, yellow, cyan, red, and blue, respectively. The diffusion trajectory is highlighted by the orange spheres in the zoomed-in representation at right.

Table 7. Summary of nudged elastic band (NEB)-computed activation energies for Li-ion diffusion in bulk LLZO under various strains.

Hydrostatic strain	Single-ion hopping	Dimer	Trimer
+ 2.5%	0.146 eV (0.190 eV)	0.272 eV (0.142 eV)	N.A.
0	0.151 eV (0.148 eV)	0.152 eV (0.097 eV)	0.158 eV
- 2.5%	0.216 eV	0.253 eV (0.225 eV)	0.234 eV
Hydrostatic strain (with single vacancy)	Single-ion hopping	Dimer	Trimer
+ 2.5%	0.221 eV (0.203 eV)	0.186 eV (0.558 eV)	0.433 eV (0 eV)
0	0.344 eV (0 eV)	0.375 eV (0.537 eV)	0.491 eV (0.312 eV)
- 2.5%	0.378 eV (0 eV)	0.422 eV (0.632 eV)	0.547 eV (0.345 eV)
Uniaxial strain, <i>a</i>	Single-ion hopping	Dimer	Trimer
+ 5%	0.331 eV (0.059 eV)	0.124 eV (0.542 eV)	0 eV (0.271 eV)
0	0.151 eV (0.148 eV)	0.152 eV (0.097 eV)	0.158 eV
- 5%	0.142 eV (0.294 eV)	0.187 eV (0.292 eV)	0.399 eV (0.246 eV)
Uniaxial strain, <i>a</i> (with single vacancy)	Single-ion hopping	Dimer	Trimer
+ 5%	0.119 eV (0.106 eV)	0.191 eV (0.625 eV)	0.340 eV (0.147 eV)
0	0.344 eV (0 eV)	0.375 eV (0.537 eV)	0.491 eV (0.312 eV)
- 5%	0.268 eV (0.518 eV)	0.510 eV (0.687 eV)	0.758 eV (0.468 eV)
Uniaxial strain, <i>b</i>	Single-ion hopping	Dimer	Trimer
+ 5%	0.131 eV	0.141 eV (0.381 eV)	0.147 eV (0.368 eV)
0	0.151 eV (0.148 eV)	0.152 eV (0.097 eV)	0.158 eV
- 5%	0.153 eV	0.174 eV (0.116 eV)	0.222 eV (0.179 eV)
Uniaxial strain, <i>b</i> (with single vacancy)	Single-ion hopping	Dimer	Trimer
+ 5%	0.268 eV (0.266 eV)	N. A.	0.404 eV (0.066 eV)
0	0.344 eV (0 eV)	0.375 eV (0.537 eV)	0.491 eV (0.312 eV)
- 5%	0.218 eV (0.396 eV)	0.419 eV (0.535 eV)	0.474 eV (0.354 eV)
Uniaxial strain, <i>c</i>	Single-ion hopping	Dimer	Trimer
+ 5%	0.304 eV (0.152 eV)	0.337 eV (0.342 eV)	0.160 eV (0.309 eV)
0	0.151 eV (0.148 eV)	0.152 eV (0.097 eV)	0.158 eV
- 5%	0 (0.273 eV)	0.043 eV (0.263 eV)	0.439 eV (0.210 eV)
Uniaxial strain, <i>c</i> (with single vacancy)	Single-ion hopping	Dimer	Trimer
+ 5%	0.192 eV (0.438 eV)	0.315 eV (0.455 eV)	0.847 eV (0.405 eV)
0	0.344 eV (0 eV)	0.375 eV (0.537 eV)	0.491 eV (0.312 eV)
- 5%	0.106 eV (0.082 eV)	0.333 eV (0.526 eV)	0.439 eV (0.180 eV)

**Modeling of Microstructural Effects on Electrochemical Impedance Spectra.** Last quarter, the team demonstrated a model to simulate the EIS of a polycrystalline SE, which allows them to bridge understanding of microstructure with an experimentally measurable quantity. This quarter, they report an initial parametric study to quantitatively identify the influence of material parameters: ionic conductivities of the grain ( $\sigma_g$ ) and the GB ( $\sigma_{gb}$ ), permittivities of the grain ( $\epsilon_g$ ) and GB ( $\epsilon_{gb}$ ), and microstructural parameters: grain size ( $\delta_g$ ) and GB thickness ( $\delta_{gb}$ ). This initial analysis identifies parameters that have strong or weak effects on the overall impedance to inform experimental fabrication. For example, the GB permittivity has a very weak effect on the overall impedance, except at very high frequencies ( $> 1$  MHz). The ionic conductivity of both the grain and the GB have strong effects and increase the DC or low frequency impedance almost proportionally to the volume occupied by the grain and the GB. The model is also currently being explored for further validation from modeling efforts at German collaborators at DLR, and available experimental results from LLNL and the VTO U.S.-Germany collaboration. Future quarters will include focus on understanding the influence of GB space charge and stress effects.



**Figure 82.** Parametric study of an electrochemical impedance spectroscopy (EIS) model for a polycrystalline sample. A sinusoidally varying voltage with a varying frequency (zero to  $10^8$  Hz) is applied, simulating an EIS experiment. Grain and grain boundary (GB) conductivity play a strong effect, while the GB permittivity plays a weak effect for the considered example system.

## Patents/Publications/Presentations

### Publication

- Heo, T. W., A. Grieder, B. Wang, S. A. Akhade, L. F. Wan, L-Q. Chen, N. Adelstein, and B. C. Wood. “Microstructural Impacts on the Ionic Conductivity of Garnet Solid Electrolytes: A Combined Atomistic-Mesoscale Approach.” In review.

## Task 3.10 – First-Principles Modeling of Cluster-Based Solid Electrolytes (Puru Jena, Virginia Commonwealth University)

**Project Objective.** The objective of the project is to use cluster-ions, which are stable atomic clusters that mimic the chemistry of individual atoms, as the building blocks of new SEs for Li-ion batteries and the corresponding battery system. The advantages of using cluster-ions to replace elemental ions is that the size, shape, and composition of the former can be tailored to achieve higher superionic conductivity, electrochemical stability, and charge transfer across the solid-solid interfaces than the conventional materials. More specifically, the goal is to develop superior SEs based on cluster-ions and to model these SEs and their interfaces with electrodes, especially with the Li-metal anode, for successful integration into high-performance SSBs for EVs. The team will model and screen cluster-based SEs that, compared to conventional SEs, have low activation energies, practical room-temperature ionic conductivities, wide electrochemical stability windows, and desired mechanical properties that, for example, can inhibit the Li-metal anode dendrite growth. They will provide a fundamental understanding of the ionic conduction mechanism in the newly developed, cluster-based SEs and identify means to further improve property metrics via chemical and defect engineering. The team will model the interfacial properties, such as the structural, chemical, electrochemical, and ion/charge transfer properties, between the cluster-based SEs and electrodes at the atomic level, as well as find the interfacial coating materials with desired properties. Based on accumulated data from modeling, they will establish links between the basic parameters of the cluster-ions and the bulk/interface properties, which can directly guide experiments. Meanwhile, the team will work closely with experimentalists in the BMR Program to complement the project's theoretical efforts and to guide them in focused development of the predicted cluster-based SEs and the interfaces.

**Project Impact.** The proposed project will open a new avenue for guiding experiments in the synthesis of SSBs equipped with cluster-based SEs and capable of operating over a wide temperature range. Modeling and understanding of the ionic conduction of cluster-based electrolytes and their interfacial properties with electrodes, especially with Li-metal anode, will enrich current battery science and also train the future work force in SSB development for next-generation EVs by supporting postdoctoral fellows.

**Approach.** This project will employ multi-scale theoretical methods and computational techniques.

**Out-Year Goals.** The out-year goals involve modeling development of new cluster-based SE materials and database.

**Collaborations.** The team is working with Dr. J. Nanda of ORNL on antiperovskite-based SSEs.

### Milestones

1. Structural studies of the designed cluster-based SE materials with selected cluster-ions. (Q1, FY 2020; Completed, December 31, 2019)
2. Property characterizations of stable cluster-based SE materials. (Q2, FY 2020; Completed, March 31, 2020)
3. Ionic conductivity characterization for cluster-based SE materials and the ionic conduction mechanism. (Q3-Q4, FY 2020; In progress)
4. Complete development of new cluster-based SE materials with a database. (Q4, FY 2021)

## Progress Report

Research toward this quarter's milestone (ionic conductivities characterization of the cluster-based SE materials) is proceeding as planned. The number of SE materials covered in this period accounts for half of the total number of materials under study. The other half will be covered by the end of next quarter, according to the plan. The team has conducted the MD and data analysis for ionic conductivities on the newly developed cluster-based SE materials. For each material, they have studied the ionic diffusion coefficients and conductivities at different temperatures. The diffusivity at room temperature and activation energy of each material are obtained by extrapolation or direct calculation using the Arrhenius relationship.

All the studied new SE materials exhibit high ionic conductivities and low activation energies. A demonstration of this is given in Figure 83, showing the cases of five out of more than a dozen new SE materials in the current study. The major findings are as follows: (1) All newly developed SE materials under the current study exhibit room-temperature ionic conductivities over the range of  $10^{-4}$ - $10^{-2}$  S/cm and activation energies in the range of 1.5-3.5 eV. (2) Presence of multiple polyatomic clusters is preferred. (3) Note that the current room-temperature ionic conductivities and activation energies are for stoichiometric materials. Therefore, each of the newly developed SE materials here should be viewed as a prototype material based on which a number of nonstoichiometric (for example, with Li-excess) or chemically altered (for example, with group element substitutions) SE candidates can be further developed. These should exhibit even higher ionic conductivities, as already well-known in the case of, for example,  $\text{Li}_6\text{PS}_5\text{Cl}$ , where the nonstoichiometric counterpart (with lithium excess)  $\text{Li}_{6.72}\text{PS}_5\text{Cl}$  exhibits a room-temperature ionic conductivity over  $10^{-3}$  S/cm, which is 3 orders of magnitude higher than that of the stoichiometric case.

The AIMD simulations are carried out for each material using a large supercell with its three sides well above  $10 \text{ \AA}$  and containing hundreds of atoms. In each case, AIMDs are performed at 5 to 8 different temperatures. A typical AIMD lasts over 120 ps with a 2 fs time step, where 20 ps is allowed for the system to reach thermal equilibrium before the data are collected to calculate the MSD for all the atomic species in the system. The diffusivity at each temperature is then calculated by linear fitting to the MSD. Those data points of the diffusivity will be discarded if phase transitions or vibrational instabilities are spotted from the analysis. Those remaining points are applied to the Arrhenius relationship to extrapolate to the room temperature and extract the activation energy.

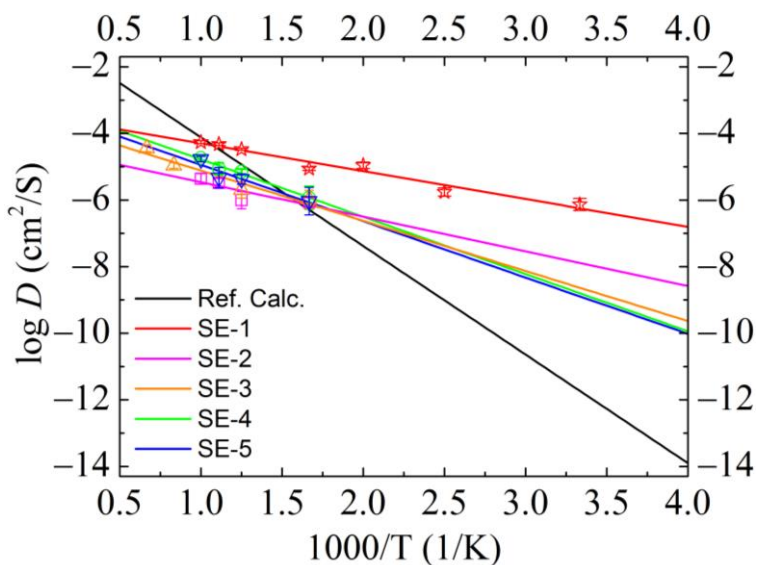


**Figure 83.** Calculated diffusivities of five typical cluster-based solid electrolytes (SE) fitted by the Arrhenius relation. The diffusivity of stoichiometric  $\text{Li}_6\text{PS}_5\text{Cl}$  (Ref. Calc.) is used as a benchmark for comparison, with a poor room-temperature (RT) ionic conductivity in the order of  $10^{-7}$ - $10^{-6}$  S/cm and a high activation energy between 5.0-6.0 eV. Clearly, these new SE materials exhibit much (3 to 5 orders of magnitude) higher RT diffusivity than that of the stoichiometric  $\text{Li}_6\text{PS}_5\text{Cl}$ . The corresponding ionic conductivities at RT are over  $10^{-4}$ - $10^{-2}$  S/cm, with activation energies between 1.5-3.5 eV. In particular, the calculated RT conductivity of “SE-1” is 0.08-0.09 S/cm with a low activation energy just over 1.5 eV.

## Patents/Publications/Presentations

### Publication

- Fang, H., and P. Jena. “Solid Electrolytes based on Multiple Polyatomic Units with Liquid-Like Ionic Conductivity.” In preparation, 2020.

### Presentation

- EERE Progress Meeting (April 6, 2020): “First-Principles Modeling of Cluster-Based Solid Electrolytes.”

## Task 3.11 – Predictive Engineering of Interfaces and Cathodes for High-Performance All-Solid-State Lithium-Sulfur Batteries (Badri Narayanan, University of Louisville)

**Project Objective.** The primary goal of this project is to leverage data-driven methods and ML strategies to develop accurate multi-physics models for all-solid-state Li-S battery (ASLSB) materials that can capture electrochemical and transport phenomena over atomic-to-mesoscopic length/timescales; these models will be rigorously validated by synthesis and advanced characterization experiments. The team will leverage the predictive power of these models, alongside synthesis/characterization experiments and battery fabrication to address longstanding issues at the electrode/electrolyte interfaces in ASLSBs. The project’s proposed technology involves the following: (1) halide-doped solid sulfide electrolytes that can concurrently provide high  $\text{Li}^+$  ion conductivity and suppress dendrite growth; (2) novel mesoporous cathode composed of interconnected carbon nano-cages co-infiltrated with sulfur and sulfide electrolyte, which hold potential to allow high sulfur loading and optimal ion/electron pathways; and (3) functionalization of sulfide electrolyte with ionic liquids to improve physical contact and minimize impedance at the cathode/electrolyte interface.

**Project Impact.** ASLSBs remain far from commercialization due to poor understanding of the fundamental electrochemical/chemical and transport processes that occur at the interfaces, especially at atomic to mesoscopic scales. Successful development of the proposed predictive models (at multiple scales) will bridge this knowledge gap and will advance fundamental understanding of reaction chemistry, kinetics, charge transfer, and dendrite growth at electrified solid-solid interfaces. This, in turn, would enable predictive design of effective strategies to mitigate interfacial problems in ASLSBs, including poor interfacial contact, interfacial impedance to  $\text{Li}^+$  ion transport, and poor electron/ion conduction within cathodes. Ultimately, the fundamental knowledge gained by this work will lead to development of high-performance ASLSBs that meet DOE targets of specific energy (350 Wh/kg @C/3), sulfur loading ( $> 6 \text{ mg/cm}^2$ ), and high cycle life (1000).

**Approach.** The project brings together innovative solutions in multi-scale materials modeling, electrolyte synthesis, fabrication of cathode architecture, and electrolyte functionalization to overcome the issues at electrode/electrolyte interfaces in ASLSBs. The central idea is to employ a data-driven and ML-based approach to develop accurate multi-physics battery models at atomic-to-mesoscopic scales. This approach overcomes critical problems with existing model development methods by foregoing need for pre-defined functional forms, introducing deep-learning technique to describe reactivity, and employing optimization methods that do not require human intuition. Multi-scale simulations based on the newly developed models will provide insights into electrochemical phenomena at electrode/electrolyte interfaces.

**Out-Year Goals.** In Year 1, the goal is to optimize electrolyte composition and to develop accurate reactive atomic-scale interaction models of representative SSE system and ionic liquids.

**Collaborations.** The team collaborates with the groups under Dr. A. Ngo and Dr. L. A. Curtiss at ANL for quantum simulations of battery systems; they plan to collaborate with Dr. J. Nanda at ORNL for advanced spectroscopic *in situ* characterization of interfaces.

### Milestones

1. Demonstrate scalable electrolyte synthesis with precise composition control. (Q1, FY 2020; Completed)
2. Computationally optimize electrolyte composition for high  $\text{Li}^+$  conductivity ( $10^{-3} \text{ S/cm}$ ) and good electrochemical stability. (Q2, FY 2020; Completed)
3. Synthesize cathode architectures based on interconnected carbon nano-cages with co-infiltrated sulfur and SSE; obtain baseline for battery performance. (Q3, FY 2020; Completed)
4. Develop reactive models for electrolyte, and ionic liquid. (Q4, FY 2020; In progress)

## Progress Report

This quarter, the team made good progress in the following: advancement of fundamental understanding of the role played by halogen dopant in electrolyte decomposition at the interface between anode and sulfide electrolyte using AIMD; synthesis/characterization of composite cathodes; and fabrication and electrochemical testing of preliminary coin-cell batteries with the project's synthesized cathodes and halide-doped sulfide electrolyte.

### AIMD Simulations to Understand Evolution of the Interface between Lithium Anode and Electrolyte.

Last quarter, the team employed AIMD and DFT calculations to computationally identify key sulfide compositions that provide high  $\text{Li}^+$  ion conductivity. Specifically, they found that co-doping sulfide electrolytes (SSEs) with multiple halogens (X) results in S/X disorder in the crystal; this, in turn, enables faster  $\text{Li}^+$  ion conduction than that possible in SSEs with one type of halogen. For instance, the AIMD simulations showed that  $\text{Li}^+$  ion diffusivity in  $\text{Li}_6\text{PS}_5\text{F}_{0.5}\text{Cl}_{0.5}$  is  $\sim 2.5$  times higher than that in  $\text{Li}_6\text{PS}_5\text{Cl}$ , and  $\sim 4$  times that in  $\text{Li}_6\text{PS}_5\text{F}$ ; consistent with the team's experimental observations. Aside from faster  $\text{Li}^+$  ion conduction, aliovalent doping of SSE with multiple halogens (with fluorine as one halogen) also offers promise to simultaneously achieve a stable SEI (containing  $\text{LiX}$ ) at the anode during battery operation.

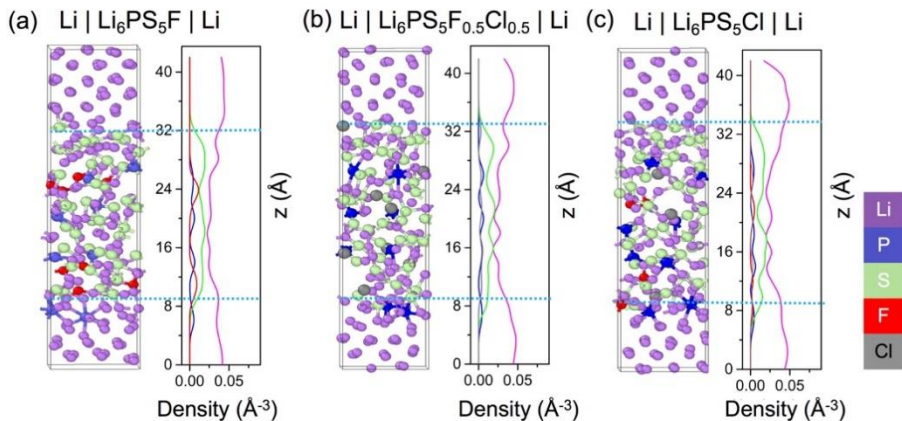


**Figure 84.** *Ab initio* molecular dynamics simulations of evolution of anode / solid-state electrolyte (SSE) interface at 300 K. The equilibrated atomic-scale structure of the interface between Li (001) and SSE (001) is shown for three electrolyte compositions, namely (a)  $\text{Li}_6\text{PS}_5\text{F}$ , (b)  $\text{Li}_6\text{PS}_5\text{F}_{0.5}\text{Cl}_{0.5}$ , and (c)  $\text{Li}_6\text{PS}_5\text{Cl}$ . In each panel, the spatial distribution of lithium (purple), phosphorus (blue), sulfur (green), fluorine (red), and chlorine (grey) atoms (in terms of number density) is shown in the direction normal to the interface.

and  $\text{Li}_6\text{PS}_5\text{Cl}$  at 300 K for 20 ps. For all cases, they investigated the interface between the Li-anode and SSE oriented such that their crystallographic 001 directions are aligned normal to the interface (Figure 84); note this interface [that is,  $\text{Li} (001) | \text{Li}_6\text{PS}_5\text{X} (001) | \text{Li} (001)$ ] was chosen since the as-formed hetero-structure was nearly epitaxial ( $< 1\%$  strain) for all electrolyte cases. They employed  $1 \times 1 \times 2$  supercell of SSE (001) and slabs of  $3 \times 3$  Li (001) slabs containing 6 layers on each side of the SSE. In all the cases, the team finds three distinct atomic processes: (a) breaking of  $\text{PS}_4^{3-}$  structural units, (b) formation of new Li-P and Li-S bonds (forming  $\text{Li}_3\text{P}$  and  $\text{Li}_2\text{S}$  clusters), and (c) migration of halogens from SSE into anode forming Li-X bonds (Figure 84). These observations are consistent with previous reports in the literature. However, the frequency of occurrence of the three processes is strongly governed by the composition of the electrolyte (Figure 85).

Careful analysis of the PDFs of Li-P, Li-S, Li-X, and P-S for the three electrolyte cases indicates new Li-P and Li-S bonds are most prevalent in  $\text{Li} | \text{Li}_6\text{PS}_5\text{Cl} | \text{Li}$  which is completely devoid of any fluorine (Figure 85a-b). Consistent with this observation, dissociation of P-S bonds is highest in  $\text{Li} | \text{Li}_6\text{PS}_5\text{Cl} | \text{Li}$  interface (Figure 85d). This finding can be attributed to the strong preference of lithium to bind with fluorine (as compared S/P/Cl), as illustrated by the significantly higher first neighbor peak for Li-F (in  $\text{Li}/\text{Li}_6\text{PS}_5\text{F}$ ) as compared to Li-Cl (Figure 85c). In all F-containing SSEs, nearly all fluorine from SSE migrate to the anode/SSE interface

at the anode during battery operation. This promise is fueled by experimental reports indicating that functionalization of lithium anode with fluorine enables stable battery cycling. Despite these findings, a fundamental understanding of the interfacial reactions for electrolytes doped with multiple halogens is scarce.

The team performed AIMD simulations to track the structural evolution of anode/SSE interfaces for three electrolyte cases:  $\text{Li}_6\text{PS}_5\text{F}$ ,  $\text{Li}_6\text{PS}_5\text{F}_{0.5}\text{Cl}_{0.5}$ ,

coordinating with lithium in a near-tetrahedral arrangement (Li-F shows an average coordination number is  $\sim 3.8$ ). Note that this coordination number is significantly lower than that observed in rock-salt crystal of LiF (6); nevertheless, there is preponderance of new Li-F bonds near the interface. The co-doped electrolyte  $\text{Li}_6\text{PS}_5\text{F}_{0.5}\text{Cl}_{0.5}$  demonstrates clear energetic preference for Li-F bonds over Li-Cl bonds (the first peak for Li-F is nearly twice as high as Li-Cl). Interestingly, this co-doping also results in the highest number of surviving P-S bonds. These findings indicate that F-containing SSEs are more likely to form stable SEI owing to lower dissociation of P-S bonds. More importantly, the project's AIMD simulations indicate that SSE containing multiple halogen dopants (with high  $\text{Li}^+$  ion conductivity) are at least similar to single-halogen counterparts in terms of stability against lithium metal. Electrochemical experiments on symmetric Li | SSE | Li cells to validate the theory findings are in progress.

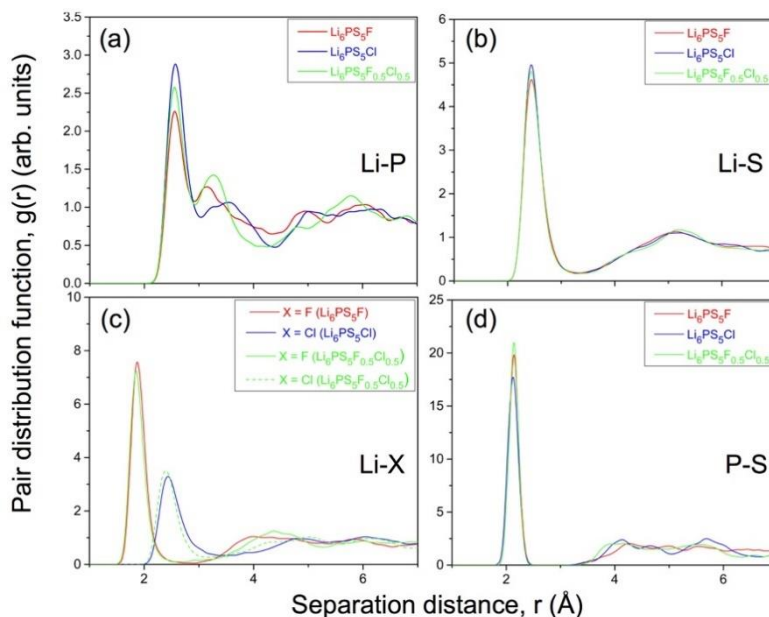


Figure 85. Partial distribution function (PDF) of (a) Li-P, (b) Li-S, (c) Li-X, and (d) P-S pairs in equilibrated structure of the anode / solid-state electrolyte interfaces obtained from *ab initio* molecular dynamics (AIMD) simulations. The PDFs for the three electrolyte compositions  $\text{Li}_6\text{PS}_5\text{F}$ ,  $\text{Li}_6\text{PS}_5\text{Cl}$ , and  $\text{Li}_6\text{PS}_5\text{F}_{0.5}\text{Cl}_{0.5}$  are shown as red, blue, and green lines, respectively. The PDFs are averaged over the last 3 ps.

**Synthesis of Mesoporous Composite Cathode.** Mesoporous composite cathodes made up of carbon nanocages

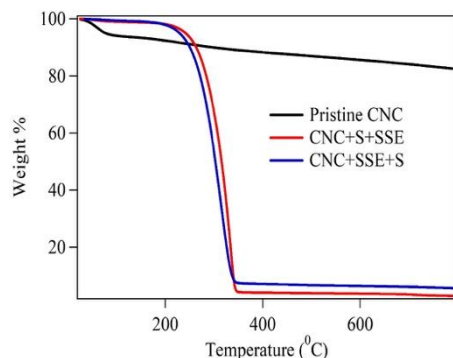
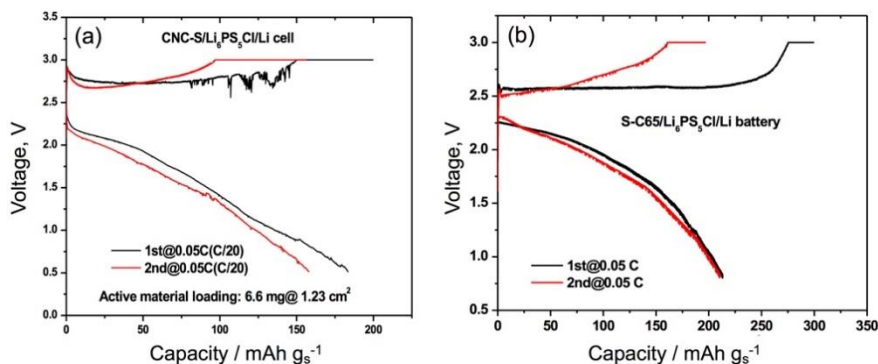


Figure 86. Thermogravimetric analysis of mesoporous carbon architectures made up of pristine carbon nanocages (CNCs, black), and those containing CNCs infiltrated with sulfur and solid-state electrolyte. The team has also investigated the effect of order of infiltration (red: S first; blue: S last).

mesoporous composite cathodes made up of carbon nanocages (CNCs) encapsulating SSE and sulfur are lucrative to achieve large surface area  $\sim 1000$   $\text{m}^2/\text{g}$  and high sulfur loading ( $> 6$   $\text{mg}/\text{cm}^2$ ). In the last two quarters, the team successfully demonstrated that CNC architectures can be precisely engineered using their recently patented process involving thermolysis of sol-gel precursor consisting of nickel salt and carbon precursor, and templating on nickel nanoparticles. Additionally, they successfully achieved co-infiltration of sulfur and SSE into CNC cathodes. This quarter, the team performed further characterization of as-prepared pristine CNCs and CNCs infiltrated with sulfur and SSE using TGA (Figure 86). The sample of CNCs first infiltrated with sulfur followed by SSE infiltration is identified as CNC+S+SSE, while the sample with reverse infiltration process is identified as CNC+SSE+S. TGA results indicate that the weight loss of pristine CNCs is only  $\sim 10\%$ , while both infiltrated samples show  $> 93\%$  weight loss. The TGA curves for both infiltrated samples show typical features for the loss of sulfur in the given temperature window. However, there is a loss of components from the SSE, and accordingly the team made a conservative estimate of 60% sulfur in the cathode material for the estimation of the discharge current and hence the capacity.

**Fabrication and Electrochemical Testing of Coin-Cell Batteries with Different Mesoporous Carbon Cathode Architectures and  $\text{Li}_6\text{PS}_5\text{Cl}$  SE.** The team prepared coin-cell batteries with two types of mesoporous cathode architectures: (1) the CNC-based cathode co-infiltrated with sulfur and SSE; and

(2) S-C65 cathode featuring an existing architecture in the literature. For CNC cathode, they mixed 11 mg of CNC-S with 6.6 mg of teflonized acetylene black (TAB-2) binder ratio (5:3 by weight) in agate mortar.



**Figure 87.** Charge-discharge characteristics of coin-cells made up of (a) CNC-S-SSE (60% sulfur based on thermogravimetric analysis) cathode, and (b) S-C65 cathode with  $\text{Li}_6\text{PS}_5\text{Cl}$  electrolyte. The team used a current of C/20 for the tests.

Subsequently, the team pressed the electrode on to stainless-steel mesh having area of  $1.13 \text{ cm}^2$ , which is annealed at  $100^\circ\text{C}$  for 5 hours in a vacuum oven. The entire cell assembly is carried out in an argon-filled dry glove box. The active material CNC-S was used as a working electrode, and lithium foil as an anode separated by SSE  $\text{Li}_6\text{PS}_5\text{Cl}$  in a 2032 coin-type cell. The Galvano static discharge-

charge measurements were carried out using Arbin instrument. Discharge-and charge measurement is carried out at the voltage range of 3.0-0.5 V with a current of 83.5 mA/g based on the sulfur weight determined by the TGA data discussed in Figure 86. Li- $\text{Li}_6\text{PS}_5\text{Cl}$ -CNC/S composite electrode showed a capacity of 180 mAh/g (0.5 C) after the 1<sup>st</sup> cycle and could be recharged to 3 V (Figure 87a). The observed capacity is similar to that observed in LiIn- $\text{Li}_6\text{PS}_5\text{Cl}$ -C-65:S full cell in literature using a current at 0.1 C rate [100 mAh/g; Ohno et al. *Chemistry of Materials* 31 (2019): 2930]. Detailed investigation into cycle life of Li-  $\text{Li}_6\text{PS}_5\text{Cl}$ -CNC/S coin cells is in progress. The team will focus ongoing efforts on optimizing the architecture and synthesis process for composite cathodes to simultaneously achieve high cycle life, high S-loading, and high capacity; in all these cases, electrolyte compositions identified by computations for high  $\text{Li}^+$  conductivity will be employed.

For S-C65 cathode, the team first mixed S:C-65 (2:1 ratio) using a ball milling machine for 5 hours at 300 rpm and calcined at  $115^\circ\text{C}$  for 1 hour at inert atmosphere. The slurry of the cathode material was prepared by mixing 92 wt% of S:C-65(2:1) with 3 wt% of conducting binder (AB), and 5 wt% of PVDF-NMP. The CMC water-based binders show much better coating compared to PVDF-NMP based coating, which shows inhomogeneity and cracks. With S-loading of  $1.5\text{-}2 \text{ mg/cm}^2$ , Li- $\text{Li}_6\text{PS}_5\text{Cl}$ -C-65/S composite electrode showed a capacity of  $\sim 220 \text{ mAh/g}$  (0.5 C) after the 1<sup>st</sup> cycle and could be recharged to 3 V (Figure 87b). These results are consistent with literature on LiIn- $\text{Li}_6\text{PS}_5\text{Cl}$ -C-65:S full cell in terms of charge-discharge capacity. Further efforts to improve the sulfur loading, as well as optimization of S-C synthesis process by using different carbon and sulfur mix ratio are under way.

### Patents/Publications/Presentations

The project has no patents, publications, or presentations to report this quarter.

## Task 3.12 – First-Principles Modeling and Design of Solid-State Interfaces for the Protection and Use of Lithium-Metal Anodes (Gerbrand Ceder, University of California Berkeley)

**Project Objective.** The project objective is to determine the design principles that control the SE / lithium electrode interfaces by determining the reaction products stemming from pairing SEs and lithium metal. A rigorous analysis is based on computing electrolyte phase-diagrams closed and open to lithium. Li-ion transport properties in bulk electrolytes and interfacial products will be assessed through AIMD and NEB calculations. Simultaneously, develop a robust framework to identify factors controlling Li-dendrite propagation within SEs and interfacial products by accounting for irregularities, defects, and GBs, through a model that includes elements of fracture mechanics, thermodynamics, and electrochemistry.

**Project Impact.** The project will lead to understanding of the complex evolution of Li-metal / SE interfaces during electrochemical cycling. The understanding of such a process is necessary to determine design principles to develop reliable ASSBs.

**Approach.** A HT computation method is used to screen suitable SEs with high electro-chemical stability and high ionic conductivity, by incorporating NEB and AIMD method. Meanwhile, DFT is used to calculate bulk elastic constants of involved material, and surface energies and interface de-cohesion energies of GBs; finally, continuum theorem (elastic-plastic-fracture mechanics) is used to assess the resilience of SEs and grain/particle boundaries toward lithium dendrite growth and propagation. The finite element method is used to couple several physical processes, including electro-chemical deposition, ionic diffusion, thermal expansion, and mechanical contacting.

**Out-Year Goals.** Obtain design criteria for SEs that can resist unstable lithium propagation by computing elastic properties surface energies, and decohesion energies. Adapt fracture mechanics models describing crack propagation to lithium dendrite propagation in different scenarios.

**Collaborations.** There are no collaborative activities this quarter.

### Milestones

1. Determine materials design criteria based on developed failure models. (Q1, FY 2020; Completed)
2. Extend ionic conductor failure model to include effects of mixed ionic and electronic conduction. (Q2, FY 2020; Completed)
3. Adapt fracture models that describe crack propagation in materials to lithium dendrite propagation in perfect crystal with GBs. (Q3, FY 2020; On target)
4. Assess resistance to metal propagations and failure in candidate solid ionic conductor materials. (Q3, FY 2020; On target)

## Progress Report

### Lithium Metal can Propagate and Completely Fill in Voids in the SE

Lithium metal can be deposited within voids inside the SE when the surface overpotential at the location of the void is large enough. Figure 88 presents a schematic illustration of the metal deposition process in the voids.

Before cell cycling, no lithium metal is present in the voids. If the surface overpotential requirement is satisfied, a thin layer of lithium metal is plated on the surface of the void at an initial deposition rate (Stage I: metal initiation). After initiation stage, the void is gradually filled by lithium metal at a higher deposition rate (Stage II: metal growth). After the void is fully occupied by lithium metal at the end of the growth stage, the hydrostatic pressure ( $P$ ) starts to build up as new lithium metal continues to be deposited into the confined space.

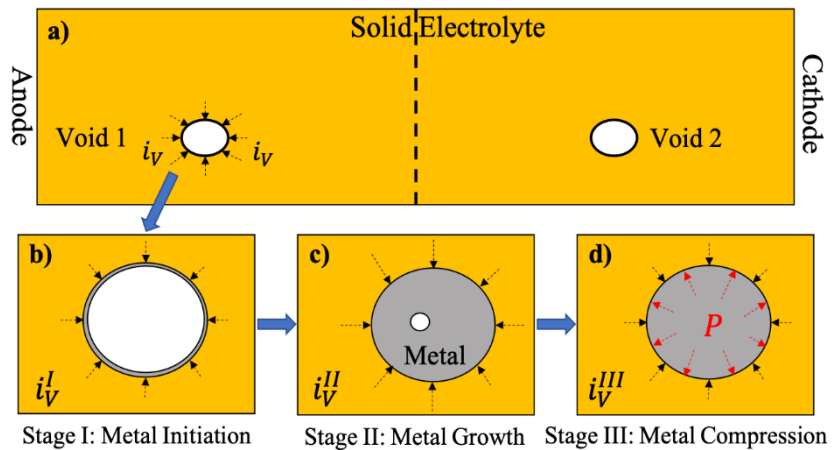


Figure 88. Schematic illustration of different stages of metal deposition in the void.

The increase in hydrostatic pressure in turn reduces the surface overpotential and decreases the deposition rate until no more metal can be inserted (Stage III: metal compression).

### Fracture of the SE can Happen if Developed Pressure in the Void is Large Enough

The Li-metal deposition in the confined void leads to an increase in the hydrostatic pressure in the metal, which further decreases the overall deposition overpotential and the deposition rate in the void. As shown in Figure 89, the pressure is zero before the void is completely filled by the lithium metal, but shortly after the void

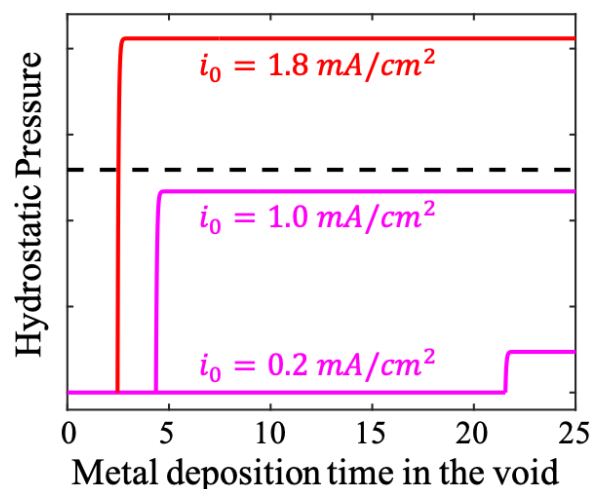


Figure 89. Pressure developed in the metal under three applied current densities.

completely filled, the pressure rapidly increased to a stable maximal value within several minutes. The horizontal black line represents the critical pressure that the SE material can withstand before fracture. For a given SE material (such as LPS or LLZO) and SE microstructure (such as porosity or pore size), different maximal hydrostatic pressure can be developed under different applied current density. When the applied current density is large enough (such as  $> 1 \text{ mA/cm}^2$ , as shown in Figure 89), the developed hydrostatic pressure in the lithium metal is higher than the critical pressure allowed for the SE, which will cause fracture of the SE. More deposition will happen in the newly fractured area due to the higher curvature, which leads to further fracture and propagation of lithium metal.

## Patents/Publications/Presentations

The project has no patents, publications, or presentations to report this quarter.

## Task 3.13 – Predicting the Nucleation and Evolution of Interphases in All-Solid-State Lithium Batteries

(Sabrina (Liwen) Wan, Lawrence Livermore National Laboratory)

**Project Objective.** The goal of this project is to develop and apply a suite of new computational tools to predict early-stage formation of metastable interphases in SSBs. To achieve this goal, this project focuses on meeting three primary objectives corresponding to different regimes within the early-stage interphase formation: (1) identify chemical motifs for pre-nucleation; (2) predict possible interphase structures; and (3) model the kinetics of interphase formation.

**Project Impact.** Degradation of SSE and formation of undesired secondary interphases at the solid electrolyte / electrode interfaces are some of the key issues that limit SSB technology from practical applications. The computational tools developed in this project will allow modeling of nucleation and formation of interphases with quantum-level accuracy and significantly improved efficiency compared to currently available methods. Completion of this project will also provide valuable insights into the correlation between local chemistry and interphase formation, which can be used to inform the design of interfacial structures to lower interfacial resistance and to extend the cycling life of SSBs.

**Approach.** The project approach centers on close integration of *ab initio* simulations, ML, and stochastic methods to probe chemistry and nucleation across broad ranges of time and length scales. First, the team will identify chemical motif, which acts as chemical precursor for pre-nucleation based on ML and large-scale AIMD simulations. Second, they will predict possible interphase structures based on stochastic minimizations of population-weighted chemical motifs identified from the MD simulations. Third, they will model the kinetics of interphase formation and evolution using kinetic MC. To test the general applicability of the proposed computational methods, the team considers a variety of commercially viable SE and cathode materials, including cubic LLZO and LiPON SEs and LiCoO<sub>2</sub> (LCO) and LiFePO<sub>4</sub> (LFP) cathodes. These materials also represent a range of degrees of stability arising from their intrinsic properties—in particular, LiPON|LCO, LLZO|LCO, and LLZO|LFP are expected to form stable, less stable, and reactive interfaces, respectively.

**Out-Year Goals.** The future goal is to predict practical strategies to either facilitate the formation of desired interphase that allows for fast Li<sup>+</sup> diffusion and is stable on cycling or suppress the formation of undesired interphase to reduce interfacial impedance of ASSBs.

**Collaborations.** There are no collaborative activities this quarter.

### Milestones

1. Construct initial interfacial models for LiPON|LCO, LLZO|LCO, and LLZO|LFP. (Q1 FY 2020; Completed)
2. Perform AIMD simulations for these interfaces. (Q2, FY 2020; In progress)
3. Train and validate ML potentials. (Q3, FY 2020; Initiated)
4. Apply ML potentials to sample interfacial chemistry. (Q4, FY 2020; On schedule)

## Progress Report

**Construction of Interfacial Models.** The team has created different initial interfacial models of LiPON|LCO, LLZO|LCO, and LLZO|LFP. For LiPON, which exhibits an amorphous structure, they considered two distinct surface terminations, with and without nitrogen atoms exposed on the surfaces. For LCO, they considered three surface facets, that is, (100), (110), and (104), which are known low-energy, non-polar surfaces. For LLZO, they considered the (001) surface with different Li/La terminations. At last, for LFP, they considered the (010), (101), (111), and (201) surfaces, which all have relative low surface energies. In addition, when constructing the initial interfacial models of LiPON|LCO, LLZO|LCO, and LLZO|LFP, the team varies lithium concentration at the interfaces to represent charge and discharge conditions during battery operation. These initial interface models are then fully relaxed using DFT. (See Figure 90 as an example of relaxed atomic configurations of LiPON(100)|LCO(100), LLZO(001)|LCO(100), and LLZO(001)|LFP(010) interfaces.)

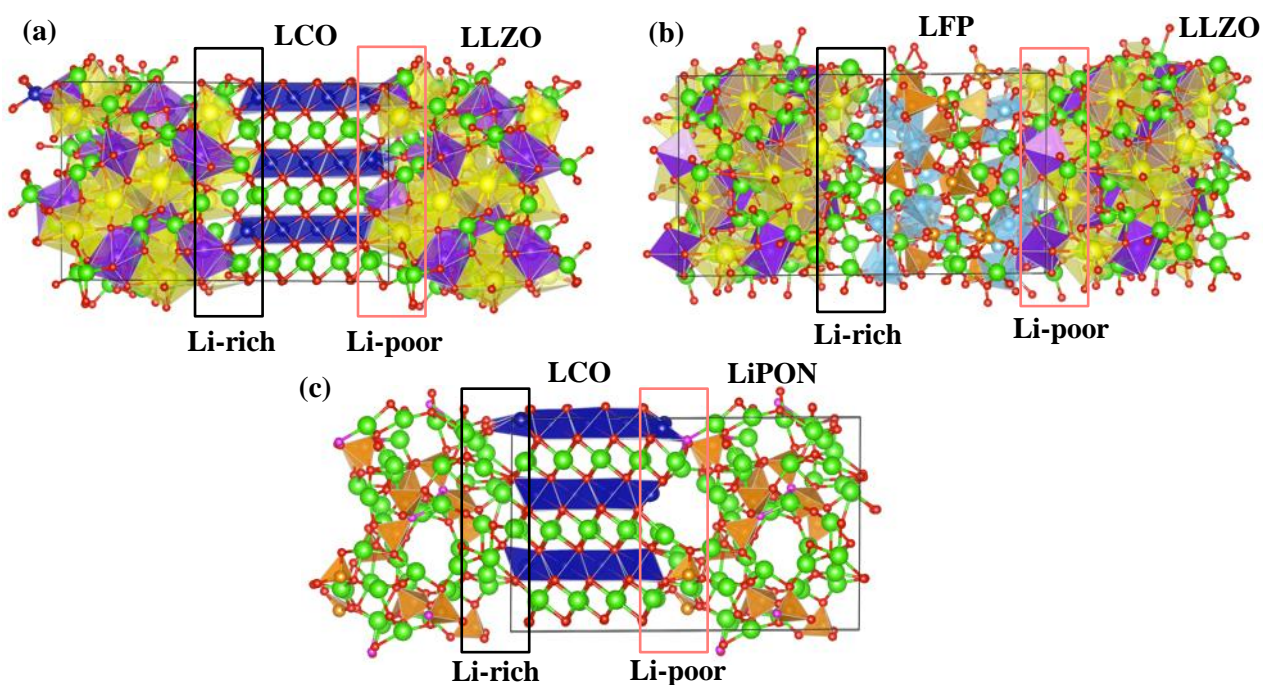


Figure 90. Initial structure models of (a) LLZO(001)|LCO(100), (b) LLZO(001)|LFP(010), and (c) LiPON(100)|LCO(100) interfaces. The lithium, lanthanum, zirconium, oxygen, cobalt, iron, phosphorus, and nitrogen atoms are represented as green, yellow, purple, red, dark blue, light blue, orange, and magenta spheres, respectively.

**Atomistic Simulations of Interfaces.** With the aim to study interdiffusion of ions across various interfaces and to identify chemical motifs that may lead to nucleation of new interphases, the team employs two approaches. The first approach relies on using high-temperature AIMD simulations to trace the dynamics of ions at interfaces. The simulation temperature here has to be carefully tuned to ensure sufficient sampling of ion dynamics while preventing melting of battery components. As an illustration, in Figure 91, the team presents the atomic configurations of the LLZO(001)|LCO(100) interface obtained from AIMD trajectory, which show the starting of cobalt and lanthanum interdiffusion. During the AIMD runs, rearrangement and migration of lithium and lanthanum ions toward both Li-rich and Li-poor LLZO(001)|LCO(100) interface are observed (Figure 91a). The migration of lithium ion effectively leaves behind a series of vacancies, which triggers cobalt diffusion to fill up these vacancy sites (Figure 91c). At Li-poor interface, cobalt diffusion is more significant due to higher concentration of vacancies. Similar behavior is also observed at the LLZO(001)|LCO(104) and LLZO(001)|LCO(110) interfaces. Next quarter, the team will continue the AIMD runs for these interfacial structures and identify distinct chemical motifs forming at various interfacial regions.

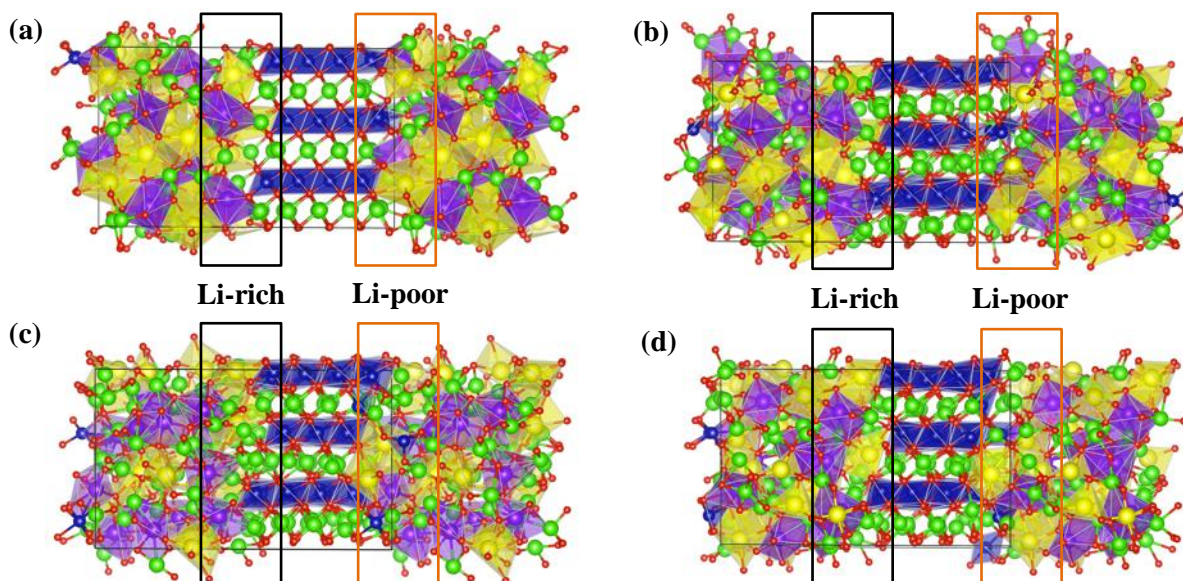


Figure 91. (a) Initial density functional theory relaxed interfacial structure of LLZO(001)|LCO(100). (b-d) Snapshots from *ab initio* molecular dynamics trajectory showing lithium, lanthanum, and cobalt migration toward the interfacial region.

The other approach the team is exploring to optimize the interfacial structure is based on basin hopping. Figure 92 shows the potential energy surface minimization of the LLZO(001)|LCO(100) interface, with a series of snapshots (M1-M3) taken along the energy curve. Similar to the AIMD results, lithium and lanthanum migration toward the interfacial region is observed during initial minimization, as shown in M1. Diffusion of cobalt into the vacant lithium sites is observed in M2, which corresponds to the sharp increase in the potential energy in Figure 92. The team observes continuous rearrangement and diffusion of lithium at the interfacial regions followed by cobalt migration in M3. They note that these basin hopping calculations are still in progress, and they will discuss the “final” atomic configuration and its implication in the next report.

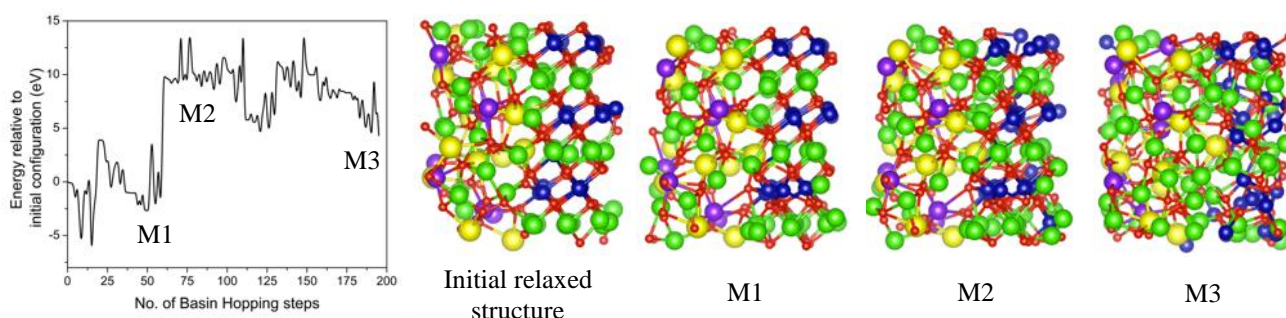


Figure 92. Representative structures of the LLZO(001)|LCO(100) interface during minimization of potential energy surface using basin hopping. The lithium, lanthanum, zirconium, oxygen, and cobalt ions are shown in green, yellow, purple, red, and blue, respectively.

## Patents/Publications/Presentations

The project has no patents, publications, or presentations to report this quarter.

### Task 3.14 – Design of Strain Free Cathode – Solid-State Electrolyte Interfaces Using Chemistry-Informed Deep Learning (Hakim Iddir, Argonne National Laboratory)

**Project Objective.** The main objective of this project is to use state of the art ML techniques and high-performance computing to model complex oxide materials that will allow the team to develop cathode-solid electrolyte interfaces that exhibit minimal or no strain as well as provide the chemical stability at the interface between the cathode material and the SSE. A deep understanding and control of the cathode/SSE interface (including its chemical and mechanical stability) is needed to develop effective SSB. The active cathode material changes volume during cycling, particularly at high SOC.<sup>[1]</sup> This volume change leads to strained interfaces triggering loss of contact, delamination, and hence reduction/elimination of electron and ion transport pathways. The increased strain could also generate cracks within the SSE, creating new paths for lithium dendrite growth channels. These structural changes degrade the electrochemical performance of the battery. Several strategies have had limited success in alleviating these drawbacks, including mixed SSE, buffer layers between the cathode and the SSE, and dopants to improve the chemical stability of the interface.<sup>[2]</sup> These approaches, although promising, could not solve both the chemical and mechanical stability of the interface. In this project, we propose a new approach that takes advantage of well-established ML techniques and high-performance computing (HPC) to screen for candidate dopants of high-Ni content NMC cathodes that would both reduce the volume expansion and the chemical reactivity (mixing) at the interface, with minimum impact on the electrochemical performance and energy density of the cathode

**Project Impact.** Structure-property relationships are at the heart of most fundamental scientific approaches. However, the link between structure and property remains a challenge in the materials science of complex systems, such as the oxides that form battery components. In particular, the chemical and mechanical stability of the cathode-SSE interface presents a challenge to the development of SSBs. High-performance DFT calculations provide the necessary framework to understand such systems. Unfortunately, given the limited number of atoms and time scales accessible by the method and the myriad calculations required to achieve satisfactory results, the computational cost of simulating all the possible configurations of a multicomponent oxide is prohibitive. In this work, the team augments the DFT data with ML—especially deep learning—techniques that allow them to access large system sizes and longer time scales necessary to build thermodynamic models. They focus on understanding the nature of benchmark  $\text{Li}_{1-\alpha}\text{Ni}_{1-x-y-z}\text{Mn}_x\text{Co}_y\text{M}_z\text{O}_2$  structures (M dopant,  $\alpha, x, y, z < 1$ ), their volume change with lithium content, the nature and concentration of the dopants, and the chemical stability of the SSE-cathode interface. The DFT and ML approach will provide new cathode compositions that will reduce the strain of the SSE-cathode interface and hence improve its mechanical and chemical stabilities

In this project, the team aims at developing a methodology that will allow them to explore and expand the configurational space using HPC approaches in a systematic and efficient way. The methodology will encompass, DFT, AIMD, MD, and ML. The methodology will also take advantage of the variety of software already developed at ANL and at other DOE laboratories (for example, Balsam) to automate, manage, and control the large number of calculations needed to achieve the project goal.

**Approach.** All calculations will be performed by spin-polarized DFT as implemented in the Vienna *Ab Initio* Simulation Package (VASP).<sup>[3-4]</sup> After geometry optimization within the DFT+U framework, electronic relaxation will be performed using a single-point calculation with the hybrid functional HSE06.<sup>[5]</sup> For production calculations, they will use the message-passing interface (MPI) parallelized version of VASP.

Exploration of the potential energy surface (PES) is needed to predict the structure of solid materials and interfaces. Such calculations are infeasible using MD or DFT calculations alone. Thankfully, the PES of a system can be represented by the sum of the energies of the local neighborhoods surrounding each atom. This enables the use of ML surrogate models trained with DFT calculations to capture the energies in local neighborhoods. The input to the ML surrogate must be a unique representation of the system under study.

Consequently, the local environment of each ion is described using a local environment descriptor that renders the atomic configuration invariant to rotations, translations, and permutations of the atoms. In recent years, several different descriptors have come to prominence with advantages and disadvantages. Once the ML surrogate is trained, the total energy and forces over all the ions of any structural configuration can be determined. Such information can be used for atomistic simulations, namely, MD and MC.

In this project, the team proposes to use the open-source DeepMDkit python/C++ package to construct the ML PES and force fields. The promise of DeepMDkit in this work is to provide near-DFT accuracy at orders of magnitude lower computational expense, comparable to traditional MD simulations. Efficiency in training is facilitated through integration with TensorFlow and MPI/GPU support.

One of the challenges of the development of a ML PES is achieving accurate predicted forces and energies across the entire configurational space, while minimizing the total number of calculations required for training. In recent years, active learning has been highlighted for its ability to target training examples most likely to improve the model quality or to achieve some other objective (that is, maximizing a predicted material property). DP-GEN, an open source python package based on DeepMDkit, implements a similar active learning scheme with HPC support, and has been employed to construct a ML PES with accuracy approaching DFT and sometimes exceeding embedded atom potential for experimentally measured properties of interest.<sup>[6]</sup> In this work, the team proposes to leverage DeepMDkit and DP-GEN to efficiently generate ML-PESs for cathode-electrolyte systems including a variety of dopants.

**Out-Year Goals.** One out-year goal involves developing a DFT-trained ML model on NMC/LLZO interface, ready to use for large screening of new cathodes, SSE compositions, and cathodes/SSE interfaces. A second is to provide fundamental understanding on critical parameters that limit the performance and stability of the cathode/SSE interface and hence of the SSB

**Collaborations.** Collaborations in this project include J. Croy, C. Johnson, and E. Lee from ANL Chemical Sciences and Engineering Division for the synthesis phase of the project

### Milestones

1. Develop a DFT-trained ML model to determine the low energy configurations for NMC-811. (Q1, FY2020; Completed)
2. Implementation of the ML models to NMC-based oxides. (Q2, FY2020; Completed)
3. DFT-trained ML model for delithiated LiNiO<sub>2</sub> and NMC-811. (Q3, FY2020; In progress)
4. ML model based on NMC/LLZO interfaces data. (Q4, FY2020)

## Progress Report

The scientific and technology challenge is illustrated in Figure 93, which shows the relative change in volume for several known cathode materials as a function of lithium content. Contrary to most compositions,  $\text{LiCoO}_2$  shows a different behavior, suggesting that volume change of the NMC materials can be controlled with dopants. In fact, the relative change in volume is reduced with increased cobalt content. This significant volume reduction is mainly due to the sudden collapse of the inter-layer spacing in these layered oxides as lithium is removed, when accessing higher capacities. The shrinkage in the inter-layer spacing is itself the result of bulk phase transition that involves a change in the relative stacking of the oxide layers (H2 to H3); see Figure 94. To accurately capture this phase transition using DFT, the team explored different DFT methods and compared their abilities to capture the right physics, and hence the volume change. The results from their initial screening of these methods point to SCAN+rVV10<sup>[7-8]</sup> as a viable option. SCAN+VV10 seems to better capture the binding between the TM layers in the absence of (or little) lithium content compared to SCAN without Van De Waals (VDW) or PBE (see Figure 95).

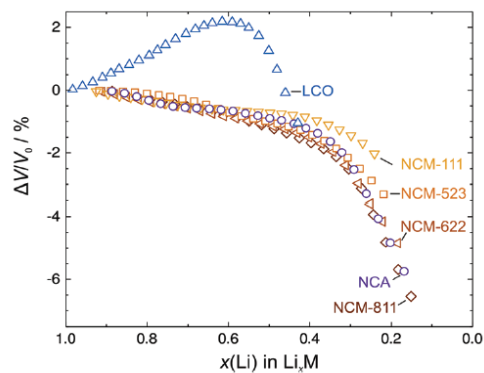


Figure 93. The unit cell volume obtained from crystallographic data versus the state of lithiation of positive electrode materials.<sup>[1]</sup>

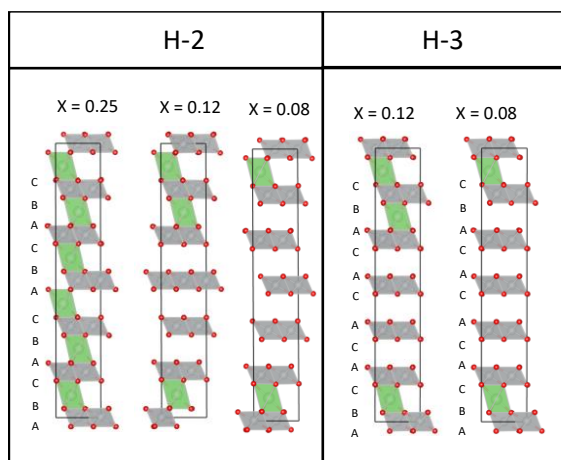


Figure 94. Polyhedral representation of  $\text{LiNiO}_2$  super cell at different lithium content ( $x$ ) with oxygen stacking in the H-2 (ABC) and H-3 (AC) phases. Grey octahedrons represent nickel sites, green octahedrons represent lithium sites, and small red spheres represent oxygen atoms.

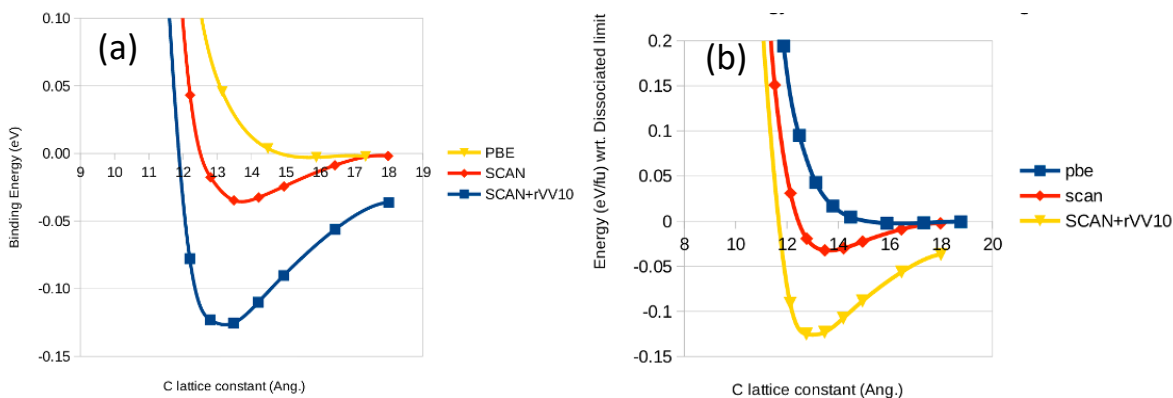


Figure 95. Energy of the dissociated limit as a function of the interlayer spacing for PBE, SCAN, and SCAN+rVV10 for  $\text{NiO}_2$  (a) in O1 stacking and (b) in O3 stacking.

Before studying the response of the system to lithium content during cycling, it is imperative to know the TM cation distribution within the material. For instance, for  $\text{LiNi}_x\text{Mn}_y\text{Co}_z\text{O}_2$  (NMC-xyz) materials, the distribution of cobalt and manganese within and across the TM layers determines the material properties. To get a better realistic cation distribution, a large simulation cell is necessary to allow the system to reproduce the local configurations that appear in the real system. Figure 96a shows a top view of the super-cell used to model NMC-811, while Figure 96b shows a side view of the whole supercell. The cell is composed of 432 atoms, which makes the structure optimization using DFT challenging.

The procedure used to screen for the configuration that minimizes the total energy of the system is summarized in Figure 96c. First, a batch of randomly generated configurations is built. Second, a predictive model for the total energy, the ML approach, is used to fit the DFT-generated data. The fitted model is a feed-forward NN as implemented in the Atomistic ML Package (*Amp*).<sup>[9]</sup> Next, a new batch of random configurations is generated. The ML model is used to estimate the energies for each configuration. Using a Bayesian optimization procedure, a new set of configurations is selected. If the minimum energy criterion is not met, the newly selected configurations are sent through the entire process again.

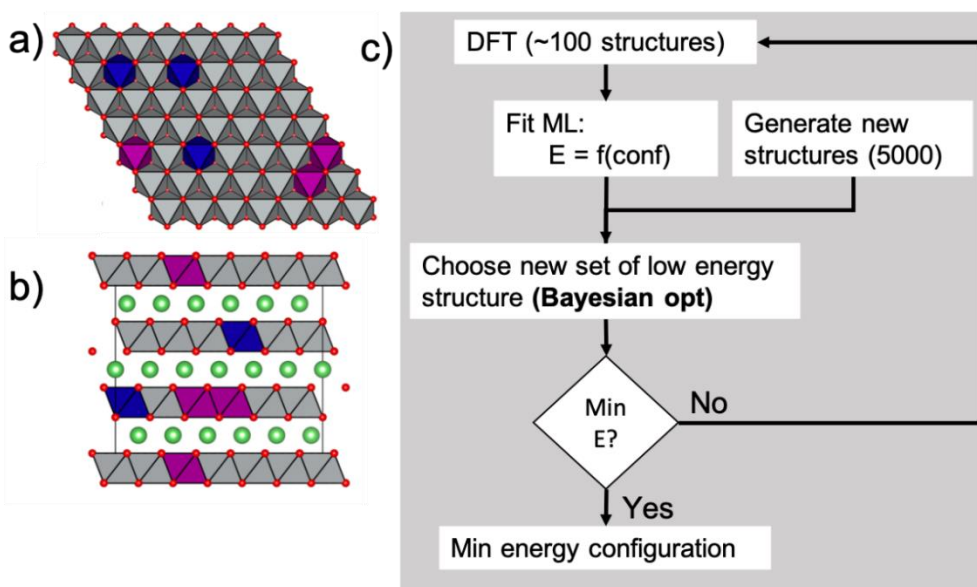
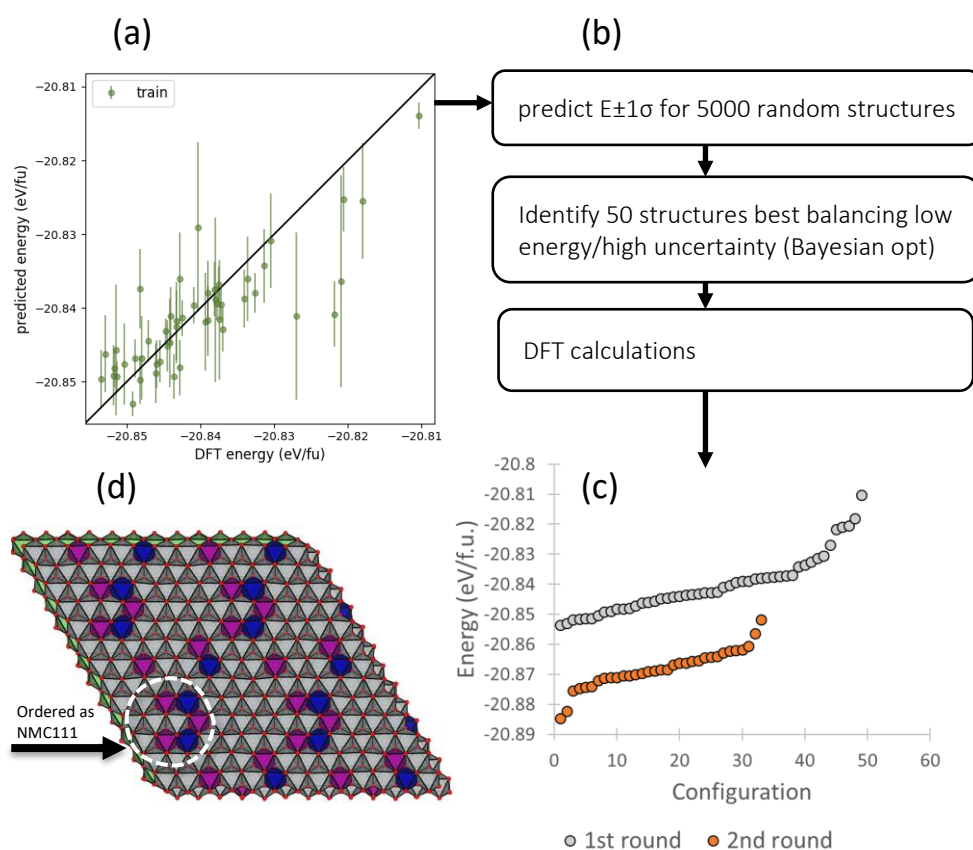


Figure 96. Polyhedral representation of  $\text{LiNi}_{0.8}\text{Mn}_{0.1}\text{Co}_{0.1}\text{O}_2$ ; (a) transition metal (TM) layer top view, and (b) whole super-cell side view. The grey polyhedral represents nickel site, blue polyhedral represents cobalt site, purple polyhedral represents manganese site, and green sphere represents lithium ion. (c) Procedure to find minimal energy TM configuration.

The energies for the first and second round of DFT calculations are presented in Figure 97c, where the configurations are sorted by total energies. The performance of the ML model (trained on round 1) is shown in Figure 97a. An active learning scheme is employed to identify 50 additional structures (round 2) to evaluate with DFT and improve the NN model. Specifically, the team employs a Bayesian optimization scheme with the lower confidence bound (LCB) acquisition function to select structures on the continuum of low predicted energies and high predicted uncertainties.<sup>[10]</sup> By probing this continuum, they hope to minimize the number of DFT calculations necessary to construct an accurate NN model. In practice, they used the bootstrapped NN model trained on all available training structures and predicted the energies (with uncertainty estimates) for 5000 random structures. The 50 most promising structures according to the batch LCB strategy were then selected and evaluated with further DFT calculations. Indeed, the new set of DFT results show lower energies than the initial random set (see Figure 97c, round 2). The new low energy configurations exhibit more uniform distribution of cobalt and manganese within the different TM layers and promote more of the NMC-111 domains (see Figure 97d).



**Figure 97.** (a) Neural network (NN) predicted versus density functional theory (DFT) predicted energies. Additionally, 1-sigma uncertainty intervals are plotted for the NN predictions. (b) Procedure to find minimal energy transition metal (TM) configuration. (c) DFT-calculated energies for 50 configurations (round 1) where TMs are positioned randomly in the TM layers and energies after Bayesian optimization (round 2). (d) TM layer top view polyhedral representation of  $\text{LiNi}_{0.8}\text{Mn}_{0.1}\text{Co}_{0.1}\text{O}_2$ . The grey polyhedral represents nickel site, blue polyhedral represents cobalt site, purple polyhedral represents manganese site, and green sphere represents lithium ion.

Additionally, they are validating the above NN-based ML approach implemented in *Amp* with two other ML MD potential generation formalisms. One, a Gaussian process regression approach, called the Gaussian Approximation Potential (GAP), has shown promising structural predictions for electronic materials.<sup>[11]</sup> Another, is DeepMD-kit, which is a NN-based approach that has shown promise in predicting properties of multi-component material systems.<sup>[12]</sup>

## References

- [1] Koerver, R., W. Zhang, L. de Biasi, S. Schweidler, A. O. Kondrakov, S. Kolling, T. Brezesinski, P. Hartmann, W. G. Zeier, and J. Janek. “Chemo-Mechanical Expansion of Lithium Electrode Materials – On the Route to Mechanically Optimized All-Solid-State Batteries.” *Energy & Environmental Science* 11 (2018): 2142–2158.
- [2] Kerman, K., A. Luntz, V. Viswanathan, Y-M. Chiang, and Z. Chen. “Review—Practical Challenges Hindering the Development of Solid State Li Ion Batteries.” *Journal of the Electrochemical Society* 164, no. 7 (2017). <https://iopscience.iop.org/article/10.1149/2.1571707jes>.
- [3] Kresse, G., and J. Furthmüller. “Efficiency of *Ab-Initio* Total Energy Calculations for Metals and Semiconductors using a Plane-Wave Basis Set.” *Computational Materials Science* 6 (1996): 15–50.
- [4] Kresse, G., and J. Hafner. “*Ab Initio* Molecular Dynamics for Liquid Metals.” *Physical Review B* 47 (1993): 558–561.
- [5] Heyd, J., G. E. Scuseria, and M. Ernzerhof. “Hybrid Functionals based on a Screened Coulomb Potential.” *The Journal of Chemical Physics* 118 (2003): 8207–8215.
- [6] Zhang, L., J. Han, H. Wang, W. Saidi, R. Car, and W. Ee. *Advances in Neural Information Processing Systems 31*, edited by S. Bengio, H. Wallach, H. Larochelle, K. Grauman, N. Cesa-Bianchi, and R. Garnett, Curran Associates, Inc. (2018): 4436–4446.
- [7] Sun, J., A. Ruzsinszky, and J. P. Perdew. “Strongly Constrained and Appropriately Normed Semilocal Density Functional.” *Physical Review Letters* 115 (2015): 036402.
- [8] Sun, J., R. C. Remsing, Y. Zhang, Z. Sun, A. Ruzsinszky, H. Peng, Z. Yang, A. Paul, U. Waghmare, X. Wu, M. L. Klein, and J. P. Perdew. “Accurate First-Principles Structures and Energies of Diversely Bonded Systems from an Efficient Density Functional.” *Nature Chemistry* 8 (2016): 831–836.
- [9] Khorshidi, A., and A. A. Peterson. “*Amp*: A Modular Approach to Machine Learning in Atomistic Simulations.” *Computer Physics Communications* 207 (2016): 310–324.
- [10] Snoek, J., H. Larochelle, and R. P. Adams. *Advances in Neural Information Processing Systems 25*, edited by F. Pereira, C. J. C. Burges, L. Bottou, and K. Q. Weinberger, Curran Associates, Inc. (2012): 2951–2959.
- [11] Bartók, A. P., M. C. Payne, R. Kondor, and G. Csányi. “Gaussian Approximation Potentials: The Accuracy of Quantum Mechanics, without the Electrons.” *Physical Review Letters* 104 (2010): 136403.
- [12] Zhang, L., D-Y. Lin, H. Wang, R. Car, and W. Ee. “Active Learning of Uniformly Accurate Interatomic Potentials for Materials Simulation.” *Physical Review Materials* 3 (2019): 023804.

### Patents/Publications/Presentations

The project has no patents, publications, or presentations to report this quarter.

### Task 3.15 – Tackling Solid-State Electrochemical Interfaces from Structure to Function Utilizing High-Performance Computing and Machine Learning Tools (Shinjae Yoo, Feng Wang, and Deyu Lu, Brookhaven National Laboratory; Nongnuch Artrith and Alexander Urban, Columbia University)

**Project Objective.** This project aims at elucidating the structural evolution and other dynamic properties of the interphases at the solid-solid interfaces (SSIs) in SSBs under processing and electrochemical cycling conditions that strongly impact the cell performance. By leveraging synergies of first-principles theory, HPC, ML, and computational/experimental spectroscopy, this project involves a comprehensive investigation of SE systems and SSIs that may enable the practical use of lithium anodes and high-nickel NMC cathodes in SSBs. Specific project objectives are: (1) develop realistic atomic-scale structure models of the SSIs, (2) develop SSB systems designed for integrated experimental spectroscopy and computational modeling of SSIs, (3) determine the impact of structural evolution on the stability and transport properties of the SSIs, and (4) identify the coating/doping chemistry that may stabilize SSIs during formation and electrochemical cycling.

**Project Impact.** Interfacial properties and the dynamical evolution of interphase structures are crucial for the stability and performance of SSBs. This project will lead to fundamental understanding of current materials limits and will identify key materials parameters for optimizing the performance of SSBs. By corroborating atomic-scale theory with experiment, the project will identify structure–property relationships of the heterostructural SSIs in SSB systems that are relevant for EVs. The outcomes of this project will therefore accelerate development of high-energy-density, safe SSBs for EVs.

**Approach.** Accurate ML potentials will be trained on an extensive database from DFT calculations to simulate the structure evolution and electrochemical properties of the SSIs. Using a second ML model, key physical descriptors will be extracted from EELS and XAS measurements. This spectral fingerprinting will enable the automated interpretation of spectroscopy measurements, thereby bridging between atomistic modeling and experiment. In combination, the two ML models and the spectroscopic data will facilitate the construction of a physics-based model to unravel the structure–property relationships of the SSIs.

**Out-Year Goals.** The project will progress toward establishing dynamic composition-structure-property relationships for interface stability and transport within and across the electrochemical SSIs in SSBs. The ML approach will be further developed to a general model for thermodynamic and transport properties of dynamic hetero-structural electrochemical interfaces and will eventually be applied to the practical SSB systems.

**Collaborations.** There are no collaborative activities this quarter.

#### Milestones

1. Complete experimental measurements of the XAS reference data for NMC cathodes. (Q1, FY 2020; Completed)
2. Benchmark the performance of computational spectroscopy methods against reference experimental nickel K-edge XAS spectra. (Q2, FY 2020; Completed)
3. Complete compiling the extensive reference database of NMC/Al-LLZO DFT calculations needed for the development of ML models. (Q3, FY 2020; Completed).
4. Develop accurate machine-learning potentials (MLPs) for large-scale modeling of LiTMO<sub>2</sub> and LLZO, and validate by comparison with DFT. (Q4, FY 2020; In progress)

## Progress Report

### Structure Libraries for Cathode and Electrolyte Materials.

Modeling the atomic structure of the dynamic NMC:SE interface requires an accurate description of the NMC cathode, the SE, and the interface region. In this report, the team focuses on NMC-811 and Al-doped LLZO (Al-LLZO; aluminum doping stabilizes the cubic LLZO phase, which is crucial for good lithium conductivity). These both exhibit substitutional disorder: Ni/Mn/Co disorder in NMC-811, and Li/Al/vacancy disorder in Al-LLZO, which is a key factor determining the lithium transport properties of the material. A first important objective toward the first and second milestones is therefore the compilation and energetic ranking of atomic configurations for both NMC-811 and Al-LLZO that capture the characteristic short-range ordering in the compounds and can be used for the construction of predictive ML models.

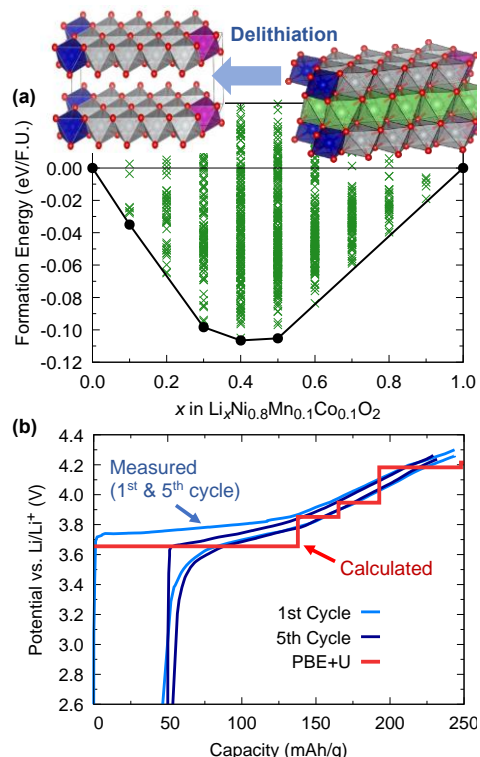
The team performed a systematic enumeration of 230 symmetrically distinct Ni/Mn/Co orderings in NMC-811. Nearly a third of the enumerated configurations exhibit an energy that is less than the thermal energy at room temperature ( $\sim 0.026$  eV) above the most stable configuration, in agreement with the experimental observation that the TM layer is disordered.<sup>[1]</sup>

Figure 98a shows the calculated formation energies of  $\sim 1,000$  NMC-811 structures with varying lithium content. Although only four of the considered compositions are predicted to be stable at  $T = 0$  K (black points), the other compositions are only few meV per  $\text{LiMO}_2$  formula unit (F. U.) above the convex hull. Considering temperature effects and kinetics, NMC-811 can therefore be expected to behave as a solid solution, also in agreement with the team's experimental observations.

The predicted voltage profile that corresponds to this computational phase diagram is shown in Figure 98b. Also shown are measured voltage profiles from the 1<sup>st</sup> and 5<sup>th</sup> charge-discharge cycles. As seen, the predicted voltage traces the measured profile well, and the change in slope at  $\sim 130$  mAh/g is correctly predicted. This indicates that the team's calculations describe the redox behavior of NMC-811 correctly and provides validation of the DFT approach and structure models. The  $\sim 200$  lithiated and  $\sim 1,000$  partially and fully delithiated NMC-811 atomic configurations will be combined with the project's existing data on  $\sim 1,000$  structures of  $\text{LiNiO}_2$ ,  $\text{LiCoO}_2$ ,  $\text{LiMnO}_2$ , and  $\text{LiNi}_{0.5}\text{Mn}_{0.5}\text{O}_2$  into a single database. This combined reference data set will form the basis for the construction of a robust ML model for NMC-811.

While compiling reference structures for the cathode material, the team has also been generating a first-principles library of Al-LLZO structures for which they considered different Li/vacancy. Currently, the Al-LLZO data set comprises  $\sim 6,000$  atomic configurations.

**Development of the MLP Method.** The construction of robust MLP based on artificial neural networks (ANN) for MD and MC simulations is an iterative process: first a *preliminary potential* is trained, which is then refined by iteratively extending the reference data set. A schematic of this process as implemented with the software  $\text{\ae}net$  is shown in Figure 99.



**Figure 98.** (a) Calculated formation energies of NMC-811 with varying lithium content. The thermodynamically stable compositions lie on the lower convex hull (black points). Metastable and unstable compositions are shown as green crosses. (b) Comparison of the predicted voltage profiles with experimentally measured voltage profiles.

For complex applications such as the NMC-811:LLZO interface modeling, typically large reference data sets with tens of thousands of structures are needed to obtain an accurate MLP. Interface structures contain many atoms (typically ~ 200-300), so that performing a large number of DFT interface calculations is computationally demanding.

The team therefore developed a methodology for the training of accurate MLP on smaller data sets.<sup>[3]</sup> The new methodology allows reducing the size of the expensive DFT reference data set by up to one order of magnitude. The method will be used for the construction of the NMC:SE interface MLP.

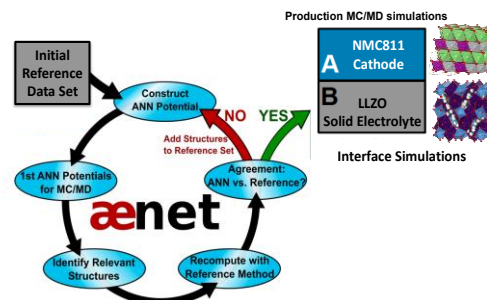


Figure 99. Iterative refinement of the artificial neural network (ANN) potential using interface structures from Monte Carlo / molecular dynamics simulations with aenet.<sup>[2]</sup> The newly developed approach facilitates training potentials on fewer density functional theory reference calculations.<sup>[3]</sup>

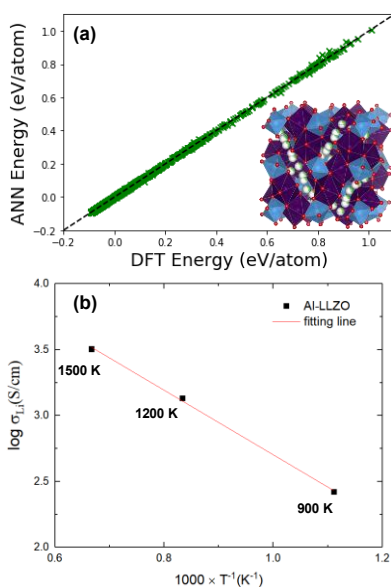


Figure 100. (a) LLZO structure energies predicted by artificial neural network (ANN) potential compared to the density functional theory reference (green crosses). The dashed line indicates ideal agreement. (b) Arrhenius plot with lithium conductivities in Al-LLZO from molecular dynamics simulations at different temperatures.

**Preliminary MLP for the Al-LLZO SE.** Using the new ANN potential training methodology, the team has made initial progress in constructing universal MLP for Al-LLZO. The MLP was trained on ~ 6,000 LLZO and Al-doped LLZO configurations, and a comparison of energies predicted by the project's MLP with the DFT references is shown in Figure 100. As seen, the agreement of the MLP with DFT is already excellent, and the resulting preliminary MLP could be used in MD simulations. For further validation, the team performed MD simulations of Al-LLZO and determined the lithium conductivity. The lithium conductivity at different temperatures is shown in Figure 100b and the extrapolated room-temperature conductivity and activation energy are compared to experimental reference values in Table 8.

Table 8. Comparison of calculated room-temperature lithium conductivity and activation energy for lithium transport in the bulk of Al-doped LLZO with measured values from two references.

	Conductivity (S cm <sup>-1</sup> )	Act. Energy (eV)
<b>Simulations (ours)</b>	<b>7.1×10<sup>-4</sup></b>	<b>0.22</b>
Experiment <sup>1</sup>	1.0×10 <sup>-4</sup>	0.34
Experiment <sup>2</sup>	6.0×10 <sup>-4</sup>	0.25

1 = Buschmann et al., *Phys. Chem. Chem. Phys.* **13**, 2011, 19378-19392.

As seen in Table 8, the predicted lithium bulk conductivities are within  $5 \times 10^{-4}$  S cm<sup>-1</sup> and the activation energies within 0.1 eV of the experimental values, which is an encouraging validation of the MLP simulation results. The team notes that the uncertainty in the experimental data is also significant, since the bulk conductivity can only be indirectly deduced from the total lithium conductivity. The team's aim is therefore to complete construction of the MLP toward interface structures, so that lithium transport across interfaces can also be accurately modeled.

## References

- [1] Zhang, W., et al. *Advanced Energy Materials* 9 (2019): 1901915.
- [2] Artrith, N., and A. Urban. *Computational Materials Science* 114 (2016): 135–150.
- [3] Cooper, A. M., J. Kästner, A. Urban, and N. Artrith. *npj Computational Materials* 6 (2020): 54.

## Patents/Publications/Presentations

### Publication

- Cooper, A. M., J. Kästner, A. Urban, and N. Artrith. *npj Computational Materials* 6 (2020): 54.

## TASK 4 – METALLIC LITHIUM

### Summary and Highlights

The use of a metallic lithium anode is required for advanced battery chemistries like Li-ion, Li-air, and Li-S to realize dramatic improvements in energy density, vehicle range, cost requirements, and safety. However, use of metallic lithium with liquid and solid polymer or ceramic electrolytes has so far been limited due to parasitic SEI reactions and dendrite formation that eventually short circuit the battery. Adding excess lithium to compensate for such losses negates the high-energy-density advantage of a Li-metal anode and leads to further concern for battery safety. For a long lifetime and safe anode, it is essential that no lithium capacity is lost either (1) to physical isolation by roughening, dendrites, or delamination processes, or (2) to chemical isolation from side reactions. The key risk, and current limitation, for this technology is the gradual loss of lithium over the cycle life of the battery.

BMR, Battery500, and other DOE programs are addressing this challenge with many innovative and diverse approaches. Key to all is the need for a much deeper analysis of the degradation processes and new strategies to maintain a dense, fully connected lithium and a dendrite-free electrolyte so that materials can be engineered to fulfill the target performance metrics for EV application, namely 1000 cycles and a 15-year lifetime, with adequate pulse power. Projecting the performance required in terms of just the lithium anode, this requires a high rate of lithium deposition and stripping reactions, specifically about 30  $\mu\text{m}$  of lithium per cycle, with pulse rates up to 10 and 20 nm/s (15 mA/cm<sup>2</sup>) charge and discharge, respectively, with little or no excess lithium inventory. This is daunting in the total mass and rate of material transport that must be achieved without failures.

The efficient and safe use of metallic lithium for rechargeable batteries is then a great challenge, and one that has eluded R&D efforts for years. This project takes a broad look at this challenge for both SSBs and batteries continuing to use LEs. Electrolytes reported here include nonflammable liquid solutions, gel type polymer-in-a-salt, composites of ceramic polymer phases, common and novel PEs, and both oxide and sulfide ceramic electrolytes. In most studies, the electrolyte phases were modified by addition of plasticizers or interface coatings to improve transport, stability, and ease of manufacturing. Researchers are typically working toward cycling of full cells with relevant and balanced capacities for the lithium anode and cathode using measures of CE, interface resistance, and post-cycling observation of the disassembled cell components to assess stability of the Li-metal anode and chosen electrolyte.

**Highlights.** The highlights for this quarter are described below. Due to COVID-19, all programs had limited access to labs and so pivoted from the originally planned research. Nevertheless, important progress was made and results have been presented to the research community.

At PNNL (Task 4.1), W. Xu and associates report two studies. In one, they explore Li-Mg alloy anodes, as the magnesium alters the surface energy of the lithium. Coin cells with the alloy anodes and an excess of a LE, cycled at C/10 rates, show that anodes with 5 or 10% magnesium reach 300 cycles with 80% capacity, which is a significant improvement over cells with the pure lithium anode that failed abruptly at < 200 cycles. In a second study and publication, beautiful cryo-TEM images, with Fast Fourier Transform (FFT) analysis, were used to examine the structure of the SEI formed at a copper contact with a standard LiPF<sub>6</sub> LE with and without addition of VC. The SEIs differed in the structure and formation of crystalline Li<sub>2</sub>O particles within the amorphous SEI layer as the voltage is reduced from 1 V to 0.5 V and 0 V prior to the lithium electrodeposition.

Researchers X. C. Chen and N. Dudney at ORNL (Task 4.2) report additional achievements using composite polymer+ceramic electrolytes. Stable cycling with low interface resistivity was obtained with a lithium versus 532 NMC cell using cross-linked PEO formed as a gel with addition of tetraethylene glycol dimethyl ether (TEGDME) and 50 wt% doped-LATP ceramic particles. There are two effects that enhance the transport properties. The anions TFSI<sup>-</sup> are immobilized near the ceramic for higher lithium transport number, while the

TEGDME promotes higher dissociation of the salt. Further experimental chronoamperometry of the electrolytes, combined with simulation, is revealing how the equilibrium salt concentration gradients decrease for composite and laminated electrolytes compared to the pure PEs.

Work at ANL from the N. M. Markovic team (Task 4.3) features sample preparation and initial results for analysis of the interfaces between  $\text{LiCoO}_2$  and LLTO by neutron reflectometry and X-ray reflectivity. Thin films of LLTO followed by  $\text{LiCoO}_2$  were grown by pulsed laser deposition (PLD) onto single crystal  $\text{SrTiO}_3$  and silicon surfaces. Various amorphous and crystalline bi- and multi-layer films were fabricated and examined with consideration of the film densities and interdiffusion at the interfaces.

J. Ye at LLNL (Task 4.4) reports analysis of experiments and modeling for both milling and sintering of LLZTO powder. While milling with ethanol leads to severe  $\text{H}^+/\text{Li}^+$  exchange, using acetonitrile/Triton X-100 as the milling solution avoids this reaction. Not surprisingly, the milled powders sinter more readily so the temperature can be reduced over  $100^\circ\text{C}$ . Simulations of sintering to date include only 3 particles, but a larger model with thousands of particles is under development.

Using sulfide-based electrolyte materials, J. Nanda's team at ORNL (Task 4.5) has fabricated full cells with NMC(111) and LFP cathodes. While details of fabrication and application of stack pressure affect the performance, it appears that an interface reaction between the  $\text{Li}_3\text{PS}_4$  and the cathodes dominates the degradation processes. Separately, solid-state NMR reveals a broader  $^7\text{Li}$  NMR resonance at 0 ppm for amorphous composites of solvent-mediated  $\text{Li}_3\text{PS}_4$  mixed with 1% PEO, compared to that of the crystalline  $\beta\text{-Li}_3\text{PS}_4$  electrolyte; this is consistent with the relative ionic conductivities.

Thin lithium foils were prepared at Stanford University in Y. Cui's program (Task 4.6). Here the effective thickness of the lithium is adjusted from 500 nm to  $20\ \mu\text{m}$  by using reduced graphene oxide (rGO) as the host. The calendered rGO absorbed a controlled thickness of molten lithium as demonstrated by voltage-capacity profiles on lithium stripping and by SEM imaging. The Li-permeated rGO films will then be used for a controlled, dry prelithiation of a silicon anode.

## Task 4.1 – Lithium Dendrite Prevention for Lithium Batteries (Wu Xu and Ji-Guang Zhang, Pacific Northwest National Laboratory)

**Project Objective.** The objective of this project is to enable lithium metal to be used as an effective anode in rechargeable Li-metal batteries with good stability and high safety. The investigation this fiscal year will focus on two aspects. First, develop nonflammable PEs and investigate effects of various flame-retardant solvents and polymers on ionic conductivity, lithium CE, Li-anode morphology, flammability, and battery performances in terms of long-term cycling stability and rate capability at various temperatures. Second, establish correlation of morphologies of SEI layer and deposited lithium with electrolyte formulation, current density, and lithium deposition/stripping cycling.

**Project Impact.** Lithium metal is an ideal anode material for rechargeable batteries, but the application of Li-metal anode is hindered by lithium dendrites and low CE. Although much progress has been achieved in suppressing lithium dendrites and increasing lithium CE in LEs, most of the LEs are flammable and may pose a safety hazard in case of extreme conditions. Therefore, development of electrolytes with improved safety for advanced battery chemistry is imperative. An ideal electrolyte for Li-metal anode should not only suppress lithium dendrite growth and have high CE, but also be intrinsically nonflammable. This fiscal year, the team will develop low flammable or nonflammable hybrid polymeric composite electrolytes (NHPCEs) that have high lithium CE, suppress lithium dendrites, and are stable with high-voltage cathodes. The success of this project will increase safety of Li-metal and Li-ion batteries and accelerate market acceptance of EVs, especially for PEVs as required by the EV Everywhere Grand Challenge.

**Approach.** The approach will encompass several areas: (1) develop appropriate high-concentration phosphate LEs (HCEs) that have high lithium CE over 98% and can suppress lithium dendrites, (2) add flame-retardant phosphate monomers into the HCEs and utilize radical polymerization to form crosslinked polymer gel electrolyte, and (3) investigate ionic conductivity, electrochemical window, flammability, lithium CE, and morphology; battery performance of HCEs and NHPCEs will also be investigated.

**Out-Year Goals.** The long-term goal of the proposed work is to enable Li-metal and Li-ion batteries with a specific energy of > 350 Wh/kg (in cell level), 1000 deep-discharge cycles, 15-year calendar life, and less than 20% capacity fade over a 10-year span to meet the goal of EV everywhere.

**Collaborations.** This project collaborates with C. Wang of PNNL on characterization by TEM/SEM; Dr. K. Xu and Dr. M. Ding of U. S. Army Research Laboratory (ARL) on solvent purification and DSC measurements; and Dr. B. Polzin at ANL on coated electrode sampling.

### Milestones

1. Develop polymerization method to achieve nonflammable PEs with lithium CE > 98%. (Q1, FY 2020; Completed, February 19, 2020)
2. Characterize morphologies of SEI layers and deposited lithium films at different current densities and deposition capacities. (Q2, FY 2020; Completed, March 31, 2020)
3. Investigate lithium CE, deposited lithium morphology, and flammability of hybrid polymer composite electrolytes. (Q3, FY 2020; Delayed to August 15, 2020, due to COVID-19)
4. Achieve over 100 cycles for Li||NMC-622 batteries with nonflammable hybrid polymer composite electrolytes. Characterize compositions of SEI layers and deposited lithium films at different current densities and deposition capacities. (Q4, FY 2020; In progress)

## Progress Report

Due to the COVID-19 outbreak and the consequent lab lockdown, the previously planned development of nonflammable hybrid polymer composite electrolytes (NHPCEs) was interrupted. As the lab reopens under a limited operation mode, the synthesis and characterization of NHPCEs are now resumed. In this report, the team will focus on the studies using Li-Mg alloys as anode materials of the Li-metal batteries as well as the structure and composition of SEIs formed at different voltages.

### Li-Mg Alloys as Anode Materials

According to theoretic calculations, the surface energy of lithium deposition substrate plays an important role in influencing lithium deposition behavior. The surface energy of lithium can be altered by the introduction of small amount of magnesium in the Li-metal foil. Figure 101 exhibits the cycling performance of Li||NMC-811 and Li-Mg||NMC-811 coin cells using flooded electrolyte of LiFSI-1.2DME-3TTE. It is seen that both Li95-Mg5 and Li90-Mg10 based cells exhibit superior cycling stability and capacity retention to the pure lithium based cells. Results indicate that the certain lithium alloys may be a promising substitute to the pure lithium metal as anode materials for development of high-energy-density batteries. More cell testing and characterization are under way.

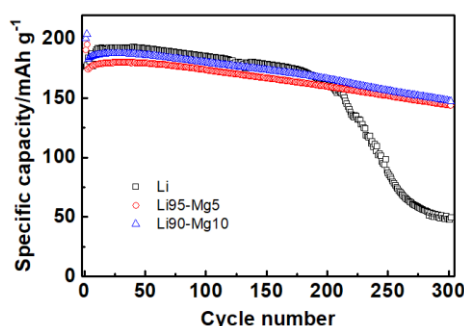


**Figure 101.** Room-temperature cycling performance of Li||NMC-811 and Li-Mg||NMC-811 coin cells comprising flooded electrolyte of LiFSI-1.2DME-3TTE at 1C charge and discharge rate after two formation cycles at C/10 rate in the voltage range of 2.8-4.4 V. Cathode areal capacity loading is  $\sim 1.5 \text{ mAh cm}^{-2}$ .

### SEI on Copper Substrate at Different Cut-Off Voltages

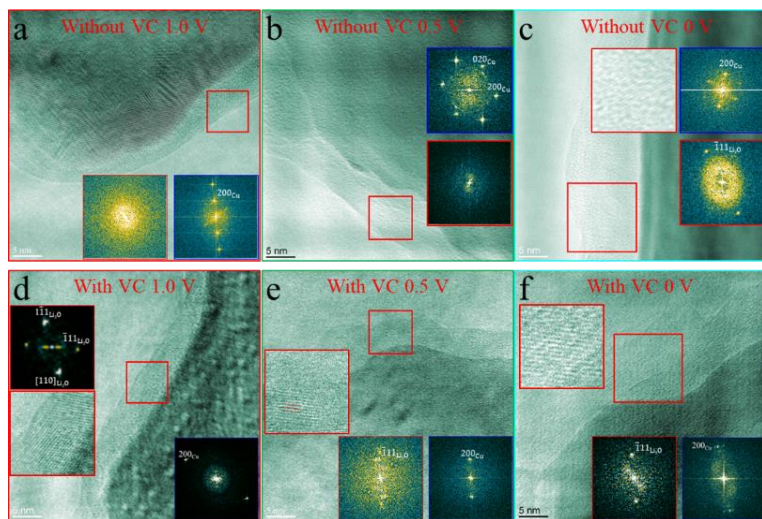


**Figure 102.** Cryo – transmission electron microscopy (TEM) images of SEI formed on TEM copper foil in the electrolytes without and with 5% VC additive. (a-c) At different cut-off voltages of 1.0 V, 0.5 V, and 0 V in the electrolyte without VC additive. (d-f) At different cut-off voltages of 1.0 V, 0.5 V, and 0 V in the electrolyte with VC additive. Insets: Fast Fourier transform patterns from SEI (red) and copper foil (blue).

In collaboration with Dr. C. Wang, the influence of electrode potential on the morphology and composition of SEI formed on copper substrate before and after lithium deposition was systematically studied under the US-Germany Collaboration project. By using XPS, EDS, and cryo-TEM imaging, it is revealed, as shown in Figure 102, that, in the conventional LiPF<sub>6</sub>/EC-EMC electrolyte without VC additive, the SEI formed at 1.0 V exhibits a monolithic amorphous structure, which evolves to amorphous matrix embedded with crystalline Li<sub>2</sub>O particles as the voltage decreases to 0 V where no lithium deposition occurs. In the case of VC-containing electrolyte, crystalline Li<sub>2</sub>O can be observed in the entire selected voltage range. The thickness of SEI formed on copper foil increases with decreasing voltage. When lithium deposition occurs, the composition of

SEI further evolves, whereas the SEI thickness remains almost unchanged. Results have confirmed that the SEI composition is highly dependent on the potential electrode.

## Patents/Publications/Presentations

### Publications

- Xu, Y., H. Wu, H. Jia, M. H. Engelhard, J-G. Zhang, W. Xu, and C. Wang. “Sweeping Potential Regulated Structural and Chemical Evolution of Solid-Electrolyte Interphase on Cu and Li as Revealed by Cryo-TEM.” *Nano Energy* (2020). doi: 10.1016/j.nanoen.2020.105040.
- Xu, Y., H. Wu, H. Jia, J-G. Zhang, W. Xu, and C. Wang. “Current Density Regulated Atomic to Nanoscale Process on Li Deposition and Solid Electrolyte Interphase Revealed by Cryogenic Transmission Electron Microscopy.” *ACS Nano* (2020). doi: 10.1021/acsnano.0c03344.

## Task 4.2 – Composite Electrolytes to Stabilize Metallic Lithium Anodes (Nancy Dudney and X. Chelsea Chen, Oak Ridge National Laboratory)

**Project Objective.** The project has several objectives: (1) prepare novel polymer and ceramic electrolyte materials that can work together to achieve thin membranes that have the unique combination of electrochemical and mechanical properties required for practical manufacturing and to stabilize the metallic lithium anode for good power performance and long cycle life, (2) identify key features of the composite composition, architecture, and fabrication that optimize performance, and (3) fabricate thin electrolyte membranes to use with a thin metallic lithium anode that provides good power performance and long cycle life.

**Project Impact.** A stable lithium anode is critical to achieve high energy density with excellent safety, lifetime, and cycling efficiency. This study will identify key design strategies that should be used to prepare composite electrolytes to meet the challenging combination of physical, chemical, and manufacturing requirements to protect and stabilize the Li-metal anode for advanced batteries. By utilizing well characterized and controlled component phases, design rules developed for composite structures will be generally applicable toward substitution of alternative and improved SE component phases as they become available. Success will enable DOE technical targets: 500-700 Wh/kg, 3000-5000 deep discharge cycles, and robust operation.

**Approach.** This project seeks to develop practical SEs to provide stable, long-lived protection for Li-metal anode. Current electrolytes have serious challenges when used alone; oxide ceramics are brittle, sulfide ceramics are air sensitive, polymers are too resistive and soft, and many electrolytes react with lithium. Composites provide a clear route to address these issues. While work continues to emphasize study of ceramic electrolyte / PE interfaces, this effort has expanded to address the following: (1) practical processing routes to fabricate full batteries using better composite electrolytes with a composite cathode and thin Li-metal anode, and (2) introduction of alternative polymer and ceramic phases to replace well-known model materials and develop improved composite electrolytes. In addition to solid-state devices, hybrid batteries are investigated using a fluid or gel catholyte within the porous cathode. Coatings have also been employed to stabilize electrode interfaces. These directions increase complexity of the studies, but are needed to improve cycling stability and rate performance and to advance practical implementation of the SE and Li-anode technology.

**Out-Year Goal.** The goal is to use advanced manufacturing processes where the architecture of the composite membrane can be developed and tailored to maximize performance and cost-effective manufacturing.

**Collaborations.** Work is conducted by Dr. Y. Zhang and Dr. X. Chen. Ceramic electrolyte powders (LICGC™) are obtained from Ohara Corporation. ORNL internal collaborators include Dr. B. Armstrong and Dr. S. Kalnaus. For the single ion conducting (SIC) polymers, the team partnered with Prof. J. L. Schaefer at University of Notre Dame.

### Milestones

1. Develop methods to minimize interconnected composite electrolytes' interfacial resistance with lithium by varying polymer chemistry. (Q1, FY 2020; Completed)
2. Fabricate interconnected ceramic network with different ceramic chemistry and particle size to increase strength of the composite. (Q2, FY 2020; Partially completed, pending LLZO powders)
3. Investigate the trade-off between  $\text{Li}^+$  transference number and ionic conductivity of the gel composite electrolytes, and optimize it. (Q3, FY 2020; Completed)

- Fabricate full batteries using NMC cathode, composite electrolyte, and Li-metal anode. Identify cell failure mode. (Q4, FY 2020; In progress)
- Create chemical/physical bonding between polymer and interconnected ceramic network that leads to optimized interface to improve mechanical modulus and ionic conductivity. (Annual stretch milestone).

## Progress Report

In FY 2019, the team reported the fabrication of a gel composite electrolyte. The project goal remains to develop a fully dry composite electrolyte, but completion of this work provides insight into the ion transport processes (milestone 3). The matrix of the composite electrolyte was crosslinked PEO, denoted as XPEO, with LiTFSI. LICGC™ particles from Ohara Corp. were dispersed in the polymer matrix as ceramic fillers. The composite electrolyte was plasticized with TEGDME to form the gel. The team demonstrated that the addition of LICGC™ led to lower interfacial impedance with lithium metal, lower overvoltage, and improved lithium symmetrical cell cycle life (Q2, FY 2019). Efficient cycling of the lithium metal, with little excess, is yet to be demonstrated, but for a hybrid battery, this cell appears to function well.

This quarter, the underpinnings of the improved performance from the composite gel electrolytes were discovered. Raman spectroscopy revealed that the addition of LICGC™ immobilized the TFSI<sup>-</sup> anions in the polymer matrix (data not shown). Simultaneously, with the presence of LICGC™ particles, although the volume fraction of TEGDME in the gel membrane was the same, the molar ratio of TEGDME to Li<sup>+</sup> increased as a result of lower volume fraction of the polymer phase. The increase in TEGDME/Li<sup>+</sup> led to enhanced Li<sup>+</sup> dissociation. Figure 103a shows that there is a two-fold increase in Li<sup>+</sup> conductivity in the gel composite membrane with 50 wt% LICGC™ (denoted as CEM-50). For this plot, the Li<sup>+</sup> conductivity was calculated as the product of the experimental transference number and the total conductivity. The simultaneous Li<sup>+</sup> transport promotion and TFSI<sup>-</sup> immobilization led to improved Li-Li symmetrical cell cycling performance of CEM-50.

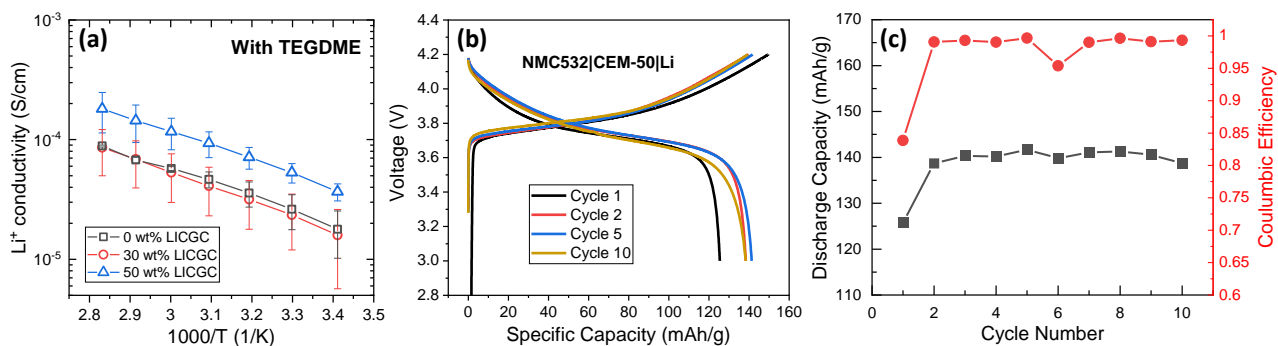


**Figure 103.** (a) Li<sup>+</sup> conductivity of gel polymer and composite electrolytes. (b) Charge and discharge curves of full cell NMC-532|CEM-50|Li at cycle number 1, 2, 5, and 10, and (c) cycling performance of the cell.

To evaluate composite membrane's performance in actual batteries, the team assembled a full cell using NMC-532 cathode, CEM-50 membrane, and Li-metal anode. The cell was cycled at 50  $\mu\text{A}/\text{cm}^2$  (C/30) at room temperature between 2.8 and 4.3 V (Figure 103b-c). To cycle this cell, the porous cathode was wet with 20  $\mu\text{L}$  of LiPF<sub>6</sub> in EC/DMC as the catholyte. Further, the composite electrolyte membrane was made without LiTFSI salt, but plasticized with the LiPF<sub>6</sub>/EC/DMC LE. This substitution was necessary because TEGDME is known to have a low voltage stability limit. The initial discharge capacity was relatively low, probably because thorough wetting of the catholyte with the cathode particles was still forming. After the 1<sup>st</sup> cycle, stable discharge capacity and good CE were achieved.

The team has expanded their polarization study to include these gel composite electrolytes. Last quarter, they reported the initial Li//Li DC polarization (10mV) of a wide variety of dry polymers, as well as various

laminated and dispersed composite electrolytes. Modeling of the polarization was also initiated. Similar Li//Li symmetric cells have now been assembled using the gel electrolytes that were plasticized using TEGDME. The

Membrane	THICKNESS ( $\mu\text{m}$ )	
	before	After plasticization
XPEO thick	304	342
XPEO thin	139	187
30 wt%	88	109
50 wt%	92	102
70 wt%	86	95

Table 9. Thickness of the polymer composite membranes showing swelling with TEGDME.

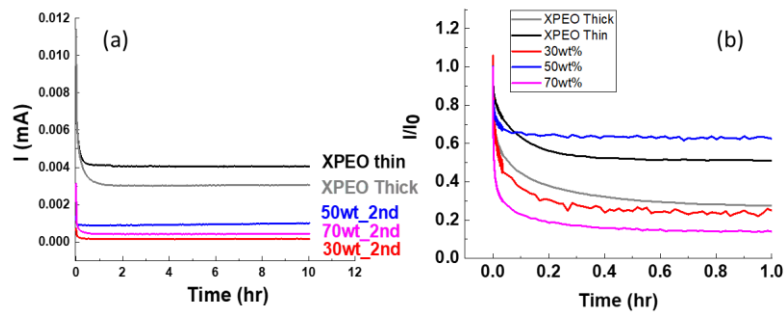


Figure 104. (a) The current as a function of relaxation time with 10-mV bias for the polymer electrolyte, XPEO, and the composites containing 30-70 wt% LICGC<sup>TM</sup>. (b) Expanded plot of the same results, plotted as the ratio of the current to the initial current.

thicknesses of each film before and after plasticizing show significant swelling (Table 9). The relaxation curves, shown in Figure 104a-b, are under 10-mV voltage bias at 30°C. The relaxation of the current was recorded for 10 hours, although most samples equilibrated at much shorter times. In Figure 104b, the same results are plotted as the current ratio normalized to the initial current ( $I_0$ ) recorded at 5 ms. (For two samples, the current increased until peaking at 20 ms, so the  $I/I_0$  ratio exceeds 1.0.) The 50% composite, with a transference number for  $\text{Li}^+$  of 0.44 and the highest conductivity, reached its steady state most quickly and with a relatively high steady state current ( $I_{ss}$ ). More testing is required to assure reproducibility, followed by modeling to understand the polarization kinetics in these complex composite gel PEs.

Modeling initiated last quarter is needed to aid interpretation of the results of the Li//Li polarization kinetics, particularly when the electrolyte includes single-ion conductors along with the binary PEs. The modeling results reported for this quarter reflect properties of polymers and composites *different from the gel XPEO and associated composites described above*. The polarization of the gel electrolytes will be analyzed in future work.

Three different arrangements were considered in the project's models for the electrolyte polarization studies. These are as follows: binary PE; laminated Ohara glass ceramic (LiCGC<sup>TM</sup>) sandwiched between two PE layers; and composite polymer electrolyte (CPE), of PEO with dispersed LICGC particles, sandwiched between two PE layers. Experimental results corresponding to these cases and materials were presented last quarter. The model is based on Nernst-Planck equations for calculation of transport of charge carriers, which are represented by  $\text{Li}^+$  and TFSI in the binary PE and  $\text{Li}^+$  in LiCGC<sup>TM</sup>. As such, the movement of cations by migration is considered in LiCGC<sup>TM</sup>. It should be mentioned that the model provides *qualitative* analysis since the exact values of many of the material constants are yet to be extracted from experiment. Nevertheless, the trends can be discussed together with the experimental results. In determination of effective properties of PE-LiCGC<sup>TM</sup> composite, the McLachlan Generalized Effective Medium Theory (GEMT)<sup>[1]</sup> was used with equations modified to include a resistive interface between LiCGC<sup>TM</sup> and polymer matrix. Ionic conductivity of this interface was assumed as one half of the ionic conductivity of PE matrix ( $1.4 \times 10^{-6}$  S/cm at room temperature). The results

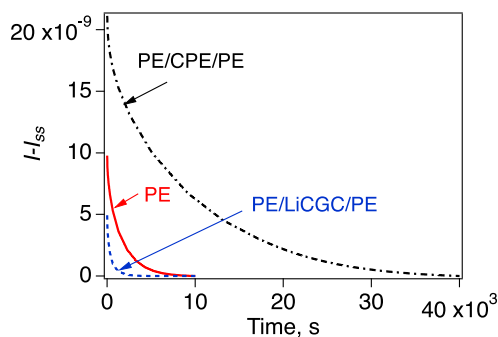
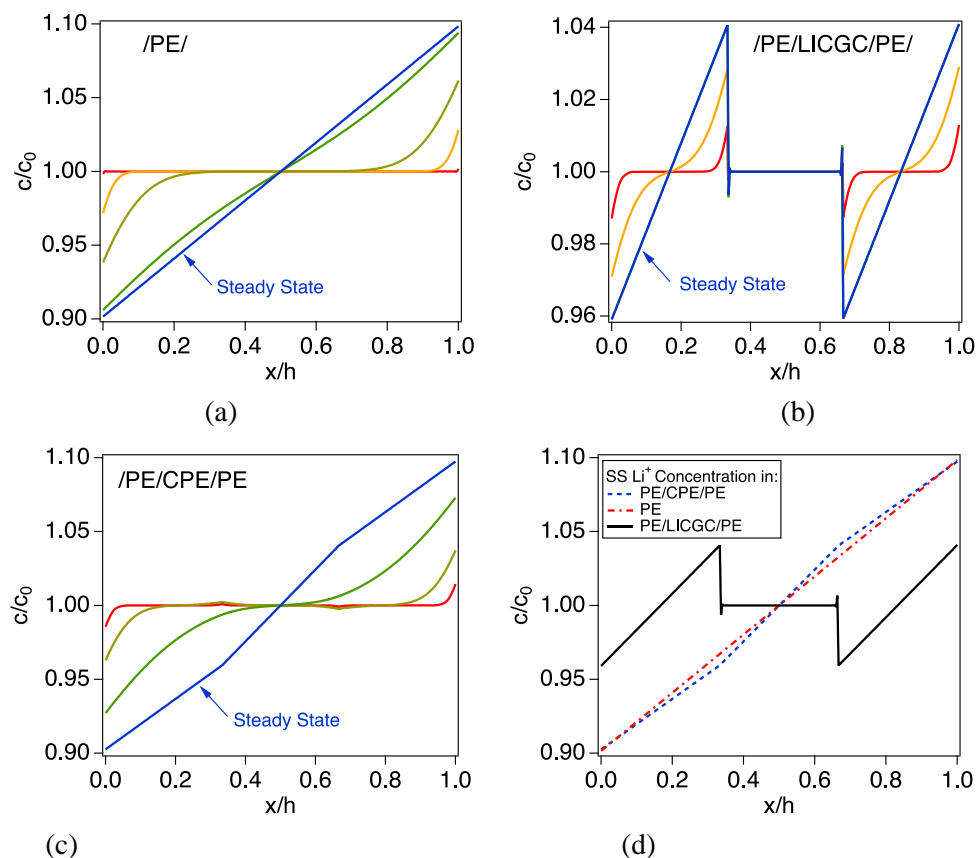


Figure 105. Simulated relaxation behavior of different electrolyte arrangements under 10-mV DC bias.

showing current relaxation to the steady state ( $I_{ss}$ ) are in Figure 105 for a constant applied DC voltage of 10 mV. The relaxation time is dictated by development of a steady state concentration profile in PE, where charge transport occurs through migration and diffusion of ions. Introduction of a LiCGC™ plate into the sandwich reduces this relaxation time since no diffusion-driven concentration gradients develop in LiCGC™. In the composite (simulated here at 50 vol% LiCGC™), the presence of resistive interface shell surrounding each of the particles reduces overall conductivity compared to LiCGC™ and increases time required to develop steady state current. The team notes that evaluation of the gel polymer composites shown in Figures 103 and 104 suggests that an enhanced conducting interface shell surrounds the ceramic particles embedded in the gel polymer matrix. This can account for the different relative relaxation times of Figures 104 and 105.

Development of concentration gradients across the polarized cell is illustrated in Figure 106. The different colors illustrate progression of  $\text{Li}^+$  concentration profile (normalized to the initial concentration before application of 10-mV bias across the electrolyte) from the initial to the final, steady state, shown in blue in Figure 106a-c. The through-thickness coordinate  $x$  is normalized with respect to the total electrolyte stack thickness, to aid comparing among the three configurations. The steady state profiles are shown in Figure 106d. It is interesting to note that the presence of the SIC plate reduces the deviation from the initial concentration in the PE sections of the electrolyte stack. This effect can be very pronounced when high current densities are involved in discharge of electrochemical cells. The corresponding numerical study is under way to quantify the benefit of a single-ion conductor in full-cells containing a binary electrolyte.



**Figure 106. Simulated development of lithium cation concentration profiles in (a) PEO:LiTFSI; (b) PE/Ohara/PE; and (c) PE/CPE/PE. (d) Comparison of steady state concentration profiles among the three configurations.**

#### Reference

- [1] McLachlan, D. S., M. Blaszkiwicz, and R. E. Newnham. *Journal of the American Ceramic Society* 73, no. 8 (1990): 2187–2203.

## Patents/Publications/Presentations

### Patent

- Chen, X. C., and Y. Zhang, T. Saito, F. M. Delnick, N. J. Dudney, and M. Lehmann. Composite Gel Electrolyte Membrane for Lithium Metal Batteries. May 2020, Patent application pending. S-138,862.

### Publications

- Merrill, L. C., X. C. Chen, Y. Zhang, H. O. Ford, J. L. Schaefer, and N. J. Dudney. “Polymer-Ceramic Composite Electrolytes for Lithium Batteries: A Comparison between Single Ion Conducting Polymer Matrix and Its Counterpart.” *ACS Applied Energy Materials*. In revision.
- Han, L., M. L. Lehmann, J. Zhu, T. Liu, Z. Zhou, X. Tang, C. Heish, A. P. Sokolov, P. Cao, X. C. Chen, and T. Saito. “Recent Developments and Challenges in Hybrid Solid Electrolytes for Lithium-Ion Batteries.” *Frontiers Energy Research*. In revision.

## Task 4.3 – Enabling Solid-State Batteries through Characterization and Modeling (Nenad M. Markovic and Larry A. Curtiss, Argonne National Laboratory)

**Project Objective.** The project objectives are multi-faceted, including development of a new mechanically and chemically stable and Li-ion conductive ( $\geq 2 \times 10^{-4}$  S/cm at 298 K) crystalline/amorphous SE for SSB. The anode and cathode are composed of lithium metal and a Li-based oxide, respectively, allowing operation at cathode potentials  $> 5$  V (denoted as a  $S_{Li}$ - $S_{EL}$ - $S_C$  system).

**Project Impact.** Protective organic and inorganic compounds can enhance stability of the interface, improve Li-ion interfacial transport, minimize dendrite formation, and increase safety in Li-ion batteries.

**Approach.** The project proposes to develop and use interdisciplinary, atomic-/molecular-level insight obtained from integrating both experimental- and computational- based methodologies to define the landscape of parameters that control interfacial properties for a new generation of the Li-ion solid-solid battery systems. The strategy will involve transferring knowledge gained from well-characterized thin-film materials to real-world materials. This strategy forms a closed loop wherein the knowledge gained from model systems is used to design more complex, real-world materials, and vice versa. The work will focus on utilizing existing in-house synthesis and characterization methods to enable rapid transition from fundamental science to realistic cells.

**Out-Year Goals.** The out-year goals are to use and develop the physical and chemical synthesis methods for design of solid-solid interfaces with unique chemical/mechanical/conductivity properties. The proposed work will develop and exploit a variety of *ex situ* and *in situ* experimental optical and surface sensitive techniques and electrochemical methods to explore and explain bulk and interfacial properties of the selected materials. The results will serve to unravel many puzzling bulk and interfacial properties of  $S_{Li}$ - $S_{EL}$ - $S_C$  systems, including various types of ceramic and glass materials.

**Collaborations.** This project funds work at ANL and collaboration with J. Sakamoto at UM.

### Milestones

1. Chemical stability, evaluation, and correlation with interfacial and bulk chemical reactivity for Li/PEO interfaces. (Q1, FY 2020; Completed)
2. Characterization of lithium /  $Li_{0.33}La_{0.55}TiO_3$  (LLTO) interfaces: effect of crystallinity on surface and bulk reactivity and electrochemical stability. (Q2, FY 2020; Completed)
3. Characterization of LCO/electrolyte interfaces: effect of crystallinity and orientation on surface and bulk reactivity. (Q3, FY 2020; Completed)
4. Characterization of lithium interfaces with doped and undoped LLZO, with experimental and modeling study. (Q4, FY 2020)

## Progress Report

**Effect of LLTO(hkl) Orientation and Crystallinity on the LLTO/Li Interface.** LLTO is a perovskite SE that crystallizes in a pseudo-perovskite structure with ordered lanthanum (A-site) vacancies along the c-axis in a tetragonal unit cell. Although LLTO exhibits orientation-dependent differences in bulk reactivity after short-term exposure to a lithium overlayer, long-term exposure (~ 3 days) eventually results in identical bulk reduction behavior regardless of orientation, indicating that the orientation-dependent differences observed are kinetic, rather than thermodynamic in origin. This stands in contrast to *amorphous* LLTO thin films, which surprisingly exhibit no evidence of surface or bulk reactivity after deposition of thin lithium films. This suggests that amorphous materials may represent a promising path toward realizing conductive SEs with reduced interfacial reactivity.

**Effect of LLTO(hkl) Orientation and Crystallinity on LLTO/LiCoO<sub>2</sub> Interface.** The team is also interested in the interface between the electrolyte and the cathode—here between thin films of LLTO and LiCoO<sub>2</sub>—and measuring the impact of interfacial structure on kinetics. To do this, they synthesized several distinct interfaces with use of epitaxial thin film growth by PLD.

LLTO thin films with different orientations and crystalline forms were deposited on NdGaO<sub>3</sub> (110), SrTiO<sub>3</sub> (001), and silicon substrates with PLD; this was followed by growth of the LiCoO<sub>2</sub> cathode films. Due to the similarity in lattice parameters, the surface unit cell of NdGaO<sub>3</sub> (110) promotes the LLTO (001) orientation, while SrTiO<sub>3</sub> (001) leads to the LLTO (100) orientation. As stated, LLTO is tetragonal, and the different orientations should vary in the rate of lithium transfer across the interface, at least in the short term. In both cases, the LiCoO<sub>2</sub> overlayer is epitaxial, with the (104)-orientation. In the case of the silicon substrate, deposition was conducted at room temperature to promote growth of amorphous LLTO and amorphous LiCoO<sub>2</sub>. For another sample, this was repeated four times, effectively making an amorphous superlattice.

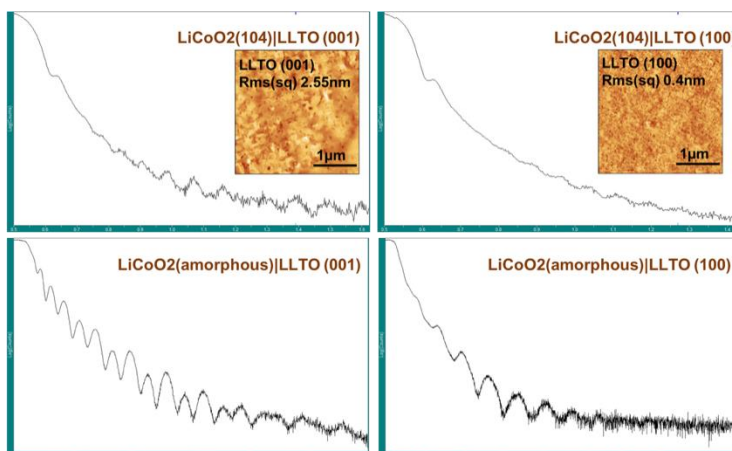


**Figure 107.** Atomic force microscopy measurements on bare LLTO films for the (001) and (100) orientations are shown in the insets. X-ray reflectivity for crystalline LiCoO<sub>2</sub> / LLTO (hkl) is shown at the top, and amorphous LiCoO<sub>2</sub> / LLTO (hkl) is shown at the bottom.

Figure 107 shows results from X-ray reflectivity (XRR) and AFM. AFM on the (001)-oriented LLTO film gives a surface roughness of ~ 2.5 nm, while that of the (100) film is only ~ 0.4 nm. However, after depositing LiCoO<sub>2</sub> (either crystalline or amorphous), the LiCoO<sub>2</sub> (104) / LLTO (100) interface appears rougher than that of the LiCoO<sub>2</sub> (104) / LLTO (001) interface, at least based on the XRR results.

As the scattering length densities of LLTO and LiCoO<sub>2</sub> differ by only 8% at 8048 eV (Cu K $\alpha$  radiation), it is difficult to accurately measure the chemical width of the interface (and interdiffusion). On the other hand, the neutron scattering length densities differ by 160%, making neutron reflectometry a much more sensitive probe for interdiffusion. The team therefore also performed neutron reflectometry studies at the Spallation Neutron Source (SNS) at ORNL on these systems, starting with measurements on the initial LLTO films to serve as benchmarks. They find a surface roughness of ~ 5 nm for LLTO (001) and ~ 3 nm LLTO (100), suggesting that the difference in the XRR can be normal sample variation due to stochastic processes that occur during deposition. More importantly, neutron reflectivity allows a good measure of the atomic density profile. They find that both the LLTO (100) and (001) films have ~ 100% atomic density, as would be expected for epitaxial layers.

Deposition of  $\text{LiCoO}_2$ , however, leads to a relatively complex density profile, as shown in Figure 108. The reflectivity must be modeled with two distinct  $\text{LiCoO}_2$  layers, with the layer near the surface only  $\sim 50\%$  dense on average; the layer closest to the substrate is  $\sim 100\%$  dense. This could indicate some loss of crystallinity in the  $\text{LiCoO}_2$  during the PLD process. Regardless, the interface width between  $\text{LiCoO}_2$  and LLTO remains very narrow, on the  $\sim 1$  to  $2$  nm level despite the fact that deposition took place  $\sim 800^\circ\text{C}$ .

When the  $\text{LiCoO}_2$  and LLTO films are grown at room temperature, the interfaces remain relative sharp ( $\sim 1$ - $2$  nm), as shown in Figure 109a-b, but the atomic densities are lower than the bulk densities, ranging from  $80\%$  to  $94\%$  (Figure 109c). This is presumably due to greater free volume per atom in the amorphous structure. Although the film is amorphous, the superlattice structure still provides a diffraction peak at low angles, as shown in the XRR scan of Figure 109a. One can monitor the behavior of this “superlattice peak,” which originates from the  $\text{LiCoO}_2$  / LLTO interface at elevated temperatures to measure the activation energy for interdiffusion. The team performed this measurement at the APS using a coherent X-ray beam to detect the behavior of the lithium ions as they fluctuate across the  $\text{LiCoO}_2$  / LLTO interface. They have plotted the results in the form of a two-time correlation function, as shown in Figure 109d. By measuring this for different temperatures, they arrive at Figure 109e, which is an Arrhenius plot showing the activation energy for Li-ion migration across the interface. While the data are still being analyzed, the activation energy appears to be quite low.

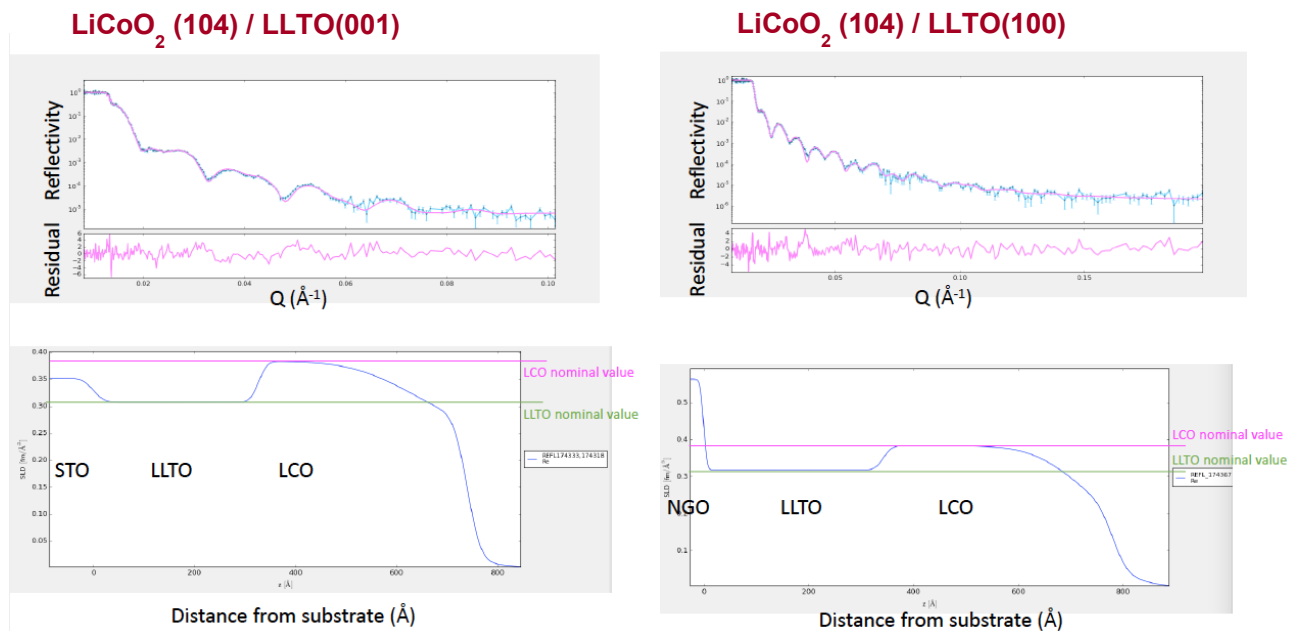


Figure 108. Neutron reflectometry measurement on bilayer thin films of  $\text{LiCoO}_2$  (104) / LLTO (hkl), where (hkl) is (001) for films grown on  $\text{SrTiO}_3$  (001) and is (100) for films grown on  $\text{NdGaO}_3$  (110).

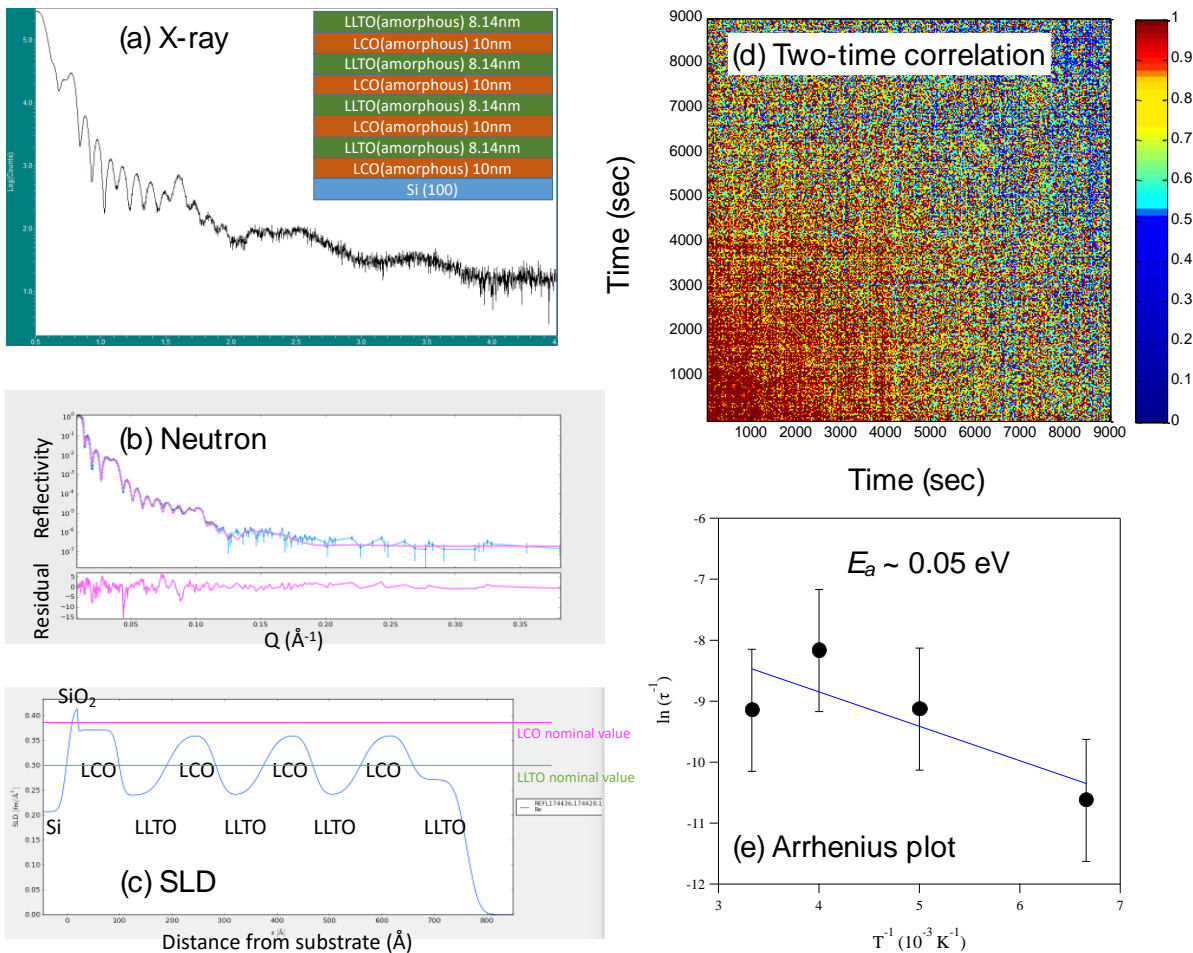


Figure 109. (a) X-ray reflectivity and (b) neutron reflectivity, along with the fitted density profile for the amorphous LiCoO<sub>2</sub> / LLTO superlattice (c). (d) The two-time correlation function, as measured using a coherent X-ray beam at the APS. The results at different temperatures allow measurement of the activation energy for Li-ion fluctuations across the interface (e).

### Patents/Publications/Presentations

The project has no patents, publications, or presentations to report this quarter.

## Task 4.4 – 3D Printing of All-Solid-State Lithium Batteries (Jianchao Ye, Lawrence Livermore National Laboratory)

**Project Objective.** This project has three objectives: (1) tuning microstructures of 3D-printed SSE separators, (2) determining material and processing compatibilities with cathode printing, and (3) 3D printing of sintering-free SSE separators.

**Project Impact.** All-solid-state lithium batteries are difficult to process due to the brittleness of ceramic materials, poor solid-solid contact, and electrolyte-electrode stability issues. As a result, the energy and power density and also cycling stability are far from satisfying. This project will address fabrication difficulties by using state-of-the-art 3D-printing techniques that can introduce 3D interfaces and architectures to enhance solid-solid contact and reduce charge transfer resistance. Success will benefit the DOE by establishing the best manufacturing methods for ASSBs to achieve VTO goals on the performance of beyond Li-ion batteries.

**Approach.** The project employs 3D-printing techniques to manufacture SSEs and related components for ASSBs. The team starts with direct ink writing (DIW) to develop ink recipes with desired rheological properties and explore post-sintering approaches to achieve high densification. In parallel with DIW 3D printing, the team also explores other 3D printing options, such as projection microstereolithography (PuSL). Both sintering and sintering-free approaches can gain benefit from 3D printing and therefore will be investigated.

**Out-Year Goals.** The team will determine particle sizes and morphologies as well as post-processing conditions that deliver good ionic conductivity and charge transfer properties of LLZTO separators. They will examine co-sintering of LLZTO/cathode and determine the effects of material, particle size, surface coating, and sintering conditions.

**Collaborations.** Microstructures, ionic conductivities, and mechanical properties will be provided to the LLNL simulation team, led by PI B. Wood, for establishing and validating phase-field modeling methods.

### Milestones

1. ALD coating on LLZTO/electrode powders. (Q1, FY 2020; Completed)
2. Thermochemical stabilities of electrolyte-electrode-conductive additive mixtures. (Q2, FY 2020; In progress)
3. Down selection of electrolyte-electrode-conductive additive mixtures with good electronic and ionic conductivities. (Q3, FY 2020; In progress)
4. Evaluation of half-cell stability and failure mechanisms. (Q4, FY 2020)

## Progress Report

Due to the shelter-in-place order for COVID-19, no experimental work could be carried out in the whole third quarter. The lab work for the project was gradually restarted at the end of June.

This quarter, the team focused on preparation of manuscripts and experimental planning. One manuscript is to explore the relationship between solvent-assisted ball milling, particle size, and sintering temperature in garnet-type SEs. Careful analysis of the particle size distribution before and after ball milling was further conducted using Image J software, which showed the best milling efficiency under the milling condition with acetonitrile / Triton X-100 liquid medium. Rietveld refinement on the calibrated XRD data proved that no chemical changes on the LLZTO powders after high-energy ball milling in acetonitrile / Triton X-100. In contrast, severe  $H^+/Li^+$  exchange occurred for the powders milled in ethanol, which explained poor densification and secondary phase formation after sintering. The particle size reduction plus the maintenance of the right chemistry led to the accelerated densification and over  $100^\circ\text{C}$  lower sintering temperature. Figure 110a shows SEM image of a highly densified LLZTO sample at  $1000^\circ\text{C}$  sintering temperature made of acetonitrile/Triton ball-milled powders. In contrast, the LLZTO sample made from raw powders with much larger particle size shows poor densification (Figure 110b).

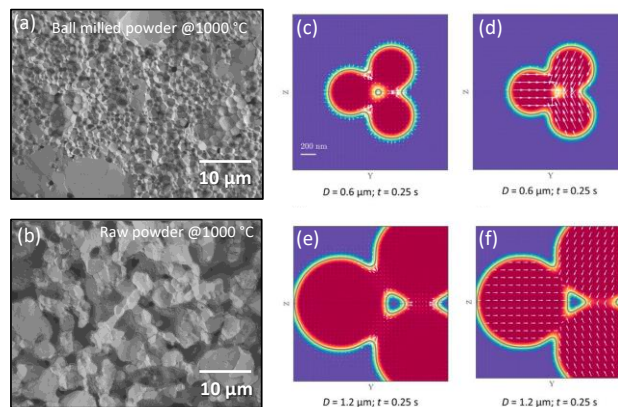


**Figure 110.** (a) and (b) are scanning electron microscopy images of  $1000^\circ\text{C}$  sintered LLZTO made from ball milled powder ( $D_{v50} = 238 \text{ nm}$ ) and raw powder ( $D_{v50} = 7 \mu\text{m}$ ), respectively. Diffusion flux (c/e) and advection flux (d/f) associated with particle translational motion during sintering of three particles with diameters equal to  $0.6 \mu\text{m}$  (c-d) or  $1.2 \mu\text{m}$  (e-f). The white arrows represent the flux vectors, with the arrow size proportional to the flux magnitude. Both diffusion and advection flux, which transport mass to the pore region in the center, increase with decreasing particle size. The scale bar in (c) also applies to (d-f).

To better understand the particle size effect, multi-phase field modeling was employed to simulate the microstructure evolution of a representative motif consisting of three particles. It was attributed to the enhanced mass transport kinetics; the faster surface diffusion and larger advection flux (Figure 110c-f) result in faster neck growth between particles and greater rigid-body translation. A more realistic model considering thousands of particles with defined size distributions is being developed. Results will be compared with *in situ* ultra-small-angle X-ray scattering (USAXS) data to explain the variation of pore size and density as a function of temperature and time.

## Patents/Publications/Presentations

### Publications

- Wood, M., X. Gao, R. Shi, J. Espitia, T. W. Heo, J. A. Espitia, E. B. Duoss, and J. Ye. “Exploring the Relationship between Solvent-Assisted Ball Milling, Particle Size, and Sintering/Temperature in Garnet-Type Solid Electrolytes.” Submitted.
- Espitia, J., J. Hammons, E. Ramos, M. Wood, M. Ceron., and J. Ye. “*In Situ* USAXS/WAXS Studies on Sintering of  $\text{Li}_{6.4}\text{La}_3\text{Zr}_{1.4}\text{Ta}_{0.6}\text{O}_{12}$ .” In preparation.

## Task 4.5 – Interfacial Studies on Lithium Thiophosphate Based Solid Electrolytes and Cathodes (Jagjit Nanda, Oak Ridge National Laboratory)

**Project Objective.** Capacity fading and the underlying interfacial side reactions between thiophosphate SEs and cathode active materials are not well understood. A key project deliverable is to combine EIS measurements with complementary *in situ* and *ex situ* spectroscopy and microscopy to identify decomposition reaction products at the cathode/electrolyte interface. Ultimately, this work will enable a mechanistic understanding of factors that limit the rate performance and capacity loss of SSBs. The goal here is to combine the information from these techniques to provide a unified overview of the interfacial layer's composition, structure, and morphology. In this multi-year work, the team will investigate a number of SEs [ $\text{Li}_3\text{PS}_4$  (LPS),  $\text{Li}_{10}\text{GeP}_2\text{S}_{12}$  (LGPS), and  $\text{Li}_{9.54}\text{Si}_{1.74}\text{P}_{1.44}\text{S}_{11.7}\text{Cl}_{0.3}$  (LSiPCI)] and cathode compositions belonging to different structural families [ $\text{LiFePO}_4$  (olivine),  $\text{FeS}_2$  (sulfide-based conversion cathode), and  $\text{LiNi}_{0.6}\text{Mn}_{0.2}\text{Co}_{0.2}\text{O}_2$  (NMC-622, layered oxide)].

**Project Impact.** SSBs are poised to be the next-generation battery technology for meeting EV goals in terms of energy density, cycle life, and safety. Among other technical barriers, the success of this technology relies on design of stable electrode/electrolyte interfaces. Sulfide-based SEs have high ionic conductivity ( $> 10^{-4}$  S/cm) and are mechanically soft, which simplifies processing compared to their oxide counterparts. Furthermore, sulfide SEs are comprised of earth abundant materials (for example, sulfur and phosphorus) and can be easily synthesized using scalable, low-temperature solution-based routes.

**Approach.** A low-temperature ( $< 350^\circ\text{C}$ ) solution-based synthesis method will be used to synthesize the LPS family of SEs. The structure of these materials is characterized using XRD, Raman spectroscopy, and neutron scattering. Standard AC/DC electrochemical methods are used to characterize ionic conductivity, electrochemical stability, and CCD. The work scope includes using various *in situ* and *ex situ* electrochemical, microscopic, and spectroscopic tools for characterizing the structure, morphology, and kinetics of the interfacial reaction layer formed between thiophosphate SEs and cathodes.

**Out-Year Goals.** Develop thiophosphate SEs – sulfide cathode interfaces with low ASRs for ASSBs.

**Collaborations.** This project will collaborate with Profs. G. Ceder (UC Berkeley) and P. Jena (Virginia Commonwealth University) on modeling and synthesis guideline, as well as with Prof. S. Greenbaum on solid-state NMR to measure ion-diffusivity and local bonding.

### Milestones

1. Identify synthesis, doping, and processing conditions to prepare  $\text{Li}_3\text{PS}_4$ -based SEs with  $\text{Li}^+$  conductivity exceeding  $10^{-4}$  S/cm. (Q1, FY 2020; Completed, December 31, 2019)
2. Develop binder systems for  $\text{Li}_3\text{PS}_4$  family of SEs for improving processability and stability at the Li-metal and cathode interfaces. (Q2, FY 2020; In progress)
3. Measure and compare the  $\text{Li}^+$  diffusion coefficient for pristine  $\text{Li}_3\text{PS}_4$  and substituted  $\text{Li}_3\text{PS}_4$  SEs using solid-state NMR. (Q3, FY 2020; In progress)
4. Undertake *in situ* Raman and electron microscopy including cryo-TEM for characterizing  $\text{Li}_3\text{PS}_4$  and cathode- $\text{Li}_3\text{PS}_4$  interfaces as part of determining the ASR. (Q4, FY 2020)

## Progress Report

To identify appropriate cell configurations for *in situ* spectroscopic measurements, studies this quarter focused on benchmarking performance of SSBs containing a  $\beta$ - $\text{Li}_3\text{PS}_4$  SE (prepared using the solvent-mediated route developed in FY 2019), Li-metal anode, and two different Li-ion cathodes [ $\text{LiFePO}_4$  (LFP) and  $\text{LiNi}_{1/3}\text{Mn}_{1/3}\text{Co}_{1/3}\text{O}_2$  (NMC-111)]. The cells were constructed by the following steps: (i) cold-pressing bilayer  $\beta$ - $\text{Li}_3\text{PS}_4$ /cathode pellets (diameter of 13 mm, thickness of  $\sim 1$  mm, and densities of  $\sim 1.6$   $\text{g}/\text{cm}^3$  for the overall bilayer structure) followed by (ii) adhering thin lithium anodes (20-45  $\mu\text{m}$  on copper foil) to the pellets. Stack pressures up to 80 MPa were applied using a vice and measured with an external load cell. Figure 111 shows details on the cell configuration and cathode compositions.

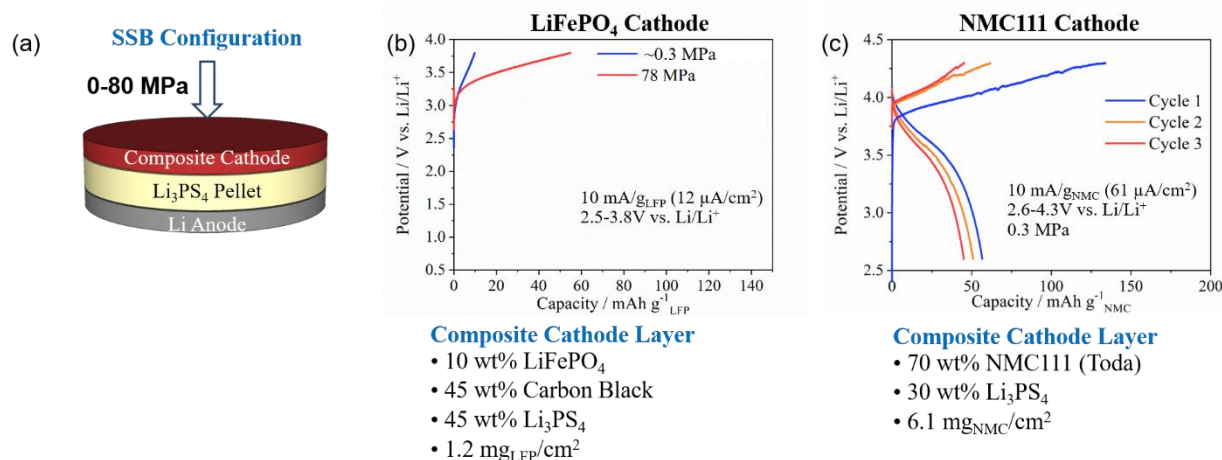


**Figure 111. (a) Solid-state battery configuration and corresponding galvanostatic charge/discharge curves for cells containing (b) LiFePO<sub>4</sub> and (c) NMC-111 cathodes.**

Figure 111b shows galvanostatic charge/discharge curves for a SSB containing an  $\text{LiFePO}_4 + \text{C} + \text{Li}_3\text{PS}_4$  cathode. With a stack pressure of  $\sim 0.3$  MPa, the cathode exhibited a very low charging capacity of 10  $\text{mAh}/\text{g}_{\text{LFP}}$  and negligible reversible capacity (0.01  $\text{mAh}/\text{g}_{\text{LFP}}$ ). Increasing the stack pressure to 80 MPa had little impact on these metrics. On the other hand, a SSB containing NMC-111 +  $\text{Li}_3\text{PS}_4$  cathode operated under 0.3 MPa showed significantly better performance (see Figure 111c). During the first charging step, the cell exhibited the expected voltage profile with moderate active material utilization (that is, 134  $\text{mAh}/\text{g}_{\text{NMC111}}$ ). The low reversible capacity (57  $\text{mAh}/\text{g}_{\text{NMC111}}$ ) and CE during the 1<sup>st</sup> cycle (43 versus 80+% when using liquid carbonate electrolytes) are attributed to irreversible reactions between the sulfide SE and NMC-111 cathode. Subsequent cycles exhibited gradual capacity fade and increasing voltage hysteresis, which indicates further optimization of the cathode/electrolyte interface is required. Overall, these studies indicate that the performance of SSBs containing sulfide-based SEs is highly dependent on the cathode chemistry and composition. Importantly, these results demonstrate that moderate stack pressures  $< 1$  MPa may be adequate for some cell configurations. Studies next quarter will explore various cathode coating strategies and interfacial buffer layers to improve the compatibility of sulfide SEs with high-energy Li-ion cathodes. Further optimization of the stack pressure on cell performance will also be reported.

In addition to electrochemical studies on SSBs, the structure of several sulfide SEs developed in this program was evaluated using solid-state NMR spectroscopy in collaboration with Prof. S. Greenbaum's team at Hunter College. Figure 112 shows  $^7\text{Li}$  NMR spectra of crystalline  $\beta$ - $\text{Li}_3\text{PS}_4$  and amorphous composites containing  $\text{Li}_3\text{PS}_4 + 1\%$  PEO. All samples exhibited a single peak centered at 0 ppm. After annealing  $\text{Li}_3\text{PS}_4 + 1\%$  PEO at 140°C to remove coordinated acetonitrile, the  $^7\text{Li}$  peak width decreased substantially, which correlates with higher  $\text{Li}^+$  cation mobility. This finding is consistent with ionic conductivity measurements reported last quarter

in which annealing at 140°C increased the conductivity of  $\text{Li}_3\text{PS}_4+1\%\text{PEO}$  by 3 orders of magnitude (for example, from  $4.5 \times 10^{-9}$  to  $8.4 \times 10^{-6}$  S/cm at room temperature).  $^7\text{Li}/^1\text{H}$  cross-polarization NMR measurements are under way to better understand the influence of coordinated solvent and PEO binder on the  $\text{Li}^+$  dynamics and local bonding environment. Combining these NMR measurements with other characterization methods (such as vibrational spectroscopy, X-ray/neutron scattering, and electrochemical testing) will help establish structure/function correlations for sulfide SEs produced via solvent-mediated routes.

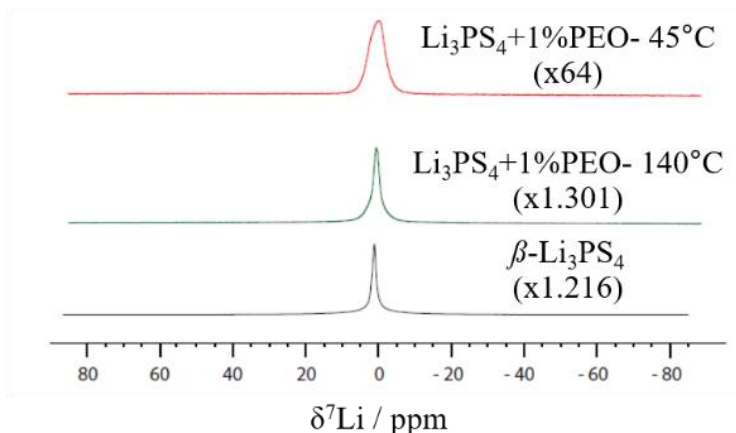


Figure 112.  $^7\text{Li}$  solid-state nuclear magnetic resonance spectra of  $\beta\text{-Li}_3\text{PS}_4$  and amorphous  $\text{Li}_3\text{PS}_4+1\%$  PEO solid electrolytes prepared through solvent-mediated routes developed in FY 2020-2021. Notably, these materials exhibit significantly different peak intensities, and thus have been linearly scaled to facilitate direct comparisons. All spectra are referenced to lithium triflate ( $\delta = 0$  ppm).

## Patents/Publications/Presentations

### Publication

- Self, E. C., Z. D. Hood, T. Brahmabhatt, F. M. Delnick, H. M. Meyer III, G. Yang, J. L. M. Rupp, and J. Nanda. “A New Class of Amorphous Sulfide-Based Solid Electrolytes: Synthesis, Characterization, and Electrochemical Properties.” *Chemistry of Materials* (2020). In revision.

### Presentation

- DOE VTO Annual Merit Review, virtual poster presentation (June 1–4, 2020): “Sulfide-Based Solid Electrolytes for Solid-State Li Batteries”; J. Nanda, E. C. Self, G. Yang, and F. M. Delnick.

## Task 4.6 – Prelithiation of Silicon Anode for High-Energy Lithium-Ion Batteries (Yi Cui, Stanford University)

**Project Objective.** Prelithiation of high-capacity electrode materials is an important means to enable those materials in high-energy batteries. This study pursues three main directions: (1) developing facile and practical methods to increase 1<sup>st</sup> cycle CE of anodes, (2) synthesizing fully lithiated anode to pair with high-capacity Li-free cathode materials, and (3) prelithiation from the cathode side.

**Project Impact.** Prelithiation of high-capacity electrode materials will enable those materials in next-generation high-energy-density Li-ion batteries. This project's success will make high-energy-density Li-ion batteries for EVs.

**Approach.** Silicon electrode film will be prepared by coating the slurry of silicon nanoparticles, carbon black, and binder mixture on copper foil through a doctor-blading method. The silicon electrode film will be prelithiated by pressing a Li-metal foil on top of it and heating it in an argon glovebox for a certain time. Then,  $\text{Li}_x\text{Si}$  electrode film can be obtained by removing the redundant lithium foil through a peeling-off approach. The redundant lithium foil is reusable for the next prelithiation. The structure, morphology, and other properties can be analyzed by SEM, TEM, XPS, Raman spectroscopy, XRD, etc. In the first year, the team aims to fabricate  $\text{Li}_x\text{Si}$  freestanding electrode film and improve its air stability. In the second year, the team aims to improve the electrochemical stability in full cells.

**Out-Year Goals.** Materials containing a large quantity of lithium will be synthesized for pre-storing lithium ions inside batteries. Materials and process will be developed to be compatible with battery electrode and cell fabrication. First-cycle CE of anodes will be improved and optimized by prelithiation materials. Develop materials for prelithiation from the cathode side.

**Collaborations.** This project engages in collaboration with the following: BMR PIs; SLAC: Dr. M. Toney (*in situ* X-ray); and Stanford: Prof. Nix (mechanics).

### Milestones

1. Demonstrate a new solvent-free dry method for anode prelithiation. (Q1, FY 2020; Completed)
2. Demonstrate control of prelithiation amount by adjusting contact duration between thick lithium foil and anode materials. (Q2, FY 2020; Completed)
3. Demonstrate synthesis of thin lithium foil with different thickness (5-20  $\mu$ ) for use in dry prelithiation method. (Q3, FY 2020; Completed)
4. Demonstrate thin lithium foil with different thicknesses as dry prelithiation reagents for anode materials to pair with different-capacities cathode materials. (Q4, FY 2020; In progress)

## Progress Report

Substantial improvements on energy density of Li-ion batteries require development of high-capacity electrodes. Alloy anodes with much higher capacity have been recognized as promising alternatives to graphites. However, the low Initial Coulombic efficiency (ICE) accompanied with alloying chemistry limits the full usage of the designed capacity in battery. Silicon, as an example of a typical alloy anode, has ICE as low as  $\sim 70\%$ , indicating  $\sim 30\%$  of the capacity will be lost after the 1<sup>st</sup> cycle. Therefore, prelithiation as a strategy to compensate the irreversible capacity loss in the 1<sup>st</sup> cycle has become critically important for battery performance improvement.

In the last report, the team presented a novel one-step, heat-free, solvent-free prelithiation approach by electrochemical shorting between silicon anode and a layer of thin lithium foil. They are further developing it to be controllable prelithiation by designing a series of lithium masks with different porosity as prelithiation reagent. However, the thickness of lithium foil ( $\sim 25 \mu\text{m}$ ) and the technical difficulties in increasing porosity limit the range of designed prelithiation capacity ( $1\text{-}5 \text{ mAh/cm}^2$ ). To further broaden the lower limit to widen the prelithiation application, here, the team develops another strategy to achieve controllable prelithiation by designing a series of lithium foils with different thickness.

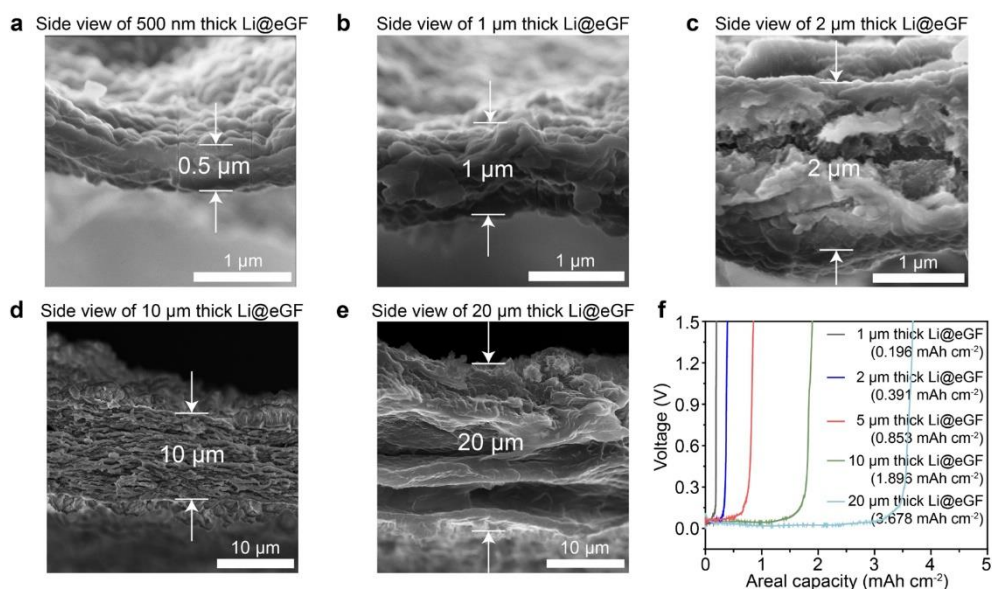


**Figure 113.** (a-e) Cross-sectional scanning electron microscopy images of Li@eGF films with tunable thickness from 500 nm to 20 μm. (f) Voltage-capacity profiles of Li@eGF films with different thickness, showing the capacities exhibited in them.

Different thickness lithium foils were fabricated by using rGO as the host. First, the team controllably calendered the rGO to a few microns (0.3 to 20 μm). After an edge-containing molten lithium absorption procedure, the rGO host loaded metallic lithium inside its internal channels and retained the micron-level thickness. As a result, a hosted Li-metal film (Li@eGF) with tunable micron-level thickness (0.5 to 20 μm) was successfully fabricated. The cross-sectional SEM images of Li@eGF (Figure 113a-e) demonstrates that most of the original submicron-wide void channels in fabricated Li@eGF were filled with metallic lithium, supporting the successful fabrication of lithium foils hosted by rGO with different thickness. This wide range of thickness (500 nm, 1 μm, 2 μm, 10 μm, and 20 μm) enables the Li@eGF to exhibit a wide range of designed prelithiation amounts (0.089 mAh/cm<sup>2</sup>, 0.196 mAh/cm<sup>2</sup>, 0.391 mAh/cm<sup>2</sup>, 1.896 mAh/cm<sup>2</sup>, and 3.678 mAh/cm<sup>2</sup>), which is verified by the voltage-capacity profiles of Li@eGF (Figure 113f) measured in lithium stripping test. Therefore, this series of Li@eGF foils with varied thickness broadens the lower limit of designed prelithiation capacity to  $\sim 0.1 \text{ mAh/cm}^2$ , expanding the application of one-step dry prelithiation method to silicon batteries with lower designed capacities and even making it possible to be applied to a relatively high ICE anode material like graphite.

## Patents/Publications/Presentations

### Presentations

- Elsevier Webinar (April 3, 2020): “From Innovation to Commercialization for Materials, Energy and Environment.” Invited.
- American Chemical Society (ACS) Webinar (May 14, 2020): “Facial Masks during COVID-19: Disinfection, Homemaking and Imaging.” Invited.
- African Society for Laboratory Medicine Webinar (May 26, 2020): “Facial Masks during COVID-19: Disinfection, Homemaking and Imaging.” Invited.
- Massachusetts Institute of Technology (MIT) InnoTherm Symposium Webinar (June 17, 2020): “Thermal Effects on Battery Materials and Chemistry.” Invited.

## TASK 5 – SULFUR ELECTRODES

### Summary

The collected work in this Task involves six projects that have focused on the following areas:

- Conducting focused fundamental research on the mechanism of “shuttle effect” inhibition for rechargeable Li-S batteries.
- Developing electrode and electrolyte systems that can mitigate the “shuttle effect” so the low self-discharge and long cycle life can be achieved.
- Synthesizing sulfur composite materials with an emphasis on polymer sulfur composite materials.
- Developing creative electrode-making processes to improve processability and aerial capacity; for example, polymeric sulfur composites may not be suitable for the traditional slurry casting process.
- Developing a novel  $S_xSe_y$  cathode material for rechargeable lithium batteries with high energy density and long life, as well as low cost and high safety.
- Delivering an electrochemically responsive self-formed hybrid LIC as a protective layer for Li-metal anodes, enabling Li-metal anodes to cycle with a high efficiency.
- Developing high-energy, low-cost Li-S batteries with long lifespan.

**Highlights.** The highlights for this quarter are reported below.

Dr. K. Amine’s group at ANL has used XPS to characterize the SEI of lithium metal after cycling in conventional based electrolytes and HFE-based electrolytes in Li||Cu half cells. They observed that the Li-metal surface is covered by SEI layer containing stronger Li-F signals on cells cycled with HFE compared to DME electrolytes based on both Li 1s and F 1s XPS spectra. They therefore concluded that in DME-based system, there could be parasitic reactions between lithium and the electrolyte resulting in dendrite formation. On the other hand, the HFE electrolytes lead to a robust SEI containing stronger Li-F bonds that passivate the surface of lithium, likely leading to stable cycling performance with good CE. Identification of such electrolytes and creation of a stable SEI that conducts lithium ions, effectively controlling the concentration and potential gradients, could be critical for generating dendrite-free Li-metal anodes.

The PNNL group led by Drs. D. Lu and J. Liu continued their studies on different carbon systems containing varying particle sizes. They tested electrodes of large particle size in excess of 70  $\mu\text{m}$  at porosity levels lower than 50% and at high sulfur loadings of 4mg S/cm<sup>2</sup> using two new electrolytes, one with limited polysulfide solubility and another hybrid electrolyte containing PE additive. The former gave a high initial discharge capacity of ~ 1300 mAh/g under lean electrolyte of E/S = 4 $\mu\text{l}$ /mg sulfur due to the suppression of polysulfide solubility. However, after 80 cycles, the capacity drops to 800 mAh/g due to loss of active sulfur and increase in polarization. Alternatively, the hybrid electrolyte affords a lower porosity of less than 40% and for the same loading under same lean electrolyte condition yields a stable capacity of ~ 900 mAh/g, dropping to ~ 792 mAh/g after 80 cycles and signifying the efficacy of PE addition. Further optimization exploiting the benefits of each system is in progress. Such an approach will be key for attaining high-energy-density Li-S batteries.

Dr. Y. Cui’s group at Stanford has studied mechanisms contributing to better battery performance of Ni-based electrodes compared to carbon electrodes. They studied the decomposition of Li<sub>2</sub>S on the nickel surface, graphene basal plane, and graphene edge using DFT calculations. The calculations reveal that strong interaction of Li<sub>2</sub>S on graphene edge promotes Li<sub>2</sub>S dissociation, but limits the diffusion of lithium away. On the other hand, the interaction of Li<sub>2</sub>S on graphene basal plane is too weak to initiate Li<sub>2</sub>S dissociation with weak

interaction of lithium and LiS intermediates, thereby preventing Li<sub>2</sub>S dissociation. However, the interaction of Li<sub>2</sub>S on nickel is moderate, presenting a lower barrier for decomposition and thus suggesting that nickel is a good electrode candidate for Li-S batteries, which validates the experimental observation. Such mechanistic studies will be useful in identifying optimal current collectors for facile operation of high-energy-density Li-S batteries.

Dr. D. Qu's group at UWM has continued their studies using the series of semi-graphitic ordered mesoporous carbons with metal/nitrogen doping (Me-N-GOMCs; Me = Fe, Co, Ni, and Cu). The Me-N-GOMCs systems developed previously were studied this quarter for their electrochemical performance by embedding them in the void space of carbon paper (CP) to construct a free standing sulfur cathode and testing in a 2016 coin cell. The integrated 3D CP/Fe-N-GOMC/S electrode shows good cycling performance at loadings of ~ 3 mg/cm<sup>2</sup>, exhibiting a high initial capacity of 1473 mAh/g and good cycling stability up to 500 cycles. Areal capacities of ~ 6 mAh/cm<sup>2</sup> have also been attained up to 120 cycles. They are also screening electrolytes and additives showing evidence of improved performance. Such electrode architecture generation will be useful for high-density Li-S batteries.

Dr. G. Liu's group at UC Berkeley has focused on studying their new class of amphiphilic electrolyte additives based on HFE generating micellar structures containing lithiophilic and lithiophobic ends. This quarter they employed Li||Cu cells to study the cycling stability and CE of the designed trifluoroethylene oxide (F<sub>3</sub>EO<sub>1</sub>) additive electrolytes for anode performance. They studied the plating and stripping efficiency of lithium on copper, with these electrolytes at current densities of 0.5 mA/cm<sup>2</sup>, 1 mA/cm<sup>2</sup>, and 2 mA/cm<sup>2</sup>, showing promise of the system for forming a passivating LiF layer on lithium. They observed the surface of the lithium deposited at all three current densities at areal capacity of 1 mAh/cm<sup>2</sup>, showing smooth surface formation, while nodules were seen for current density of 2 mA/cm<sup>2</sup> with absence of dendrites. Creation of these electrolytes could likely facilitate use of dendrite free Li-metal anodes.

## Task 5.1 – Novel Chemistry: Lithium Selenium and Selenium Sulfur Couple (Khalil Amine, Argonne National Laboratory)

**Project Objective.** The project objective is to develop a novel  $S_xSe_y$  cathode material for rechargeable lithium batteries with high energy density and long life, as well as low cost and high safety.

**Project Impact.** Development of a new battery chemistry is promising to support the goal of PHEV and EV applications.

**Approach.** The dissolution of lithium polysulfides in nonaqueous electrolytes has been the major contribution to the low energy efficiency and short life of Li-S batteries. In addition, insulating characteristics of both end members during charge/discharge (sulfur and  $Li_2S$ ) limit their rate capacity. To overcome this problem, sulfur or  $Li_2S$  is generally impregnated in a carbon-conducting matrix for better electronic conductivity. However, this makes it difficult to increase the loading density of practical electrodes. It is proposed to solve these barriers using the following approaches: (1) partially replace sulfur with selenium, (2) nano-confine the  $S_xSe_y$  in a nanoporous conductive matrix, and (3) explore advanced electrolytes with suppressed shuttle effect.

**Out-Year Goals.** This new cathode will be optimized with the following goals:

- A cell with nominal voltage of 2 V and energy density of 600 Wh/kg.
- A battery capable of operating for 500 cycles with low capacity fade.

**Collaborations.** This project engages in collaboration with the following: Dr. Y. Ren and Dr. C. Sun of APS at ANL, Dr. L. A. Curtiss at ANL, and Prof. A. X. Sun at Western University, Canada.

### Milestones

1. Synthesize new carbon materials to prepare  $SeS_x$ /carbon composites with high sulfur loading in the composite. (Q1, FY 2020; Completed)
2. Optimize cathode structures to increase  $SeS_x$  areal loading, and improve battery performance. (Q2, FY 2020; Completed)
3. Gain interface understanding on the cycled  $SeS_x$  cathode using TOF-SIMS and XPS. (Q3, FY 2020; Ongoing)
4. Gain interface understanding on the cycled lithium metal using TOF-SIMS and XPS. (Q4, FY 2020; Ongoing)

## Progress Report

Due to the COVID-19 pandemic, ANL has been operated under Minimum safe mode. Thus, the team has very limited access to run the planned experiments. This quarter, the team used XPS to characterize the SEI of lithium metal after cycling in conventional DME-based and HFE-based electrolytes.

As shown in the Li 1s XPS spectra (Figure 114), the peaks located at 54.8 eV were assigned to the Li-S bond, and the peaks located at 56.1 eV were assigned to the Li-F bond. Thus, a much higher Li-F content SEI can be clearly identified on the surface of Li-metal foil after cycling in the Li|Cu cell with HFE-based electrolyte than is the case with DME-based electrolyte. Similar results were confirmed in the F 1s XPS spectra. As shown in Figure 115, the peaks located at ~ 685 eV correspond to Li-F bond, while the peaks at ~ 689 eV are related to the C-F of CF<sub>3</sub> from the LiTFSI salt. Obviously, the intensity of Li-F bond in the cycled lithium metal using HFE-based electrolytes is also higher than that using the conventional DME-based electrolytes. Therefore, in the DME-based electrolyte, the parasitic reactions between lithium metal and electrolyte molecules leads to dendrite formation and low CE, resulting in poor cycling stability and a severe safety concern.

In contrast, with the HFE-based electrolyte, a robust SEI layer is uniformly formed on the Li-metal surface to effectively eliminate the parasitic reactions between lithium metal and electrolyte molecules, significantly improving cycling stability and CE. This information is critical to unravel the underlying mechanism of improved electrochemical performance of HFE-based electrolytes over DME-based electrolytes.

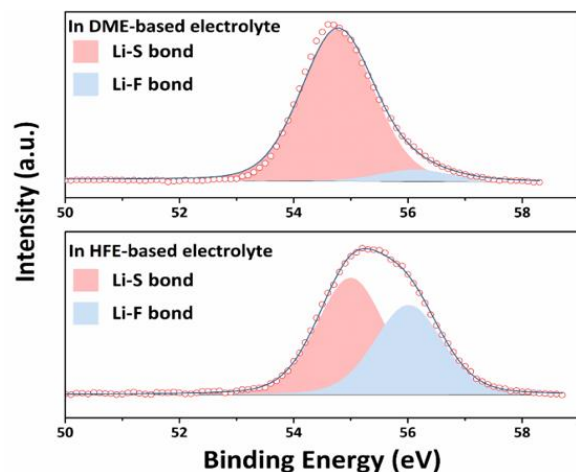


Figure 114. High-resolution X-ray photoelectron spectroscopy Li 1s spectra of cycled Li-metal anode of Li|Cu cells in DME- and HFE-based electrolytes.

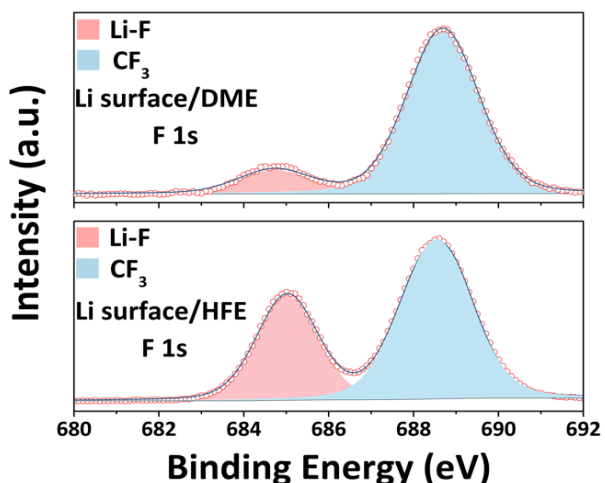


Figure 115. High-resolution X-ray photoelectron spectroscopy F 1s spectra of cycled Li-metal anode of Li|Cu cells in DME- and HFE-based electrolytes.

## Patents/Publications/Presentations

### Publication

- Xu, G. L., K. Amine, et al. “Regulating the Hidden Solvation-Ion-Exchange in Concentrated Electrolytes for Stable and Safe Lithium Metal Batteries.” *Advanced Energy Materials* 10 (2020): 2000901.

## Task 5.2 – Development of High-Energy Lithium-Sulfur Batteries (Dongping Lu and Jun Liu, Pacific Northwest National Laboratory)

**Project Objective.** The project objective is to develop high-energy, low-cost Li-S batteries with long lifespan. All proposed work will employ thick sulfur cathode ( $\geq 2$  mAh/cm<sup>2</sup> of sulfur) at a relevant scale for practical applications. The diffusion process of soluble polysulfide out of thick cathode will be revisited to investigate cell failure mechanism at different cycling. The fundamental reaction mechanism of polysulfide under the electrical field will be explored by applying advanced characterization techniques to accelerate development of Li-S battery technology.

**Project Impact.** The theoretical specific energy of Li-S batteries is  $\sim 2300$  Wh/kg, which is almost three times higher than that of state-of-the-art Li-ion batteries. The proposed work will design novel approaches to enable Li-S battery technology and accelerate market acceptance of long-range EVs required by the EV Everywhere Grand Challenge.

**Approach.** The project proposes to (1) identify and address key issues of applying high-energy sulfur cathodes including materials, binders, electrode architectures, and functional electrode additives, (2) advance the mechanism study of sulfur cathode and electrolyte by using *in situ* / *ex situ* techniques and custom-designed hybrid cell setup, and (3) verify effectiveness of the new approaches with coin/pouch cells by using high-loading electrodes ( $> 4$  mg/cm<sup>2</sup>), limited lithium ( $< 200\%$  lithium excess), and lean electrolyte (E/S  $< 4$   $\mu$ L/mg).

**Out-Year Goals.** This project has the following out-year goals:

- Fabricate Li-S pouch cells with thick electrodes to understand sulfur chemistry/electrochemistry in environments similar to real application.
- Leverage the Li-metal protection project funded by the DOE and PNNL advanced characterization facilities to accelerate development of Li-S battery technology.
- Develop Li-S batteries with a specific energy of 400 Wh/kg at cell level, 1000 deep-discharge cycles, improved abuse tolerance, and less than 20% capacity fade over a 10-year period to accelerate commercialization of EVs.

**Collaborations.** This project engages in collaboration with the following: Dr. X-Q. Yang (BNL), Dr. D. Qu (UWM), Dr. G. Zhang (University of Alabama), and Dr. J. Tao (PNNL).

### Milestones

1. Synthesis of IKB with controlled secondary particles from 5 to 100  $\mu$ m for high-loading sulfur electrodes ( $> 4$  mg S/cm<sup>2</sup>). (Q1, FY 2020; Completed)
2. Realize sulfur utilization rate  $> 1200$  mAh/g in dense sulfur electrodes (S  $> 4$  mg/cm<sup>2</sup>, porosity  $\leq 50\%$ ) at an E/S  $\leq 4$   $\mu$ L/mg through electrode architecture control. (Q2, FY 2020; Completed)
3. Demonstrate  $> 80$  cycles (80% capacity retention) in dense sulfur electrodes at E/S  $\leq 4$   $\mu$ L/mg through the hybrid electrode design. (Q3, FY 2020; Completed)
4. Complete evaluation of high-loading sulfur electrodes at E/S  $\leq 3$   $\mu$ L/mg and transfer sufficient materials to Battery500 for high-energy pouch cell demonstration. (Q4, FY 2020; Ongoing)

## Progress Report

Cycle life of a Li-S cell is highly dependent on available volume and durability of the LE. For high-energy Li-S cells, utilization of electrode structures featuring low porosity avoids filling electrode pores and instead conserves the limited amount of electrolyte, thus extending cell cycle life. For that purpose, large S/C composite particles with controlled particle size were synthesized and used as example materials to investigate the correlations between electrode structure and cell performance. This study found that dense electrodes composed of different sized particles exhibit distinct cell performance. At the same level of porosity (for example, < 50%), the electrodes using > 70  $\mu\text{m}$  particles show much better performance compared to those using the < 20  $\mu\text{m}$  particles. However, one remaining problem associated with the low porosity electrode is the accelerated cell decay under lean electrolyte conditions, potentially resulting from the stimulated polysulfide diffusion and physical loss. For a given electrode loading, higher lithium polysulfide concentration gradient and shorter diffusion length (electrode thickness) are expected for dense electrodes with lower porosities and accelerate the polysulfide diffusion, cross-over, and irreversible loss. Moreover, the increased tortuosity in the dense electrodes not only slows down the electrolyte diffusion, but also makes electrode passivation by Li-sulfide deposits easier.

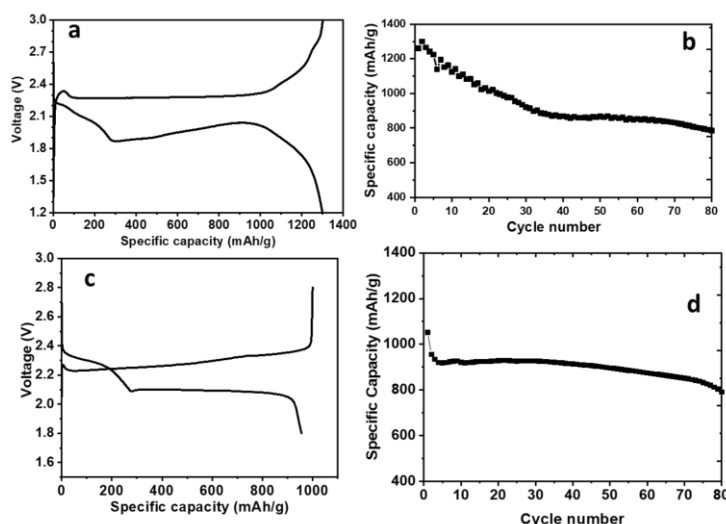


**Figure 116.** Typical charge/discharge curves and cycling performance of sulfur electrodes cycled in low-polysulfide-soluble electrolytes (a-b) and liquid/polymer hybrid electrolytes (c-d). (Electrode: 4 mg S/cm<sup>2</sup>, porosity < 50%, and E/S = 4  $\mu\text{L}/\text{mg S}$ ; 0.05C for one formation cycle, then 0.1C for cycling, at room temperature).

To address this issue in high-loading and dense sulfur cathodes, two approaches were used in the project's research. To suppress the polysulfide dissolution, new electrolytes with limited polysulfide solubility were prepared and tested (Figure 116a-b). Compared to conventional 1 M LiTFSI/DOL/DME electrolyte, the new electrolyte enables much higher reversible capacities in the dense sulfur electrodes (4 mg/cm<sup>2</sup>), although discharge plateau was slightly lower. The polarization increase results from low solubility of polysulfide in the new electrolytes. Significant increase of the overall capacity (~ 1300 mAh/g) indicates that suppressing polysulfide dissolution plays a positive role in improving the sulfur utilization rate in the dense electrodes. After 80 cycles, the cell capacity drops gradually from 1300 to 800 mAh/g, indicating that an irreversible loss of active sulfur species on cycling is still a problem, despite improved sulfur utilization rate. Inspired by the findings in the low-polysulfide-soluble electrolytes, the team designed a new approach by integrating a second phase of PE into the electrode architecture. Thanks to the improved electrode wettability, electrode porosity can be reduced further to < 40% without notably sacrificing sulfur reactivity. Figure 116c shows typical charge/discharge curves of the dense sulfur electrode (4 mg/cm<sup>2</sup>, < 40% porosity) with the hybrid electrolytes. The reversible capacity stabilizes eventually at ~ 900 mAh/g at 0.1C after a formation cycle at 0.05 C. Although the sulfur utilization rate decreases, a better capacity retention during the cycling was observed. After 80 cycles, a capacity of 792 mAh/g was obtained, which is 83% of the 1<sup>st</sup> cycle capacity (955 mAh/g) at 0.1 C. This implies that introduction of the PE is helpful to enhance cell capacity retention in very dense electrodes and under lean electrolyte conditions. A careful optimization of the electrode architecture and electrolyte composition is in progress to take advantage of both low-polysulfide-soluble electrolytes and hybrid electrolyte design.

## Patents/Publications/Presentations

### Publication

- Shi, L., S-M. Bak, Z. Shadik, C. Wang, C. Niu, P. Northrup, H. Lee, A. Baranovskiy, J. Qin, S. Feng, X. Ren, D. Liu, X. Yang, F. Gao, D. Lu, J. Xiao, and J. Liu. “Reaction Heterogeneity in Practical High-Energy Lithium-Sulfur Pouch Cells.” *Energy & Environmental Science*. Under review.

### Presentation

- DOE VTO Annual Merit Review, virtual presentation (June 1–4, 2020): “Development of High Energy Li-S Battery”; D. Lu and J. Liu.

## Task 5.3 – Nanostructured Design of Sulfur Cathodes for High-Energy Lithium-Sulfur Batteries (Yi Cui, Stanford University)

**Project Objective.** The charge capacity limitations of conventional TM oxide cathodes are overcome by designing optimized nano-architected sulfur cathodes. This study aims to enable sulfur cathodes with high capacity and long cycle life by developing sulfur cathodes from the perspective of nanostructured materials design, which will be used to combine with Li-metal anodes to generate high-energy Li-S batteries. Novel sulfur nanostructures as well as multi-functional coatings will be designed and fabricated to overcome issues related to volume expansion, polysulfide dissolution, and the insulating nature of sulfur.

**Project Impact.** The capacity and cycling stability of sulfur cathode will be dramatically increased. This project's success will make Li-S batteries to power EVs and decrease the high cost of batteries.

**Approach.** The approach involves three main efforts:

- Advanced nanostructured sulfur cathodes design and synthesis, including (1) engineer empty space into sulfur cathode to solve problem of electrode volume expansion, (2) develop novel sulfur nanostructures with multi-functional coatings for confinement of S/Li polysulfides to address issues of active materials loss and low conductivity, (3) develop/discover optimal nanostructured materials that can capture the polysulfide dissolved in the electrolyte, (4) develop space-efficiently-packed nanostructured sulfur cathode to increase volumetric energy density and rate capability, and (5) identify interaction mechanism between sulfur species and different types of oxides/sulfides, and find optimal material to improve capacity and cycling of sulfur cathode.
- Structure and property characterization, including *ex situ* SEM, XPS analysis, and *in operando* XRD and optical microscopy.
- Electrochemical testing including coin cells and pouch cells as well as a set of electrochemical techniques.

**Out-Year Goals.** The cycle life, capacity retention, and capacity loading of sulfur cathodes will be greatly improved (200 cycles with 80% capacity retention, > 0.3 mAh/cm<sup>2</sup> capacity loading) by optimizing material design, synthesis, and electrode assembly.

**Collaborations.** This project collaborates with the following: BMR PIs; SLAC: Dr. M. Toney (*in situ* X-ray); and Stanford: Prof. Nix (mechanics) and Prof. Bao (materials).

### Milestones

1. Understanding the mechanism of liquid sulfur on the surface of 3D materials. (Q1, FY 2020; Completed)
2. Demonstrate improvement by utilizing liquid sulfur in Li-S batteries. (Q2, FY 2020; Completed)
3. Develop high sulfur loading cathode based on understanding of liquid sulfur. (Q3, FY 2020; Completed)
4. Enable Li-S batteries with high sulfur loading, low E/S ratio, and fast kinetics. (Q4, FY 2020; Ongoing)

## Progress Report

Last quarter, the team demonstrated improvement by utilizing liquid sulfur in Li-S batteries. In this report, the team developed high sulfur loading cathode based on the understanding of liquid sulfur.

To gain deeper insight and understand the mechanism of why Ni-based electrodes show better battery performance as compared with carbon electrodes, the team studied the decomposition of  $\text{Li}_2\text{S}$  on the nickel surface, graphene basal plane, and graphene edge through DFT calculations. The overall  $\text{Li}_2\text{S}$  decomposition reaction includes two elemental steps: first, one lithium atom dissociating from  $\text{Li}_2\text{S}$ , and second, the dissociated lithium then diffuses away from the  $\text{LiS}$  cluster. The barriers of these two elemental steps are obtained via the climbing-image nudged elastic band (CI-NEB) method, as shown in Figure 117a. It is well known that the reaction barriers are very sensitive to the adsorption energy of the key intermediates. The adsorption energy of  $\text{Li}_2\text{S}$  (the key intermediate) on substrates is considered as an important parameter to explain and distinguish  $\text{Li}_2\text{S}$  decomposition behavior on nickel surface, graphene basal plane, and graphene edge. The very strong interaction between  $\text{Li}_2\text{S}$  and the graphene edge ( $E_{\text{ad}} = -6.04$  eV) promotes the  $\text{Li}_2\text{S}$  dissociation into lithium and  $\text{LiS}$ , but hampers the Li-ion diffusion away from the edge with a barrier of 1.55 eV (Figure 117b). On the other hand, the interaction of  $\text{Li}_2\text{S}$  with the graphene basal plane ( $E_{\text{ad}} = -0.78$  eV) is too weak to activate the  $\text{Li}_2\text{S}$  dissociation. In addition, the dissociation intermediates (lithium and  $\text{LiS}$ ) are more unstable on graphene basal plane than that of  $\text{Li}_2\text{S}$  by 1.85 eV (Figure 117c), indicating that the lithium and  $\text{LiS}$  will be recombined into  $\text{Li}_2\text{S}$  automatically on graphene basal plane. Therefore, the ideal interaction between  $\text{Li}_2\text{S}$  and the substrate material for  $\text{Li}_2\text{S}$  decomposition should be between the range of  $-0.78$  eV and  $-6.04$  eV. The interaction of  $\text{Li}_2\text{S}$  on the nickel surface is relatively moderate ( $E_{\text{ad}} = -5.13$  eV), and the rate-determining step of  $\text{Li}_2\text{S}$  decomposition exhibits a barrier of 1.07 eV (Figure 117d). The theoretical calculations combined with the above experimental analysis explain the improved reversibility, active material utilization, and improved electrochemical reaction kinetics on the surface of Ni-based electrodes.

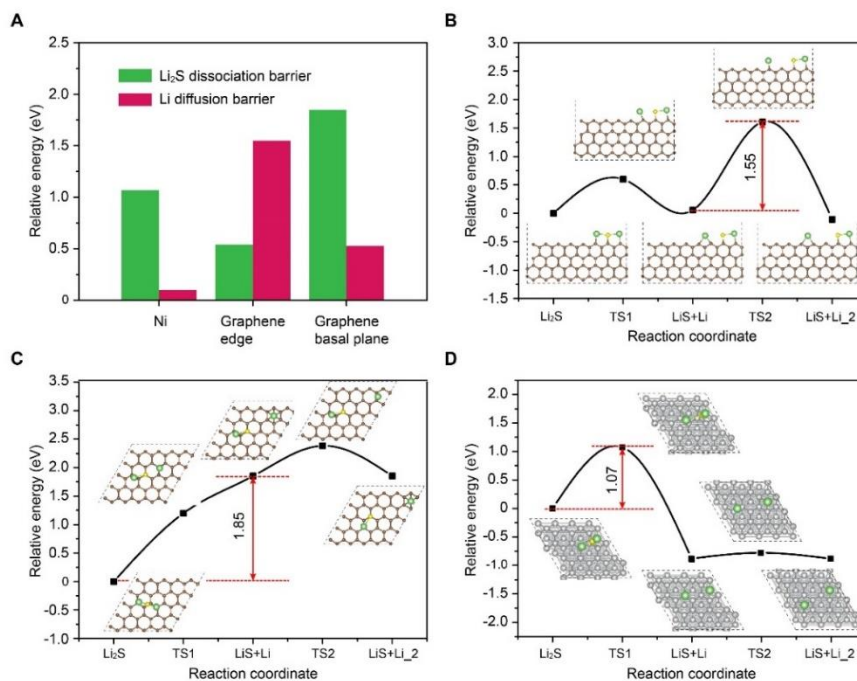


**Figure 117.**  $\text{Li}_2\text{S}$  decomposition and Li-ion diffusion barriers on surface of nickel and graphene. (a) Comparison of the  $\text{Li}_2\text{S}$  decomposition and Li-ion diffusion barriers on the surface of nickel, graphene basal plane, and graphene edge. Energy profiles for the decomposition of  $\text{Li}_2\text{S}$  cluster and Li-ion diffusion on the surface of (b) graphene edge, (c) graphene basal plane, and (d) nickel. Inset figures are top view schematic representations of the corresponding decomposition and Li-ion diffusion pathways for graphene edge, graphene basal plane, and nickel. Note: green, yellow, gray, and beige balls symbolize lithium, sulfur, nickel, and carbon atoms, respectively.

## Patents/Publications/Presentations

### Presentations

- Elsevier Webinar (April 3, 2020): “From Innovation to Commercialization for Materials, Energy and Environment.” Invited.
- ACS Webinar (May 14, 2020): “Facial Masks during COVID-19: Disinfection, Homemaking and Imaging.” Invited.
- African Society for Laboratory Medicine Webinar (May 26, 2020): “Facial Masks during COVID-19: Disinfection, Homemaking and Imaging.” Invited.
- MIT InnoTherm Symposium Webinar (June 17, 2020): “Thermal Effects on Battery Materials and Chemistry.” Invited.

## Task 5.4 – Investigation of Sulfur Reaction Mechanisms (Enyuan Hu, Brookhaven National Laboratory; Deyang Qu, University of Wisconsin at Milwaukee)

**Project Objective.** The primary objectives are as follows:

- To continue conducting focused fundamental research on the mechanism of “shuttle effect” inhibition for rechargeable Li-S batteries.
- To continue developing the polymeric sulfur electrode, adequate anode, and corresponding electrolyte to achieve high-energy-density, long-cycle Li-S batteries.
- To carry out spatially resolved XRF image and S-K edge XAS [including X-ray absorption near edge structure (XANES) and X-ray absorption fine structure (XAFS)] studies of polymeric sulfur compounds.
- To investigate the alternative anode materials so they will not react with dissolved polysulfide ions.
- To continue developing and optimizing creative electrode-making processes to improve processability and aerial capacity, for example, dry process and thick electrode.

**Project Impact.** Further understanding of the mechanisms of all reactions in a Li-S cell will lead to mitigation of the “shuttle effect.” The project results will thus guide development of sulfur cathode and Li-S designs with significant increase of energy density and of cycle life and with reduction of cost. This will greatly accelerate deployment of EVs and reduce carbon emission associated with fossil fuel consumption.

**Approach.** This project will use not only *in situ* electrochemical high-performance liquid chromatography (HPLC)/MS, XPS and TXM, but also synchrotron-based *in situ* X-ray diagnostic tools such as XRD and XAS to study sulfur electrodes. The team will continue to develop thicker sulfur electrode with high areal capacity using dry process.

**One-Year Goals.** The major goal this fiscal year is to extend successful investigation of dissolved polysulfides to the polysulfides in the solid phase. This includes the following actions: (1) synthesize cross-linked polymerized sulfur compounds, (2) explore additives that can rapidly catalyze polysulfide radicals, (3) continue exploring alternative anode materials, and (4) develop *in situ* synchrotronic method to investigate sulfur and polysulfide in the solid phase.

**Collaborations.** The PI works closely with beamline scientists at synchrotron facilities to develop novel Li-S characterization tools. The PI and co-PI collaborate closely with top scientists at ANL, LBNL, and PNNL, as well as U. S. industrial collaborators at GM, Duracell, Clarios, etc. The PI and co-PI also collaborate with scientists in China, Japan, and South Korea. These collaborations will be strengthened and expanded to give this project a vision on both today’s state-of-the-art technology and tomorrow’s technology in development, with feedback from the material designer and synthesizers upstream and from industrial end users downstream.

### Milestones

1. Test the newly synthesized polymeric sulfur compounds. Conduct spatially resolved XRF image and S-K edge XAS (including XANES and XAFS) studies of polymeric sulfur compounds. (Q1, FY 2020; Completed)
2. Survey alternative anode materials and determine their interaction with dissolved polysulfide ions. Continue synthesis and testing of polymeric sulfur compounds, and optimize electrode-making processes. (Q2, FY 2020; Completed)

- Investigate radical disproportionation catalyst, and test alternative electrolytes in which the solubility of polysulfide ions is lower than ether-based electrolyte. (Q3, FY 2020; Completed)
- Complete initial design of the full cell consisting of polymeric sulfur compounds, alternative anode, and adequate additive in either coin-cell or pouch-cell format. (Q4, FY 2020; Ongoing)

## Progress Report

This quarter, the third milestone was completed. Progress on the final FY 2020 milestone is being made. The BNL and UWM teams have been working together: (1) to continue to synthesize new polymer compounds, sulfur-containing composites with inorganic anchors, and optimize the electrode making processes; and (2) to accomplish screening electrolyte and additives.

**Synthesis of Sulfur-Containing Materials with Inorganic Anchors.** Last quarter, the team reported the synthesis of a series of semi-graphitic ordered mesoporous carbons with metal/nitrogen doping (Me-N-GOMCs; Me = Fe, Co, Ni, and Cu). The materials are aimed to be used as the sulfur hosts with abundant porosity and high electrical conductivity. Through *ex situ* analysis and DFT calculation, it was revealed that the doping did have positive impact on assisting the polysulfide localization through the synergistic effect of metal and nitrogen in the matrix of carbon. Iron dopant was suggested as having the best effect.

Figure 118 shows electrochemical performance of the Me-N-GOMCs. Cyclic voltammetry, AC impedance, galvanostatic cycling, and rate capability of all materials are illustrated in Figure 118. The high areal loadings of 3 mg and 6 mg per cm<sup>2</sup> were tested. The Me-N-GOMCs were embedded in the void space of a CP to construct

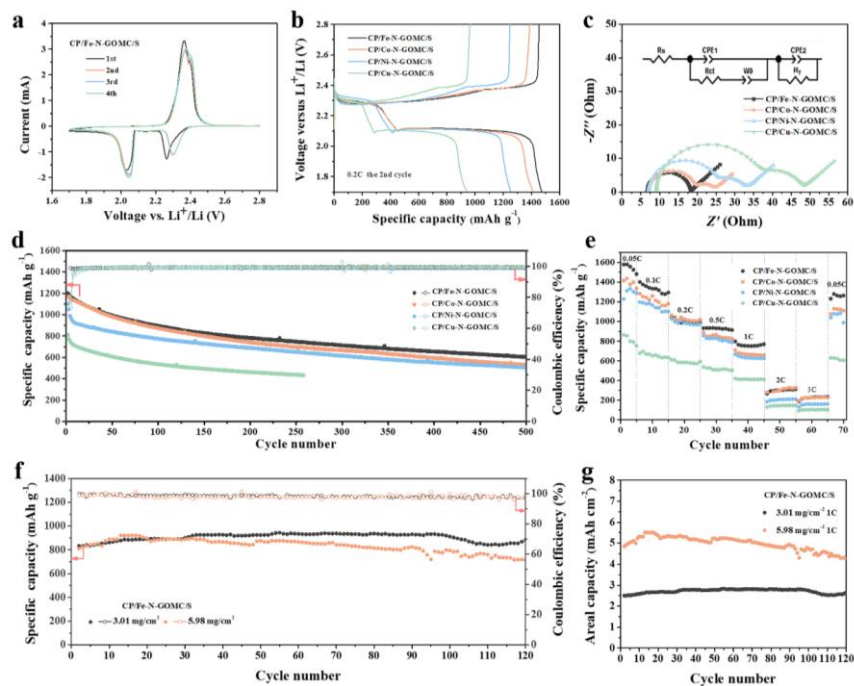


**Figure 118. Electrochemical performances for CP/Me-N-GOMC/S cathodes.** (a) Cyclic voltammetry curves of the CP/Fe-N-GOMC/S electrode for initial several cycles at a scan rate of 0.05 mV s<sup>-1</sup>. (b) Galvanostatic discharge-charge profiles of electrodes for the 2<sup>nd</sup> cycle at 0.2 C. (c) Experimental Nyquist plots of electrodes after initial cycle of the cells as well as the fitting results (solid lines) based on the equivalent circuit shown in the inset. (d) Cycling performances of electrodes at 0.5 C, and (e) rate capability of electrodes at various rates with a sulfur loading of ~3 mg cm<sup>-2</sup>. (f) Cycling performances of CP/Fe-N-GMOC/S electrodes with different sulfur loading at 1 C, and (g) the corresponding areal capacities.

free-standing sulfur cathode. Electrochemical tests were done in CR2016 coin cell with lithium anode. Integrated 3D CP/Fe-N-GOMC/S electrode with a sulfur loading of ~3 mg cm<sup>-2</sup> delivers a high initial capacity of 1473 mA h g<sup>-1</sup> at 0.2 C and good cycling stability (a decay rate of 0.075% per cycle over 500 cycles at 0.5C, and a decay rate of 0.001% per cycle over 120 cycles at 1C). Even at a sulfur loading of ~6 mg cm<sup>-2</sup>, steady areal capacity (~5 mA h cm<sup>-2</sup>) for over 120 cycles at 1C can still be attained.

**Electrolyte Developments.** A group of electrolytes and additives was also screened. Cycling tests are in progress. Better performance was evident, and results will be reported next quarter.

## Patents/Publications/Presentations

### Publication

- Li, H., D. Liu, X. Zhu, D. Qu, Z. Xie, J. Li, H. Tang, D. Zheng, and D. Qu. “Integrated 3D Electrodes Based on Metal-Nitrogen-Doped Graphitic Ordered Mesoporous Carbon and Carbon Paper for High-Loading Lithium-Sulfur Batteries.” *Nano Energy* 73 (2020): 104763.

## Task 5.5 – New Electrolytes for Lithium-Sulfur Battery (Gao Liu, Lawrence Berkeley National Laboratory)

**Project Objective.** The project objective is to develop new electrolytes, additives, and electrode compositions for Li-S battery with high ion-conductivity, stable toward polysulfide and promoting the polysulfide affiliation with the electrode substrate to prevent polysulfide dissolution.

**Project Impact.** This work will address the high cost and low energy density of Li-ion rechargeable batteries. The emerging Li-S batteries could feature both high energy density and low cost. This project enables applications of the low-cost, abundant sulfur element as a major chemical component for electrical energy storage. This project will develop new approaches for electrolytes and electrode compositions of Li-S rechargeable batteries.

**Approach.** This project aims to develop new electrolytes and additives for Li-S battery. The properties of the ideal electrolyte for sulfur electrode would be high ion conductivity, stable towards polysulfide, and promoting the polysulfide affiliation with the electrode substrate to prevent polysulfide dissolution. The project is designed to first understand the electrode substrate interaction with the polysulfides in different electrolytes. This will lead to better understandings of the polysulfide nucleation and precipitation mechanisms in common electrolytes. The second stage of the project will focus on chemically modifying the structures of the solvent and salt electrolyte molecules to increase electrolyte stability and ionic conductivity and to prevent polysulfide dissolution and promote polysulfides precipitation.

**Out-Year Goals.** The team will also investigate the contribution of Li-metal electrodes to overall Li-S battery performance and will develop methods to stabilize Li-metal surface.

**Collaborations.** This project collaborates with Dr. J. Guo and Dr. W. Yang (ALS/LBNL), Prof. A. Minor (National Center for Electron Microscopy at LBNL/UC Berkeley), Dr. L-W. Wang (LBNL), and Prof. P. B. Balbuena, TAMU.

### Milestones

1. Use the synchrotron analyses in studying new electrolytes. (Q1, FY 2020; Completed)
2. Measure and optimize compositions of the new electrolyte for conductivities, Li-ion transference numbers, and amount of polysulfide dissolution. (Q2, FY 2020; Completed)
3. Study cycling properties of lithium metal under new electrolytes. (Q3, FY 2020; Completed)
4. Select two electrolyte compositions to test in Li-S battery. (Q4, FY 2020; Ongoing)

## Progress Report

A new class of amphiphilic electrolyte additive based on HFEs has been synthesized. The HFE amphiphilic additives in combination with lithium salt (for example, LiFSI) and fluorocarbon solvents (for example, 1,1,2,2-Tetrafluoroethyl 2,2,2-Trifluoroethyl Ether, TTE) form micelle structures. These HFE amphiphilic additives have special structure design: a lithiophilic head (ethyleneoxide moiety) attached to a lithiophobic tail (hydrofluorocarbons). The lithium salts follow a micelle solvation mechanism on dissolution in the HFE amphiphilic additives. The dissociated  $\text{Li}^+$  ions readily coordinate with ethyleneoxide (EO) moiety to induce self-assembly of the amphiphilic HFE additive into micelle structures.

Li||Cu cells were employed to study the cycling stability and CE of the designed  $\text{F}_3\text{EO}_1$  additive electrolyte in regard to anode performance. As previously discussed, HFEs are hypothesized to have better chemical compatibility with lithium metal due to their rapid breakdown into passivating LiF; thus, high CE and cycling stability are expected over long-term cycling. First, the effect of various current densities was investigated to study rate capability of the cell. As displayed in Figure 119a, at  $0.5\text{ mA/cm}^2$ , initial CE was only about 90%, but continuously increased with stripping/plating cycles after the copper surface became passivated. Notably, greater than 99% CE was observed after 200 cycles, and likewise the polarization decreases with cycling to 35mV because of the increasing surface area, indicating that the HFE/TTE electrolyte is highly stable with lithium deposition. Similar behavior was observed at  $1.0\text{ mA/cm}^2$  current density (Figure 119b); other than the expected slight increase in overpotential, CE also reaches  $> 99\%$  after only 100 cycles. Figure 119c shows that CE is only slightly compromised at  $2.0\text{ mA/cm}^2$  current rate. This comparison demonstrates the good rate capability of Li-metal anodes in HFE solvent electrolyte.

SEM images of deposition morphology are shown in Figure 119d-f, following  $1.0\text{ mAh/cm}^2$  deposition at varying current density. Very smooth lithium surfaces were observed at  $0.5$  and  $1.0\text{ mA/cm}^2$  rate. A slightly rougher surface with lithium nodule formation appears at  $2.0\text{ mA/cm}^2$  rate; however, no dendritic growth was found on these surfaces, indicating good suppression of dendrite formation using this HFE additive electrolyte.

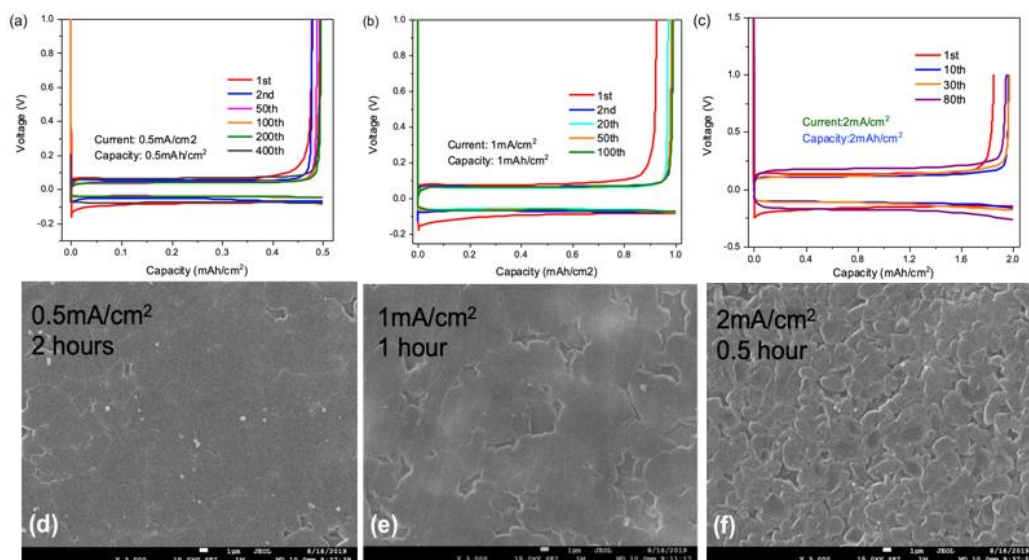


**Figure 119.** Voltage profiles for lithium plating/stripping test by using  $0.5\text{ M LiFSI}$  in  $\text{F}_3\text{EO}_1/\text{TTE}$  (1:5) electrolyte under various conditions: (a)  $0.5\text{ mA/cm}^2$  current density and  $0.5\text{ mAh/cm}^2$  deposition capacity; (b)  $1.0\text{ mA/cm}^2$  current density and  $1.0\text{ mAh/cm}^2$  deposition capacity; (c)  $2.0\text{ mA/cm}^2$  current density and  $2.0\text{ mAh/cm}^2$  deposition capacity; and (d-f) scanning electron microscopy images ( $3000\times$ , magnification) of deposited surfaces at various current density and constant  $1.0\text{ mAh/cm}^2$  deposition capacity.

## Patents/Publications/Presentations

### Publications

- Zhao, Y., C. Fang, G. Zhang, D. Hubble, A. Nallapaneni, C. Zhu, Z. Zhao, Z. Liu, J. Lau, Y. Fu, and G. Liu. “A Micelle Electrolyte Enabled by Fluorinated Ether Additives for Polysulfide Suppression and Li Metal Stabilization in Li-S Battery.” *Frontiers in Chemistry* 8 (2020): 484. doi: 10.3389/fchem.2020.00484.
- Liu, Z., X. He, C. Fang, L. E. Camacho-Forero, Y. Zhao, Y. Fu, J. Feng, R. Kostecki, P. B. Balbuena, J. Zhang, J. Lei, and G. Liu. “Reversible Crosslinked Polymer Binder for Recyclable Lithium Sulfur Batteries with High Performance.” *Advanced Functional Materials* (2020): 2003605.

### Presentation

- DOE VTO Annual Merit Review, virtual presentation, bat423 (June 1–4, 2020): “Development of New Electrolytes for Lithium-Sulfur Batteries”; G. Liu.

## TASK 6 – AIR ELECTRODES / ELECTROLYTES

### Summary and Highlights

High-density energy storage systems are critical for EVs required by the EV Everywhere Grand Challenge. Conventional Li-ion batteries still cannot fully satisfy the ever-increasing needs because of their limited energy density, high cost, and safety concerns. As an alternative, the rechargeable lithium-oxygen (Li-O<sub>2</sub>) battery has potential to be used for long-range EVs. The practical energy density of a Li-O<sub>2</sub> battery is expected to be ~ 800 Wh kg<sup>-1</sup>. The advantages of Li-O<sub>2</sub> batteries come from their open structure; that is, they can absorb the active cathode material (oxygen) from the surrounding environment instead of carrying it within the batteries. However, the open structure of Li-O<sub>2</sub> batteries also leads to several disadvantages. The energy density of Li-O<sub>2</sub> batteries will be much lower if oxygen must be provided by an onboard container. Although significant progress has been made in recent years on fundamental properties of Li-O<sub>2</sub> batteries, research in this field is still in an early stage, with many barriers to be overcome before practical applications. These barriers include:

- Instability of electrolytes—The superoxide species generated during discharge or O<sub>2</sub> reduction process is highly reactive with electrolyte and other components in the battery. Electrolyte decomposition during charge or O<sub>2</sub> evolution process is also significant due to high over-potentials.
- Instability of air electrode (dominated by carbonaceous materials) and other battery components (such as separators and binders) during charge/discharge processes in an O-rich environment.
- Corrosion of Li-metal anode in an electrolyte saturated with oxygen.
- Low energy efficiency associated with large over-potential and poor cyclability of Li-O<sub>2</sub> batteries.
- Low power rate capability due to electrode blocking by the reaction products.
- Absence of a low-cost, high-efficiency oxygen supply system (such as oxygen selective membrane).

The main goal of this Task is to provide a better understanding on the fundamental reaction mechanisms of Li-O<sub>2</sub> batteries and identify the required components (especially electrolytes and electrodes) for stable operation of Li-O<sub>2</sub> batteries. This task will investigate several new approaches to improve stability of Li-metal anode in Li-O<sub>2</sub> batteries:

- Li-metal anodes will be protected using two approaches: (1) *in situ* formation of a stable SEI layer before Li-O<sub>2</sub> cell operation through various electrolyte formulations and treatment protocols, and (2) *ex situ* formation of stable inorganic/polymeric hybrid electrolyte layers through dip-coating or tape-casting method to coat the inorganic/polymeric hybrid electrolyte layer on Li-metal surface.
- A joint theoretical/experimental approach for design and discovery of new cathode and electrolyte materials will act synergistically to reduce charge overpotentials and increase cycle life. Synthesis methods, in combination with design principles developed from computations, will be used to make new cathode architectures. Computational studies will be used to help understand decomposition mechanisms of electrolytes and how to design electrolytes with improved stability.
- A new cathode will be developed based on high-efficiency catalyst such as 2D TMDs. These cathode materials will be combined with new electrolyte blends and additives that work in synergy to reduce charge potentials and increase stability of the Li-air system.

State-of-the-art characterization techniques and computational methodologies will be used to understand charge and discharge chemistries. Success of this Task will establish a solid foundation for further development of Li-O<sub>2</sub> batteries toward practical applications for long-range EVs. The fundamental understanding and breakthrough in Li-O<sub>2</sub> batteries may also provide insight on improving performance of Li-S batteries and other energy storage systems based on chemical conversion process.

**Highlights.** The Task highlights for this quarter are as follows:

- The ANL group (K. Amine, L. Curtiss, and J. Lu) reported use of a novel fabrication technique to construct noble metals enabled air electrode recognized as powerful cathode for oxygen evolution reaction (OER) system. By using this method, the system solves the questionable key issue in Li-O<sub>2</sub> battery: the catalyst promotes electrochemical reaction, but spontaneously toward a wrong direction by enhancing the parasitic reactions, leading to invalidity of the electrochemical system.
- The PNNL Group (J. Zhang and W. Xu) developed a new protection method to stabilize Li-anode surface by using a polymer-supported artificial SEI layer and then *in situ* forming another SEI layer through a pre-charging step to 5 V for 1 hour before regular discharge-charge cycling of Li-O<sub>2</sub> batteries. This method significantly prolongs the cycle life of Li-O<sub>2</sub> batteries even without any precious metal or metal oxide catalysts and high surface area air electrodes, compared to the batteries with bare lithium anode or pre-charged bare lithium anode without polymer-supported artificial SEI.
- The Argonne/UIC Group (L. Curtiss, A. Ngo, and A. Salehi-Khojin) conducted density functional calculations to investigate how two electrolyte additives, InI<sub>3</sub> and InBr<sub>3</sub>, give a protective interphase on the lithium anode that promotes long cycle life in Li-O<sub>2</sub> batteries found in their previous work. The computations reveal that the InX<sub>3</sub> additive (X = I, Br) can react and dissociate on the lithium surface forming an LiX interphase that can protect against oxygen cross-over and other deleterious reactions.

## Task 6.1 – Rechargeable Lithium-Air Batteries (Ji-Guang Zhang and Wu Xu, Pacific Northwest National Laboratory)

**Project Objective.** The objective of this project is to develop rechargeable Li-O<sub>2</sub> batteries with long-term cycling stability through in-depth research on more stable electrolytes and highly efficient catalysts for air electrodes, protection of Li-metal anodes, and deeper understanding on the oxygen reduction reaction (ORR) and OER mechanisms behind the electrochemical performance of Li-O<sub>2</sub> cells. In FY 2020, the team will further investigate stability of electrodes and electrolytes to build more stable Li-O<sub>2</sub> batteries with long-term cycling capability.

**Project Impact.** The project will develop rechargeable Li-O<sub>2</sub> batteries with long-term cycling stability through in-depth research on more stable electrolytes and highly efficient catalysts for air electrodes and protection of Li-metal anodes. This fiscal year, the team will further investigate stability of electrodes and electrolytes to build more stable Li-O<sub>2</sub> batteries with long-term cycling capability.

**Approach.** Develop highly stable electrolytes, including localized high concentration electrolytes (LHCEs) and optimize their compositions to prevent the irreversible parasitic reactions at the electrodes (cathode and anode). The electrochemical test of Li||Li symmetric cell containing above stable electrolyte will be first measured comparatively with typical ether (TEGDME) based electrolyte to evaluate the stability of the electrolyte itself and the SEI layer. Then, the stability of proposed electrolytes at the cathode side with reactive oxygen species during ORR/OER will be further characterized in the Li-O<sub>2</sub> cells. In addition, with comparative measurements for physical properties of electrolytes, the team will find the key parameters of suitable electrolyte in Li-O<sub>2</sub> batteries.

**Out-Year-Goals.** The long-term goal of the proposed work is to enable rechargeable Li-air batteries with a specific energy of 800 Wh/kg at cell level, 1000 deep-discharge cycles, improved abuse tolerance, and less than 20% capacity fade over a 10-year period to accelerate commercialization of long-range EVs.

**Collaborations.** This project collaborates with C. Wang of PNNL on characterization of cycled air electrodes by TEM/SEM, and with Dr. P. Gao of PNNL on computational calculations and simulations and with Dr. J. Read of ARL on oxygen solubility tests.

### Milestones

1. Develop stable electrolyte to minimize parasitic reactions at the electrodes. (Q1, FY 2020; Completed, December 31, 2019)
2. Protect anodes to prevent the lithium dendrite and LiOH formation. (Q2, FY 2020; Completed, March 31, 2020)
3. Develop stable additives (solid or soluble) or methods for sustainable catalytic effect. (Q3, FY 2020; Completed, June 30, 2020)
4. Complete evaluation of cycling performance of Li-O<sub>2</sub> batteries with optimized cell components and conditions. (Q4, FY 2020; In progress)

## Progress Report

This quarter, the team developed a new protection method to stabilize Li-anode surface with a polymer-supported SEI (PS-SEI) layer for the long-term operation of rechargeable Li-O<sub>2</sub> batteries (LOBs). A thin gel-polymer electrolyte (GPE) film containing PEO (PEO-GPE, PG) is first coated on Li-metal surface as an artificial SEI by spin coating method inside the glovebox filled with purified argon. Then, LOBs are assembled using GPE precoated Li-metal anode and CP air electrode. After filling O<sub>2</sub> into the cells, but prior to performing regular discharging/charging cycles of the LOBs, a pre-charging step to 5 V for 1 hour is applied to the LOBs. A new thin, robust, and *in situ* built SEI layer on Li-metal surface is generated by this electrochemical charging step (Figure 120a). The surface characteristics of PS-SEI layer generated on Li-metal surface were investigated (Figure 120b) and compared with normal SEI layer generated by the same electrochemical charging step without PG coating. Digital photographs (DPs), SEM images, and FTIR spectra exhibit that the Li-metal surface is very smooth with PS-SEI layer and PEO and can be maintained without decomposition even after electrochemical pretreatment at 5 V for 1 hour. XPS results demonstrate that PEO-GPE layer contributes to stabilize the newly formed SEI film without severe electrolyte decomposition due to the covering by PG, while the pretreated bare lithium metal has a rough surface consisting of LiF, S-S, and Li<sub>2</sub>S<sub>2</sub> resulting from severe decomposition of lithium salt and solvent during pre-charging step.

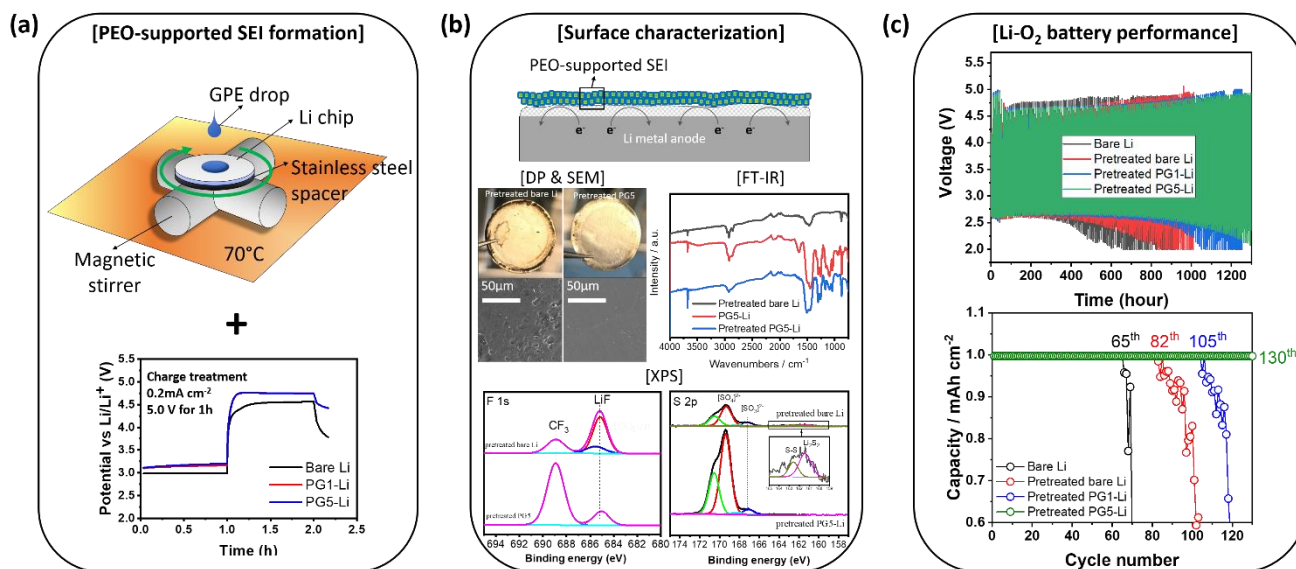


**Figure 120.** (a) Formation process of PEO-supported SEI layer on the surface of Li-metal anode, by combination steps consisting of pre-GPE coating by spin coating method and pre-charging to 5 V electrochemically. (b) Schematic illustration of the role of PEO-supported SEI layer and surface characterization results of Li-metal surfaces after pre-charging step with and without pre-PG coating. (c) Voltage profiles of Li-O<sub>2</sub> battery cells with and without PEO-supported SEI layer cycling at a current density of 0.2 mA cm<sup>-2</sup> under a capacity limited protocol of 1.0 mAh cm<sup>-2</sup>. Cycling performance of Li-O<sub>2</sub> batteries corresponding to voltage profiles with repeated discharge and charge cycles at same testing condition.

The performance of LOBs largely depends on the characteristics of SEI layers. The effect of PEO content (1 and 5 wt%) in PS-SEI on LOB cell performance was also investigated. The higher PEO content leads to better LOB cell performance due to its better ionic conductivity, and larger amorphous with lower crystalline regions, which generates relatively dense and closely-packed SEI during the pretreatment step. The formation of PS-SEI layer with 5 wt% of PEO significantly prolongs cycle life (130 cycles, which is two times longer cycle life than the team's previous work) of LOBs under the capacity limited protocol of 1.0 mAh cm<sup>-2</sup> at a current density of 0.2 mA cm<sup>-2</sup> without any precious metal or metal oxide catalysts and high surface area air electrodes. Bare lithium and pretreated bare lithium anodes without PG support only reach 65 and 82 cycles, respectively, under the same testing conditions (Figure 120c). Thus, this novel strategy of constructing robust polymer-supported SEI layer on lithium surface could be one of the effective solutions for practical applications of rechargeable LOBs.

## Patents/Publications/Presentations

### Publications

- Kwak, W-J., S. Chae, R. Feng, P. Gao, J. Read, M. H. Engelhard, L. Zhong, W. Xu, and J-G. Zhang. “Optimized Electrolyte with High Electrochemical Stability and Oxygen Solubility for Lithium-Oxygen and Lithium-Air Batteries.” *ACS Energy Letters* 5 (2020): 2182–2190.
- Kwak, W-J., H-S. Lim, P. Gao, R. Feng, S. Chae, L. Zhong, J. Read, M. H. Engelhard, W. Xu, and J-G. Zhang. “Effects of Fluorinated Diluents in Localized High Concentration Electrolytes for Lithium–Oxygen Batteries.” *Advanced Functional Materials* (2020). doi:10.1002/adfm.202002927.

## Task 6.2 – Lithium-Air Batteries

(Khalil Amine, Larry A. Curtiss, and Jun Lu; Argonne National Laboratory)

**Project Objective.** This project will develop new cathode materials and electrolytes for Li-air batteries for long cycle life, high capacity, and high efficiency. The goal is to obtain critical insight that will provide information on the charge and discharge processes in Li-air batteries to enable new advances to be made in their performance. This will be done using state-of-the-art characterization techniques combined with state-of-the-art computational methodologies to understand and design new materials and electrolytes for Li-air batteries.

**Project Impact.** The instability of current nonaqueous electrolytes and degradation of cathode materials limits performance of Li-air batteries. The project impact will be to develop new electrolytes and cathode materials that are stable and can increase energy density of electrical energy storage systems based on lithium.

**Approach.** The project is using a joint theoretical/experimental approach for design and discovery of new cathode and electrolyte materials that act synergistically to reduce charge overpotentials and increase cycle life. Synthesis methods, in combination with design principles developed from computations, are used to make new cathode architectures. Computational studies are used to help understand decomposition mechanisms of electrolytes and how to design electrolytes with improved stability. The new cathodes and electrolytes are tested in Li-O<sub>2</sub> cells. Characterization, along with theory, is used to understand the performance of materials used in the cell and to make improved materials.

**Out-Year Goals.** The out-year goals are to find catalysts that promote discharge product morphologies that reduce charge potentials and to find electrolytes for long cycle life through testing and design.

**Collaborations.** This project engages in collaboration with Prof. K. C. Lau (UC at Norridge), Prof. Y. Wu (Ohio State University), Dr. D. Zhai (China), and R. Shahbazian-Yassar (UIC).

### Milestones

1. Investigation of effect of salt modification on discharge product and charge overpotentials. (Q1, FY 2020; Completed)
2. Development of electrolyte blends for Li-anode protection for longer cycle life. (Q2, FY 2020; Completed)
3. Investigation of new alloys for templating LiO<sub>2</sub> discharge products with low charge potentials. (Q3, FY 2020)
4. Development of novel electrocatalysts for low charge potentials in synergy with new electrolyte blends. (Q4, FY 2020)

## Progress Report

### Highlights of Keystone Project 1: Investigation of New Alloys

The highlights for this quarter are as follows:

- The team uses a novel fabrication technique to construct noble metals enabled air electrode recognized as powerful cathode for OER system.
- By using this method, the system solves the questionable key issue in lithium-oxygen battery: the catalyst promotes the electrochemical reaction, but spontaneously toward a wrong direction by enhanced parasitic reactions, leading to invalidity of the electrochemical system.

Lithium-oxygen battery is one of the most promising energy storage systems, with energy density comparable to traditional gasoline. The electrochemical catalyst air electrode is critical to improve rate performance, cyclability, and round-trip efficiency of the lithium-oxygen battery. However, the abuse of catalysts inevitably leads to concerns such as the extra cost of materials and processing, the low areal energy density due to the limited active sites, and pore clogging due to non-uniform distribution of the materials. Here, the team uses a novel fabrication technique to construct noble metals enabled air electrode recognized as a powerful cathode for OER system. By using this method, the system solves the questionable key issue in lithium-oxygen battery: the catalyst promotes the electrochemical reaction, but spontaneously toward a wrong direction by enhanced parasitic reactions, leading to invalidity of the electrochemical system.

As shown in Figure 121, by using the thin-film deposition technique, the reduction of catalyst dimensionality was easily realized by applying unique wettability of various metals. The dimension of catalyst is dramatically decreased from 3D, to 2D (wetting), and eventually to 0D (de-wetting). Applying in a typical lithium-oxygen cell, the achieved cathode loading with dimensionally controlled catalyst effectively exhibits low charge potential with extended cycle life (Figure 122).

This dimensionally constrained catalyst layer is responsible to improve areal energy and power density without any additional materials or complicated processes in the following discharge-charge cycles in the oxygen gas. More importantly, this technique provides huge opportunities for further R&D via optimizing the electrolyte solvents and additives. The fabrication process is straight forward, low-cost, and user-friendly, with promising potential for industrialization.

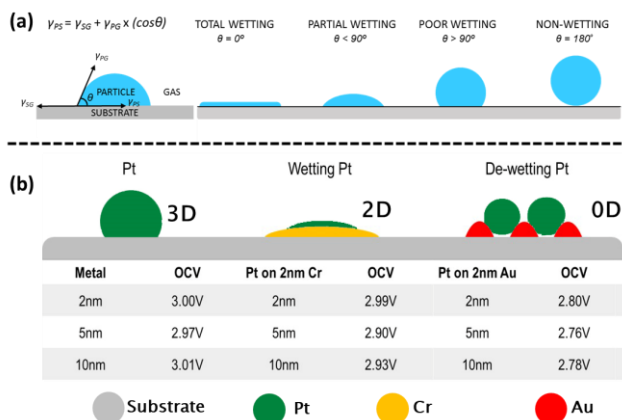


**Figure 121. Nano-engineering strategies for creating the ultra-small wetting and de-wetting dimensionality reduced platinum catalysts on the substrate. (a) Definition of wetting and de-wetting in a typical metal-nonmetallic substrate system. (b) Formation of dimensionality reduced platinum with help of functional metal layers on a carbon black substrate for lithium oxygen battery, and the relating regular open circuit voltage (OCV) for each cell.**

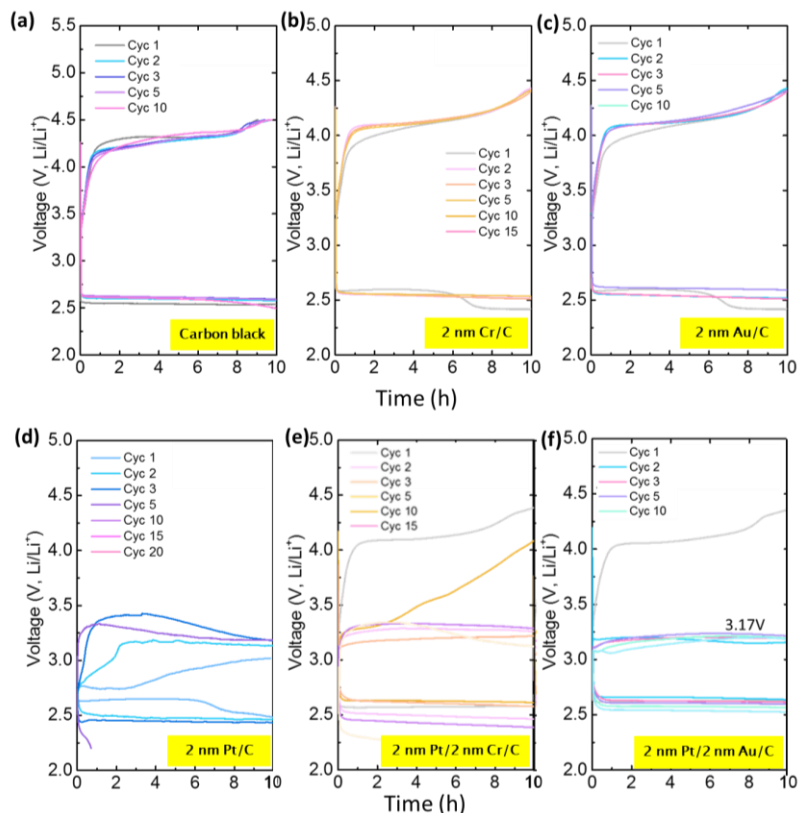


Figure 122. Examples of galvanostatic charge/discharge profiles of Li-O<sub>2</sub> batteries with (a) carbon black, (b) Cr/C, (c) Au/C, (d) 3D Pt/C, (e) 2D Pt/Cr/C, and (f) 0D Pt/Au/C in the voltage range of 2.2 V to 4.5 V versus Li<sup>+</sup>/Li within the fixed capacity.

## Patents/Publications/Presentations

### Patent

- Zeng, X., J. Lu, A. Khalil, and Y. Guo. IN-18-073. Catalytic Cathode for Lithium-Oxygen Battery. In preparation.

### Publications

- Li, M.; X. Bi, R. Wang, Y. Li, G. Jiang, L. Li, C. Zhong, Z. Chen, and J. Lu. “Relating Catalysis between Fuel Cell and Metal-Air Batteries.” *Matter* 2, no. 1 (2020) 32-49.
- Li, M., T. Liu, X. Bi, Z. Chen, K. Amine, K. Zhong, and J. Lu. “Cationic and Anionic Redox in Lithium-Ion Based Batteries.” *Chemical Society Reviews* 49 (2020): 1688–1705.
- Lu, J., D. Ma, and I. Mora-Seró. *ACS Energy Letters* 2020, 5, 1662-1664.

## Task 6.3 – Lithium Oxygen Battery Design and Predictions (Larry A. Curtiss/Anh Ngo, Argonne National Laboratory; Amin Salehi-Khojin, University of Illinois at Chicago)

**Project Objective.** The objective of this work is to develop new materials for Li-O<sub>2</sub> batteries that give longer cycle life and improved efficiencies in an air environment. New electrolyte blends and additives will be investigated that can reduce clogging and at the same time promote the cathode functionality needed to reduce charge overpotentials. New cathode and anode materials will be investigated that can work in conjunction with the electrolytes to improve cycle life in the presence of air components.

**Project Impact.** Li-air batteries are considered as a potential alternative to Li-ion batteries for transportation applications due to their high theoretical specific energy. The major issues with the existing Li-O<sub>2</sub> systems include degradation of the anode electrode, reactions with air components, clogging of the cathode, and electrolyte instability. Thus, this project is using a comprehensive approach to improve cycle life and efficiency through developing new materials for electrodes, anodes, and electrolytes that work in synergy.

**Approach.** The experimental strategy is to use cathode materials based on 2D TM dichalcogenides (TMDs) that the team has found to be among the best oxygen reduction and evolution catalysts. These cathode materials will be combined with new electrolyte blends and additives that work in synergy to reduce charge potentials and increase stability of the Li-air system. DFT and AIMD simulations are used to gain insight at the electronic structure level of theory of the electrolyte structure, and function both in the bulk and at interfaces with the cathode, anode, and discharge product. Classical MD is used to obtain understanding at longer length and time scales of processes occurring in the electrolyte and growth mechanisms of discharge products. The team will also utilize a HT screening strategy based on experiment and theory to develop a large database of properties and outcomes of electrolyte combinations that can be analyzed using ML to predict electrolytes and additives that will have the best performance.

**Out-Year Goals.** The out-year goals are to find electrolytes that give high capacities and long cycle life in an air atmosphere using HT screening.

**Collaborations.** This project engages in collaboration with R. Assary and J. G. Wen of ANL, B. Narayanan of University of Louisville, T. Li of Northern Illinois University, and F. Khalili-Araghi and R. Klie of UIC.

### Milestones

1. Investigate various salt combinations for Li-O<sub>2</sub> electrolytes for both lithium anode protection and low charge potentials for the performance of Li-O<sub>2</sub> batteries with use of computations to provide understanding. (Q1, FY 2020; Completed)
2. Investigate bromine-based redox mediators (RMs) by experiment and theory for comparison with iodine-based RMs with MoS<sub>2</sub> cathode materials. (Q2, FY 2020; Completed)
3. Perform density functional studies of InX<sub>3</sub> additive mechanisms in Li-O<sub>2</sub> batteries. (Q3, FY 2020; Completed)
4. Investigate electrolytes and cathodes that can greatly increase Li-O<sub>2</sub> coin cell capacities compared to current capacities through optimization of ORRs. (Q4, FY 2020; Initiated)

## Progress Report

Li-O<sub>2</sub> batteries are considered as an advanced energy storage system that could provide a much higher specific energy than Li-ion batteries for electrical transportation. However, there are major issues with the existing Li-O<sub>2</sub> systems, including degradation of the anode electrode, poor volumetric energy density, electrolyte instability, and high charge overpotential. The team is focused on finding a combination of electrolytes, additives, and cathode catalysts to enable a Li-O<sub>2</sub> battery that can operate in an air atmosphere with a low charge potential while maintaining a long cycle life. Last quarter, they finished a study comparing two bifunctional additives with one of the functions being that of a RM to reduce the charge potential, and the other function being to provide anode protection. The additives, based on InI<sub>3</sub> and InBr<sub>3</sub>, were found to give low charge potentials and cycle lives of ~ 200 cycles. This quarter, the team reports on computational results on the protective interphase formed on lithium by the InX<sub>3</sub> additive.

The mechanism by which the InX<sub>3</sub> forms a layer on the lithium surface was investigated with DFT. In this investigation, the team assumed that the addition of indium to the surface of the lithium anode, as observed in the SEM, EDX, and XPS studies, predominantly occurs during the first discharge cycle. The calculated oxidation potentials of the InI<sub>3</sub> and InBr<sub>3</sub>, including solvent effects, are 6.07 and 7.13 eV, respectively. This means that these species will not be oxidized at the anode during discharge, but rather chemically react as shown in the DFT calculations described below. Furthermore, the calculated reduction potentials of the InI<sub>3</sub> and InBr<sub>3</sub> (< 2.6 eV) are less than the discharge potential, so they will not likely be involved in the discharge process at the cathode. A possible chemical reaction between InX<sub>3</sub> and the lithium surface is given by:



The team investigated this chemical reaction for both InI<sub>3</sub> and InBr<sub>3</sub>, with a (100) lithium surface using DFT periodic calculations. In these calculations, the halides are in a mixed electrolyte of 21 DMSO molecules, one EMIM-BF<sub>4</sub> (9:1 volumetric ratio), and LiTFSI salt. All molecules were initially randomly arranged in the simulation box. The results of AIMD simulations at the electrolyte/anode interface are shown in Figure 123. They indicate that for both InI<sub>3</sub> and InBr<sub>3</sub>, the indium dissociates from the trihalide and moves into the lithium surface with the halide ions reacting with the lithium to form LiX species on the surface (Figure 123a-b). When the InX<sub>3</sub> reacts and dissociates (shown by DFT calculations) on the surface, the In<sup>3+</sup> picks up three electrons from the lithium anode because indium is more electronegative than the lithium. Three lithium from the surface can then form LiX where the Li<sup>+</sup> (formed by loss of the electrons to indium) reacts with X<sup>-</sup>. The reaction of InX<sub>3</sub> with the lithium surface is consistent with the experimental results from SEM, EDX, and XPS that there is indium on the lithium surface.

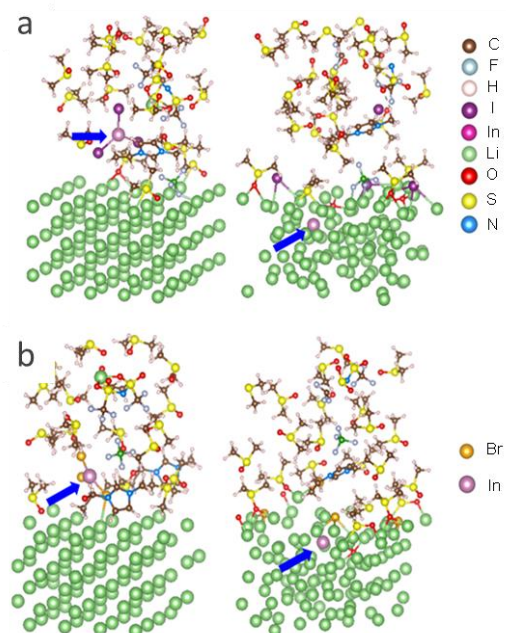


Figure 123. *Ab initio* molecular dynamics simulation of Li(100) interface with DMSO/IL electrolyte with InX<sub>3</sub> molecule added to the electrolyte. (a) Initial (left) and optimized (right) structures for InI<sub>3</sub>; arrow indicates the initial and final position of indium atom. (b) Initial (left) and optimized (right) structures for InBr<sub>3</sub>; arrow indicates the initial and final position of indium atom.

## Patents/Publications/Presentations

### Publications

- Zhang, C., N. Dandu, S. Rastegar, S. N. Misal, Z. Hemmat, A. T. Ngo, L. A. Curtiss, and A. Salehi-Khojin. “A Comparative Study of Redox Mediators for Improved Performance of Li-Oxygen Batteries.” *Advanced Energy Materials* (June 2020). doi: 10.1002/aenm.202000201.  
Ahmadiparidari, A., S. Fuladi, L. Majidi, S. Plunkett, E. Sarnello, Z. Hemmat, S. Rastegar, S. Misal, P. C. Redfern, J. Wen, T. Li, A. T. Ngo, F. Khalili-Araghi, L. A. Curtiss, and A. Salehi-Kojin. “Lowering Charge Potentials with Negligible Capacity Loss in High Rate Lithium Oxygen Batteries.” Submitted.
- Rastegar, S., Z. Hemmat, C. Zhang, S. Plunkett, J. G. Wen, N. Dandu, T. Rojas, L. Majidi, S. Misal, A. T. Ngo, L. A. Curtiss, and A. Salehi-Khojin. “A Lithium-Oxygen Battery that Operates in Dry Air with a Bifunctional  $\text{InX}_3$  (X = Br, I) Electrolyte Additive.” Submitted.

## TASK 7 – SODIUM-ION BATTERIES

### Summary

During FY 2019, the BMR added new projects, including several in the area of Na-ion batteries. Four of these projects are continuously funded into FY 2020. Progress on these four projects is described in this report. The Na-ion battery will require investigations to identify optimal electrode materials, electrolytes, separators, and binders to reach full potential. The BMR program will therefore have a limited effort directed toward identifying Na-ion battery materials that have potential value for vehicle applications. More detailed information on this BMR Task will be provided in upcoming reports.

**Highlights.** The highlights for this quarter are as follows:

- The ANL team reported a low-cost red phosphorus-based anode that can demonstrate a high specific capacity of  $2000 \text{ mAh g}^{-1}$ , with stable cycle performance and high ICE of 86% as well as thin SEI during cycling.
- The BNL team carried out synchrotron-based XAS studies for NaCrSeS cathode material at different SOCs. Their results show that the charge compensation of NaCrSeS cathode is partly achieved by the reversible redox of selenium anions.
- The LBNL team studied the effect of electrolyte composition on the 1<sup>st</sup> cycle CE, and best results were obtained with 0.5 M NaClO<sub>4</sub> in diethylene glycol dimethyl ether (DEGDME).
- The PNNL team developed LHCE (NaFSI-TEP/TTE 1:1.5:2 in mole), which enables inorganic F-rich and S-rich components (by XPS) in the CEI layer on NaCu<sub>1/9</sub>Ni<sub>2/9</sub>Fe<sub>1/3</sub>Mn<sub>1/3</sub>O<sub>2</sub> cathode and SEI layer on hard carbon anode, ensuring excellent cycling stability of both cathode and anode for Na-ion batteries.

## Task 7.1 – Exploratory Studies of Novel Sodium-Ion Battery Systems (Xiao-Qing Yang and Enyuan Hu, Brookhaven National Laboratory)

**Project Objective.** The objective of this project is to develop new advanced *in situ* material characterization techniques and apply these techniques to explore the potentials, challenges, and feasibility of new rechargeable battery systems beyond the Li-ion batteries, namely, the Na-ion battery systems for EVs, such as PHEV and BEV. To meet the challenges of powering PHEVs and BEVs, new rechargeable battery systems with high energy and power density, low cost, good abuse tolerance, and long calendar and cycle life need to be developed. This project will use the synchrotron-based *in situ* X-ray diagnostic tools, combined with TEM and STEM imaging techniques developed at BNL, to evaluate the new materials and redox couples to obtain fundamental understanding of the reaction mechanisms of these materials aiming for improvement of and guidance for new material and new technology development regarding Na-ion battery systems.

**Project Impact.** In the VTO MYPP, the goals for battery were described: “Specifically, lower-cost, abuse-tolerant batteries with higher energy density, higher power, better low-temperature operation, and longer lifetimes are needed for the development of the next-generation of HEVs, PHEVs, and EVs.” The knowledge learned from diagnostic studies and collaborations with U. S. industries through this project will help U. S. research institutions and industries to develop new materials and processes for a new generation of rechargeable battery systems, namely, Na-ion battery system, in their efforts to reach these VTO goals.

**Approach.** This project will use the synchrotron-based *in situ* X-ray diagnostic tools developed at BNL to evaluate the new materials and redox couples to enable a fundamental understanding of the mechanisms governing performance of these materials and provide guidance for new material and new technology development regarding Na-ion battery systems.

**Out-Year Goals.** Complete the synchrotron-based *ex situ* XRD, PDF, XAS, and XRF studies of novel anion redox-based cathode materials  $\text{NaTi}_{1/3}\text{Cr}_{2/3}\text{S}_2$  and  $\text{NaCrSeS}$  at different SOCs.

**Collaborations.** The BNL team has been closely working with top scientists on new material synthesis at ANL, LBNL, and PNNL and with U. S. industrial collaborators at GM and Johnson Controls, as well as with international collaborators.

### Milestones

1. Complete chromium, titanium, and sulfur K-edge XAS (including XANES and EXAFS) studies of  $\text{NaTi}_{1/3}\text{Cr}_{2/3}\text{S}_2$  cathode material at different SOCs. (Q1, FY 2020; Completed)
2. Complete synchrotron-based *ex situ* XRD and PDF analysis of novel anion redox-based cathode material  $\text{NaCrSeS}$  at different SOCs. (Q2, FY 2020; Completed)
3. Complete the chromium and selenium K-edge XAS study and analysis of  $\text{NaCrSeS}$  cathode material at different SOCs. (Q3, FY 2020; Completed)
4. Complete the sulfur K-edge XANES and EXAFS studies of  $\text{NaCrSeS}$  cathode material at different SOCs. (Q4, FY 2020; In progress)

## Progress Report

This quarter's milestone has been completed. BNL has been focusing on synchrotron-based XAS studies for NaCrSeS cathode material at different SOCs. *Ex situ* XAS measurements at chromium K-edge are carried out to examine valance states of chromium at different charge/discharge states. As shown in Figure 124a, no clear shifts of the Cr K-edge can be observed during charge/discharge processes, indicating that the contribution of chromium ions in the charge compensation during the electrochemical process is quite limited. A small reversible rise/drop in pre-edge should be attributed to the reversible distortion of Cr-S/Se octahedron; this allows the transition of electrons from Cr 1s to Cr 3d- $t_{2g}$  and 3d- $e_g$ , which is forbidden for the undistorted octahedral symmetry. XAS spectra at selenium K-edge at different charge/discharge stages are also measured. As shown in Figure 124b, obvious changes in the selenium K-edge XAS spectra can be observed during the charge and discharge processes, indicating the oxidation/reduction of selenium. The peak A (red area, Figure 124b) at  $\sim 12660$  eV could be assigned to the transition of 1s electron to unoccupied Cr 3d-Se 4p hybrid orbitals. The relative intensity of peak A also increases on charging. This can be attributed to the increased population of the unoccupied valence 4p levels caused by the charging process, indicating oxidization of selenium ions. During discharge process, the intensity of peak A decreases, indicating that the redox of selenium ions during cycling is fully reversible. In addition, the broad peak B at  $\sim 12670$  eV (blue area, Figure 124b) caused by multiple scattering in the coordination sphere shifts to high energy, and its intensity reduces on charging. It shifts back to pristine state after full discharge. All these changes demonstrate that the charge compensation is partly achieved by the redox of selenium anions.

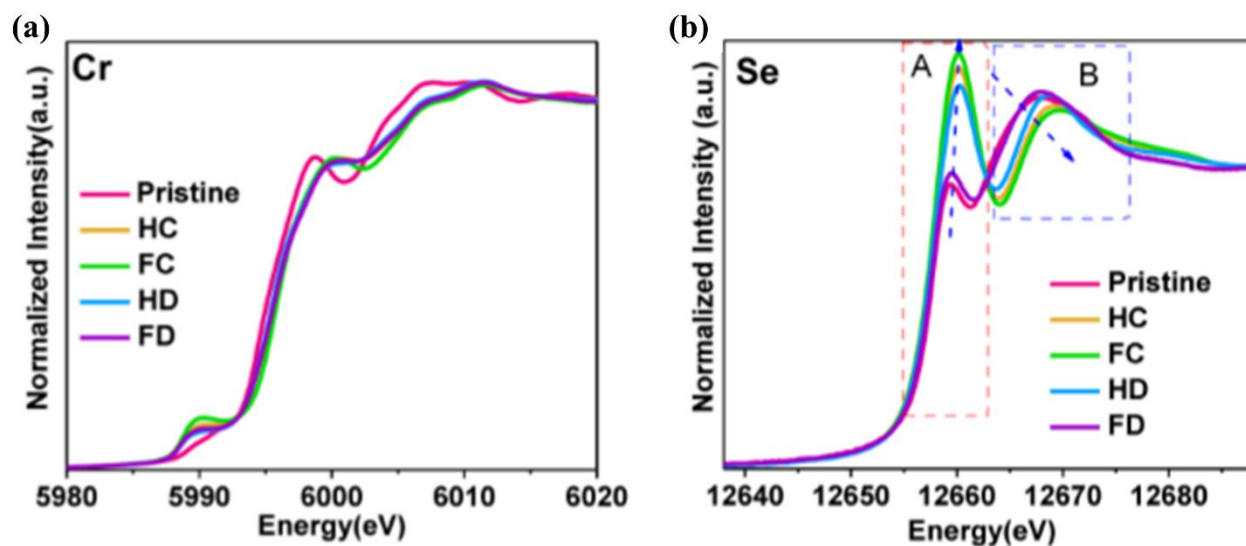


Figure 124. *Ex situ* X-ray absorption spectroscopy of chromium (a) and selenium (b) X-ray absorption near-edge structure (XANES) spectra of NaCrSeS electrodes at various charge/discharge states, which include pristine, half-charged (HC, charged to a capacity of 70 mAh g<sup>-1</sup>), full charged (FC, full charged to 3.3 V), half discharged (HD, discharged to a capacity of 70 mAh g<sup>-1</sup> after full charged), and full discharged (FD, full discharged to 1.5 V after full charged).

## Patents/Publications/Presentations

### Publications

- Wang, P-F., Y. Xiao, N. Piao, Q. Wang, X. Ji, T. Jin, Y-J. Guo, S. Liu, T. Deng, C. Cui, L. Chen, Y-G. Guo, X-Q. Yang, and C. Wang. “Both Cationic and Anionic Redox Chemistry in a P2-Type Sodium Layered Oxide.” *Nano Energy*. doi: 10.1016/j.nanoen.2020.104474; Publication Date (Web): January 10, 2020.
- Jin, T., P-F. Wang, Q-C. Wang, K. Zhu, T. Deng, J. Zhang, W. Zhang, X-Q. Yang, L. Jiao, and C. Wang. “Realizing Complete Solid-Solution Reaction in High Sodium Content P2-Type Cathode for High-Performance Sodium-Ion Batteries.” *Angewandte Chemie*. doi: 10.1002/ange.202003972; Publication Date (Web): June 5, 2020.

## Task 7.2 – Development of a High-Energy Sodium-Ion Battery with Long Life (Chris Johnson and Khalil Amine, Argonne National Laboratory)

**Project Objective.** The project objective is to develop a high-energy Na-ion battery with long life. Moreover, the battery chemistry should utilize low-cost materials. The energy density target is 200 Wh/kg and/or 500 Wh/L, wherein the anode and cathode capacity targets are 600 mAhg<sup>-1</sup> and 200 mAhg<sup>-1</sup>, respectively.

**Project Impact.** A Na-ion battery on par with the energy density of a Li-ion battery can have a high impact in the transportation sector with the assumption that the cost is significantly below \$85/kWh and that the battery pack provides a 300-mile range. The consumer is not concerned about the battery chemistry employed if these metrics can be met. Development of these battery chemistries will situate the United States in a strong position as relates to new low-cost energy storage systems beyond lithium ion.

**Approach.** In a team approach, the Na-ion battery group will create a versatile Na-ion battery chemistry with beneficial advantages such as low cost, safety, recycling, and sustainability of materials used. The team will work synergistically so that the final design is the culmination of advances in phosphorus carbon composites mated with optimized lead or other highly dense metalloids, such as tin and/or antimony and derivatives thereof, for the recyclable anode. Synthesis and optimization of such blended composite anodes will be conducted in parallel to diagnostic characterization of structures, phase formation, and cycling stability. Cathode work will begin at the end of the first year and will involve gradient cathodes consisting of Fe-Mn compositions, as well as intergrowths of layer stacking sequenced oxides. If resources allow, the team also will attempt to stabilize cathode surfaces using ALD methods, particularly for the benefit of staving off dissolution of manganese and iron/electrolyte reactivity. Electrolytes will be partly procured from Dr. H. Li at PNNL.

**Out-Year Goals.** The state-of-the-art Na-ion battery in the literature has now been surpassed by this team, but performance is still too low for commercialization. Thus, the goal is to move forward and continually invent the most superior Na-ion battery chemistry that can compete worldwide through work output from this project.

**Collaborations.** Researchers from PNNL who are developing electrolytes for Na-ion batteries will provide this project with formulations to test with the various electrode combinations investigated at ANL. The team also exchanges commercial samples with Dr. J. Barker of Faradion Ltd. in the United Kingdom.

### Milestones

1. Investigate reaction mechanism of P-based and Pb-based anode. (Q1, FY 2020; Completed)
2. Synthesize high-performance layered oxide cathodes using continuous stirred tank reactor (CSTR) method. (Q2, FY 2020; In progress)
3. Optimize the interface of P-based and Pb-based anode for long cycle life and high ICE. (Q3, FY 2020; In progress)
4. Develop composition-gradient oxide cathodes. (Q4, FY 2020; In progress)

## Progress Report

Due to the COVID-19 pandemic, ANL has been under minimum safe operations mode this quarter. Thus, the team had limited access to run planned experiments. They reported a low-cost, red phosphorus (RP) based anode for Na-ion batteries via scalable high-energy ball milling. The electrochemical performance and SEI after cycling were revealed by XPS. As shown in Figure 125, the new RP-based anode can deliver stable capacity of  $\sim 2000 \text{ mAh g}^{-1}$  up to 40 cycles at a charge/discharge rate of C/3 ( $1\text{C} = 2600 \text{ mA g}^{-1}$ ). Moreover, the ICE was measured at 85%, indicating significantly suppressed initial irreversible capacity loss.

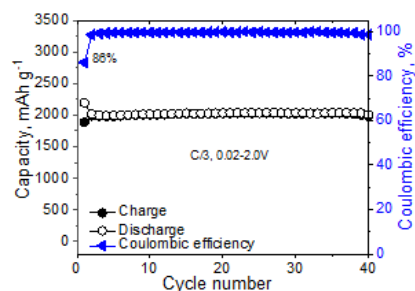


Figure 125. Cycling performance of Argonne National Laboratory red phosphorus anode at C/3.

To reveal the underlying mechanism, the team used XPS to probe the SEI of the cycled RP-based anode. Figure 126 shows the P2p XPS spectra of RP at different charge/discharge states. As shown, the pristine RP anode shows two major peaks at 129.0 eV and 130.0 eV, which can be assigned to the P 2p<sub>3/2</sub> and P 2p<sub>1/2</sub> doublet of the element P. When the cell was discharged to 0.02 V, two new peaks appeared at 136.9 eV and 126.8 eV. The peak at 126.8 eV is attributed to the formation of Na<sub>3</sub>P, which leads to a significant decrease of the P2p peaks at 130 eV and 129 eV. The peak at 136.9 eV is assigned to Na<sub>x</sub>PF<sub>y</sub>O<sub>z</sub>, which is due to the decomposition of NaPF<sub>6</sub> salt, resulting in the simultaneous increase of the P-O peak at 132.8 eV due to the deposition of PO<sub>4</sub><sup>3-</sup>. After charging back to 2.0 V, the Na<sub>x</sub>PF<sub>y</sub>O<sub>z</sub> and PO<sub>4</sub><sup>3-</sup> peaks remained stable, while the P2p peaks of RP were recovered along with the disappearance of the Na<sub>3</sub>P peak due to the desodiation of Na<sub>3</sub>P to phosphorus during charge. The identification of the Na<sub>3</sub>P and P2p peaks of RP during charge/discharge in the XPS clearly demonstrates that the SEI layer on the RP70/C30 is very thin (< 10 nm due to the penetration depth limit of XPS). Therefore, the project's new RP anode can demonstrate excellent cycle stability and high ICE.

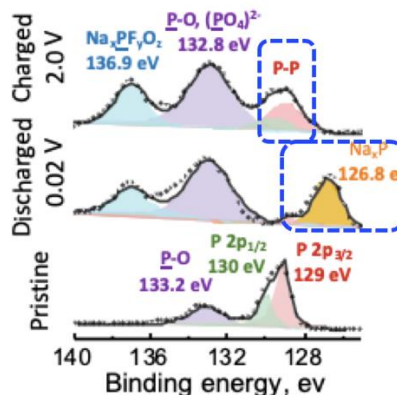


Figure 126. P2p X-ray photoelectron spectroscopy spectra of red phosphorus anode at different charge/discharge states.

## Patents/Publications/Presentations

### Publications

- Liu, Z. J., A. Daali, G. L. Xu, M. H. Zhuang, X. Zuo, C. J. Sun, Y. Liu, Y. Cai, M. D. Hossai, H. W. Liu, K. Amine, and T. Luo. "Highly Reversible Sodiation/Desodiation from a Carbon-Sandwiched SnS<sub>2</sub> Nanosheet Anode for Sodium Ion Batteries." *Nano Letters* 20 (2020): 3844–3851.

- Amine, R., A. Daali, X. Zhou, X. Liu, Y. Liu, Y. Ren, X. Zhang, L. Zhu, S. Al-Hallaj, Z. Chen, G. L. Xu, and K. Amine. “A Practical Phosphorus-Based Anode Material for High-Energy Lithium-Ion Batteries.” *Nano Energy* 74 (2020): 104849. Publication Date (Web): April 26, 2020.
- Han, J., J. Park, S-M. Bak, S-B. Son, J. Gim, C. Villa, X. Hu, V. P. Dravid, C. C. Su, Y. Kim, C. Johnson, and E. Lee. “New High-Performance Pb-Based Nanocomposite Anode Enabled by Wide-Range Pb Redox and Zintl Phase Transition.” Submitted.

## Task 7.3 – High-Capacity, Low-Voltage Titanate Anodes for Sodium-Ion Batteries (Marca Doeff, Lawrence Berkeley National Laboratory)

**Project Objective.** The objectives are to understand differences in the sodium intercalation mechanism of various sodium titanate anodes through an array of synthetic, electrochemical, and structural characterization techniques, and to overcome practical impediments to their use, such as the high 1<sup>st</sup> cycle Coulombic inefficiencies that are currently observed. The ultimate goal is to produce a 200-250 mAh/g anode that cycles reversibly.

**Project Impact.** Although several suitable cathode materials for Na-ion batteries exist, there are few suitable anode materials due to low potential instabilities. Therefore, sodium titanate variations will be synthesized through different routes to develop materials with various morphologies and dopants. Decreasing the 1<sup>st</sup> cycle inefficiencies and improving cycling performance will allow enabling technology for a practical high-energy Na-ion battery.

**Approach.** Candidate stepped layered titanates will be synthesized by appropriate routes (hydrothermal, solid-state routes, etc.). Materials will then be characterized electrochemically and physically. Structure-function relationships will be built to correlate the effect of changing structure (for example, step size) on electrochemical properties.

**Out-Year Goals.** A series of synchrotron characterization techniques will be used to further develop sodium titanate anode materials with stable cycling while delivering high capacities.

**Collaborations.** TXM is done in collaboration with Dr. Y. Liu (SSRL). Synchrotron hard, sXAS, and X-ray Raman efforts are in collaboration with Dr. D. Nordlund and Dr. D. Sokaras (SSRL). Electrolyte design is done in collaboration with Dr. K. Xu (ARL).

### Milestones

1. Conduct SEI studies. (Q1, FY 2020; In progress, pending beam time at SSRL)
2. Synthesize lepidocrocite titanates. (Q2, FY 2020; In progress)
3. Select best electrolyte solution. (Q3, FY 2020; In progress)
4. *Go/No-Go Decision:* On sodium nonatitanate, stop if problems are not solved. (Q4, FY 2020; In progress)

## Progress Report

This quarter, the team optimized testing of the electrolyte in cells containing lepidocrocite-type  $\text{Na}_x\text{Ti}_{2-x/4}\text{O}_4$  electrodes, aiming at improving 1<sup>st</sup> cycle CE and long-term cycling stability. Their first consideration is the residual structural water in  $\text{Na}_x\text{Ti}_{2-x/4}\text{O}_4$ , since a heating temperature of 120°C might not fully dehydrate  $\text{Na}_x\text{Ti}_{2-x/4}\text{O}_4$  because they are prepared in aqueous media.  $\text{H}_2\text{O}$  is known to induce the decomposition of EC and sodium hexafluorophosphate ( $\text{NaPF}_6$ ) [Journal of the Electrochemical Society 163, no. 7 (2016): A1219–A1225; Journal of Power Sources 447, no. 31 (2020): 227363] present in the project’s baseline electrolyte (1 M  $\text{NaPF}_6$  in EC/DEC). Therefore, the team should be able to improve the 1<sup>st</sup> cycle CE and long-term cycling stability by using more water-tolerant salts and solvents. To check this hypothesis, six electrolytes with different salts and solvents were tested; the obtained 1<sup>st</sup> cycle CE of  $\text{Na}_{0.69}\text{Ti}_{1.827}\text{O}_4$ ||Na cells with all electrolytes is summarized in Figure 127 (the long-term cycling results will be reported next quarter). Indeed, an improved 1<sup>st</sup> cycle CE of 70.2% was obtained with 0.5 M sodium tetraphenylborate ( $\text{NaPhB}_4$ ) in DEGDME as compared to 57.4% obtained with the baseline electrolyte. Electrolyte of 0.5 M sodium perchlorate ( $\text{NaClO}_4$ ) in DEGDME improves the 1<sup>st</sup> cycle CE to 70.8%; however, it induces faster capacity decay in the following cycles. In contrast, the electrolyte consisting of 1 M  $\text{NaPF}_6$  in propylene carbonate (PC) drastically decreases the 1<sup>st</sup> cycle CE to 28.7%. More studies are needed and planned the next quarter to understand more about the varied values of 1<sup>st</sup> cycle CE obtained in these electrolytes.

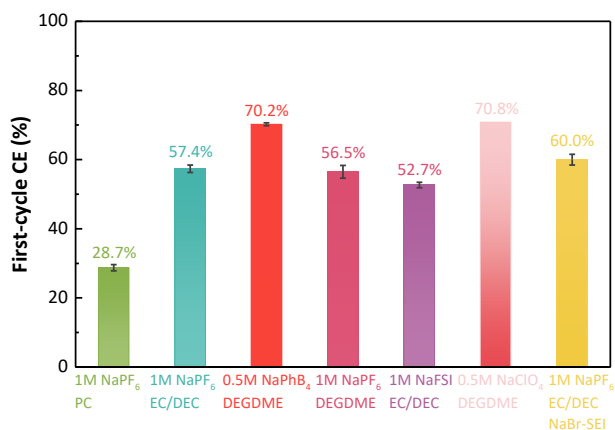


**Figure 127.** Average 1<sup>st</sup> cycle Coulombic efficiency (CE) of  $\text{Na}_{0.69}\text{Ti}_{1.827}\text{O}_4$ ||Na cells with different electrolytes. All cells were cycled at current rate of C/20 (that is, 8 mA g<sup>-1</sup>, 0.012 mA cm<sup>-2</sup>). With each electrolyte, two to three cells were tested to obtain better statistics. The error bar represents the standard deviation of the average values of CE. ‘NaBr-SEI’ stands for cells cycled with NaBr-coated sodium metal. The NaBr coating was created from a spontaneous chemical reaction between 1-Bromopropane and metallic sodium, following the same procedure reported in *Nature Communications* 8 (2017): 898. No noticeable improvement in 1<sup>st</sup> cycle CE was observed with NaBr-coated sodium metal in electrolyte of 1 M  $\text{NaPF}_6$  in EC/DEC.

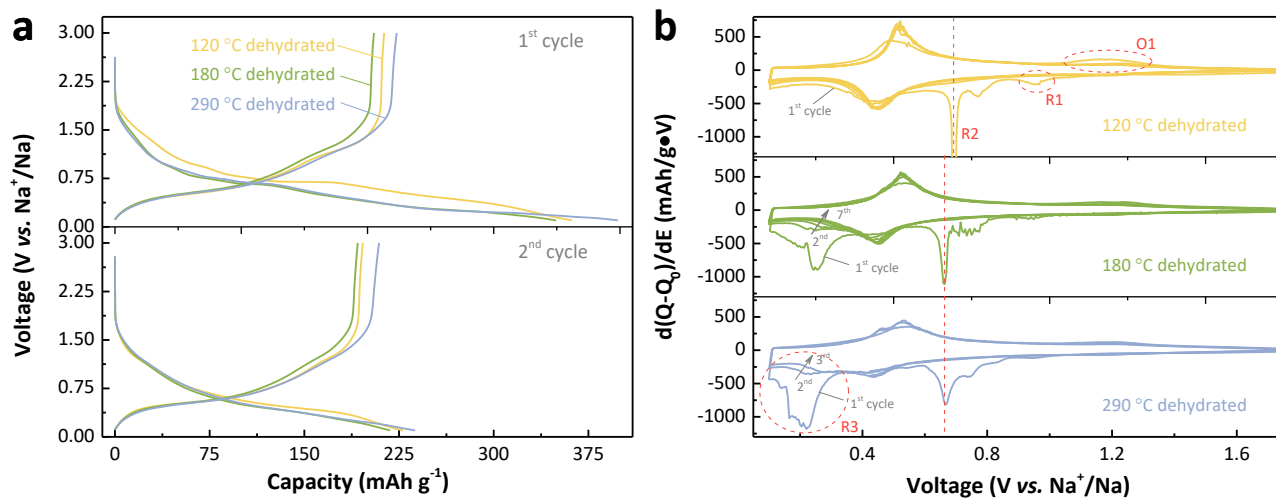


**Figure 128.** Electrochemical performance of  $\text{Na}_{0.69}\text{Ti}_{1.827}\text{O}_4$  electrodes in half-cells. (a) Typical 1<sup>st</sup> cycle (top panel) and 2<sup>nd</sup> cycle (bottom panel) discharge/charge profiles of  $\text{Na}_{0.69}\text{Ti}_{1.827}\text{O}_4$  dehydrated at 120°C (yellow curve), 180°C (green curve), and 290°C (blue curve). (b) Corresponding  $dQ/dV$  plots. All cells were cycled in 1 M  $\text{NaPF}_6$  in EC/DEC at current rate of C/20.

To investigate the effect of dehydration temperature on the electrochemical properties of  $\text{Na}_x\text{Ti}_{2-x/4}\text{O}_4$  electrodes, three temperatures (120°C for absorbed water removal, 180°C for structural water removal, and 290°C for further structural water removal and new phase development) were selected to vacuum dry  $\text{Na}_x\text{Ti}_{2-x/4}\text{O}_4$  powder based on previous TGA and temperature-dependent powder XRD results. Their electrochemical performance is presented in Figure 128. Significant changes were observed in the 1<sup>st</sup> cycle. After dehydration at higher temperatures (180°C and 290°C), the first reduction peak centered at ca. 1 V versus  $\text{Na}^+/\text{Na}$  and the oxidation peak located at ca. 1.2 V versus  $\text{Na}^+/\text{Na}$  become almost invisible, suggesting that they are related to the structural-water-driven reactions. Moreover, the very sharp reduction peak located at ca. 0.7 V versus  $\text{Na}^+/\text{Na}$  becomes less prominent and shifts to lower voltage, although its origin is unclear at this stage. Another striking difference was observed below ca. 0.7 V versus  $\text{Na}^+/\text{Na}$ , a new broad reduction peak develops and gradually decreases its intensity in the following cycles. Equally interesting, no noticeable variation of discharge capacity and capacity retention above the experimental error was observed during the 2<sup>nd</sup> cycle and onward. Next quarter, the team plans to further increase the dehydration temperature, hoping to obtain more clear information at more extreme conditions. In parallel, conducting the same study in the optimal (more water-tolerable) electrolyte might provide additional information.

Electrochemical characterization of  $\text{Na}_x\text{Ti}_{2-x/4}\text{O}_4$  electrodes as a function of composition is also on going. All cells are running, and the results are expected to be reported next quarter since some cells are not yet finished with their 1<sup>st</sup> cycles.

Work next quarter will include the following: electrochemical characterization of  $\text{Na}_x\text{Ti}_{2-x/4}\text{O}_4$  electrodes with different electrolytes; electrochemical characterization of  $\text{Na}_x\text{Ti}_{2-x/4}\text{O}_4$  electrodes as a function of dehydration temperature and composition; and investigation of the role of electrolyte, dehydration temperature, and composition using spectroscopy techniques.

### Patents/Publications/Presentations

The project has no patents, publications, or presentations to report this quarter.

## Task 7.4 – Electrolytes and Interfaces for Stable High-Energy Sodium-Ion Batteries (Ji-Guang Zhang, Pacific Northwest National Laboratory)

**Project Objective.** This project will develop innovative electrolytes and enable fundamental understanding on the interface between electrode and electrolyte for stable operation of high-energy Na-ion batteries. The proposed research will enhance the achievable capacities of both anode and cathode for Na-ion battery and improve the stability of electrodes/electrolyte interface, establish correlation (electrolyte design rule) between electrochemical performances of Na-ion batteries and the electrolyte/interface properties, and enable long cycle life and safe operation of high-energy Na-ion batteries.

**Project Impact.** Success of this project will provide a solid understanding on the electrolyte/electrode interphase of Na-ion batteries and significantly improve their energy density, cycle life, and safety. It will also accelerate the practical application of Na-ion batteries in both EV and stationary energy storage.

**Approach.** This project will optimize the electrolyte components and concentrations to develop innovative electrolytes and additives with improved electrochemical and physical properties. *In situ* and *ex situ* spectroscopy methods will be used to unravel the origin of the SEI at the dynamic interface, providing guidance for the electrolyte and interface design and enabling high capacity and long life of Na-ion batteries.

**Out-Year Goals.** This project will select the electrolyte compounds and identify the formation of interfacial SEI layer on hard carbon and CEI layer-on-layer oxide cathode and its effect on the electrode materials. It will also provide guidance to electrolyte optimization and improve CE of sodium deposition/stripping to be more than 99%.

**Collaborations.** This project will collaborate with ANL, LBNL, and other leading scientists in the field of cathode and anode materials for Na-ion batteries. It will also collaborate with Dr. C. Wang and Dr. M. Engelhard of PNNL for TEM and XPS characterization.

### Milestones

1. Optimize electrolyte composition: Na-based LHCE will be developed to improve cycling stability. (Q1, FY 2020; Completed)
2. Develop electrolyte additives to improve stability of SEI on anode and of CEI layer on cathode. (Q2, FY 2020; Completed)
3. Develop compatible polymer separator (or PE) to stabilize long-term cycling and provide a stable/adequate interphase. (Q3, FY 2020; Completed)
4. Apply the new electrolytes and additives in Na-ion batteries to improve CE to more than 99%. (Q4, FY 2020; In progress)

## Progress Report

The team has focused on electrode/electrolyte interphase composition analysis by XPS this quarter to understand stable electrochemical performance of both cathode and anode in LHCE (NaFSI-TEP/TTE; 1:1.5:2 in mole) compared with baseline electrolyte, or BE (1 M NaPF<sub>6</sub>/EC+DMC; 1:1 in weight).

The CEI formed in BE was dominated by organic species, as shown in Figure 129a. The C1s peaks indicate the existence of C-C/C-H, C-O and poly(CO<sub>3</sub>) groups in the CEI layer originated from the decomposition of the organic carbonate solvent (Figure 129a). F 1s (Figure 129b) and P2p (Figure 129c) peaks suggest the decomposition of NaPF<sub>6</sub> salt. While for the CEI formed in LHCE, in addition to the C-C/C-H, C-O, C=O peak, substantial C-SO<sub>x</sub> and C-F peaks were also found (Figure 129d), indicating possible TTE and NaFSI decomposition. The F 1s spectrum showed much higher fluorine contents, including S-F/C-F and NaF (Figure 129e). S2p spectrum also showed the components from NaFSI salt decomposition (Figure 129f). The high inorganic composition, and higher fluorine- and sulfur-based components in the CEI layer formed in the NaFSI-TEP/TTE electrolyte enable the fast Na<sup>+</sup> transport at the cathode/electrolyte interphase, providing stable cathode electrochemical performance.

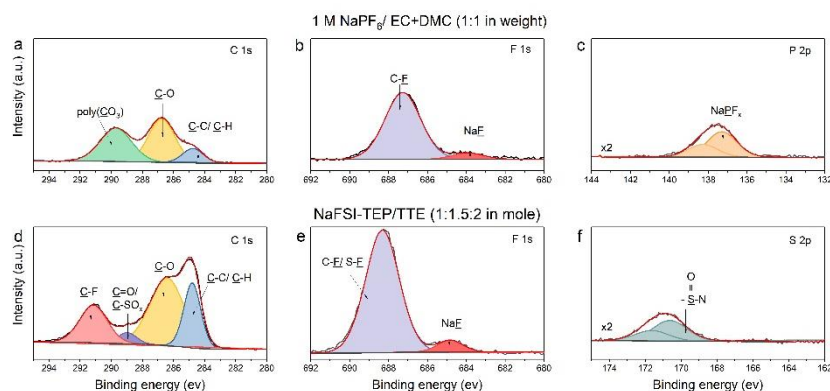


**Figure 129. X-ray photoelectron spectroscopy characterization of the CEI components on Na-CNFM (NaCu<sub>1/9</sub>Ni<sub>2/9</sub>Fe<sub>1/3</sub>Mn<sub>1/3</sub>O<sub>2</sub>) cathode electrodes after the 10<sup>th</sup> cycles in different electrolytes. (a/d) C 1s spectra, (b/e) F 1s spectra, (c) P 2p spectra, and (f) S 2p spectra for 1 M NaPF<sub>6</sub>/EC+DMC (1:1 in weight) electrolyte (a-c) and NaFSI-TEP/TTE (1:1.5:2 in mole) electrolyte (d-f).**

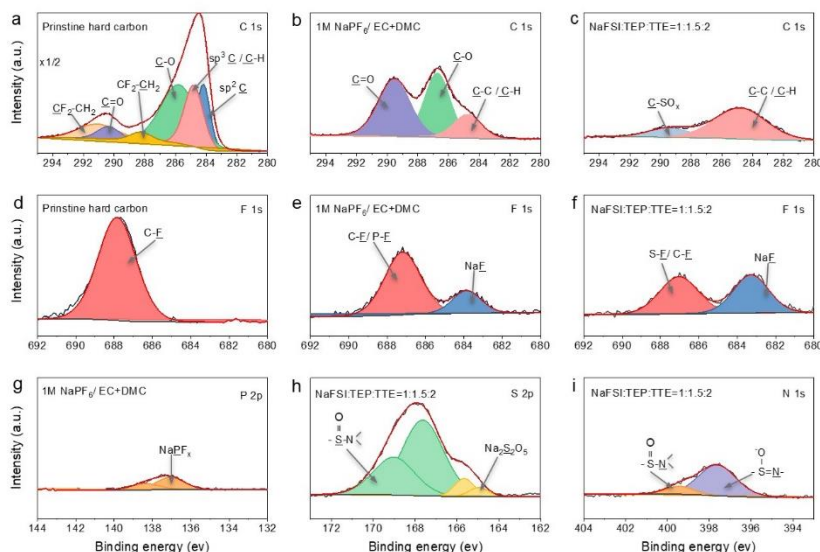


**Figure 130. Characterization of SEI components on pristine and cycled hard carbon (HC) electrodes by X-ray photoelectron spectroscopy. (a-c) C 1s, (d-f) F 1s, (g) P 2p, (h) S 2p, and (i) N 1s XPS profiles of the pristine HC anode (a/d) and the HC anode after 20 cycles in 1 M NaPF<sub>6</sub>/EC+DMC (1:1 in weight) electrolyte (b/e/g) and NaFSI-TEP/TTE (1:1.5:2 in mole) electrolyte (c/f/h/i).**

Figure 130 shows that the XPS analysis on SEI formed on HC in different electrolytes. C 1s of a pristine HC electrode showed strong sp<sup>2</sup> carbon and sp<sup>3</sup> carbon/C-H peaks (Figure 130a). After cycling in the BE (Figure 130b), the main C 1s peaks in the HC electrode were dominated by C-C/C-H, C-O, C=O groups, revealing carbonate solvent decomposition. F 1s peaks of NaF and P2p peaks of NaPF<sub>x</sub> in the SEI layer are probably from the decomposition of NaPF<sub>6</sub> salt (Figure 130e/g). While in LHCE, the C 1s peak intensity significantly decreased as compared to BE (Figure 130c), suggesting greatly reduced solvent decomposition. In addition to the C-C peak from the HC, the C-SO<sub>x</sub> peak was formed due to the decomposition of the NaFSI salt (Figure 130c). NaFSI salt decomposition also resulted in F 1s spectra with more NaF (Figure 130f), S2p peaks (Figure 130h) from sodium sulfur oxynitride (NaSON), Na<sub>2</sub>S<sub>2</sub>O<sub>5</sub>, and N 1s peaks (Figure 130i) from NaSON. Inorganic dominated SEI layer on HC anode in the LHCE ensures a robust SEI layer and excellent cycling stability of Na||HC cells.

## Patents/Publications/Presentations

### Presentation

- DOE VTO Annual Merit Review, virtual presentation (June 1–4, 2020): “Electrolytes and Interfaces for Stable High-Energy Na-Ion Batteries”; J-G. Zhang, R. Yi, P. M. Le, T. D. Vo, and Y. Jin.

## Innovation Center for Battery500

(Jun Liu, Pacific Northwest National Laboratory; Yi Cui, Stanford University)

**Project Objective.** The project aims to develop commercially viable lithium battery technologies with a cell-level specific energy of 500 Wh/kg through innovative electrode and cell designs that enable the extraction of the maximum capacity from advanced electrode materials. In addition to achieving high specific energy, the project aims to be able to achieve 1,000 cycles for the developed technologies.

**Project Impact.** The Battery500 Consortium will develop next-generation lithium battery technologies that will significantly increase energy density, improve cycle life, and reduce cost. This will greatly accelerate deployment of EVs and reduce carbon emission associated with fossil fuel consumption. The consortium will utilize first-class expertise and capabilities in battery research in the United States and develop an integrated and multi-disciplinary approach to accelerate development and deployment of advanced electrode materials in commercially viable high-energy batteries. The advances made in this consortium will also benefit the improvement of current Li-ion battery technologies.

**Approach.** This project will utilize an assortment of national resources located at the national laboratory level and university level. The lithium anode combined with a compatible electrolyte system and two cathodes—one high-Ni  $\text{LiNi}_x\text{Mn}_y\text{Co}_z\text{O}_2$  and another sulfur—will be studied and developed to reach high energy density. The project focus is to design novel electrode and cell architectures to meet the 500 Wh/kg goal. The consortium will work closely with R&D companies, battery/materials manufacturers, and end users/OEMs to ensure that the developed technologies are aligned with industry needs and can be transitioned to production.

**Out-Year Goals.** This project aims for the following out-year goals. (1) Fabricate and test a pouch cell capable of 350 Wh/kg and 350 cycles. (2) Fabricate and test a pouch cell capable of 400 Wh/kg and 100 cycles.

**Collaborations.** Collaboration among consortium team members will be well coordinated by the leadership team, which includes the keystone project leads and co-leads along with PIs at all member institutions. Collaboration with the community outside of this consortium and with industry will be facilitated by the executive committee, the advisory board, and the industry committee.

## Milestones

1. Deliver pouch-cell design and pouch-cell parameters for over 400 Wh/kg pouch cells. (Q1, FY 2020; Completed)
2. Develop new 3D anode structures; test and validate such using coin-cell standard protocols. (Q2, FY 2020; Completed)
3. Fabricate and test 350 Wh/kg Li-S pouch cells with over 50 stable cycles. (Q3, FY 2020; Completed)
4. Fabricate and test a pouch cell capable of 400 Wh/kg and 100 cycles. (Q4, FY 2020; In progress)

## Progress Report

## Keystone Project 1: Materials and Interfaces

The goal of Keystone 1 is to provide materials and chemistry support for Keystone Projects 2 and 3. This quarter, neutron powder diffraction data were used to quantify defects in NMC cathodes (BNL); two different approaches are being pursued for enabling TFEO-based LHCEs (PNNL and Stanford), and columnar lithium deposits were achieved by optimizing stack pressure in combination with ether-based electrolytes (UCSD).

Researchers from BNL performed neutron powder diffraction to examine the defect fraction in a variety of NMC cathodes. To realize maximal performance achievable using NMC layered cathodes, it is necessary to optimize not just the cathode composition, but also the concentration of defects within the cathode material, as these defects have potential to modify both the electronic and ionic conductivity of the cathode. While it has long been recognized that anti-site defects are present in layered NMC compounds, to date it has not been possible to elucidate structure-properties relationships due to the difficulty of accurately quantifying defect compositions. To address this unmet need, the team carried out a comprehensive study of more than a dozen NMC compounds using the highest quality of synchrotron and neutron powder diffraction data attainable in this country. Using these data along with new analysis methods that the team developed, they have been able to independently determine defect concentrations using the X-ray and neutron data with an agreement of 0.1% (absolute), a sensitivity to defects that appears to be unprecedented both for these compounds and for the entire field of powder diffraction (Figure 131). This sensitivity to defects exceeds that of traditional chemical methods.

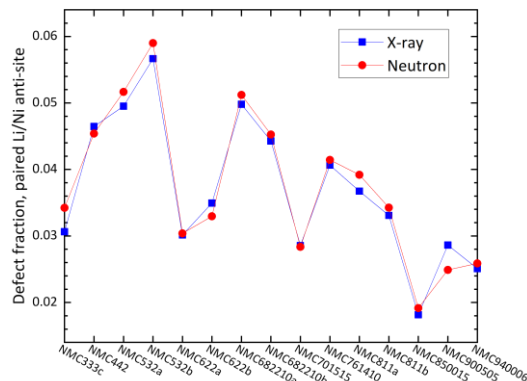


Figure 131. Close agreement in paired anti-site (PAS) defect concentration determined from X-ray (blue) and neutron (red) powder diffraction data.

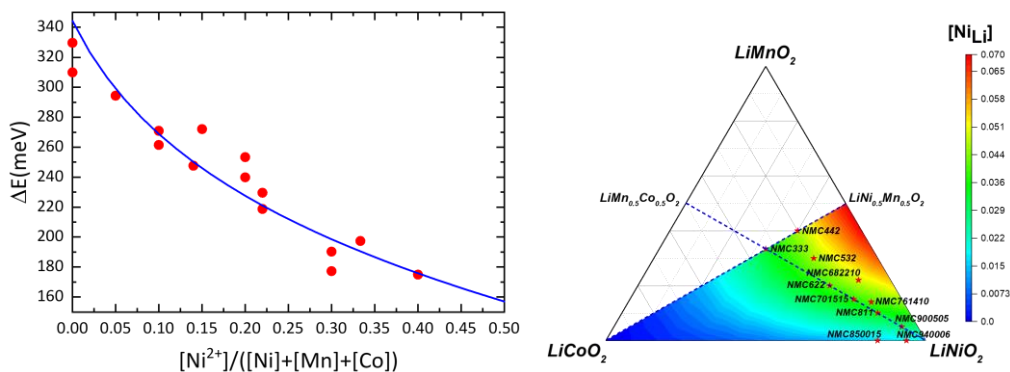
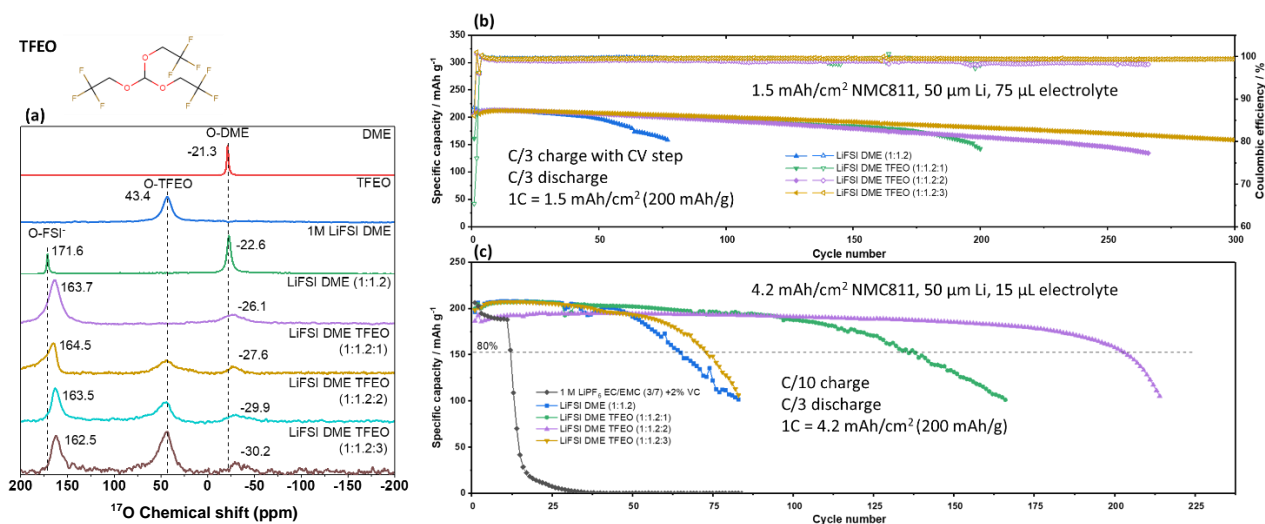


Figure 132. (left) Energy of paired anti-site (PAS) defect formation is found to depend on the total concentration of  $\text{Ni}^{2+}$  in the NMC phase. (right) Predicted PAS defect composition as a function of NMC composition. For the range of experimentally measured samples (symbols), predictions are accurate within  $\sim 0.5\%$  (absolute).

From the defect compositions refined in this manner, it has been proven that the dominant defect for almost all NMC compositions is paired anti-site (PAS) defects of  $\text{Ni}_{\text{Li}}$  and  $\text{Li}_{\text{Ni}}$  (Figure 132). It was previously assumed that PAS defects occur due to the similar sizes of  $\text{Ni}^{2+}$  and  $\text{Li}^+$ . If this is the case, the defect formation energy should be independent of the sample composition, something that can be now tested using the team's high-precision measurements of defect concentration to calculate defect formation energies through the Boltzmann relationship. It can be clearly seen that the defect formation energy is not composition-independent,

that thermodynamic and not kinetic considerations primarily determine the defect concentration, and that the defect formation energy is non-zero even for NMC compositions that lack  $\text{Ni}^{2+}$ . It is concluded that the composition-dependence is due to variation in the average size of octahedra in the TM layer (which continuously increases as the  $\text{Ni}^{2+}$  fraction increases). Furthermore, the team's derived relationship between chemical composition and defect formation energy can be used to predict the defect concentration for any NMC composition and any synthesis temperature.

The PNNL team systematically investigated the TFEO-based LHCEs. It was found that TFEO does not coordinate with  $\text{Li}^+$  ions; instead, it forms highly concentrated clusters (Figure 133a). TFEO-based LHCEs endow highly robust and protective interphases on the high-Ni NMC cathode (CEI) and Li-metal anode (SEI) to suppress undesirable side reactions. The lattice reconstruction from layered structure to rock salt structure in NMC-811 is apparently minimized. The continuous SEI growth on lithium metal is also significantly diminished in LHCEs, thus greatly improving cycling performances of Li||NMC-811 cells. Under moderate loading condition (that is,  $1.5 \text{ mAh cm}^{-2}$  NMC-811,  $50 \mu\text{m}$  of lithium anode, and flooded electrolyte) the Li||NMC-811 cell has longer cycling life with the increase of TFEO. For the cell using LiFSI-1.2DME-3TFEO electrolyte, it shows capacity retention of 80% after 300 cycles (Figure 133b). Under highly demanding conditions required by practical applications (that is,  $4.2 \text{ mAh cm}^{-2}$ -NMC-811,  $50 \mu\text{m}$  of lithium anode, and lean electrolyte), the cells using LHCEs of LiFSI-1.2DME-2TFEO and LiFSI-1.3DME-2TFEO have demonstrated 80% capacity retention over 200 cycles (Figure 133c). Furthermore, it was found that the cell performance highly depends on its testing condition: great CEI properties and cathode stability are crucial under moderate cathode loading and flooded electrolyte, while balanced CEI characters and sufficient salt concentration for salt-derived SEI determine the cell performance under practical conditions. These crucial findings highlight the importance of electrode/electrolyte interphase chemistries and the criteria for designing an electrolyte under practical conditions to enable long-life stability for realistic high-energy-density Li-metal batteries.



**Figure 133.** (a) Solvation structure ( $^{17}\text{O}$ -NMR spectra) of different solvents and electrolytes with different LiFSI concentrations and TFEO ratios. Cycling performance of Li||NMC-811 cells under (b) moderate and (c) practical conditions with different electrolytes, where the cells were cycled between 2.8–4.4 V after two formation cycles at C/10 rate.

The PNNL team is also systematically studying the effects and mechanisms of four model solvent molecules (carbonate, sulfone, phosphate, and ether) in LHCEs for 4.4 V Li||NMC-811 cells. Electrochemical tests and electron microscopies show largely different cathode/electrolyte and anode/electrolyte stabilities with the solvents selected. Among the four LHCEs, the DME-LHCE demonstrates the best capabilities to stabilize both the LMA and the Ni-rich cathode. XPS analysis proves both the salt and the solvent in the LHCEs are involved in the reactions at the electrode/electrolyte interfaces. Further theoretical analysis reveals that the strong interactions between the salt and the solvent in the inner solvation sheath of the LHCEs greatly influence

their individual reactivities. Their intermolecular proton/charge transfer processes are likely the key steps for the interfacial reactions. This work provides new crucial insights in understanding the electrolyte solvation structure and its implications on the electrode/electrolyte interfacial chemistry.

An alternative electrolyte approach is being pursued by the Stanford team to enable Li-metal anodes. They demonstrated a design strategy for electrolytes that enables anode-free Li-metal batteries with single-solvent single-salt formations at standard concentrations (*Nature Energy* 2020). Rational incorporation of –CF<sub>2</sub>– units yields fluorinated 1,4-dimethoxybutane (FDMB) as the electrolyte solvent. Paired with 1 M lithium bis(fluorosulfonyl)imide, this electrolyte possesses unique Li–F binding and high anion/solvent ratio in the solvation sheath, leading to excellent compatibility with both Li-metal anodes (CE ~ 99.52%, and fast activation within five cycles) and high-voltage cathodes (~ 6 V stability). Unlike typical transparent and colorless electrolytes, 1 M LiFSI/FDMB is brownish in color, as shown in Figure 134a. The 50- $\mu\text{m}$ -thick Li|NMC batteries retain 90% capacity after 420 cycles, with an average CE of 99.98%. Industrial anode-free pouch cells achieve ~ 325 Wh/kg single-cell energy density and 80% capacity retention after 100 cycles.

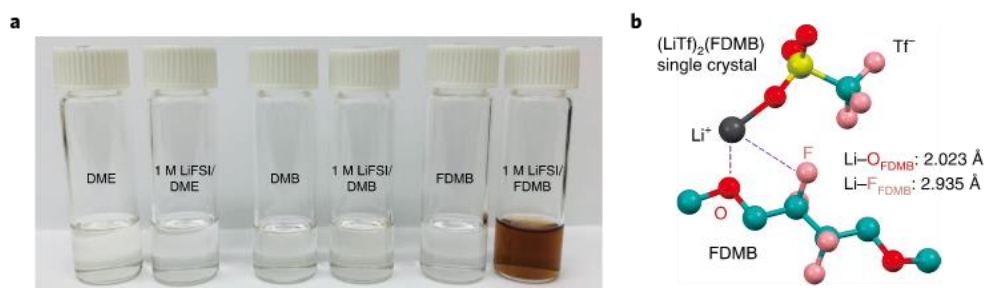


**Figure 134.** (a) Optical image of three liquids and their 1 M LiFSI electrolytes. (b) Single crystal of LiTf/FDMB showing Li–F interactions. For clarity, only one LiTf and one FDMB are shown.

UCSD is studying the deposition of lithium metal. It is qualitatively believed that increased uniaxial stack pressure can help to alleviate lithium dendrite formation and improve CE and cycling performance of Li-metal batteries. Quantitatively understanding the role of stack pressure on lithium nucleation, growth, and dissolution, and building the pressure-morphology-performance relationship, will open up new opportunities to rationally solve issues regarding Li-metal anodes in high-energy Li-metal batteries. In this study, researchers at UCSD used a custom-designed split cell with a load cell to precisely control the stack pressure applied to the battery during cycling, with a pressure measurement resolution of 0.1 psi. Figure 135a shows the 1<sup>st</sup> cycle CE of Li-Cu cells as a function of applied stack pressure under current densities up to 2 mA/cm<sup>2</sup>, using an advanced ether-based electrolyte. At 0 psi, the CE decreased from 92.5% at 1 mA/cm<sup>2</sup> to 85.5% at 2 mA/cm<sup>2</sup>. When slightly increasing the stack pressure to 5 psi, the CE at 2 mA/cm<sup>2</sup> significantly increased to 92%; the CE also increased from 87% to 92.5% at 1.5 mA/cm<sup>2</sup>. A gradual increment of CE at three current densities was observed when gradually increasing the stack pressure to 20 psi. At 20 psi, the CE was boosted to 97.5%, 96.5%, and 96% at 1, 1.5, and 2 mA/cm<sup>2</sup>, respectively. Further increasing the stack pressure from 20 psi to 50 psi, the CE remains almost unchanged. For the electrochemical performance testing, the pressure was set as the on-set value. Two representative pressures (0 and critical pressure) were selected to study the deposited lithium morphology using cryo-FIB-SEM. A high current density of 2 mA/cm<sup>2</sup> was applied for the morphological study. At 0 psi, highly porous and whisker-like lithium deposits were formed even using advanced ether-based electrolyte, as shown in Figure 135b (top view) and Figure 135d (cross-section). This type of morphology is highly similar to the one formed in commercial carbonate electrolyte using coin cells with internal stack pressure of ~ 30 psi. When applying a critical pressure, the lithium deposits become highly close-packed (Figure 135c). The cross-section morphology (Figure 135e) shows that the lithium deposits form a perfect columnar structure with large granular diameter of ~ 4  $\mu\text{m}$ , near-theoretical thickness of ~ 10  $\mu\text{m}$  and minimum electrode-level porosity, indicating that pressure plays an important role in tuning lithium deposition morphology. The researchers predicted in their previous study that the columnar lithium deposits may help to

improve the CE of lithium metal by mitigating the isolated metallic lithium formation. This study proves that the columnar lithium deposits can be achieved by optimizing stack pressure, in combination with ether-based electrolytes. The role of pressure during the stripping process will be studied.

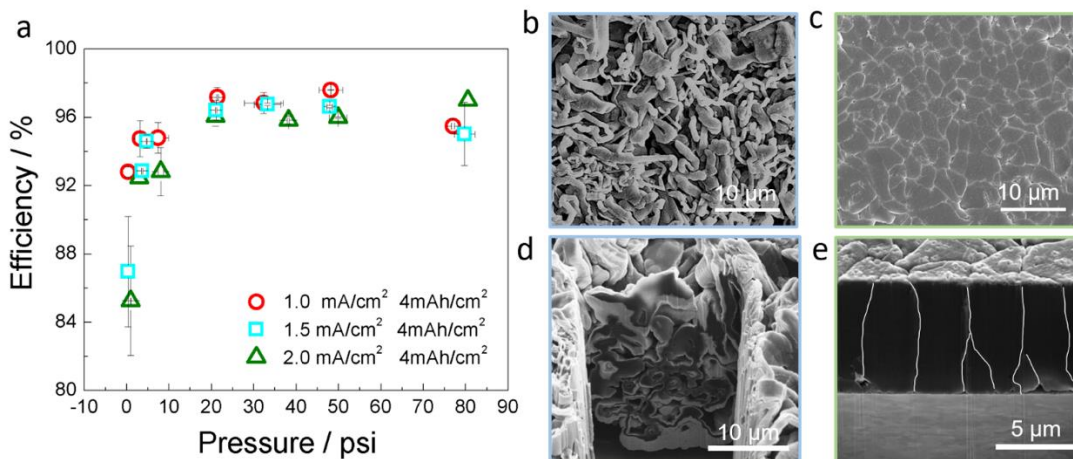


Figure 135. (a) Coulombic efficiency as a function of stacking pressure under various current densities. (b/d) Top view and cross-section view of deposited lithium morphology formed under no pressure. (c/e) Top view and cross-section view of deposited lithium morphology formed under critical pressure. The lithium in (b-e) was deposited at 2 mA/cm<sup>2</sup> for 1 hour.

## Highlights of Keystone Project 1

The highlights for this quarter are as follows:

- The defects in NMC cathodes were quantified by neutron powder diffraction (BNL).
- TFEO-based LHCEs with formulation of LiFSI-(1.2~1.3)DME-2TFEO have demonstrated 80% capacity retention over 200 cycles in 4.4 V Li||NMC-811 cells under practical conditions (PNNL).
- Four model solvent molecules (carbonate, sulfone, phosphate, and ether) in LHCEs for 4.4 V Li||NMC-811 cells were investigated, and DME-LHCE demonstrates the best stabilities on both lithium metal and NMC-811 (PNNL).
- New electrolyte approach reported for Li-metal/NMC cells with > 99.95% CE (Stanford).
- Columnar lithium deposits were achieved by optimizing stack pressure in cells in combination with the ether-based electrolytes (UCSD).

## Keystone Project 2: Electrode Architecture

The goal of Keystone 2 is to design, model, fabricate, and characterize the effect of electrode architecture on electrode and cell performance in support of reaching the project goal of 500 Wh/kg cell specific energy. Included in this Keystone are architecture design of thick cathodes (UCSD), Li-metal electrode architectures (PNNL, UCSD, and Stanford), inorganic (UT-Austin) and polymer (Stanford) electrolytes, and electrode performance modeling (UW). Highlighted this quarter are recent advancements at multiple institutions in advancing 3D Li-metal architecture and interfacial protection to improve its cycle life.

The Stanford group discovered that tortuosity is a critical parameter affecting the morphology and electrochemical performances of hosted lithium anodes. They synthesized three types of hosts: vertically aligned (VGA), horizontally aligned (HGA), and random rGO (RGA) electrodes with tortuosity of 1.25, 4.46, and 1.76, respectively. They show that high electrode tortuosity causes locally higher current density on the top

surface of electrodes, resulting in thick lithium deposition on the surface and degraded cycling performance. Low electrode tortuosity in the vertically aligned rGO host enables homogeneous lithium transport and uniform lithium deposition across the host, realizing greatly improved cycling stability (Figure 136). Using this principle of low tortuosity, the designed electrode shows through-electrode uniform morphology with anodic CE of 99.1% under high current and capacity cycling conditions (Figure 137).

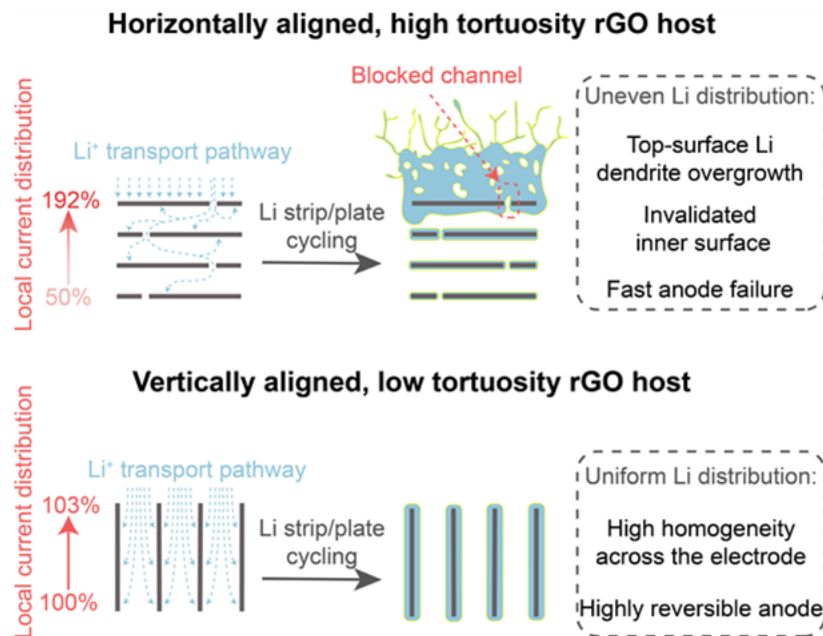


**Figure 136.** The tortuosity of reduced graphene oxide as a lithium host has a profound impact on lithium deposition. Vertically aligned host with minimal tortuosity results in more uniform lithium deposition in the host.

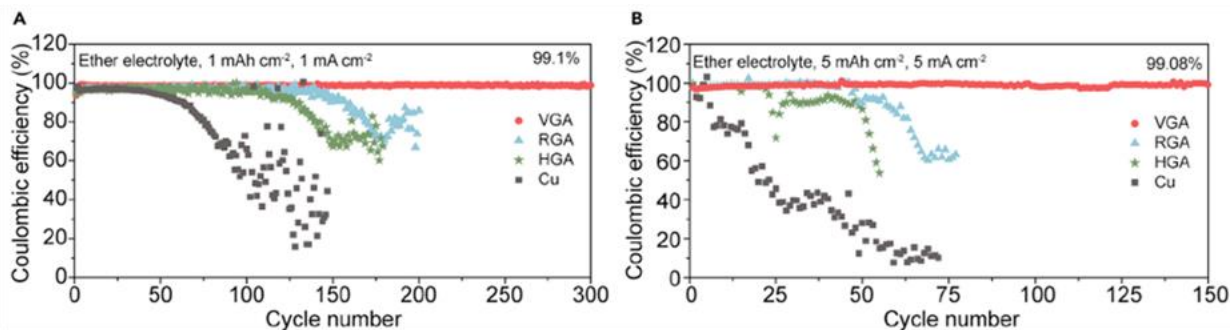


**Figure 137.** In an ether electrolyte (1 M of LiTFSI in 1:1 v/v DOL/DME with 1% LiNO<sub>3</sub>), VGA clearly outperforms RGA and HGA due to its low tortuosity. (LiTFSI: lithium bis(trifluoromethanesulfonyl)imide; DOL: dioxalane; DME: dimethoxyethane)

The UCSD group explored a 3D host based on porous copper obtained from dealloying Cu-Fe alloys to examine the effects of key physical properties (such as the surface area, pore size, and tortuosity) on the Li-plating morphology and cycling performances. By tuning the melting method and the atomic percentage (at%) of copper during the synthesis, four types of copper current collectors with a variety of pore sizes have been synthesized: 30Arc (30 at% of copper with Arc-melting), 20Arc, 10Arc, and 30Furnace (30 at% of copper with Furnace-melting). The three key physical parameters (that is surface area, pore size, and tortuosity) of the porous copper films mentioned above were quantified by laboratory X-ray microscale computed tomography (micro-CT). With spatial resolutions of 0.7834 μm or 1.07 μm depending on the pore size of the sample, the 3D tomography of each porous copper film was obtained from micro-CT (Figure 138d-e). With high-resolution 3D tomography, post measurement analysis was performed by Amira-Avizo software to calculate pore size

distribution, tortuosity, and surface area of the porous copper films. The pore size distribution in each porous copper film is shown in Figure 138a. Because of the high at% of copper and the fast melting rate, 30Arc gives the smallest pore size, which averages at around  $8\mu\text{m}$ . For the Arc-melting samples, as the at% of copper decreases in the Cu-Fe alloy, the average pore size of the resulting porous copper films increases. Because of the weak structure of the 10Arc, furnace was used to make the porous copper film (30Furnace) with the largest pore size, which has an average pore size of  $25\mu\text{m}$ . The tortuosity was obtained from the Centroid Path Tortuosity module in the Amira-Avizo, which computes the centroid of each plane and the corresponding path length between the centroids along the z-axis (electrode thickness) to determine the tortuosity. With the smallest average pore size ( $\sim 8\mu\text{m}$ ), 30Arc shows the highest tortuosity, which ranges from 1.9 to 2.05 as the thickness increases to  $100\mu\text{m}$  (Figure 138b). With the increased pore size in the 20Arc ( $\sim 11\mu\text{m}$ ), the resulting tortuosity decreases, since the larger pores provide a transport pathway for ions with less obstacles. As the pore size further increases in the 10Arc ( $\sim 20\mu\text{m}$ ), tortuosity further decreases to around 1.10 with a thickness of  $100\mu\text{m}$ . However, when the melting method was changed to make the 30Furnace samples, because of the higher at% of copper, the tortuosity slightly increased to 1.25 in these porous copper films. The effective surface area for each porous copper film with 7-mm diameter is listed in Figure 138c. With the smallest pores, 30Arc shows the highest effective surface area of  $29.49\text{ cm}^2$  in a 7-mm diameter piece, which is 76 times larger than that of the copper foil with the same diameter. The effective surface area decreases as the pore size increases in the porous copper. Nonetheless, the porous copper with the highest pore size, 30Furnace, still has almost 10 times higher surface area than the copper foil does. With three key physical parameters of the porous copper films quantified by micro-CT, the effects of surface area, pore size, and tortuosity on electrochemical performances will be studied with the aim to provide quantitative guidance to design 3D current collectors

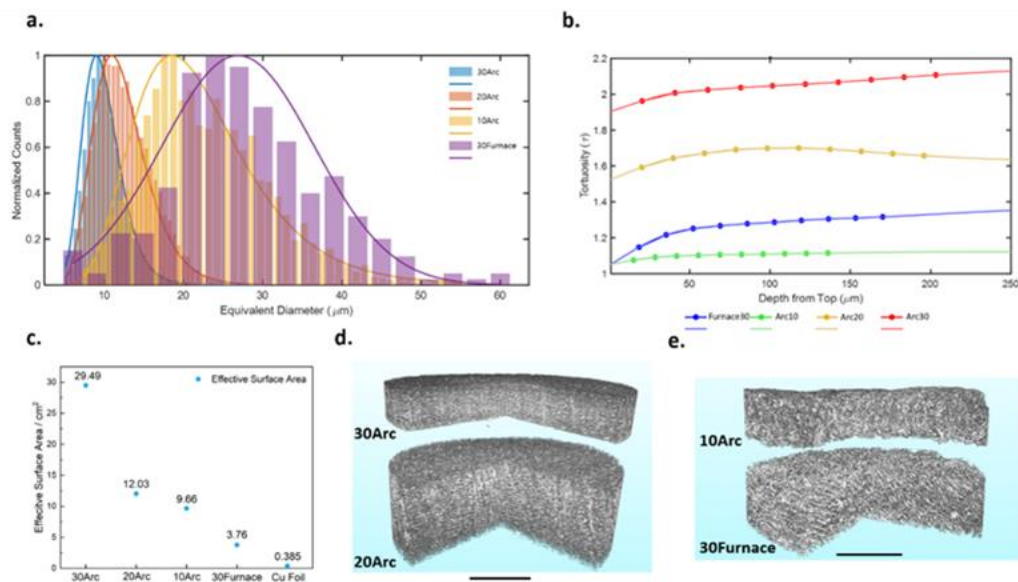


**Figure 138.** (a) Histogram of the pore size distribution of the porous copper. (b) Tortuosity of the porous copper as a function of depth. (c) Effective surface area in the porous copper. (d) The 3D tomography of 30Arc and 20Arc with resolution of  $0.7834\mu\text{m}$ . (e) The 3D tomography of 10Arc and 30Furnace with resolution of  $1.07\mu\text{m}$ ; the scale bar indicates  $200\mu\text{m}$ .

In addition to 3D hosts, a protective coating in the form of a thin polymer or inorganic film placed on the surface of Li-metal anode can enhance electrode stability, an approach being investigated by the UCSD group. The coating can reduce the permeating rate of LEs, alter ion transport properties, and change the deposition morphologies of lithium metal. In this regard, the swelling ratio of a polymeric coating in a LE can be finely tuned by varying the crosslinking density during the film formation process. In a polyacrylonitrile (PAN)-based system, they observed that reduction of the swelling ratio ( $DV/V$ ) reduces ionic conductivity ( $s$ ) while increasing the transference number of lithium cation ( $t_+$ ), as shown in Figure 139. They are studying how these ion transport properties and the swelling ratio impact the CE and morphology of Li-metal plating.

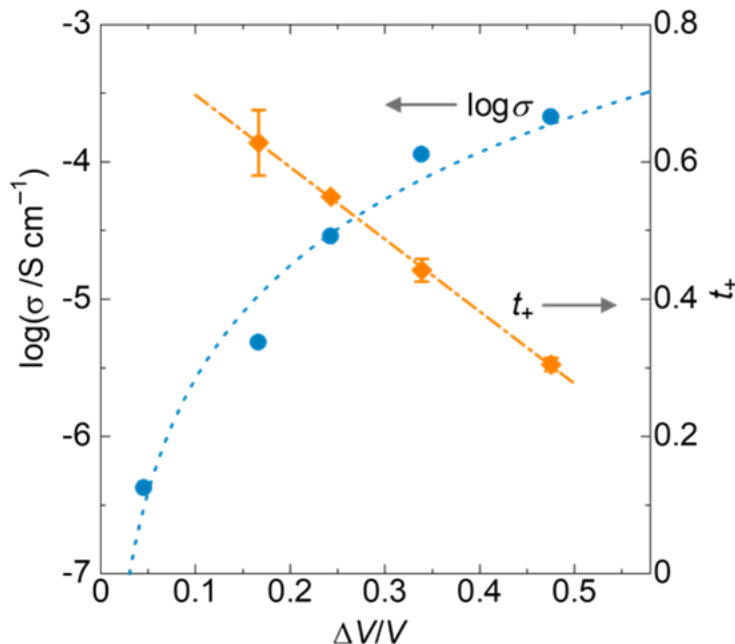


Figure 139. Cross-linking a polyacrylonitrile polymer results in a decrease in conductivity, but an increase in Li-ion transference number.

The UW Group creates ion conductive coatings on the polymer separator to regulate lithium deposition. Work this period focused on minimizing the thickness of the coating using nanomaterials. The polyethylene separator was coated with a nano-size LATP (Li-Al-Ti phosphate) by a doctor blade coating method. The average thickness of the separator is directly measured by a micrometer caliper, and it shows that the thickness of bare polyethylene and LATP-coated separator is 15.7  $\mu\text{m}$  and 17.1  $\mu\text{m}$ , respectively (Figure 140a-b). Therefore, the thickness of the coating layer is only 1.4  $\mu\text{m}$ . They also used SEM to measure the thickness of the coating layer. As shown in Figure 140c, the thickness of the LATP coating layer is  $\sim 2.6 \mu\text{m}$ , thinner than those of previous coated separators ( $\sim 5 \mu\text{m}$ ) based on micron-meter-sized LATP particles.



Figure 140. Photograph of the recorded thickness of (a) polyethylene (PE) and (b) LATP-coated PE separator by a micro-meter calliper. (c) Scanning electron microscopy image of the cross-section of the LATP-coated PE separator.

## Highlights of Keystone Project 2

The highlights for this quarter are as follows:

- Establishment of importance of tortuosity in determining Li-metal deposition in 3D hosts (Stanford).
- 3D characterization of porous metal hosts using tomography (UCSD).
- Nano-sized LATP enabling of the creation of separator coatings with much reduced thickness to regulate Li-metal deposition (UW).

### Keystone Project 3: Cell Fabrication, Testing, and Diagnosis

This quarter, multiple efforts in Keystone 3 were undertaken. Two highlighted here include the refinement of electrochemical models for Li-S cells and the advancement of rapid evaluation methods to evaluate expected cycle life for different electrode and materials level advancements. Not detailed are further advances in high-energy cell design and evaluation and refined analysis on cell-level and electrode-level materials utilization.

For the Li-S electrochemical model, a UT research team used a detailed one-dimensional (1D) model, and a Tanks-in-Series methodology was applied to generate a computationally efficient model that retains adequate physical detail while facilitating extensive parametric studies and parameterization against experimental data.<sup>[1]</sup>

Model comparisons of the Tank Model with the full 1D model are shown in Figure 141. For the Base Case parameters and discharge rates considered, the 1D model indicates negligible transport limitations in the Li-S cell. That means species concentration profiles and partial currents are relatively uniform across the electrode thickness, reducing the underlying cause of deviations between the Tank Model and the 1D model. In this limiting case, the Tank Model almost exactly matches the 1D model, as seen in Figure 141a. Convergence between two independent models under appropriate limiting conditions is reasonable evidence for computational accuracy. To further examine the Tank Model averaging and flux assumptions, the diffusion coefficient was varied over two orders of magnitude, which resulted in different transport effects on the solution. For the voltage curves in Figure 141a, the Base Case diffusion coefficient of  $1 \times 10^{-10} \text{ m}^2/\text{s}$  was used in the Tank Model and the 1D model. An analysis of characteristic time scales suggests that the Base Case parameters of Kumaresan, et al., correspond to a kinetically limited cell with negligible transport resistances.<sup>[2]</sup> Other workers have found that by changing the ionic diffusion coefficients by one to two orders of magnitude, the model was able to predict experimental data more accurately under varying rates.<sup>[3]</sup> For the simulations in Figure 141b, a reduced diffusion coefficient of  $1 \times 10^{-11} \text{ m}^2/\text{s}$  is used to induce additional transport limitations in the cell. At 0.2C and 0.5C rates, the difference in predictions between the 1D and Tank Models is negligible. The simulations at 1C indicate the overall voltage response is closely matched until the end of discharge, where increased concentration overpotentials produce deviations. For Figure 141b, a  $\delta = \frac{1}{3}$  is found to produce the least error compared to the 1D model.

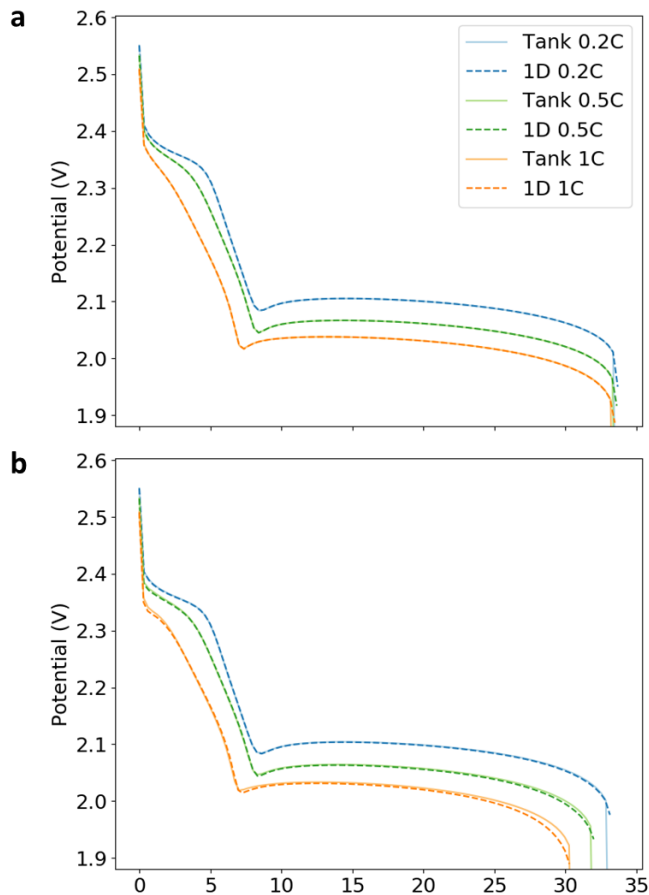


**Figure 141.** Comparison of Tank-in-Series model and 1D model predictions at rates of 0.2C (blue), 0.5C (green), and 1C (orange) (a) with the Base Case diffusion coefficient of  $1 \times 10^{-10} \text{ m}^2/\text{s}$ , and (b) with diffusion coefficient of  $1 \times 10^{-11} \text{ m}^2/\text{s}$  where transport limitations are introduced and some variation is introduced at the end of discharge.

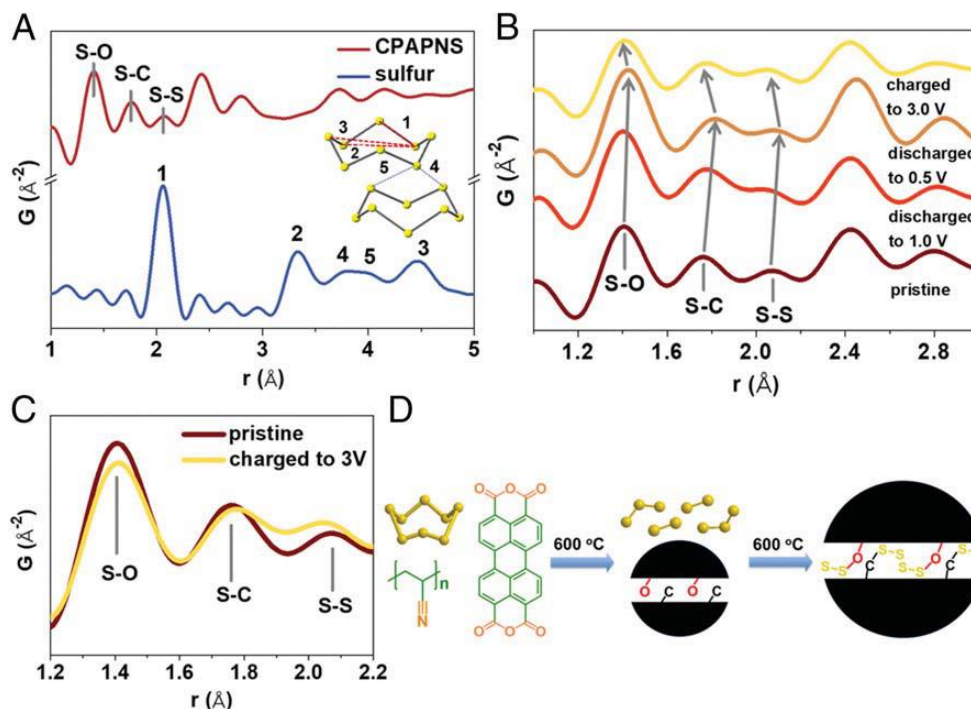


**Figure 142.** Pair distribution function (PDF) analysis and schematic illustration of the synthetic process of CPAPN-S. (a) PDF data of sulfur and CPAPN-S. Characteristic bonds and their corresponding PDF peaks are labelled. (b) PDF data of pristine and *ex situ* CPAPN-S electrodes in the 1<sup>st</sup> cycle, indicating that S-O, S-C, and S-S bond lengths generally increase during discharge and decrease during charge. (c) PDF data of charge-to-3V electrode overlaid on the pristine data (without offset), showing the decrease of S-O peak and increase of S-S peak after 1<sup>st</sup> cycle. (d) A schematic illustration of the formation of chemical bonding stabilized carbon-small sulfur composite.

The UM group synthesized and demonstrated a chemical bonding-stabilized high-capacity carbon/small sulfur composite as an improved cathode for Li-S battery using lean electrolyte. The strong chemical bonding of C-S and O-S groups in the carbonized perylenetetracarboxylic dianhydride (PTCDA) – PAN – S composite (CPAPN)–S composite is confirmed by Raman spectroscopy, FTIR, XPS, and PDF characterizations. The PDF characterization was carried out by the BNL team. The PDF analysis was adopted to analyze the activation mechanism, as it is ideal for analyzing complicated structure without crystallinity. It is possible to directly monitor the evolution of bonds of interest during electrochemical cycling. Figure 142a shows the PDF data of pristine sulfur and CPAPN–S. The PDF of S<sub>8</sub> is used as control. The puckered ring structure of S<sub>8</sub> is illustrated in the inset graph. It indicates that peaks 1 through 5 in sulfur PDF can be directly correlated with S–S atomic pairs within the S<sub>8</sub> molecule and between the molecules. Similarly, the PDF data of CPAPN–S show the presence of S–O (1.42 Å), S–C (1.76 Å), and S–S (2.07 Å) bonds in the material that are in good agreement with previous XPS studies. It is noted that the S–S bond length in CPAPN–S is very similar to that in the pure sulfur (2.06 Å, peak 1 in sulfur PDF). Figure 142b shows the PDF data of *ex situ* CPAPN–S during the 1<sup>st</sup> cycle. It clearly indicates that on lithiation the bond lengths of S–O, S–C, and S–S generally increase during discharge and decrease during charge. As illustrated by the arrows, the bond lengths generally show partially reversible change during the 1<sup>st</sup> cycle, suggesting the success of the proposed modification strategy by introducing the functional groups. A more detailed comparison between PDF data of the pristine material and the charged sample (Figure 142c) indicates that the S–O peak intensity decreases and the S–S peak intensity increases after the 1<sup>st</sup> cycle. This is very likely caused by the breakage of some of the S–O bonds and more availability of the S–S bond. Interestingly, the 2<sup>nd</sup> cycle electrochemical profile shows more capacity above 1 V, which is very likely contributed by lithium bonded to S–S parts. A schematic illustration (Figure 142d) for the synthetic process of CPAPN–S is presented based on the material characterizations and XPS and PDF results. When the mixture of sulfur, PAN, and PTCDA is annealed at 600 °C, the ring-structured S<sub>8</sub> is vaporized and dissociated into small sulfur molecules such as S<sub>2</sub> and S<sub>3</sub>, while PAN and PTCDA are carbonized to oxygen-containing

and nitrogen-containing carbon matrix at the same time. Then, the small sulfur molecules bond with -C and -O groups in CPAPN to provide the chemical bonding-stabilized high-capacity SSCCs. The resulting SSCCs are promising cathode materials for high energy lean electrolyte Li-S batteries.

PNNL has developed the *Li-Batt Design App*, which uses ML to help battery developers and researchers easily and rapidly design Li-metal-based pouch cells. The *Li-Batt Design App* helps researchers quickly obtain all possible combinations of design parameters, including those for different cathode materials and pouch cell dimensions, to achieve desired energy density.

### Highlights of Keystone Project 3

The highlights for this quarter are as follows:

- Tank-in-Series Li-S model with validation using a 1D model (UT-Austin).
- Development of methods to monitor bonding structure of modified CPAPN electrodes (BNL and UMD).
- Refinement of methods to quickly capture expected cell life using different electrochemical screening methods (INL).
- Analysis on high-energy cell designs following previously reported methods to look at material utilization and degradation (PNNL and INL).
- J. Xiao's group at PNNL developed a "Machine learning-assisted lithium metal battery design software package" (<https://www.pnnl.gov/technology/li-batt-design-app>).

#### References

- [1] Subramaniam, A., S. Kolluri, C. D. Parke, M. Pathak, S. Santhanagopalan, and V. R. Subramanian. *Journal of the Electrochemical Society* 167 (2020): 013534.
- [2] Kumaresan, K., Y. Mikhaylik, and R. E. White. *Journal of the Electrochemical Society* 155 (2008): A576.
- [3] Zhang, T., M. Marinescu, S. Walus, and G. J. Offer. *Electrochimica Acta* 219 (2016): 502.

## Patents/Publications/Presentations

### Patents

- Cao, X., J-G. Zhang, and W. Xu. Electrolytes for Rechargeable Metal-Sulfur Batteries. U.S. Patent Application No. 16/904,376. Filed on June 17, 2020.
- Yang, J., L. Yao, X. Wu, X. Jiang, and J. Liu. High Energy Lithium Batteries with Lean Lithium Metal Anodes and Methods for Prelithiation. U. S. Patent Application No. 63/046,918. Filed on June 30, 2020.

### Publications

- Xiao, J., Q. Li, Y. Bi, M. Cai, B. Dunn, T. Glossmann, J. Liu, T. Osaka, R. Sugiura, B. Wu, J. Yang, J-G. Zhang, and M. S. Whittingham. “Understanding and Applying Coulombic Efficiency in Lithium Metal Batteries.” *Nature Energy*. doi: 10.1038/s41560-020-0648-z. Publication Date (Web): June 25, 2020.
- Amanchukwu, C. V., Z. Yu, X. Kong, J. Qin, Y. Cui, and Z. Bao. “A New Class of Ionically Conducting Fluorinated Ether Electrolytes with High Electrochemical Stability.” *Journal of the American Chemical Society* 142, no. 16 (2020): 7393–7403. doi: 10.1021/jacs.9b11056. Publication Date (Web): April 1, 2020.
- Chen, H., A. Pei, J. Wan, D. Lin, R. Vilá, H. Wang, D. Mackanic, H-G. Steinrück, W. Huang, Y. Li, A. Yang, J. Xie, Y. Wu, H. Wang, and Y. Cui. “Tortuosity Effects in Lithium-Metal Host Anodes.” *Joule* (2020). doi: 10.1016/j.joule.2020.03.008. Publication Date (Web): April 8, 2020.
- Wang, H., X. Cao, H. Gu, Y. Liu, Y. Li, Z. Zhang, W. Huang, H. Wang, J. Wang, W. Xu, J-G. Zhang, and Y. Cui. “Improving Lithium Metal Composite Anodes with Seeding and Pillaring Effects of Silicon Nanoparticles.” *ACS Nano* 14, no. 4 (2020): 4601–4608. doi: 10.1021/acsnano.0c00184. Publication Date (Web): April 28, 2020.
- Chen, H., G. Zhou, D. Boyle, J. Wan, H. Wang, D. Lin, D. Mackanic, Z. Zhang, S. C. Kim, H. Ryoung Lee, H. Wang, W. Huang, Y. Ye, and Y. Cui. “Electrode Design with Integration of High Tortuosity and Sulfur-Philicity for High-Performance Lithium-Sulfur Battery.” *Matter* (2020). doi: 10.1016/j.matt.2020.04.011. Publication Date (Web): May 8, 2020.
- Zhou, G., A. Yang, G. Gao, X. Yu, J. Xu, C. Liu, Y. Ye, A. Pei, Y. Wu, Y. Peng, Y. Li, Z. Liang, K. Liu, L-W. Wang, and Y. Cui. “Supercooled Liquid Sulfur Maintained in Three-Dimensional Current Collector for High-Performance Li-S Batteries.” *Science Advances* 6, no. 21 (2020): eaay5098. doi: 10.1126/sciadv.aay5098. Publication Date (Web): May 22, 2020.
- Gao, X., X. Zheng, J. Wang, Z. Zhang, X. Xiao, J. Wan, Y. Ye, L-Y. Chou, H. K. Lee, J. Wang, R. A. Vilá, Y. Yang, P. Zhang, L-W. Wang, and Y. Cui. “Incorporating the Nanoscale Encapsulation Concept from Liquid Electrolytes into Solid-State Lithium-Sulfur Batteries.” *Nano Letters* (2020). doi: 10.1021/acsnanolett.0c02033. Publication Date (Web): June 9, 2020.
- Zhiao, Y., H. Wang, X. Kong, W. Huang, Y. Tsao, D. G. Mackanic, K. Wang, X. Wang, W. Huang, S. Choudhury, Y. Zheng, C. V. Amanchukwu, S. T. Hung, Y. Ma, E. G. Lomeli, J. Qin, Y. Cui, and Z. Bao. “Molecular Design for Electrolyte Solvents Enabling Energy-Dense and Long-Cycling Lithium Metal Batteries.” *Nature Energy* (2020): 1–8. Publication Date (Web): June 22, 2020.
- Mackanic, D. G., M. Kao, and Z. Bao. “Enabling Deformable and Stretchable Batteries.” *Advanced Energy Materials*. doi: 10.1002/aenm.202001424. Publication Date (Web): June 24, 2020.
- Kim, S., A. Raj, B. Li, E. J. Dufek, C. C. Dickerson, H. Y. Huang, B. Y. Liaw, and G. M. Pawar. “Correlation of Electrochemical and Mechanical Responses: Differential Analysis of Rechargeable Lithium Metal Cells.” *Journal of Power Sources* 463 (2020): 228180. doi: 10.1016/j.jpowsour.2020.228180. Publication Date (Web): April 29, 2020.

- Zhang, Y., Y. Lin, L. He, V. Murugesan, G. M. Pawar, B. M. Sivakumar, H. Ding, D. Ding, B. Y. Liaw, E. J. Dufek, and B. Li. “Dual Functional Ni<sub>3</sub>S<sub>2</sub>@Ni Core-Shell Nanoparticles Decorating Nanoporous Carbon as Cathode Scaffolds for Lithium-Sulfur Battery with Lean Electrolytes.” *ACS Applied Energy Materials* 3 (2020): 4173. doi: 10.1021/acsaem.0c00568. Publication Date (Web): May 5, 2020.
- Hossain, M. J., G. Pawar, B. Liaw, K. L. Gering, E. J. Dufek, and A. C. T. van Duin. “Lithium-Electrolyte Solvation and Reaction in the Anode/Electrolyte Interface of a Lithium Ion Battery: A ReaxFF Reactive Force Field Study.” *Journal of Chemical Physics* 152 (2020): 184301. doi: 10.1063/5.0003333. Publication Date (Web): May 8, 2020.
- Erickson, E. M., W. Li, A. Dolocan, and A. Manthiram. “Insights into the Cathode-Electrolyte Interphases of High-Energy-Density Cathodes in Lithium-Ion Batteries.” *ACS Applied Materials and Interfaces* 12 (2020): 16451–16461. doi: 10.1021/acsaem.0c00900. Publication Date (Web): March 17, 2020.
- Jiang, Q., P. Xiong, J. Liu, Z. Xie, Q. Wang, X-Q. Yang, E. Hu, Y. Cao, J. Sun, Y. Xu, and L. Chen. “A Redox-Active 2D Metal-Organic Framework for Efficient Lithium Storage with Extraordinary High Capacity.” *Angewandte Chemie* 132 (2020): 5311–5315. Publication Date (Web): March 23, 2020.
- Wang, X., X. Fan, X. Yu, S-M. Bak, Z. Shadik, I. Waluyo, A. Hunt, S. D. Senanayake, H. Li, L. Chen, C. Wang, R. Xiao, E. Hu, and X-Q. Yang. “The Role of Electron Localization on Covalency and Electrochemical Properties of Lithium-Ion Battery Cathode Materials.” *Advanced Functional Materials*. doi: 10.1002/adfm.202001633. Publication Date (Web): May 13, 2020.
- Luo, C., E. Hu, K. J. Gaskell, X. Fan, T. Gao, C. Cui, S. Ghose, X-Q. Yang, and C. Wang. “A Chemically Stabilized Sulfur Cathode for Lean Electrolyte Lithium Sulfur Batteries.” *PNAS* 117, no. 26 (2020): 14712–14720. doi: 10.1073/pnas.2006301117, Publication Date (Web): June 17, 2020.

#### Presentations

- Stanford Energy Storage International Online Symposium (May 2, 2020): “The Origins of the Lithium Battery and Future Challenges/Opportunities”; M. S. Whittingham. Invited.
- Lindau Nobel Laureates Meetings, Online (June 29, 2020): “Batteries”; M. Stanley Whittingham. Invited.
- Elsevier, Online Webinar (April 3, 2020): “From Innovation to Commercialization for Materials, Energy, and Environment”; Y. Cui. Invited.
- ACS Online Webinar (May 14, 2020): “Facial Masks during COVID-19: Disinfection, Homemaking and Imaging”; Y. Cui. Invited.
- MIT InnoTherm Symposium, Online Webinar (June 17, 2020): “Thermal Effects on Battery Materials and Chemistry”; Y. Cui. Invited.
- Clean Energy Institute Virtual Seminar, University of Washington: “Integrating Materials Science, Electrochemistry and Engineering in Energy Storage Technologies”; J. Xiao.
- National Science Foundation – Industry-University Cooperative Research Center Conference, Austin, Texas (April 7, 2020): “Rechargeable Battery Chemistry”; A. Manthiram. Invited plenary.
- NASA Decadal Plan – Energy Storage Needs, Austin, Texas (May 25, 2020): “High-Nickel Cathodes for Lithium-Ion Batteries”; A. Manthiram. Invited.
- Electrochemical Society Webinar, Austin, Texas (June 17, 2020): “Intricacies of High-Energy Cathodes for Lithium-Ion Batteries”; A. Manthiram. Invited.
- Virtual Workshop on Rechargeable Batteries, University of Texas, Austin, Texas (June 25, 2020): “A Perspective on Next-Generation Battery Chemistries”; A. Manthiram. Invited.